NOZZLE EROSION IN HYBRID ROCKET MOTORS

A DISSERTATION
SUBMITTED TO THE DEPARTMENT OF
AERONAUTICS AND ASTRONAUTICS
AND THE COMMITTEE ON GRADUATE STUDIES
OF STANFORD UNIVERSITY
IN PARTIAL FULFILLMENT OF THE REQUIREMENTS
FOR THE DEGREE OF
DOCTOR OF PHILOSOPHY

Pavan Narsai
December 2016

Abstract

Nozzle erosion in hybrid rocket motors is an unsolved and generally unstudied problem that poses a hurdle to small-scale and long-burning hybrid rocket motor development. While the nozzle erosion problem has been studied extensively in liquid rocket engines and solid rocket motors, it has remained largely untouched for the hybrid rocket configuration.

In this research, nozzle erosion is measured in a small lab-scale motor utilizing gaseous oxygen and paraffin wax as propellants at various chamber pressures and oxidizer to fuel (O/F) ratios. Paraffin-based fuels are of particular interest as they are inert and have proven high-performance capabilities. An ultrasound sensor along with an array of thermocouple sensors are placed at the nozzle throat plane of the motor and the combination of the recorded data allows for the reconstruction of the time-varying wall thickness at the throat plane. This data is used to determine nozzle erosion, as well as a time varying estimate of the inner wall heat flux at the nozzle throat plane. While the nozzle erosion data is the primary interest for this study, other researchers may find the heat flux estimations useful as they can be used in the validation of CFD models.

A dimensionless model is then proposed to capture the affects of O/F ratio, chamber pressure, nozzle material properties, flame temperature, efficiency, and mixing. This dimensionless model can be used to estimate nozzle erosion for any given hybrid rocket motor design, which should be useful to hybrid rocket motor designers.

Acknowledgments

None of the work I accomplished at Stanford would have been possible without the help of many people. Professor Brian Cantwell, my advisor, always provided the advice and assistance I needed while still giving me nearly absolute independence to pursue my research interests and truly learn. I recall a few instances where I thought a problem would set me back at least a few months, if not longer. A simple chat in each of those cases resulted in overcoming the problem within a few hours, if not less. I also appreciate the countless hours that Professor Cantwell spent with me going through similarity solutions for various partial differential equations.

I also thank the additional members on my reading committee, Professors Juan Alonso and Sigrid Close. They have provided valuable feedback to me regarding my research as well as given me a different perspective on my work. Without their inputs, my work would feel a lot less complete. I've actually got fond memories of both Professor Alonso and Close as the courses they've taught are some of the most memorable ones I've taken. I'm also extremely thankful to both Professor Debbie Senesky and Professor Reginald Mitchell for agreeing to participate in my defense committee. Professor Mitchell generously agreed to chair my defense even though he chaired another defense for another student in our lab just two weeks prior. Overall, I'm very happy that scheduling the defense date was quite an easy process as these professors were happy to move around their prior engagements to make the defense possible.

I'm also thankful to Stanford University and the Department of Aeronautics and Astronautics. They provided me not only an acceptance letter, but also extensive funding. I was accepted under a one-year Department Fellowship through the Stanley Robert Jorgensen Scholarship Fund, without which I would not have been able to attend Stanford University in the first place. After I passed the PhD qualifying exams, the department again came to my aid in the form of a larger three year fellowship through the Robert E. Gross Fellowship from Lockheed Martin. This fellowship allowed me to pursue my own research interests as there were very few strings attached to this funding. Additionally, a Jet Propulsion Laboratory grant titled Thermal Analysis of Hybrid Rockets provided support for my research as well. In five of the quarters where I was not funded, the department graciously selected me to be a Course Assistant or a Teaching Assistant for the compressible flows, aircraft and rocket propulsion, and the advanced rocket propulsion series courses. Without these

fun opportunities, my research would have been very difficult to complete, and my grad school experience would be incomplete as well.

In addition to all of the advice and financial aid given to me from Stanford-affiliated people, I also obtained technical advice from numerous outside people and it would be impossible to name them all. Greg Zilliac from NASA Ames was instrumental in providing feedback for my rocket motor designs as well as giving them confidence. With his opinions, hitting the "fire" button for the first time was a little less (but still very) stressful. Jerry Rutherford from NDT Systems also provided a great deal of confidence in my experiment. Although his job was primarily to sell our lab an ultrasound system, he went very much above and beyond what anyone would expect. Instead of waiting months to respond to my technical questions with "maybe" (as representatives from other larger companies did), he responded with "let's try it out" and invited me to his office to run some simple tests and answer any of my questions in person – before any commitments were made. Without this help, this experiment would probably never be built.

I'd also like to thank Vincent Gau, President of Genefluidics, Inc., and also a friend. I formerly worked with him before coming to Stanford and have maintained contact since. When it came time to build my experiment, I realized that in order to stay comfortably within budget, I would need to build some portions of the rocket motor myself. Vincent opened up the company's machine shop for my unlimited use, free of charge. At one point, I was running a laser cutter, CNC Mill, and a manual mill all at the same time. In all, I was able to fabricate the necessary components in about a week. This level of productivity and efficiency cannot be achieved at the Stanford Product Realization Lab. Without this huge favor, I imagine it would have taken me several more months (and likely a larger budget) to fabricate the necessary components.

I also thank the numerous lab members that I've had the pleasure of working with. These include Ashley Karp, Tim Szwarc, Ashely Micks, Ben Waxman, Jonah Zimmerman, Beth Jens, Javier Stober, Flora Mechentel, Ashley Coates, Adrian Boiron, Krishna Venkataraman, and Priya Challa, and anyone else I might have missed. I should also thank the students from the AA 284 series courses that I was a TA for – they voted me best TA for the year.

I had the opportunity to mentor two students throughout my stay here at Stanford. These students led projects in our lab that were instrumental to my PhD progress and success. I thank Edward Momanyi, an undergraduate Stanford student at the time, for his work on rebuilding the spin-casting machine, finding the optimal settings for my specific fuel grain size, and for obtaining density measurements on the fuel grains. He also helped in testing the early versions of the inverse heat conduction solver, where he looked specifically for problematic input heat flux profiles. I also thank Adrian Costantino, a visiting undergraduate researcher from the California Institute of Technology, for his work on ultrasound imaging of fuel grains. With this study, I was able to gain valuable experience with ultrasound, which allowed me to get usable data for the nozzle erosion measurements.

Professor Tiziana Vanorio and Dr. Andy Clark of the Stanford School of Earth, Energy, and Environmental Sciences also generously allowed use of their lab and helium pycnometer for fuel grain density measurements. Dr. Andy Clark graciously spent several hours with Edward and I over the course of a few weeks to show us how to use the helium pycnometer and how to obtain accurate density readings. I'm very thankful for this help, as we learned that the highest achievable fuel densities are actually higher than previously thought.

I'd like to thank Dr. Rajvee Bhakta for providing me with so much support and love throughout my PhD studies. As you said about me: "There are some people in your life who make you laugh a little louder, smile a little bigger, and live a bit better". You're exactly that to me too.

I'd lastly like to thank my family. I've been blessed with having a truly amazing set of people to grow up with and who I can constantly rely on. My parents always encouraged me to pursue my dreams and did whatever they could to allow me to do so. My older cousins (who I consider my siblings) supported me in countless ways so that I could attend Stanford. Without the support of my grandparents, parents, sister, and many cousins, I wouldn't be the person that I am today, nor would I be completing this PhD.

Contents

List of Tables

List of Figures

Nomenclature

α	Thermal diffusivity, Coefficient of Thermal Expansion
χ	Location of thermocouple, Mass fraction
Δr	Grid spacing
Δt	Time step size
ΔV	Change in Velocity
$\dot{m}$	Mass Flow Rate
$\dot{r}$	Regression Rate
η	Efficiency
γ	Ratio of Specific Heats
λ	Guess heat flux
μ	Dynamic viscosity
ρ	Density
τ	Thermocouple measurement
θ	Minimization function
A	Area
AR	Nozzle Area Ratio
$C*$	Characteristic Velocity
C_f	Thrust Coefficient
C_p	Isobaric specific heat capacity
D	Diameter
E	Young's Modulus
f	Applied heat flux
G	Shear Modulus, Mass Flux
g	Acceleration due to gravity
G_{ox}	Oxidizer Mass Flux
GOX	Gaseous oxygen
h_g	Estimated heat transfer coefficient
Isp	Specific Impulse
K	Thermal Conductivity, Bulk Modulus
M	Mach number, Total Mass
N	Total number of nodes
O/F	Oxidizer-to-Fuel Mass Ratio
P	Pressure
Pr	Prandtl number
Q	Total number of thermocouples
R	Radius
r	Radial coordinate
r_c	Radius of curvature
S	Number of future time steps
s	Future time step number
t	Time
t_b	Time length of burn
u	Velocity
v	Speed of Sound
Y	Numerical solution to heat equation
a,n	Regression Rate Constants
d	Thickness
L	Length of Fuel Grain
Nu	Nusselt Number
Re	Reynolds Number
St	Stanton Number
T	Thrust, Temperature

Subscripts

∞	Upstream flow condition

f	Fuel
i	Thermocouple number, initial, inside
j	Index location
o	Oxidizer, Reference Condition, outer
ox	Oxidizer
w	Wall condition
a	Ambient
c	At the Chamber
e	At the Exit
sep	Separation
t	At the Throat

Acronyms

AR	Nozzle Area Ratio
CAD	Computed Aided Design
CEA	Chemical Equilibrium with Applications
CFD	Computational Fluid Dynamics
CTE	Coefficient of Thermal Expansion
DAQ	Data Acquisition
EPDM	Ethylene Propylene Diene Monomer
FEA	Finite Element Analysis
FFT	Fast Fourier Transform
HSV	Hue Saturation Value
LED	Light Emitting Diode
LOX	Liquid Oxygen
MAV	Mars Ascent Vehicle
NI	National Instruments
P&ID	Plumbing and Instrumentation Diagram
PID	Proportional Integral Derivative Controller
PTFE	Polytetrafluoroethylene
RFNA	Red Fuming Nitric Acid
RGB	Red Green Blue
SAE	Society of Automative Engineers
SPaSE	Stanford Propulsion and Space Exploration Lab
SRB	Solid Rocket Booster
USB	Universal Serial Bus
VCP	Virtual COM Port

Superscripts

$*$	At the Throat when Choked
n	Time step

Chapter 1

Introduction

Thesis Organization

This thesis is organized into eight chapters. The first chapter introduces the reader to the hybrid propulsion system as well as the nozzle erosion problem through the means of an example design problem. Chapter Two includes the theory for the bulk of this research. This includes a discussion of the solution to the heat heat equation and its inverse solution, the nozzle material properties, and speed of sound within the nozzle material.

The third and fourth chapters describe the experiment design and set up, including descriptions of the data acquisition system, the motor ignition system, and some in depth descriptions of the internal geometries of the motor.

Chapter Five describes the data collected from the motor from the twenty two hot fire tests completed. The data set includes pressure traces, nozzle erosion measurements (through ultrasound measurements), and thermal heat flux measurements at the nozzle throat plane. Some important findings are also discussed in this chapter. The complete data set is printed in Appendix J of this thesis.

In the sixth chapter, the nozzle erosion data is combined and a nozzle erosion model is proposed. A brief description of the model is also given along with some sample calculations.

Chapter Seven deviates a bit from the nozzle erosion problem and contains some work regarding the visualization of fast burning fuels. The regression rate of paraffin is estimated through direct visual measurements and compared to model equations found in the literature.

The eighth chapter contains a recap of all of the work completed in this research along with some recommendations for future designs to minimize nozzle erosion. This chapter also contains a list of noteworthy contributions made throughout this research study.

Introduction

This chapter first introduces the hybrid rocket concept. Then the reader will be introduced to some basic nozzle performance parameters and the nozzle erosion problem through a preliminary design study of a long burning hybrid rocket motor. This study was done with the goal of learning to design a hybrid rocket motor. The result of this study was a preliminary design of the motor as well as a recognition of the key problem of nozzle erosion. This provided the motivation for the rest of my research. The experiment and research goals are briefly discussed at the end of this chapter.

1.1 An Introduction to the Hybrid Rocket Motor

The hybrid rocket motor dates back nearly 100 years to the 1930's, where a Russian group led by Tikhonravov and Korolev successfully built and flew a hybrid rocket motor [1]. However, the hybrid configuration has not been nearly as technologically developed as solid and bi-liquid propellant systems.

The hybrid rocket is essentially a cross between a solid and a bi-liquid rocket engine. The term 'hybrid' is used because the propellants are separated by phase. Hybrid rocket motors burn solid and liquid propellants, as opposed to bi-liquid engines, which burn only liquids, and solid motors, which burn only solid propellants.

This separation of phase brings about several benefits that solid and bi-liquid engines sorely lack. Arguably the most important of these is the fact that solids and gases do not mix. Because of this, a pool of unintentionally mixed propellants (such as the resulting exhaust plume when propellant tanks need to be evacuated), poses virtually no explosion hazard. Furthermore, the propellants themselves can be inert, simplifying transportation. This greatly reduces costs. In fact, a kilogram of paraffin wax, a proven high performance hybrid rocket fuel used in this research, can be purchased for just a few dollars with standard shipping. One kilogram of pre-mixed solid rocket propellant might cost several hundred dollars or more, and can only be transported as a hazardous material.

The hybrid configuration is also mechanically simple. The feed system required to pump liquid oxidizer and liquid fuel in a bi-liquid rocket engine can be very complex, as shown in Figure 1.1. In a hybrid system, the complexity is immediately halved, as only one liquid propellant is used. Furthermore, pumping hardware is not always required, as several popular hybrid oxidizers have self-pressurizing properties. Although solid rocket motors are mechanically simpler, as they do not require a feed system at all, they cannot be easily throttled. Emergency shutdown procedures generally call for a violent depressurization of the motor (destruction). Furthermore, solid rocket motors have limited performance capabilities, while hybrids have capabilities similar to those of liquid rocket engines. In short, hybrid rocket motors provide liquid engine-like performance in a simpler mechanical design that allows flexible packaging.

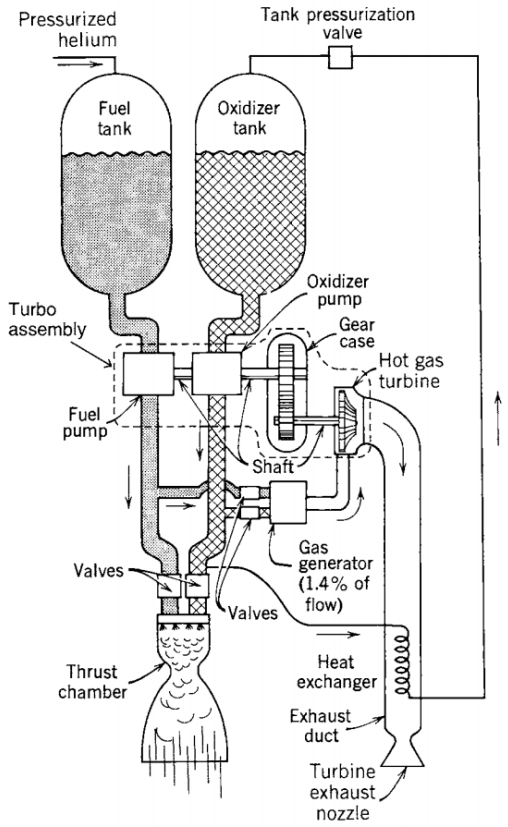

Figure 1.1: A simplified schematic diagram of a turbo-pump fed liquid propellant rocket engine highlights just how complicated these systems are. Reprinted with permission from Reference [2]

1.1.1 The Main Components of a Hybrid Rocket Motor

All hybrid rocket motors have several key components. The first is the oxidizer tank. Although hybrid rocket motors can utilize gaseous or liquid fuels and solid oxidizers, fuels are usually selected as the solid propellant as they are more abundant and easier to handle than solid oxidizers.

Hybrid rocket motors also contain a main valve. This valve controls the flow rate of oxidizer into the combustion chamber. It can be used to throttle, shutdown, or even restart a motor. The rocket motor designed and tested in this research utilized flow rates between 25 grams per second and 90 grams per second. Although the motor was not "throttled" in the literal sense, the fact that the motor burned well at such a large range of flow rates indicates that hybrids can provide deep throttling capabilities. This could be useful for systems designed to land vehicles gently.

The final component of the typical hybrid rocket motor is the combustion chamber. The combustion chamber in a hybrid rocket motor provides dual functionality. It houses the solid fuel grain

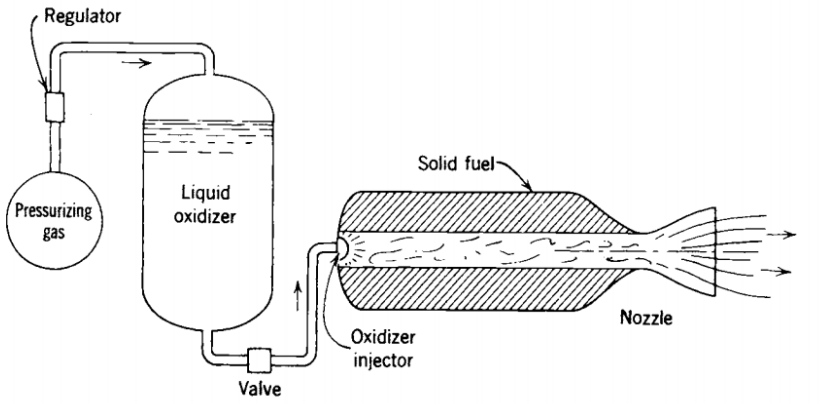

Figure 1.2: A schematic of a simple hybrid rocket motor. Reprinted with permission from Reference [2]

and also provides volume for the propellants to mix and react. One end of the combustion chamber contains the nozzle, where the combustion products are accelerated and exhausted to generate thrust.

In addition to providing potentially affordable propulsion system solutions, the hybrid rocket configuration also provides competitive performance. The Solid Rocket Boosters (SRB) on the Space Shuttle provided a specific impulse of 292 seconds [2]. Space Exploration Technologies' (SpaceX) Merlin Vacuum engine, which burns liquid oxygen (LOX) and kerosene [3], provides an ideal vacuum Isp of 342 seconds [4]. A quick ideal computation with paraffin and oxygen propellants burning at an O/F ratio of 3.0 in a combustion chamber operating at 3.4 MPa with shifting equilibrium and a nozzle expansion factor of 200 yields an ideal specific impulse of 385 seconds. However, actual delivered impulse would be considerably lower. In a vacuum, the performance could be comparable to the Merlin Vacuum engine.

It should be important to note that not any one configuration is generally "better" than the others. Propulsion systems are very expensive systems that generally need to be designed and built specifically for certain missions. In some scenarios, the liquid-liquid configuration is the best fit for the mission. For others, solids.

Hybrid fuels can be tailored to provide desirable physical properties in addition to combustion properties. This means that hybrid propellants can be designed to survive in a wide range of harsh environments, something that liquid and solid propulsion systems struggle with. The hybrid configuration is particularly well-suited for low budget missions, missions requiring a long shelf life, and for missions in harsh environments.

One scenario where the hybrid rocket configuration could be applied is the Mars Ascent Vehicle (MAV) [5]. The large temperature swings from -111C to 24C on Mars make it difficult to store a

solid rocket grain on Mars for extended periods of time. Furthermore, the relatively high freezing points of some liquid propellants pose additional challenges in utilizing a bi-liquid propulsion system for the MAV mission.

For the hybrid case, Boiron et al. have shown that oxygen can likely be derived from the Martian atmosphere [6], meaning only a fraction of the propellants would need to be sent to Mars. It should be noted however that deriving oxygen from the Martian atmosphere, cooling it to the liquid phase, and then pumping it into an oxidizer tank (all autonomously) are still difficult problems that need to be addressed.

Although there are numerous benefits that the hybrid configuration provides, critics often point out the fact that the hybrid configuration is yet to be proven. Although several large scale motors have been tested (and flown), the hybrid design has not yet been flown on a large scale mission. The most famous examples of the hybrid configurations are the previously flown Space Ship One and now the Space Ship Two, which is under development by Virgin Galactic. NASA has tested a large scale hybrid rocket motor under the Hybrid Propulsion Demonstration Program (HPDP). This motor delivered up to 1 million Newtons of thrust and was developed specifically to mature the hybrid technology readiness level [7].

1.2 An Introduction to Basic Nozzle Performance

Rocket motor nozzles are typically mechanically simple devices [8]. Their primary functions are to generate thrust from the hot gases in the combustion chamber through expansion. Critical performance parameters of nozzles include the area ratio, which is the nozzle exit area divided by the nozzle throat area, the thrust coefficient, C_f,and the operating pressure ratio, which is the chamber pressure divided by ambient pressure. Ideal nozzles have very little mass, are geometrically short, and provide maximum thrust.

1.2.1 Nozzle Performance

The most important dimensionless nozzle performance parameter of any rocket propulsion system is the thrust coefficient, C_f. It comes from the definition of thrust for ideal gas under steady flow conditions, as given by Equations 1.1-1.3. The full derivation is given in Appendix C. From Equation 1.3 [2], it can be seen that C_f is a function of few variables. Because of this, C_f curves can be generated to easily estimate nozzle performance for any given rocket motor. Figure 1.3 shows the thrust coefficient curves for γ=1.30.

$$T = \dot{m}u_e + (P_e - P_a)\,A_e \tag{1.1}$$

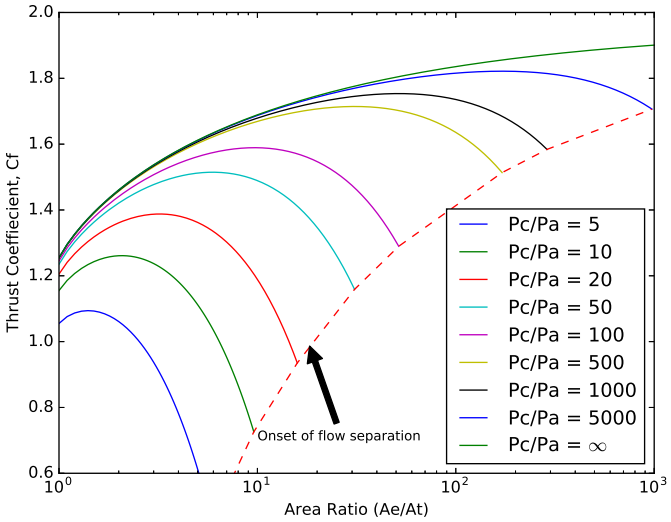

Figure 1.3: The C_f for rocket motor nozzles curves show how one can expect an ideal nozzle to behave. Note that $\gamma = 1.30$ in this case. For any given pressure ratio, a C_f maximum exists. If a nozzle operates in a region where it is significantly overexpanded, flow separation becomes unavoidable [9], as shown.

$$C_f = \frac{T}{P_c A_t} \tag{1.2}$$

$$C_f = \sqrt{\frac{2\gamma^2}{\gamma-1}\left(\frac{2}{\gamma+1}\right)^{(\gamma+1)/(\gamma-1)}\left[1-\left(\frac{P_e}{P_c}^{(\gamma-1)/\gamma}\right)\right]} + \frac{P_a - P_e}{P_c}\frac{A_e}{A_t} \tag{1.3}$$

Where T is thrust, $\dot{m}$ is the mass flow rate, u_e is the exit velocity, P_e is the exit pressure, P_a is the ambient pressure, A_e is the exit area, C_F is the thrust coefficient, A_t is the throat area, P_c is the chamber pressure, and γ is the ratio of specific heats.

Alternatively, this could be written in terms of the exit Mach Number, M_e.

$$C_f = \frac{1}{\left(\frac{\gamma+1}{2}\right)^{\frac{\gamma+1}{2(\gamma-1)}}} \frac{\left(\gamma M_e^2 + 1 - \frac{P_a}{P_e}\right)}{M_e\left(1+\frac{\gamma-1}{2}M_e^2\right)^{\frac{1}{2}}} \tag{1.4}$$

Note that for any given pressure ratio, the curve has a maximum corresponding to ideal expansion. That is, the exit pressure of the expanded flow perfectly matches the ambient pressure outside of the nozzle. Thrust is maximized at this condition. When the area ratio is larger than the optimal condition, the flow is said to be overexpanded. If the area ratio is much higher than the idea

size, flow separation becomes unavoidable. The Summerfield criterion (Equation 1.5) is used to estimate the area at which flow separation is unavoidable in Figure 1.3, although numerous other criteria exist [9]. The Summerfield criterion states that flow separation is unavoidable at the location where the flow pressure is equal to roughly a third of the ambient pressure. Flow separation is not generally a concern for designers because the onset of separation occurs when the nozzle operates so overexpanded that the C_f is far below optimal.

$$\frac{P_{sep}}{P_a} = 0.34 \; to \; 0.4 \tag{1.5}$$

Equation 1.5 predicts the location where the flow separates within the nozzle. P_sep refers to the local static pressure within the nozzle at the separation point.

When a nozzle is overexpanded, the pressure at the exit of the nozzle is less than the ambient pressure and an oblique shock forms outside of the nozzle to raise the exhaust pressure to match ambient conditions.

When the nozzle area ratio is smaller than the ideal case, the flow is said to be underexpanded. In the underexpanded case, the pressure at the exit of the nozzle is higher than the ambient pressure and this case corresponds to points on the left side of the optimal C_f curve for any given pressure ratio.

In practice, it is very difficult to achieve perfect expansion in a rocket motor, as a variety of factors come into play. For example, consider a launch vehicle ascending from ground level. The ambient pressure changes with altitude and therefore the nozzle only achieves ideal expansion at one particular altitude. However, well-designed nozzles can achieve very high nozzle efficiencies (99% is not considered unusual) [2].

The resulting expansions and oblique shock waves outside of the nozzle tend to overcompensate for the pressure difference and this results in repeated shock wave patterns. The end result is the diamond shock pattern typically seen behind rocket engines in the atmosphere, as seen in Figure 1.4.

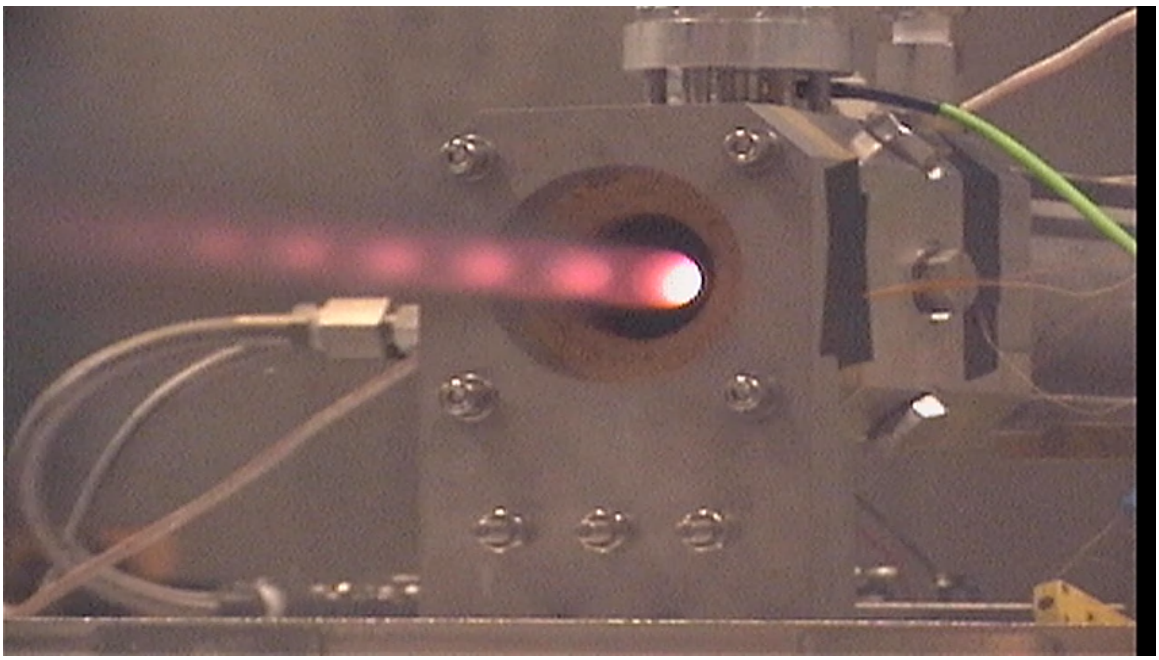

Figure 1.4: A diamond shock pattern is seen in the plume of the experimental motor during the first test. These repeated patterns are a result of repeated expansion and shocks in the plume of the motor.

1.2.2 Effect of Nozzle Erosion

Nozzle erosion is the phenomena where the surface of the nozzle wall erodes away due to the hot gases flowing through them. This phenomena is particularly problematic at the nozzle throat section, where the heat and mass fluxes are the highest in the motor [10]. This erosion has a direct impact on the performance of rocket motor nozzles as it directly reduces the nozzle area ratio. Note that typically, the exit area experiences only negligible erosion due to the fact that the heat and mass fluxes at the exit plane are smaller.This implies that the heat transfer rates into the nozzle material near the exit are significantly less than at the throat section [11]. Furthermore, the hot gases in the chamber typically experience significant expansion through the nozzle and have both lower static temperatures and pressures by the time they reach the exit plane. Additionally, the small amount of nozzle erosion in the exit plane typically only causes negligible changes in the area ratio, as the exit area is usually much larger than the throat area.

In hybrid rockets, nozzle erosion causes performance losses in two manners. The first loss is due to the obvious loss in area ratio and the shift left along the given C_f curve. The second loss is a little more subtle. In hybrid rocket motor design, the chamber pressure is determined by the nozzle throat area, propellant mass flow rate, and the C^* obtained from the combusting propellants. For a constant mass flow rate and C^*, nozzle erosion causes a loss in chamber pressure. When a system operates in a non-vacuum environment, the associated loss can be observed by shifting to lower C_f curves based on the reduced pressure ratio. Another loss that could potentially be associated with this loss in pressure could be reduced ideal Isp. It should be noted that nozzle erosion can be particularly problematic for small scale propulsion systems, because a small change in nozzle throat radius can lead to a large percentage change in throat area, as shown in Equation 1.6.

$$A(R_t) = \pi R_t^2$$

$$A(R_t + \Delta R) = \pi \left(R_t + \Delta R\right)^2$$

$$\frac{A(R_t + \Delta R)}{A(R_t)} - 1 = \frac{\pi \left(R_t + \Delta R\right)^2}{\pi R_t^2} - 1 = 2\frac{\Delta R}{R_t} + \frac{\Delta R^2}{R_t^2} \tag{1.6}$$

In Equation 1.6, A refers to the area, R_t refers to the throat radius, and ΔR refers to a change in the throat radius.

For a small throat radius, R_t, the resulting $\frac{A(R_t+\Delta R)}{A(R_t)} - 1$, or the percentage change in area due to an absolute change in radius, is much higher than for large throat radii. This percentage change approaches zero for very large R_t. Therefore, nozzle erosion, which can be represented as an absolute change in radius, or the ΔR, has much more of an impact in small scale systems and should be considered during the design of small scale motors.

Table 1.1: List of considered oxidizers.

Oxidizer	**Melting Temperature (C)** [14]	**Boiling Temperature (C)** [14]
Oxygen	-218.4	-183
Nitrous Oxide	-90.86	-88.5
Dinitrogen Tetroxide	-9.3	21.15
Inertized Red Fuming Nitric Acid (Irfna)	-65	60
Nitric Acid	-41.6	83
Hydrogen Peroxide	-0.4	150.2
Ammonium Dinitramide	92	NA

1.3 Preliminary Design of a Long Burning Hybrid Rocket Motor

A long-burn mission is proposed for a hybrid rocket motor and it is desired to perform a preliminary design study of a hybrid propulsion system that can satisfy the mission. The mission parameters given are a 3600 second burn time, a thrust requirement of 890N (200 lb), and a system capable of delivering a ΔV of 1.4 km/s. An additional 300 m/s is required for thrust vectoring during the burn. Other requirements include a separate hydrazine system for attitude control and dual feed system components for redundancy. A payload mass of 3500kg is given as well as operating temperatures between 20C and 60C. In short, the following requirements are posed:

- Burn time = 3600 seconds
- ΔV = 1.7 km/s
- Total payload = 3500 kg
- Redundancy = 2 valve system
- 20C to 60C operating conditions

A preliminary sizing of a hybrid motor meeting the specifications was completed and one of the most challenging aspects of this design study was the propellant selection. The fuel choice was paraffin, a proven high performance fuel [12], with some aluminum additive to reduce the O/F ratio requirements [13]. The oxidizer choice was more challenging as it was difficult to find an oxidizer that was storable for long periods of time at the required temperatures, is nontoxic, high-performing, and not-explosive. There is no known oxidizer that meets all of these ideal conditions. A list of popular oxidizers for hybrid rocket systems is shown in Table 1.1.

It was decided that it would be too early in the design stage to select an oxidizer for this particular mission. Instead, four liquid oxidizers were recommended for consideration. The considered oxidizers and their respective performance characteristics are listed in Table 1.2. Note that these computations were done in a software package named Chemical Equilibrium with Applications (CEA) [15] with

Table 1.3: Long burning hybrid rocket design parameters

Parameter	**Value**
Delivered Isp (s)	314.6
C* (m/s)	1678
η_c	0.96
O/F	2.18
ΔV(km/s)	1.7
Thrust (kN)	3.6
Initial Nozzle AR	200
Final Nozzle AR	26.8
Starting C_f	2.13
Ending C_f	1.92
Average C_f	2.03
Propellant Mass (kg)	4220
Payload Mass (kg)	3500
System Mass (kg)	9960
Structural Mass fraction	0.22
Initial Chamber Pressure (MPa)	1.03
Starting Exit Velocity (m/s)	3412
Ending Exit Velocity (m/s)	2948

paraffin fuel with 40% aluminum loading and a shifting equilibrium assumption at a chamber pressure of 1.03 MPa (150 psi) and a nozzle area ratio of 70.

Table 1.2: Recommended short-list of oxidizers for long-burn space mission.

Oxidizer	**Density** (g/cm^3)	**Optimal O/F**	**C*** (m/s)	γ	**Vacuum Isp** (s)
Hydrogen Peroxide	1.45	3.82	1740	1.114	363
Dinitrogen Tetroxide	1.44	2.18	1668	1.124	345
Irfna	1.51	2.64	1626	1.119	338
Nitric Acid	1.51	2.73	1618	1.119	336

It should be noted that each of the suggested oxidizers has its own set of challenges that need to be addressed should the design move forward. The sizing was carried out for all four oxidizer selections with conservative mass allowances. A conservative nozzle throat erosion rate of .00254 mm/s (0.0005 in/s) is used [2]. The sizing study results are shown in Table 1.3 for dinitrogen tetroxide as the oxidizer choice.

Note that even a conservative value of 0.00254 mm/s of nozzle erosion rate results in a large nozzle throat regression. Although at first glance the nozzle erosion problem does not seem critical (because C_f changes minimally), this problem requires further study. Recall that in hybrid rocket design, the nozzle throat area determines the operating chamber pressure given C* and propellant flow

rate. Therefore, if the throttle was held constant throughout the 3600 second burn, the combustion chamber pressure would be reduced by a factor of 7.5 *simply due to nozzle erosion!*

To highlight the performance losses associated with nozzle erosion, it can be useful to compare the ΔV while assuming the nozzle throat area remains constant. The ΔV equation is shown in Equation 1.7.

$$\Delta V = g_0 \, I_{sp} \, ln\left(\frac{M_i}{M_f}\right) = U_e \, ln\left(\frac{M_i}{M_f}\right) \tag{1.7}$$

In Equation 1.7, the ΔV refers to the change in velocity, g_0 refers to the acceleration due to gravity on Earth, I_sp refers to the thrust specific impulse, and M_i and M_f refer to the initial and final system mass, respectively.

In the first case, where the nozzle is held constant at the initial area ratio (and the starting chamber pressure of 1.03 MPa), the exit velocity would be 3412 m/s. If it was assumed that the eroded nozzle were used for the duration of the full burn, the exit velocity would be 2948 m/s.

In the first case, the system would provide a ΔV of 1879 m/s. For the second case (assuming nozzle area ratio remains constant at 26.8), the ΔV is 1623 m/s, a reduction of 250 m/s compared to the first case.

If the mission requires the original 1879 m/s, additional propellant must be added to the motor of the second case. To increase the ΔV from the second case up to 1879 m/s, 900 kg of additional propellants would be required. This is a significant change introduced solely by the change in nozzle throat areas.

Although the above example is not realistic as it considers two different nozzles at constant area ratios, it is a value that can be computed easily that highlights the extreme case losses that could be attributed to nozzle erosion.

Another less-desirable consequence of nozzle erosion is related to the structural capabilities of the motor itself. Recall for the long-burn motor the chamber pressure changes by a factor of nearly 7.5. For obvious reasons, the wall thickness of the combustion chamber must be thick enough to support the initial chamber pressure of 1.03 MPa. Towards the end of the burn, where the chamber pressure is significantly reduced, the walls of the combustion chamber are overly thick and are essentially unnecessary structural mass.

This drives the overall system design to lower chamber pressures. At some point, wall thicknesses are constrained by realistic fabrication limits, not by structural requirements. It should be noted that the selection of chamber pressure and hybrid system optimization are still open problems that are actively being researched.

1.4 Experiment Overview

The goal of this research is to measure time-varying nozzle erosion in a small-scale hybrid rocket system and to propose a method for predicting nozzle erosion in other systems based on O/F ratio,

chamber pressure, propellants, and efficiency. A small-scale hybrid rocket motor was designed and built for this purpose. The nozzle in this motor is equipped with an ultrasound transducer and several embedded thermocouples. The combination of these sensors provide enough data to allow for the tracking of the nozzle throat area while the motor is burning.

The ultrasound transducer provides time-varying nozzle wall thickness data, which is related to nozzle erosion. Because the use of the ultrasound technique requires knowledge of the speed of sound, the speed of sound of the nozzle material, graphite Grade GR001CC, is needed. Unfortunately, the speed of sound of the nozzle material is known to change with temperature, so some thermal analysis is required in order to obtain accurate ultrasound results.

Analysis of the thermocouple data is conducted using an inverse heat conduction problem solver. The output of this analysis is an estimate of the time-varying temperature profiles at the nozzle throat plane. These profiles are then used to generate a time-varying estimate of the speed of sound of the nozzle material at the throat plane by comparing to the known correlation between speed of sound and temperature. With the estimates of speed of sound, raw ultrasound data is scaled to the correct spatial dimensions and an estimate of the nozzle erosion during a burn can be computed.

An additional output of the inverse heat conduction analysis is an estimate of the heat flux applied at the inner surface at the nozzle throat plane. These heat flux estimates are useful to researchers developing CFD models of hybrid rocket systems.

The main goal of this research is to measure nozzle erosion and see how it changes with combustion pressure and O/F ratio. To date, these measurements have not been taken on a hybrid propulsion system and there is not a complete set of nozzle erosion measurements for a hybrid system in the literature. An additional goal of this research includes taking this measurements with an ultrasound sensor in real time (while the motor is burning), as well as proposing a model to the data found. The ultrasound method of tracking the nozzle erosion is a novel approach that has not been explored before and may be helpful in other future studies.

Chapter 2

Theory

This chapter introduces the background data and theory for the analysis of the presented research. This includes a small discussion on graphite material properties, temperature dependence on the speed of sound in the nozzle material, and an introduction to the ultrasound pulse-echo technique used in this research. Heat transfer in the nozzle is addressed with a numerical integration of the nonlinear heat equation, along with exact solutions to simple heat equation problems to validate the integration scheme. An inverse heat conduction solution developed specifically for the nozzle throat plane is introduced and a discussion on the validation of the solver is also included.

2.1 Graphite Material Properties

Graphite is a great nozzle material choice for many simple rocket systems. It is one of very few materials that can withstand the extreme environment of a combustion chamber in a rocket motor as well as survive the thermal shock of a rocket motor ignition sequence.

The graphite used in all of this research is Grade GR001CC [16], from www.graphitestore.com. This graphite is isostatically pressed and is considered to be nearly isotropic [17]. A single batch was purchased to manufacture all of the nozzles for this research as well as sample blocks used to determine the thermal properties. Using graphite from the same production batch ensured that the material properties would be consistent across all graphite parts made in this research. Laser flash analysis (LFA), differential scanning calorimetry (DSC), and helium pycnometry were all performed on sample blocks by Linseis to determine the thermal diffusivity, specific heat, and density of the graphite material [18]. Note that with the measured quantities, the thermal conductivity can be inferred by the definition of thermal diffusivity [19], as shown in Equation 2.1. Note that thermal diffusivity is denoted as α, the thermal conductivity is denoted as K, density is denoted as ρ, and

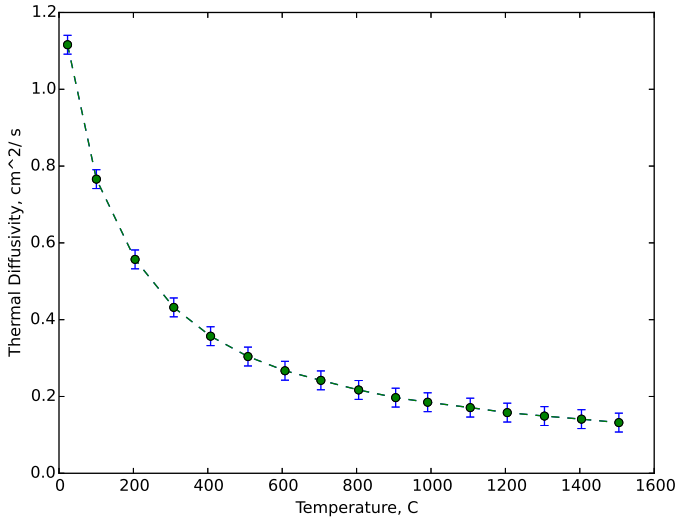

Figure 2.1: The thermal diffusivity was measured from room temperature to 1500 C by Linseis. Diffusivity measurements were taken at 100 C intervals, as shown by the blue markers. The vertical bars on the blue markers indicate the uncertainty as specified by Linseis. The data between each blue marker was linearly interpolated, as shown by the green dotted lines. Higher temperature data was linearly extrapolated to 0.11 cm^2/s at 3500 C (not shown), based on published high-temperature measurements of graphite [21].

the specific heat is denoted as C_p.

$$\alpha = \frac{K}{\rho C_p} \tag{2.1}$$

While it is standard practice to assume that graphite density remains constant throughout the full temperature range [20], the other properties change drastically, as seen in Figures 2.1 and 2.2. Because of this, the variable material properties need to be taken into account in the heat transfer analysis.

The measured density of the graphite was 1.793 g/cm^3. According to the specifications provided by the laboratory that evaluated the thermal properties, the uncertainties of the testing methods were 1% for helium pycnometry, 2.2 % for LFA, and 5% for the thermal conductivity deduction. Note that the thermal diffusivity changes by a factor of almost 10 between room temperature and 1500 C. At high temperatures, the thermal diffusivity becomes very small [21] and the graphite material behaves like an insulator. This is great for rocket nozzle applications because most of the heat is limited spatially to just a narrow region near the nozzle's inner wall, while the rest of the nozzle and nozzle retaining structures remain relatively cool. However, one should note that thermal diffusivity is not zero and for long burns, the entire nozzle and retaining structures will eventually get hot.

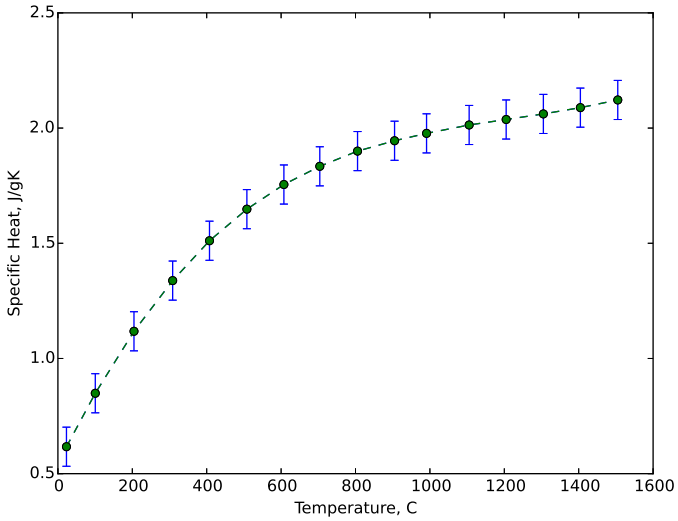

Figure 2.2: The specific heat was measured from room temperature to 1500C by Linesys using DSC. Specific heat measurements were taken at 100 C intervals, as shown by the blue markers. The vertical bars on the blue markers indicate the uncertainty as specified by Linseis. The data between each blue marker was linearly interpolated, as shown by the green dotted lines. Higher temperature data was linearly extrapolated to 2.5 J/kgK at 3500 C (not shown), based on published high-temperature measurements of graphite. [21]

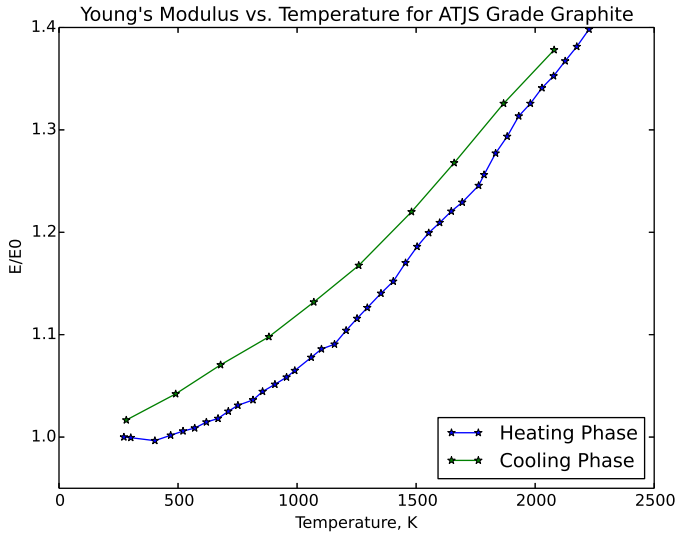

Figure 2.3: Young's Modulus varies with temperature for ATJS grade graphite. There is about a 40% increase in Young's Modulus between room temperature and 2000 Celsius. There is some hysteresis between cooling and heating data.

Because the thermal diffusivity changes in such a large manner, it is important to account for variable thermal properties for any analysis done with graphite materials in rocket motor systems. When considering variable thermal properties, the heat equation becomes nonlinear and is significantly more difficult to solve, as discussed in Section 2.3.1.

The structural properties of graphite also change with temperature. The moduli data was available for several fine grade graphites [22]. While the moduli data for graphite grade GR001CC was not available, the data for the ATJS grade of graphite was estimated to be similar because of the matching densities between the two [23] [20]. The moduli data for ATJS grade graphites are plotted in Figures 2.3 and 2.4.

Note the hysteresis in the recorded data suggests that graphite heating and cooling behavior is not linear. This was seen in the experiments for the fuel rich test cases, where the nozzle throat section seemed to shrink slightly during tests. For this research, only data in the heating phase is considered. Even more interesting than the hysteresis, the graphite seems to get stiffer with temperature. This observation has also been reproduced by other researchers [24]. This is different than many other typical materials used in rocket propulsion systems, such as aluminum [25] and stainless steel [26]. This property also makes graphite a great material choice for rocket nozzle applications. As the nozzle gets hot, it becomes stiffer, which allows it to better retain its shape despite the large shearing forces exerted on the nozzle by the hot gases from the combustion chamber. The temperature dependence of the elastic moduli also suggests that the speed of sound of the nozzle

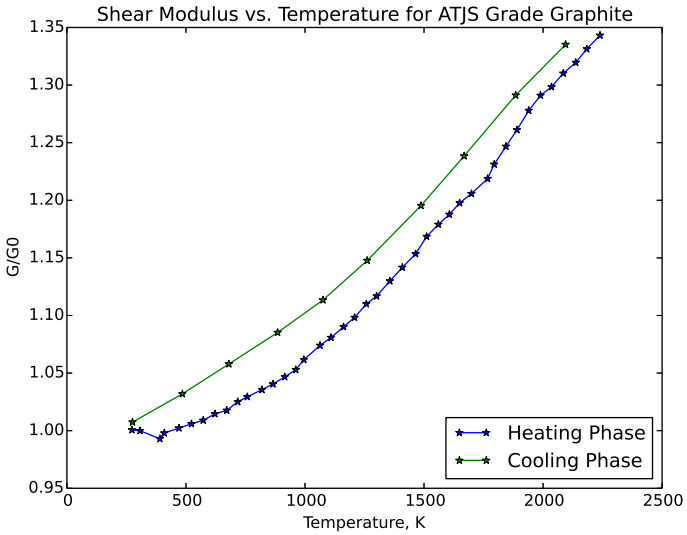

Figure 2.4: Shear modulus varies with temperature for ATJS grade graphite. There is about a 35% increase in the shear modulus between room temperature and 2000 Celsius. There is some hysteresis between cooling and heating data.

material is temperature dependent, which makes the use of ultrasound a bit more challenging.

2.1.1 Speed of Sound in Graphite

In this research, the most important time-varying parameter (other than nozzle throat area) is the speed of sound in the nozzle at the throat plane. In fact, all of the thermal analysis in this research is done to provide a good estimate for the speed of sound in the nozzle material. The speed of sound of any solid material is known to be related to its elastic properties with the relationship given by Equation 2.2 [27]. The speed of sound, v is not *exactly* equal to the root of the bulk modulus, K, divided by the density, instead, the speed of sound is proportional to the root of the bulk modulus divided by the density.

$$v \approx \sqrt{\frac{K}{\rho}} \tag{2.2}$$

For isotropic materials, the bulk modulus, K, can be evaluated by any two other elastic properties, such as Young's Modulus (E) and the Shear Modulus G, as shown in Equation 2.3 [28].

$$K = \frac{EG}{3\left(3G - E\right)} \tag{2.3}$$

The normalized speed of sound in terms of Young's Modulus and Shear Modulus is then known, as shown in Equation 2.4.

$$\frac{v}{v_0} = \sqrt{\frac{K}{K_0}} = \frac{\sqrt{\frac{EG}{3(3G-E)}}}{v_0} \tag{2.4}$$

Using the data from Figures 2.3 - 2.4 along with Equation 2.4, the full temperature-varying speed of sound profile can be generated, as seen in Figure 2.5. The uncertainty of this profile is discussed in Section 5.6. Note that between room temperature and 2000K the speed of sound increases by 25%. This indicates that the variable speed of sound must be accounted for to accurately utilize the ultrasound transducer data.

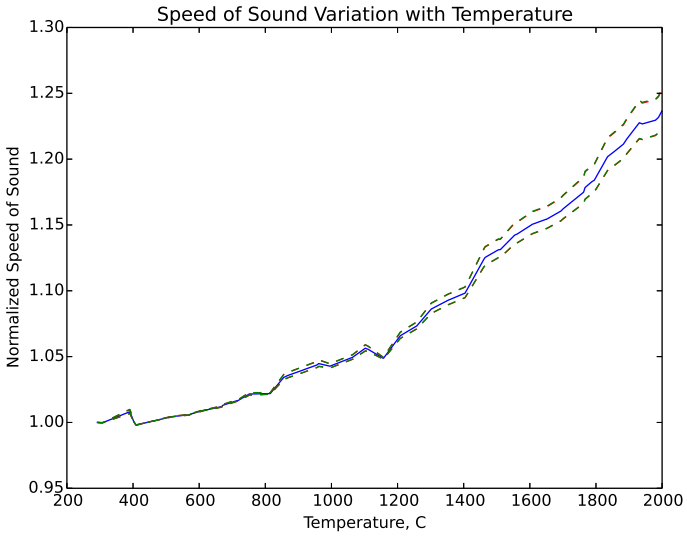

Figure 2.5: The normalized speed of sound profile shows that the speed of sound can change by over 25% between room temperature and 2000K. The green dotted lines are the computed uncertainties (See Section 5.6 based on the uncertainties of the underlying quantities of Equation 2.4.

2.1.2 Hysteresis and the Speed of Sound

The hysteresis in Figures 2.3 and 2.4 suggest some permanent changes are occurring within the graphite material that change the mechanical properties of graphite. This raises some concern as the speed of sound may also be changing as well. If the speed of sound of the graphite material is permanently altered, then without knowledge of the full temperature history of the material, it would be difficult to accurately use the ultrasound technique for the measurement of the nozzle wall thickness.

In this research, a calibration block is used to calibrate the ultrasound transducer before each test. However, if the hysteresis in the heating history of the machined graphite nozzle changes the material properties such that the speed of sound is changed, the calibration is inherently incorrect.

To understand the error introduced because of the hysteresis in the mechanical properties of the graphite, the test data from Figures 2.3 and 2.4 is used to compute the change in the speed of sound for a graphite sample heated to 2273K and then returned back to room temperature.

The shear modulus of the thermally cycled sample is increased by about 1%. Young's modulus is increased by 2%. Applying these changes to Equation 2.4 and normalizing to the original room temperature speed of sound yields an increase in the speed of sound by about 1.3%. This is a small value, especially when considering the fact that this is the change in the speed of sound when the entire sample is cycled to 2273K and back. In practice, the sample temperatures are significantly

lower and the bulk of the nozzle material remains at relatively low temperatures. This suggests that the permanent change in the speed of sound within the graphite material due to hysteresis is negligible between rocket motor firings for this research in particular. This hysteresis may need to be further investigated for longer burning systems.

2.2 Ultrasound Pulse-Echo Technique

Ultrasound is a nondestructive evaluation technique that uses high frequency waves and their reflections to get an understanding of the material being tested [27]. In typical engineering applications, ultrasound is frequently used to inspect welds for quality, pipes for corrosion, and to measure material thicknesses. Other common applications include ultrasound for therapeutic purposes as well as medical purposes.

Ultrasound is a technique that operates on the fact that acoustic waves have finite velocities in materials. Because of this, an acoustic pulse applied to the surface of a material will travel through the material and be partially reflected back at a velocity equal to the speed of sound of the material. The reflected pulse will eventually reach the surface from which the pulse originated. The time difference between when the pulse is sent and when the reflected pulse returns can be measured. With knowledge of the speed of sound, the material thickness can be deduced with Equation 2.5.

$$d = v\Delta t/2 \tag{2.5}$$

Note the factor of two present in Equation 2.5 corrects for the fact that the wave travels the depth of the material twice before it is detected at the source plane.

At material interfaces, a portion of the wave energy will be reflected back towards the source, and another portion will be transmitted through the interface into the next material. The transmitted wave will then travel through the next material at a new velocity equal to the speed of sound of the next material. This wave will eventually reach the end of the material and reflect back. If attenuation is not a problem, the reflected wave will go back through the interface and back to the source plane. Depending on the speed of sounds of the materials, the time difference between when various reflections are detected at the source plane can yield the thickness of the second block of material. In this case, the first block is called a delay line, as it is used as a delay between the ultrasound transducer and the block being evaluated.

For measuring nozzle erosion, a delay line is used to protect the sensor from the high temperatures that the nozzle can reach. Recall that ultrasound sensors are made of piezo-electric materials, which have relatively low Curie temperatures on the order of 150 C. If an ultrasound transducer goes over the Curie temperature, it can no longer function [29].

In this research, a long 2.54 cm (1 in.) delay line made from a proprietary high temperature plastic is used between the sensor and the nozzle. This ensures that the ultrasound transducer is

protected from the high temperatures. High temperature anti-seize is used as a couplant between the interfaces [30]. A high temperature couplant is desired so that good acoustic contact remains between the interfaces despite elevated temperatures.

When using ultrasound, a single speed of sound value is desired to convert time-of-flight data to a thickness measurement. Because the speed of sound in the graphite nozzle is known to vary with temperature [31], some idea of the temperature history of the nozzle is required. For accuracy, a full time-varying temperature profile is computed using embedded sensors and the solution of an inverse heat conduction problem, as described in the following sections. Once the time-varying temperature profiles are computed, the integral average speed of sound can easily be determined.

2.2.1 Thermal Expansion

Most materials expand or contract when they experience temperature changes. Usually, a constant coefficient of thermal expansion (CTE), α, is supplied and thermal expansion is modeled as a linear phenomenon. The simple linear equation for thermal expansion is shown in Equation 2.6.

$$\Delta L = L_0 \alpha \Delta T \tag{2.6}$$

Where ΔL is the total elongation, L_0 is the initial length, and ΔT is the change in temperature.

For materials that have temperature-varying coefficients of thermal expansion, the simple linear equation does not hold. The differential form of the equation, as shown in Equation 2.7 must be integrated.

$$\alpha(T) = \frac{1}{L_0}\frac{dL}{dT} \tag{2.7}$$

The differential form of the thermal expansion equation can be easily integrated by separation of variables. For a constant CTE, Equation 2.7 reduces to Equation 2.6 when integrated. For a material experiencing a temperature gradient, the thermal expansion can be estimated numerically for a finite number of points within the material.

Thermal Expansion of Graphite

The manufacturer of the graphite used in the fabrication of the nozzles for this research provides a constant coefficient of thermal expansion of 4.6 $\mu m/m^{\circ}C$. The manufacturer does not provide any other information, such as the uncertainty in the supplied value or the reference temperature. This CTE is significantly smaller than previously found by other researchers [32]. Tsang et al. have shown that the coefficient of thermal expansion is temperature dependent and larger. Figure 2.6 shows CTE measurements for a fine-grained graphite varies between about 25 $\mu m/m^{\circ}C$ and 45 $\mu m/m^{\circ}C$ within the temperatures of interest. Furthermore, the source of the bulk material used in the production of graphite has a large impact on the coefficient of thermal expansion for the graphite. Hidnert found

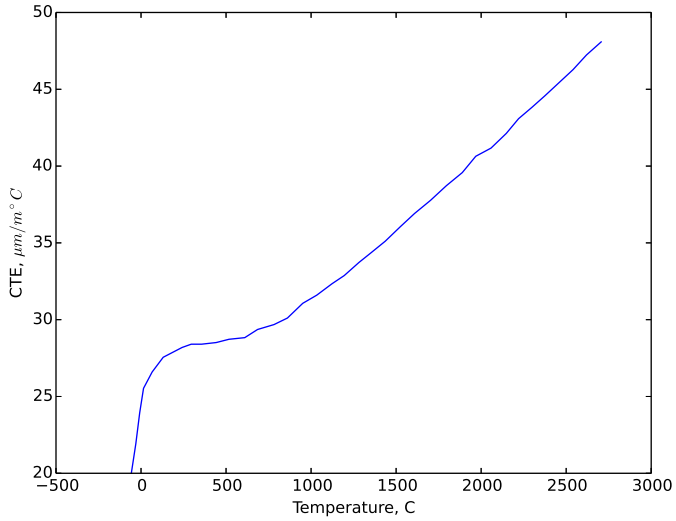

Figure 2.6: Temperature Dependence on the coefficient of thermal expansion of Graphite from Reference [32]. The coefficient of thermal expansion nearly doubles between room temperature and 2500 Celsius. This suggests that the thermal expansion of graphite is a nonlinear phenomenon.

that the CTE of graphite produced from lampblack are about three times larger than the CTE of graphite produced from petroleum coke [33]. Based on the ultrasound data, it is likely that the CTE of the graphite used in this research is significantly higher than the estimates provided by both the manufacturer and Tsang.

It should be noted that the ultrasound measurement technique measures the wall thickness of a material. This includes an increase in wall thickness for materials undergoing thermal expansion. Because of this, the ultrasound data measured in this research is the coupled thermal expansion and nozzle erosion data. At first glance, this is not ideal, as nozzle erosion is the desired measurement. However, the motor performance is based on nozzle erosion and thermal expansion. Therefore, the coupled ultrasound measurements provide actual measurements time-varying measurements.

The Density of Graphite

As mentioned earlier, the density of graphite is taken to be constant in practice. However, the CTE is nonzero and this implies that the density of the graphite must change to accommodate thermal expansion. Assuming the CTE of the graphite used in this research is roughly three times larger than Tsang's measurments [32], the worst case change in density could be estimated.

With a linear CTE estimate of 100 $\mu m/m°C$ and a change in temperature of 1000K, the change in density of a graphite sample would be just 9%. Note that the volumetric CTE is defined as

three times the linear CTE [33]. This change in density is much greater than what is experienced in the research data as the entire graphite nozzle does not get heated by 1000K. A more reasonable conservative estimate would be 300K, which would result in a density decrease of just 3%. The density change drops even further to 0.7% when using Tsang's linear CTE measurements of around 30 $\mu m/m^{\circ}C$.

This simple calculation shows why the density of graphite can be considered relatively constant. Although a worst case of 10% change in density is a rather large change, recall that the thermal diffusivity changes by a factor of about 10 over a similar range of temperatures.

2.3 Nozzle Heat Transfer

Consider a hybrid rocket motor nozzle during combustion. Hot gases enter from the combustion chamber and are accelerated out of the motor through the nozzle channel. Intuitively, the nozzle walls are expected to be heated immensely. The well-known Bartz Equation [34] provides a simple estimate for the convective heat transfer coefficient at the throat section and downstream. Upstream of the throat section, the Mach numbers are lower and radiative heat transfer is said to play a large role in heat transfer [11]. Equation 2.8 shows the Bartz equation with the suggested correction factor of 0.026 [34]. The full derivation of the equation is shown in Appendix B.

$$\begin{aligned} h_g &= \left[\frac{0.026}{D_*^{0.2}}\left(\frac{\mu^{0.26}C_p}{Pr^{0.6}}\right)\left(\frac{P_0 g}{c^*}\right)\left(\frac{D^*}{r_c}\right)^{0.1}\right]\left(\frac{A^*}{A}\right)^{0.9}\sigma \\ \sigma &= \left[\left(\frac{\rho_{ref}}{\rho}\right)\left(\frac{\mu_{ref}}{\mu_0}\right)^{0.2}\right] = \frac{1}{\left[\frac{1}{2}\left(\frac{T_w}{T_0}\right)\left(1+\frac{\gamma-1}{2}M^2\right)+\frac{1}{2}\right]^{0.8-m/5}\left[1+\frac{\gamma-1}{2}M^2\right]^{m/5}} \end{aligned} \tag{2.8}$$

Where h_g is the convective heat transfer coefficent, D_* is the throat diameter, μ is the dynamic viscosity, Pr is the Prandtl Number, C^* is the characteristic exhaust velocity, and r_c is the radius of curvature of the nozzle.

Bartz' Equation simply provides a steady estimate of the heat transfer coefficient. It does not provide a time-varying estimate of the heat transfer coefficient, and is not enough to accurately predict time-varying temperature profiles. Furthermore, a heat transfer coefficient is not a complete boundary condition because the free stream temperature is unknown. Therefore, it would not be possible to accurately estimate time-varying nozzle temperatures with just this equation. Accurate time-varying boundary condition data is required in order to obtain a good understanding of nozzle heating during combustion.

If the time-varying boundary conditions of the nozzle walls were known, it would be straightforward to compute the time-varying temperature profiles at the nozzle throat plane. Although a bit computationally expensive, the temperature profiles can be generated by integrating the non-linear

heat equations with the known time-varying boundary condition data.

Unfortunately the boundary conditions of the nozzle throat section are nearly impossible to directly measure. Any sensor placed on the inner surface of a nozzle would likely burn away within a second of ignition. Furthermore, even if a sensor could survive at the nozzle throat section of a combusting rocket motor, it would likely alter the performance and nozzle erosion characteristics of the motor. Therefore, a direct measurement of the boundary condition is not considered in this research. Instead, an indirect measurement technique known as an inverse heat conduction solution is used [35]. In this technique, thermocouples are embedded within the nozzle material in the nozzle throat plane, as shown in Figure 3.11. In theory, at least one embedded thermocouple is required for every unknown boundary condition. With the data provided by the thermocouples, the unknown boundary condition can be deduced. The solution is a time-varying estimate for every unknown boundary condition along with the full time-varying temperature profile history.

Unfortunately, inverse heat conduction problems belong to a class of problems known as ill-posed problems [35]. Unique solutions are not guaranteed and achieving stability in a solver generally requires extra work [36]. Furthermore, these inverse heat conduction problems also require knowledge of the solution to the nonlinear heat equation assuming the boundary conditions were known. Therefore, inverse heat conduction solvers generally need to solve two problems: the direct problem and the inverse problem.

2.3.1 Direct Heat Transfer Solution

The solution to the direct problem is the first step in any inverse heat conduction solver. In this problem, boundary conditions are assumed to be known along with the underlying heat conduction equation and its solution. A starting temperature profile is given and the desired result is the temperature profile after one time-step.

Within the nozzle material, the only heat transfer that occurs is conduction. The full heat conduction equation [37] is given in Equation 2.9.

$$\rho C_p \frac{\partial T}{\partial t} - \nabla \cdot (k \nabla T) = \dot{q}_v \tag{2.9}$$

For simplicity, a long and symmetric (angular) nozzle is assumed, which reduces the three-dimensional partial differential equation to just one dimension. It is also assumed that there is no heat generated within the nozzle material. The resulting simplified heat equation can then be written as:

$$\alpha(T)\frac{\partial^2 T}{\partial r^2} + \frac{1}{r}\alpha(T)\frac{\partial T}{\partial r} + \frac{1}{\rho C_p(T)}\frac{\partial k(T)}{\partial T}\left(\frac{\partial T}{\partial r}\right)^2 = \frac{\partial T}{\partial t} \tag{2.10}$$

Note that the definition of thermal diffusivity is used:

$$\alpha(T) = \frac{k(T)}{\rho C_p(T)}$$

Recall that with the exception of density, all of the thermal properties of graphite vary drastically over the range of temperatures of interest, which are from room temperature to roughly 3000 Kelvin. Accounting for the variable thermal properties, it becomes clear that the partial differential equation is nonlinear and a bit more work is required to integrate. For materials with constant thermal properties, the term $\partial k(T)/\partial T$ is zero. For these cases, the heat conduction equation is linear and simpler to integrate.

A semi-implicit Crank-Nicholson scheme is used to integrate Equation 2.10 instead of an explicit one because the heat equation is known to be very stiff [38]. The discretized equation is shown in Equation 2.11. Note that the temperature dependency for the α, C_p, and k terms have been dropped for convenience. In the following equations, Δr is the spatial grid spacing, r is the radial coordinate, Δt is the time step size, and T is the locale temperature at the grid points.

$$\begin{aligned}
\frac{T_j^{n+1} - T_j^n}{\Delta t} = \\
\frac{1}{2}\Bigg[\frac{\alpha^{n+1}}{\Delta r}T_{j+1}^{n+1}\left(\frac{1}{\Delta r} + \frac{1}{2r_j}\right) + \frac{\alpha^{n+1}}{\Delta r}T_j^{n+1}\left(-\frac{2}{\Delta r}\right) + \frac{\alpha^{n+1}}{\Delta r}T_{j-1}^{n+1}\left(\frac{1}{\Delta r} - \frac{1}{2r_j}\right) + \\
\frac{1}{\rho C_p^{n+1}}\frac{dk}{dT}^{n+1}\left(\frac{T_{j+1}^{n+1} - T_{j-1}^{n+1}}{2\Delta r}\right)^2 \\
+\frac{\alpha^n}{\Delta r}T_{j+1}^n\left(\frac{1}{\Delta r} + \frac{1}{2r_j}\right) + \frac{\alpha^n}{\Delta r}T_j^n\left(-\frac{2}{\Delta r}\right) + \frac{\alpha^{n+1}}{\Delta r}T_{j-1}^n\left(\frac{1}{\Delta r} - \frac{1}{2r_j}\right) + \\
\frac{1}{\rho C_p^n}\frac{dk}{dT}^{n}\left(\frac{T_{j+1}^{n} - T_{j-1}^{n}}{2\Delta r}\right)^2\Bigg]
\end{aligned} \tag{2.11}$$

Equation 2.11 can be rearranged for convenience:

$$\begin{aligned}
T_{j+1}^{n+1}\left(-c_{2,j}^{n+1}\right) + T_j^{n+1}\left(1 - c_{1,j}^{n+1}\right) + T_{j-1}^{n+1}\left(-c_{0,j}^{n+1}\right) - F_j^{n+1} = \\
T_{j+1}^n\left(c_{2,j}^n\right) + T_j^n\left(1 + c_{1,j}^n\right) + T_{j-1}^n\left(c_{0,j}^n\right) + F_j^n
\end{aligned} \tag{2.12}$$

where

$$c^i_{2,j} = \frac{\Delta t \alpha(T^i_j)}{2\Delta r}\left(\frac{1}{\Delta r} + \frac{2}{r_j}\right)$$

$$c^i_{1,j} = \frac{\Delta t \alpha(T^i_j)}{2\Delta r}\left(\frac{-2}{\Delta r}\right)$$

$$c^i_{0,j} = \frac{\Delta t \alpha(T^i_j)}{2\Delta r}\left(\frac{1}{\Delta r} - \frac{2}{r_j}\right)$$

$$F^i_j = \frac{1}{\rho Cp(T^i)}\left.\frac{dk}{dT}\right|_{T=T^i_j}\left(\frac{T^i_{j+1} - T^i_{j-1}}{2\Delta r}\right)^2$$

Note that the $c_{i,j}$ terms are functions of temperature. With Equation 2.12 two things are apparent: The F term contains the nonlinear terms from the heat equation and the overall system of equations is tridiagonal. This set of equations hold for all grid points between j=2 and j=N-2.

Boundary Conditions

The cases where j=1 and j=N-1 correspond to grid points at the boundaries. Here the discretization of the heat equation as seen in Equation 2.12 does not apply because the grid points at the boundaries do not have neighboring points outside of the domain. Instead, the temperature at either end must somehow be specified. Recall that at the moment boundary conditions are assumed to be known exactly.

At the inner surface, where j=1, a heat flux f is applied. An application of heat flux is selected as it can easily be compared regardless of propellant choice or nozzle size. The boundary condition is implemented by application of Fourier's Law [19]:

$$f = -k\frac{\partial T}{\partial r}$$

When discretized, this becomes:

$$f = -k_1\frac{T_1 - T_0}{\Delta r} \tag{2.13}$$

Note that at this boundary, the discretization is fairly straightforward. To implement this into Equation 2.12 for $j = 1$, the grid point must be specified in terms of temperature. Therefore, Equation 2.13 is rearranged to solve for T_0, the term that is replaced with the boundary condition:

$$T_0 = T_1 + \frac{f\Delta r}{k_1} \tag{2.14}$$

Equation 2.14 can now be placed into Equation 2.12, as shown in Equation 2.15.

$$\begin{aligned} T_2^{n+1}(-c_{2,1}^{n+1}) + T_1^{n+1}(1 - c_{1,1}^{n+1} - c_{0,1}^{n+1}) + \left(-F_1^{n+1} + \frac{f^{n+1}\Delta r}{k_1^{n+1}}(-c_{0,1}^{n+1})\right) \\ = T_2^n(c_{2,1}^n) + T_1^n(1 + c_{1,1}^n) + \left(F_1^n + T_0^n(c_{0,1}^n)\right) \end{aligned} \tag{2.15}$$

The outside surface, or the back wall boundary, which is usually contained by nozzle retainer brackets in a rocket motor, is a bit simpler to handle. Physically, it is easy to place a thermocouple on the outer surface of a nozzle. Therefore, the simplest manner of handling the outer boundary condition is an applied temperature condition with the following relation:

$$T_{N-1} = T_s$$

Recall that for the direct heat transfer solution, both boundary conditions are assumed to be known for all times. With the boundary conditions taken into account, the system of equations for the

solution of the direct heat transfer solution can be written out, as shown in Equation 2.16.

$$\begin{bmatrix} (1-c_{1,1}^{n+1}-c_{0,1}^{n+1}) & -c_{2,1}^{n+1} & 0 & & & \\ -c_{0,j}^{n+1} & (1-c_{1,j}^{n+1}) & -c_{2,j}^{n+1} & & & \\ & \ddots & \ddots & \ddots & & \\ & & & -c_{0,N-2}^{n+1} & (1-c_{1,N-2}^{n+1}) & -c_{2,N-2}^{n+1} \\ & & & 0 & c_{0,N-1}^{n+1} & (1-c_{1,N-1}^{n+1}) \end{bmatrix} \begin{pmatrix} T_1^{n+1} \\ T_2^{n+1} \\ \vdots \\ T_{N-2}^{n+1} \\ T_{N-1}^{n+1} \end{pmatrix} + \begin{pmatrix} -F_1^{n+1} + \frac{f^{n+1}\Delta r}{k_1^{n+1}}(-c_{0,1}^{n+1}) \\ -F_2^{n+1} \\ \vdots \\ -F_{N-2}^{n+1} \\ -F_{N-1}^{n+1} + T_N^{n+1}(-c_{2,N-1}^{n+1}) \end{pmatrix} =$$

$$\begin{bmatrix} (1-c_{1,1}^{n}-c_{0,1}^{n}) & -c_{2,1}^{n} & 0 & & & \\ -c_{0,j}^{n} & (1-c_{1,j}^{n}) & -c_{2,j}^{n} & & & \\ & \ddots & \ddots & \ddots & & \\ & & & -c_{0,N-2}^{n} & (1-c_{1,N-2}^{n}) & -c_{2,N-2}^{n} \\ & & & 0 & c_{0,N-1}^{n} & (1-c_{1,N-1}^{n}) \end{bmatrix} \begin{pmatrix} T_1^{n} \\ T_2^{n} \\ \vdots \\ T_{N-2}^{n} \\ T_{N-1}^{n} \end{pmatrix} + \begin{pmatrix} -F_1^{n} + T_0^{n}(-c_{0,1}^{n}) \\ -F_2^{n} \\ \vdots \\ -F_{N-2}^{n} \\ -F_{N-1}^{n} + T_N^{n}(-c_{2,N-1}^{n}) \end{pmatrix} \tag{2.16}$$

For convenience, this can be written in shortened form, as shown below:

$$[\beta^{n+1}](T^{n+1}) + (F)^{n+1} = [\beta^{n}](T^{n}) + (F)^{n} \tag{2.17}$$

The set of equations in matrix form clearly shows that some linear algebra should easily yield the desired set of temperatures, T_i^{n+1}, for the next time step. For large r and constant material properties, this is the well-known tri-diagonal solution of the heat equation in a large slab of material [38].

Unfortunately, when accounting for variable material properties, the material properties of the future time step will be different than the current time step. This means that the $\left[\beta^{n+1}\right]$ matrix will be populated with terms of unknown coefficients. This is the major difficulty that comes about in handling this nonlinear form of the heat equation.

The solution to Equation 2.17 requires determining (T^{n+1}) and $[\beta^{n+1}]$ simultaneously. Once these are known, the time step can be incremented and the solution procedure can be repeated for future time steps. To solve for both terms simultaneously, the following iterative procedure is used:

1. (T^n) is known
2. Let $(T_{guess}) = (T^n)$ to start
3. Based on (T_{guess}), determine the tri-diagonal matrices for the n+1 time step
4. Solve Equation 2.17 for (T^{n+1}), which has the solution:

$$(T^{n+1}) = [\beta^{n+1}]^{-1}\left([\beta^n](T^n) + (F^n) - (F^{n+1})\right)$$

   Where $[\beta^{n+1}]$ and (F^{n+1}) are based on (T_{guess}).
5. Compare (T_{guess}) and (T^{n+1})
6. If not trivially different, let $(T_{guess}) = (T^{n+1})$
7. Repeat from Step 3
8. If (T_{guess}) and (T^{n+1}) are equivalent within some tolerance, solution has converged and (T^{n+1}) is the converged solution

This scheme converges for most conditions. However, for very large changes in applied heat flux or large time steps, convergence fails or takes too many iterations (a maximum of 100 iterations is used in the data analysis for this research). The failure is easily remedied by reducing the size of the particular time step. It should be noted that this scheme is not necessarily the best scheme nor the fastest. However, this is a simple scheme and the efficiency improvement potential is left open for future work.

2.3.2 Validating the Direct Solution

Numerous validation tests were run on the integration scheme used. These tests provided validation that the numerical solution provided correct results. To prove that the numerical solver provides valid results, it is compared against three exact solutions to the heat equation. These exact solutions are idealized problems utilizing a boundary condition at infinity. Although these example problems are not necessarily realistic nor necessarily physically achievable, they allow for the exact solution

of the heat equation to be determined under certain conditions. It is then possible to compare how the numerical solutions differ from the exact solutions. Three different problems are used to test various conditions (such as problems with small radii and variable thermal properties).

2.3.3 Comparison to a semi-infinite slab of constant material properties

The first validation test was the simple case of a semi-infinite solid. Recall that for large r and constant material properties, the heat equation for a cylinder is equivalent to the heat equation for a semi-infinite slab, which is a common example problem in many textbooks. The developed integration algorithm could be compared to this textbook case. The exact solution for the semi-infinite slab with a constant applied heat flux is given by Equation 2.18, and the derivation can be found in Appendix A.1.

$$T(x,t) - T_i = \frac{q\sqrt{4\alpha t/\pi}}{k} exp\left(-\frac{x^2}{4\alpha t}\right) - \frac{qx}{k} erfc\left(\frac{x}{\sqrt{4\alpha t}}\right) \tag{2.18}$$

In this example, a large slab initially at 293 Kelvin everywhere. The temperature is assumed to remain constant at an infinite depth into the slab. At time t=0, a constant heat flux is placed on one surface and the resulting temperature profile is computed after 120 seconds. The thermal properties are $\alpha = 117x10^{-6}\ m^2/s$ and k=401 W/mK. The numerical solver treats this problem with an inner radius of 1E6 meters with a wall thickness of 600 millimeters. The inner radius is large enough such that the exact solution of the semi-infinite slab matches well with the numerical results.

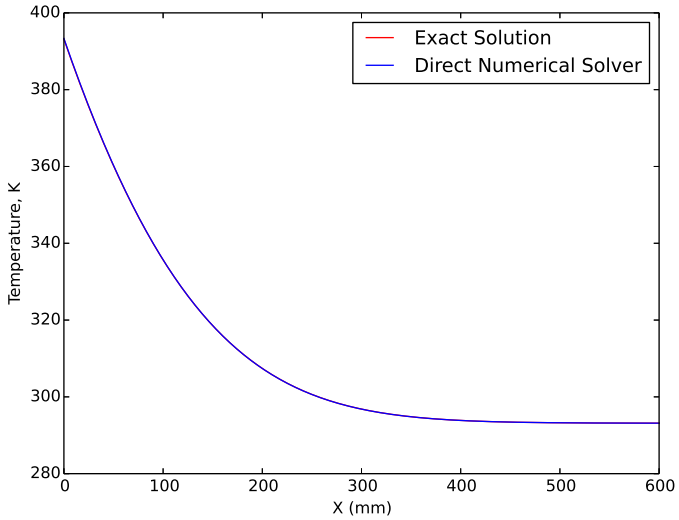

Figure 2.7: The developed solver is equivalent to the exact solution for a semi-infinite solid when material properties are constant and a large radius is used. The conditions are $\alpha = 117x10^{-6}\ m^2/s$ k=401 W/mK with a starting temperature of 293 K. The applied heat flux is a constant $3x10^5$ W/m^2 and the resulting temperature profiles are shown after 120 seconds. The developed solver uses a wall of a large inner radius of 1E6 meters and thickness of 0.6 meters. Note that both the exact solution and the numerical solver predict nearly identical solutions.

2.3.4 Comparison to an infinite cylinder of constant material properties

In the next test, r is reduced to more reasonable sizes. For smaller r values, the heat equation for a cylinder is not the same as the heat equation for a semi-infinite slab. A similarity solution exists when considering constant material properties and a constant applied temperature T_s at location $r = \sqrt{4\alpha t}$. The other boundary condition is $T(r \to \infty) = T_i$, where T_i is the initial temperature everywhere. The exact solution to this problem is given by Equation 2.19, where $Ei(x)$ is the exponential integral function, which is defined as:

$$Ei(x) = -\int_{-x}^{\infty} \frac{e^{-t}}{t} dt$$

$$T(r,t) - T_i = \frac{T_s - T_i}{Ei(-1)} Ei\left(\frac{-r^2}{4\alpha t}\right) \tag{2.19}$$

The heat flux at the inner radius of the cylinder r_i can be determined by differentiating Equation 2.19.

$$q_s = -k \left.\frac{\partial T}{\partial r}\right|_{r=r_i} = \frac{-2k\left(T_s - T_i\right)}{r_i Ei\left(-1\right)} e^{\frac{-r_i^2}{4\alpha t}} \tag{2.20}$$

Where q_s i the applied surface heat flux. The full derivation of this solution is provided in Appendix A.2. To compare the exact solution and the numerical solver, the following conditions are applied:

- α, k, and T_s are all taken to be unity with their respective units.
- r_i is 0.1 meters, and for the numerical solver, outer radius r_o is 5 meters, with 500 grid points.
- T_i is taken to be zero Kelvin everywhere.
- the numerical solver starts at $t = 0$ with time steps of $\Delta t = 0.01$ seconds and ends at $t = 5.0$ seconds. At 5.0 seconds, the numerical temperature profile is compared against the temperature profile for the exact solution.

As shown in Figure 2.8, the temperature profile computed by the numerical solver is nearly identical to that of the exact solution. This shows that the numerical solver provides valid results at least for cases without varying material properties.

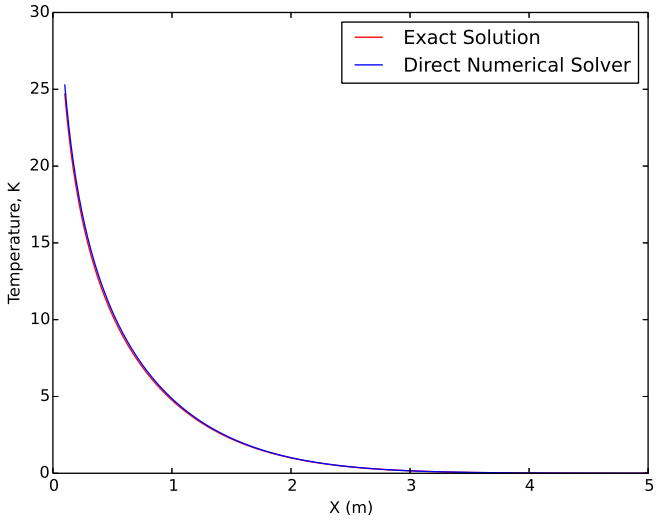

Figure 2.8: The numerical solver matches the exact solution results very well. This shows that the numerical solver predicts valid results for cases where the material properties are held constant.

2.3.5 Comparison to a semi-infinite slab of variable material properties

It is then desired to run a test against an exact solution with varying thermal properties. It turns out that the thermal diffusivity, as shown in Figure 2.1 somewhat follows the trend $\alpha \sim T^{-1}$. Note that this trend is not exact and scaling terms have been left out for simplicity. The trend of decreasing thermal diffusivity with temperature is one characteristic that makes graphite a particularly well-suited material for rocket nozzle applications. For simplicity, the condition $\alpha \sim T^{-1}$ is applied.

For convenience, a large slab of material of 10 meters thickness is considered. As in Section 2.3.3, we use a large inner diameter for the direct solver. For the case where $k = 1$ and a wall temperature is impulsively applied, the exact solution to the nonlinear heat equation can be reduced to the solution of an ordinary differential equation, as shown in Equations 2.21.

$$\frac{\partial^2 \theta}{\partial \eta^2} = -\frac{\eta}{2}\frac{\partial \theta}{\partial \eta}\theta + \frac{\left(\frac{\partial \theta}{\partial \eta}\right)^2}{\theta} \tag{2.21}$$

Where,

$$\eta = \frac{x}{t^{\frac{1}{\gamma}}} \tag{2.22}$$

$$T(x,t) = \theta(\eta) \tag{2.23}$$

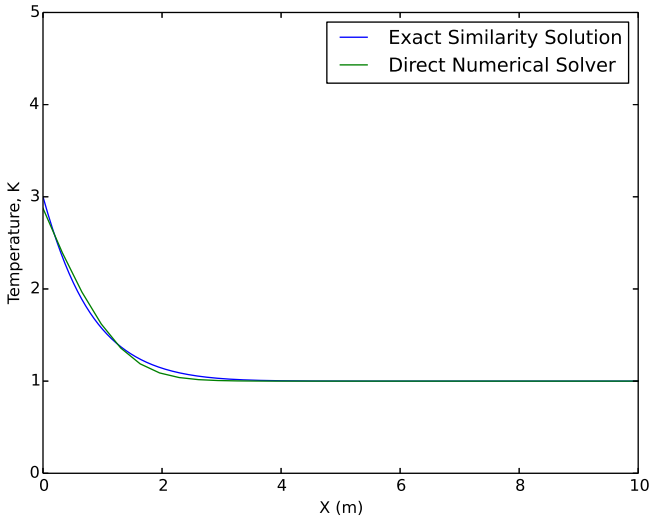

Figure 2.9: The numerical solver matches the exact solution results generally well. The numerical solver in this example uses time-step sizes of 0.05 seconds and 50 grid points.

The derivation for this similarity solution is given in Appendix A.3. The "exact" solution to the case where initial temperature is 1K and a 3K temperature is impulsively applied matches the direct solver equation generally well. To compare the two, the time-varying flux must be computed, which is related to $\theta'(0)$. If the direct solver is integrated to $t = 1\ s$, then the similarity solution matches exactly with the direct solver, as shown in Figure 2.9. Note that a perfect match is not achieved. This is likely because the direct solver assumes constant material properties between grid points. Also, this particular example problem has a large $\partial\alpha/\partial T$ at the temperatures of interest, and the discretization is likely contributing to the error. The simulation solution when plotted on top of the exact solution does appear to show some oscillatory behavior near the left boundary. The direct solver was tested with many cases and was stable in all cases. The temperature likely behaves as such for this particular example due to the drastically changing thermal properties near the boundary.

Note that this test employs only small changes in temperature. This is to keep the thermal diffusivity within reasonable limits for this simple validation test. In this similarity solution model, the thermal diffusivity changes by a factor of about 3. This change is a bit smaller than the factor of 10 change that the graphite used in this research exhibits, but still a good validation test. When the same test is run with a boundary condition of 10 K (or a factor of 10 change in thermal diffusivity), the results are similar.

2.3.6 Grid Refinement and Time Step Size Refinement

Once it was proven that the numerical solver provides valid results, the grid spacing and time step sizes needed to be optimized for the experimental data. While one could choose an extremely small grid spacing and time step sizes, this would become computationally expensive and the data analysis in this research would take an unnecessary amount time to perform. It should be noted that although any time step size achieves stability using the Crank-Nicholson scheme, errors are still present and can accumulate. Therefore, one would want to select an appropriate time step size such that performance and error were balanced.

Grid Refinement

The grid spacing was selected by monitoring the results for several different test cases. The initial temperature everywhere is 300 K and The numerical solver is run using the nominal dimensions of the graphite nozzle for the design condition. These are roughly:

$$5\ mm \leq r \leq 25\ mm$$

and an applied heat flux of 1 MW/m^2 at the inner surface. The outside boundary condition is fixed at 300 K. The time-step size for this study is purposely set to very small, at $\Delta t = .001$ seconds. This time step size is finer than needed, as shown in Figure 2.3.6. The simulation is run for 1000 time steps. The results of this study are shown in Figure 2.10. Note that there is relatively small accuracy gains above 50 grid points. When using a significantly greater number of grid points accuracy remains nearly the same while computational time vastly increases. 100 grid points are used for the experimental data to ensure accuracy at a reasonable computational cost.

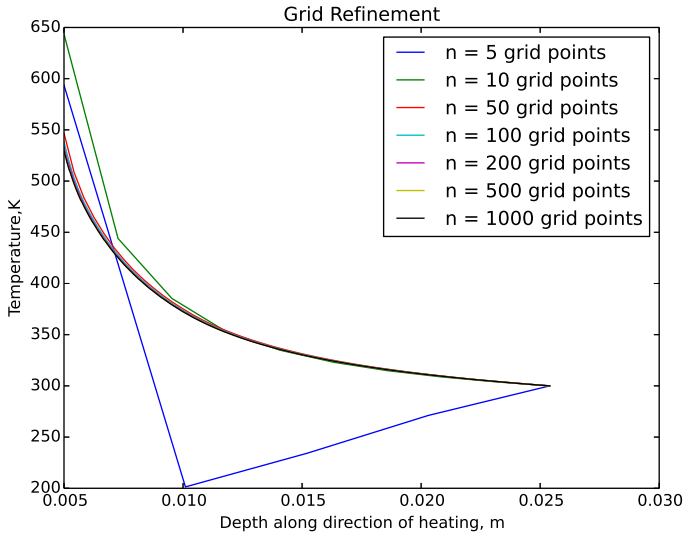

Figure 2.10: The grid refinement study showed that using 100 grid points for the experimental data should provide accurate results without using an excessive amount of computational time.

Time Step Size Refinement

The time-step size also requires refinement to achieve practical results. For this study, the same nozzle geometry is applied with 500 grid points. The number of grid points for this test is purposely set to be excessively large so that both refinement studies remain independent of each other. The initial temperature is 300K and a heat flux of 1 MW/m^2 is applied at the inner surface. The outer surface is held at a constant temperature of 300K. Various time-step sizes are used in simulating the data, which is computed up to 1 second.

Figure 2.11 shows the results of the time-step size refinement study. It is apparent that time-step sizes smaller than 0.1 seconds provide marginal benefits when compared against larger computational time requirements. For the data analysis in this research, a time-step size of 0.02 seconds is used to ensure accuracy with decent performance.

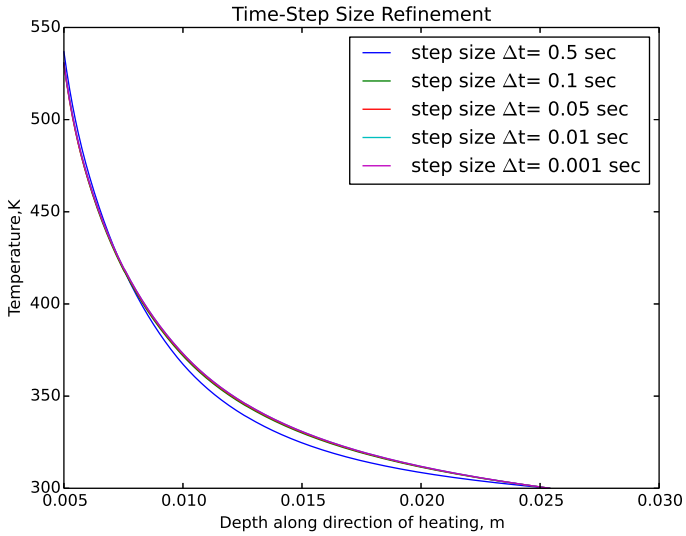

Figure 2.11: The time-step refinement study shows that time steps as large as 0.1 seconds provide accurate results. The data analysis for this research is performed at a time-step size of 0.02 seconds.

2.3.7 The Residual

As the direct solution to the heat transfer equation is nonlinear and requires iteration to solve, some amount of error is expected to be present. The residual can be computed based on the partial differential equation and can give the reader an estimate on the magnitude of the error. The residual is computed based on Equation 2.12. Here, the right side of the equation is moved over to the left, and everything is divided by $(1-c_{1,j}^{n+1})$ to normalize and allow the for units of ϵ to be in temperature. Because ϵ is computed for each node, the root of the sum of squares is computed for each time step and the resulting time-varying residual can be plotted.

$$\epsilon_j^{n+1} = T_{j+1}^{n+1}\frac{\left(-c_{2,j}^{n+1}\right)}{1-c_{1,j}^{n+1}} + T_j^{n+1} + T_{j-1}^{n+1}\frac{\left(-c_{0,j}^{n+1}\right)}{1-c_{1,j}^{n+1}} - \frac{F_j^{n+1}}{1-c_{1,j}^{n+1}} - T_{j+1}^{n}\frac{\left(c_{2,j}^{n}\right)}{1-c_{1,j}^{n+1}} - T_j^{n}\frac{\left(1+c_{1,j}^{n}\right)}{1-c_{1,j}^{n+1}} - T_{j-1}^{n}\frac{\left(c_{0,j}^{n}\right)}{1-c_{1,j}^{n+1}} - \frac{F_j^{n}}{1-c_{1,j}^{n+1}} \tag{2.24}$$

The residual history from Test 4 is shown in Figure 2.12. Note that, as expected, the residual remains quite small and bounded compared to the Temperature profiles in the nozzle throat plane. Furthermore, the residual seems to decrease after the initial spike due to the large transients from ignition. The small peak near 4 seconds is due to the secondary shift of the heat flux to near zero

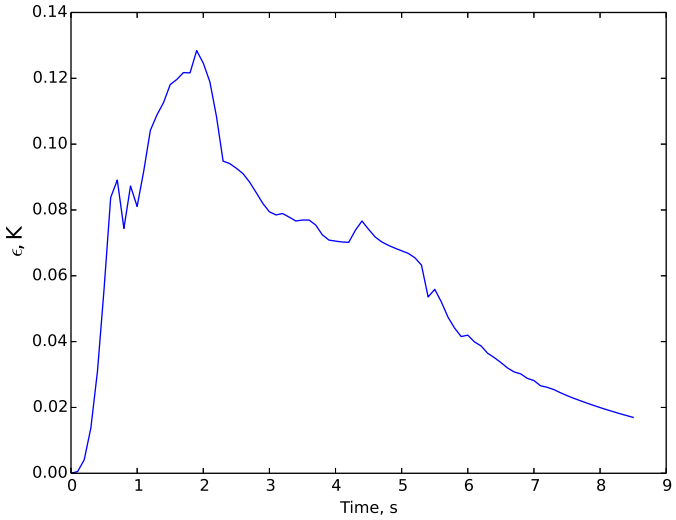

Figure 2.12: The residual time-history from Test 4 shows that the error associated with the solution of the numerical partial differential equation is acceptable. Note that the second spike near four seconds coincides with the shutdown of the motor.

conditions. Note that this does not coincide with the physical shutdown of the motor, as explained in Section 2.3.10. The relatively small values of the residual provide confidence that the partial differential equation is adequately solved numerically.

2.3.8 Inverse Heat Conduction Solution

The direct solver works great for the case when boundary conditions are known. Unfortunately, for the case of a rocket motor nozzle, the inside boundary conditions are not known. In fact, it would be very difficult to put any sensor on the surface on the nozzle wall without affecting the performance of the motor.

Inverse problems are problems where the traditionally given data and the unknown data are inverted. For example, in the inverse heat conduction case, boundary conditions are unknown and a finite number of temperature measurements are given at specific locations within the block of material. In the traditional heat transfer problem, boundary conditions are given and the interior temperatures are unknown. The solution to these inverse problems are estimates of the time-varying boundary conditions and temperature profiles within the block of material.

Inverse heat conduction problems are known as ill-posed problems [35]. The given data is not always enough to obtain a unique solution. Furthermore, it is difficult to obtain stability in these problems and there are no generic algorithms for achieving stable and accurate results. Each problem

must be approached individually and solutions must be validated with relevant simulation studies.

A typical method in which inverse heat conduction problem solvers estimate the unknown boundary condition is through a guess-and-check method. A numerical model is integrated starting from a known condition and for each time step a guess of the unknown boundary condition is applied. The solver performs the time step with the guessed boundary condition and compares the actual thermocouple data to the output of the temperature profile from the numerical solver. It is desired to minimize the difference between the numerical solver and the true thermocouple data. The method in which the two sets of data are compared is called the objective function and it is the key to a good inverse solution. Unfortunately the most intuitive objective function, shown by Equation 2.25, is known to be unstable. In fact many objective functions are unstable and this is precisely the reason why inverse heat conduction problems are difficult.

$$\theta^{n+1} = \sum_{i=1}^{Q} \left(T(\chi_i)^{n+1} - \tau_i^{n+1} \right)^2 \tag{2.25}$$

Where Q is the total number of thermocouples, τ_i is the thermocouple measurement for thermocouple i, and $T(\chi_i)$ is the numerical temperature value at the location of thermocouple i. There is no single objective function that will *always* provide stable results for any given heat conduction problem. In fact, the stability of any given objective function also depends on the placement of the thermocouple sensors and the behavior of the unknown boundary condition. In general, the ideal placement of any thermocouple sensor is as close to the unknown boundary condition(s) as possible. Usually other factors limit the location of the temperature sensors. For the case of the nozzle in a hybrid rocket motor, the thermocouple sensors cannot be placed too close to the inner wall of the nozzle. The graphite wall thickness needs to remain thick enough so that it will not crack under the thermal stresses experienced during the burn. The thermocouple placement locations for each test condition on the experimental motor are listed in Table 3.7.

The Objective Function

As mentioned earlier, the objective function is key to any inverse heat conduction problem. Their main purpose is to compare temperature sensor data and numerical model data in a stable manner. As stated in the previous section, Equation 2.25 does not achieve stability. However, it is the most intuitive way to compare two sets of data and it provides the foundation for other objective functions. Other objective functions generally build on Equation 2.25 by adding or subtracting other terms in hopes of stabilizing the solution. One popular method is by penalizing the rate of change of the flux input [39]. This is shown by Equation 2.26. Note how a constant flux guess has the least additional penalty. Generally, with these approaches, another function f scales the additional penalty with the

original difference term.

$$\theta^{n+1} = \sum_{i=1}^{Q} \left(T(\chi_i)^{n+1} - \tau_i^{n+1}\right)^2 + f\left(\lambda^{n+1} - \lambda^n\right) \tag{2.26}$$

Several of these types of objective functions were tested with the nozzle heat conduction problem. Unfortunately, the best ones were only stable either for low input heat fluxes or extremely high input heat fluxes. For the rocket nozzle case, an objective function is needed that can handle the low heat flux applied before a burn and the high heat fluxes applied during a burn.

A more computationally expensive approach is to look at 'future data'. If solving the inverse problem is conducted as a post-processing step, the full time-history temperature data provided by the temperature sensors are always available during the post-processing analysis. The objective function could then utilize this future temperature data by checking to see if the heat flux guess will be generally correct in the future. This is computationally costly because several time-steps of data will need to be computed for every heat flux guess for every time step. In addition to the computational costs, peaking into the future also impacts the computed inverse solution. Because future data is used, the numerical changes in heat flux are predicted in the solution before they physically occur. Furthermore, the numerical solutions also get smoothed out. Nonetheless, this approach seemed to provide very stable results with just a few time-steps of future data [40]. The objective function that is used for the data in this result is given by:

$$\theta = \sum_{s=1}^{S} \sum_{i=1}^{Q} \left(Y^{n+s}(s(\lambda^{n+1} - \lambda^n) + \lambda^n, \chi_i) - \tau_i^{n+s}\right)^2 \tag{2.27}$$

Where Y is the direct heat transfer solution. $Y^{n+s}(\lambda, \chi_i)$ is the temperature at location χ_i for the numerical solution profile at the n+s time step given a guess input of λ heat flux at the final time step. τ_i^{n+s} refers to the i^{th} thermocouple measurement at time step $n+s$. This objective function utilizes Q total thermocouples and peeks S time steps into the future.

This objective function essentially uses future thermocouple data along with a temporary assumption that the heat flux changes linearly [35], as shown mathematically in equation 2.27. Note that this function can account for a variable number of temperature sensors and future time-steps. For the analysis for all of the data, three future time steps were used along with 3 embedded thermocouples.

2.3.9 Validating the Inverse Solver

Because of the unstable nature of inverse heat conduction problems in general, it is always wise to run simulations with relevant conditions. One should have a general knowledge of the magnitude and behavior of the unknown boundary condition. Based on this knowledge, simulated thermocouple

data can be generated from the direct solution. With the simulated thermocouple data, the inverse solver can be tested to see whether or not it can reconstruct the boundary condition history that generated the simulated thermocouple data. The algorithm used to test the inverse solver is described below:

1. Generate a time-varying heat flux profile that the inverse solver should determine
2. For the desired time-varying heat flux, run the direct solver to generate full time-varying temperature profiles
3. From the time-varying profile data, simulate thermocouple data by saving temperature data from only a few nodes of the full time-varying data
4. Add noise, if desired, to the simulated thermocouple data
5. Feed the simulated thermocouple data to the inverse solver
6. Determine whether or not the inverse solver can accurately determine the heat flux profile that generated the simulated thermocouple data

In these tests, the full nonlinear heat equation is used, along with an inner radius of 5mm, an outer radius of 25 mm, 100 grid points, an initial temperature of 300 K, and a time step size of 0.02 seconds. The simulated thermocouple data is down-sampled so that the simulated temperature measurements are 'sampled' at an interval of 0.1 seconds. This is done because of the limits of the thermocouple response time [41](see Appendix F). The numerical integration is still conducted at an interval of 0.02 seconds. The material properties are those measured and described in Section 2.1. Thermocouple error is also simulated according to the K-type Special Limits of Error specifications [42] (the greater of 0.40% or 2.2 K). Virtual thermocouples are embedded in the material at 25%, 31%, and 41% depths, as measured from the inner wall. A virtual thermocouple is also placed at the back wall location to measure the outside boundary condition directly. This is also done experimentally.

From Equation 2.8, it is estimated that heat transfer coefficient is 12 kW/m^2K. Equation 2.28 is used to compute an estimated heat flux from the heat transfer coefficient. The estimated heat flux is then given by 33.9 MW/m^2. This heat flux is used as the normalizing parameter for the inverse heat conduction problem simulation studies. Three simulation test cases were run to prove that the developed solver provides accurate and stable results.

$$f = h(T_\infty - T_s) = -k\frac{\partial T}{\partial r} \tag{2.28}$$

The first simulation test was the step change case in heat flux. Applied heat flux is instantaneously changed from 0 to 33.9 MW/m^2. This simulation tests how well the solver can track a

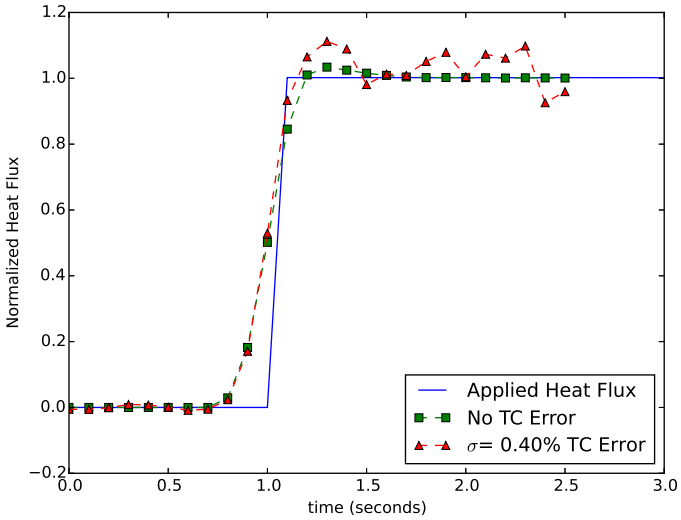

Figure 2.13: The simulation shows that the solver can correctly detect a large instantaneous change in applied heat flux. This test also proves that the solver remains stable at elevated applied heat fluxes, even when accounting for thermocouple error.

constant zero heat flux, a large step, and a large constant heat flux value. If the solver can track this applied heat flux profile, then the solver can very likely track the other test profiles as well.

Figure 2.13 shows that the solver can accurately track elevated heat fluxes as well as a zero heat flux. Furthermore, the solver remains stable throughout the simulation. Note that evidence of the use of 'future data' is present in the heat flux profiles. The solver predicts that the heat flux will increase about two time-steps before the applied heat flux actually changes. Also, the estimated applied heat flux profile is smooth, unlike the actual applied changes. While this is not ideal behavior, it is a small price to pay to achieve stability. From this data, it is understood that exact start-up transients of rocket motor ignition will be impossible to deduce. However, a decent estimate of the heat flux throughout the burn should be expected.

The second simulation test is similar to the first, except another two step changes occur following the first. The second step change is a reduction in applied heat flux to below zero, and the third brings the applied heat flux back to zero. This simulation tests how the solver responds to cooling (negative heat flux), and several step changes in succession. The result of this second test is shown in Figure 2.14. Again the solver responds well and accurately tracks the applied heat flux profile. From this test, it is apparent that the absolute minimum hot fire length should be at least one second so that the solver can stabilize to the elevated heat flux profile. The solver also does well when a negative heat flux is applied. Although this phenomena is not possible to track with the experimental data (see Section 2.3.10), it shows that the solver remains stable even outside the

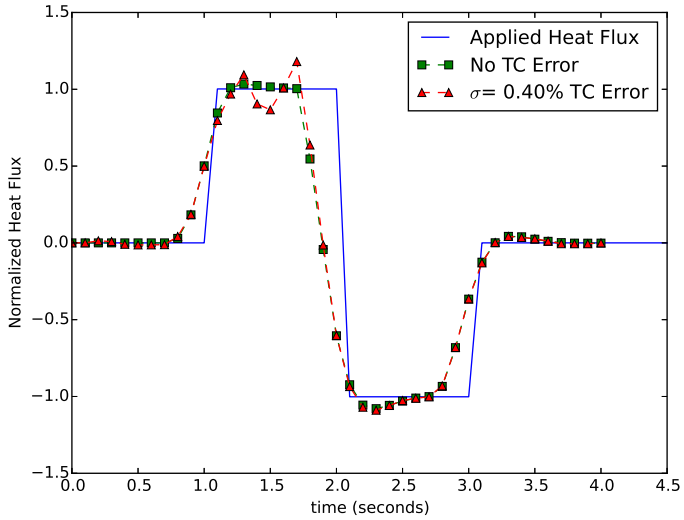

Figure 2.14: The second inverse simulation shows that the solver can track subsequent step changes in applied heat flux as well as applied heat fluxes that are negative. This shows that the solver remains stable for a wide range of applied heat fluxes.

expected range of applied heat fluxes.

The third simulation test involves a ramp. This simulation tests how well the solver can track ramp heat flux profiles as well as lower heat fluxes. Figure 2.15 shows the results of the final simulation test case. The solver does remarkably well in tracking the applied heat flux profile. Note that even in this case the solver estimates a smooth heat flux profile.

The simulations show that the solver is both stable and accurate for a wide range of applied heat fluxes. Furthermore, the solver has proven itself to be stable even when subjected to lower heat fluxes and even negative heat fluxes. Based on these results, the solver is expected to provide reasonable estimates of the true heat fluxes experienced by the nozzle throat during a motor firing.

All three simulation tests have two common features between then. The numerically predicted heat flux changes before the applied heat flux that created the data set and all of the numerically predicted heat flux profiles are smoother than the applied heat flux profiles. These two undesirable features are a consequence of using an objective function that utilizes future data. However, these are acceptable as they allow for an estimated temperature profile to be computed.

Lastly, the numerical computations with simulated thermocouple noise sometimes cause large oscillations in the computed heat flux profiles. This is a well known phenomena and the magnitude of the oscillations depends on the thermocouple error and their placements. In these simulations, the thermocouple error is modeled based on the specifications of the K-type thermocouple specifications.

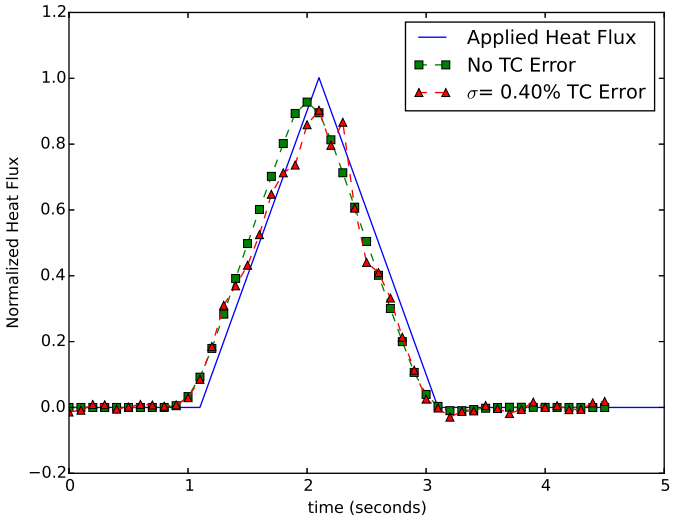

Figure 2.15: The third simulation shows that the solver can track ramp changes in applied heat fluxes very well.

2.3.10 Application of the Inverse Solver to Experimental Data

While the developed inverse heat conduction solver has proven to be very successful in the simulation studies, it must be noted that in the true experiment case, it may not be *as* accurate. Numerous reasons exist for this argument, such as various uncertainties and errors. A more subtle but important argument is the breakdown of the underlying heat equation. Recall that one of the major assumptions in the development of the heat equation solver was a 1-D heat transfer approximation. This assumption is valid during the burn, as the nozzle is subjected to extreme heating in the radial direction [11]. However, as soon as the motor is shutdown, the nozzle is no longer subjected to extreme heat fluxes and the direction of the heat diffusion is not necessarily mostly in the radial direction. Thermal soaking occurs in all directions, and the 1-D assumption fails after the burn. During the cool-down phase after a burn, the solver is fitting the thermocouple data to an incorrect heat equation, and the results are therefore not correct.

The end result of the breakdown of the 1-D simplification is that the solver only provides meaningful data during the burn. Unfortunately this means that the solver may need some adjustments to handle rocket motors with multiple restarts. However, for this research, multiple restarts are not considered and the nozzle is assumed not to erode *after* the burn has terminated. Therefore, all of the relevant data is valid and any data collected after the burn has completed is considered to be unimportant.

2.4 Ultrasound Measurements based on the Thermal Analysis

Recall the goal of the thermal analysis is to ultimately provide an estimate on the speed of sound of the nozzle material at the throat plane. The output of the inverse solution is a numerical estimate of the temperature profile for every time step as well as an estimate of the heat flux applied at the inner surface of the nozzle. A temperature estimate $T(r,t)$ is available for every time step and grid point.

This known temperature is converted to a speed of sound correction factor for every grid point using Equation 2.4, repeated for convenience in Equation 2.29.

$$\frac{v}{v_0} = \sqrt{\frac{K}{K_0}} = \frac{\sqrt{\frac{EG}{3(3G-E)}}}{v_0} \tag{2.29}$$

The time-varying average speed of sound is then computed by taking the integral average of $\frac{v(r,t)}{v_0}$ for every time step, which results in $\frac{\bar{v}(t)}{v_0}$. Recall the ultrasound data from the machine is correlated with speed of sound at room temperature, as shown in Equation 2.30.

$$d_{raw} = v_0 * \frac{\Delta t}{2} \tag{2.30}$$

A simple multiplication is needed to correctly apply the time-varying speed of sound to the ultrasound data, as shown in Equation 2.31.

$$d_{corrected} = \frac{\bar{v}(t)}{v_0} * d_{raw} = \bar{v}(t) * \frac{\Delta t}{2} \tag{2.31}$$

With this scheme, the speed of sound at room temperature is not directly used in the numerical analysis because the velocity is always treated in nondimensional form.

Chapter 3

Experiment Design

This chapter focuses on the design of the experimental motor that was fabricated for this research as well as the support systems used to run the experiments. This includes a discussion on the initial design requirements and the final design of the motor.

The features of the experimental motor are then discussed in detail for the fore end, combustion chamber, and aft end sections of the motor. The ultrasound machine specifications and specifications on the data acquisition and control systems are listed at the end of the chapter.

3.1 Initial Design Requirements

At the beginning stages of this research project, it was clear that a new motor would need to be fabricated, as no motor in lab had the capability to actively measure nozzle erosion. At the time, a newly designed feed system had just been completed for the Stanford Combustion Visualization Facility [43] . One of the major requirements for the Nozzle Erosion motor was to utilize the feed system from the Combustion Visualization Facility.

Although the requirement to use a pre-existing feed system was limiting, it allowed for a larger budget and more design time to be reserved for the motor design. For safety reasons (as the tests occur in a secured room inside of the lab), the oxidizer choice was limited to only gaseous oxygen. The maximum feed rate of the pre-existing feed system was about 130 g/s of oxygen for a combustion pressure of about 690 kPa (100 psi).

With the fresh visualization results of the Stanford Combustion Visualization Facility [44], it was desired to have optical access into a hybrid rocket motor with a conventional high-performance design. Therefore, there was an added requirement of optical access down the port of the motor. At the time, it was unclear what the results would be, but the access was desired nonetheless.

In order for this research to provide practical data for other hybrid rocket designers, the motor would need to mimic high-performance propulsion systems. This meant that the motor would need

to have supersonic flow coming out of the nozzle (a first for a rocket fired inside our lab), would need to use a high-performance fuel, would need to incorporate internal geometries to promote mixing and higher combustion efficiencies, and would need to be run at relatively high chamber pressures.

The feed system in the lab has a maximum supply pressure of 6.9 MPa (1000 psi). Accounting for flow losses, the highest combustion chamber pressure that the feed system can sustain at reasonable flow rates is 2.8 MPa (400 psi), significantly higher than the pressures tested in the Combustion Visualization Facility [45]. The other performance requirements, such as supersonic flow out of the nozzle and performance enhancing internal geometries are requirements that are addressed with a converging-diverging nozzle and the use of a mixer within the combustion chamber.

The last design requirement was the obvious one. The aft-end section would need to be designed such that the nozzle could be fitted with ultrasound transducers as well as several thermocouple sensors. Access would also need to be provided so that the sensors could be easily installed and removed. The combined design requirements are listed below.

- Utilize existing feed system.
- Oxidizer choice is limited to gaseous oxygen.
- Realistically achievable flow rates are about $100 g/s$ at 2.8 MPa (400 psi) combustion pressure.
- Allow for high-pressure combustion (up to about 2.8 MPa).
- A window at the fore-end of the motor looking through the port.
- Burn a paraffin fuel.
- Have good internal geometries inside of the motor to promote mixing and stability.
- Utilize a long nozzle (for the 1-D assumption) that has a converging-diverging flow path for supersonic flow.
- Allow for the throat section to have some finite width so that the ultrasound beam width can be accommodated.
- The aft-end must allow for easy nozzle erosion measurements.
- Aft-end assembly must allow for embedded thermocouples.

3.2 Motor Sizing

The motor sizing was completed once the initial design requirements were set. The driving factor for the design of the motor was the fast regression-rate of paraffin fuel and the relatively low flow

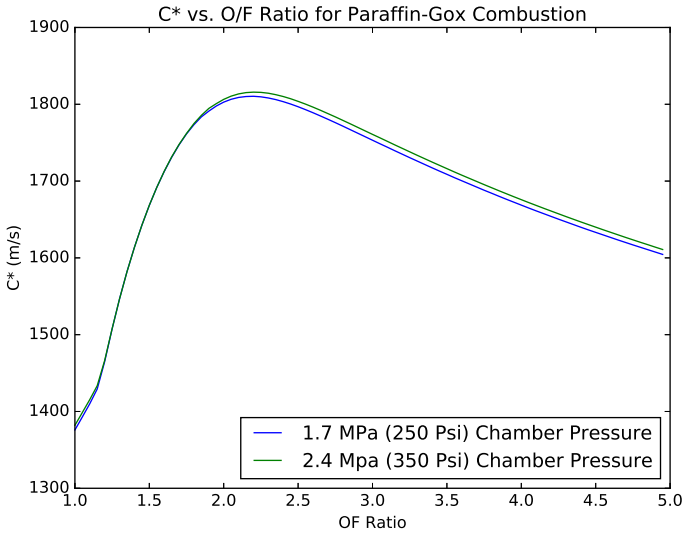

Figure 3.1: The C* values were computed in CEA and helped to size the motor. The design O/F ratio (2.1) of the motor was based on the maximum C* value.

rates available from the feed system. It was decided to utilize pure paraffin or even a custom blend developed in lab if the structural properties of the fuel grains became problematic.

Before the motor could be sized, the properties of the combustion were required. The relevant parameters from paraffin and oxygen combustion at constant temperature and pressure were computed using a rocket problem assumption in CEA. Shifting equilibrium was used along with the conditions specified in Table 3.1. The O/F ratios were varied from 1 to 5, and the resultant C* and Isp curves are shown in Figures 3.1 and 3.2. The nominal design conditions were then set at an O/F ratio of 2.1 with a combustion chamber pressure of 1.7 kPa (250 psi), with the requirement that the system could withstand variable flow rates at combustion pressures up to 4.1 MPa (600 psi). At an O/F ratio of 2.1 for paraffin and gaseous oxygen at 1.7 kPa (250 psi), the C^* is 1807 m/s.

With the combustion requirements set, the sizing study could finally be performed. Initially, the regression rate constants were estimated to be $a = 0.488\ mm/(s\ (g/cm^2 s)^n)$ and $n = 0.62$. However, it was later found that a better estimate for the regression rate constants for neat paraffin are $a = 0.672\ mm/(s\ (g/cm^2 s)^n)$ and $n = 0.6$ [46]. A commonly used simplified (space averaged) form of the regression rate equation for hybrid rocket fuels is given in Equation 3.1. A discussion on the more general space-time coupled regression rate equation is given in Chapter 7. The simplified regression rate equation can be integrated analytically, as shown in Equations 3.2 - 3.2.

$$\dot{r}(x,t) = aG_{ox}^{n} \tag{3.1}$$

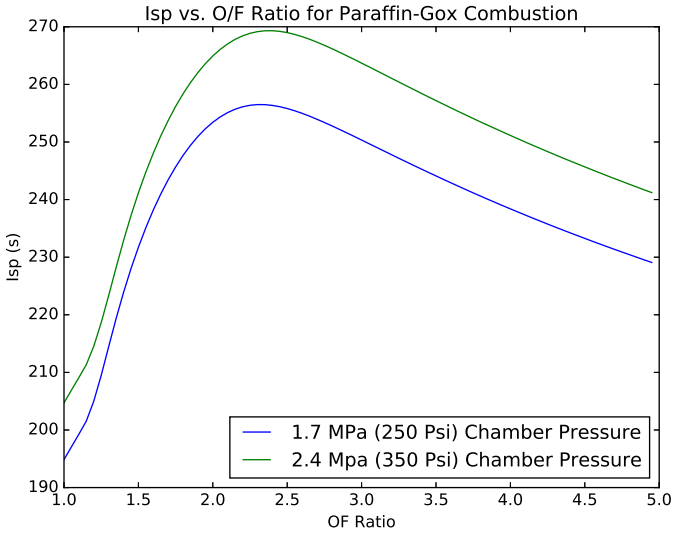

Figure 3.2: The computed Isp of the motor for various O/F ratios. Note that the Isp improves with increase chamber pressures, with roughly a 20s increase between chamber pressures of 1.7 MPa and 2.4 MPa.

Table 3.1: The conditions used for estimating the combustion and performance of the propellants used in the design of the motor.

CEA Input	**Value**
Fuel	Paraffin, C_{32} H_{66}
Oxidizer	Oxygen, O_2
Chamber Pressure	1.7 MPa (250 psi)
Ambient Pressure	1.0 MPa (14.7 psi)
Nozzle Area Ratio	3.1
Initial Temperature	300 K
O/F Ratio Values	1.0 - 5.0

$$D(t) = \left[D_i^{2n+1} + \frac{(2n+1)2^{2n+1}a}{\pi^n} \dot{m}_{ox}^n t \right]^{\frac{1}{2n+1}} \tag{3.2}$$

$$\dot{m}_f(t) = \pi \rho_f L D(t) \dot{r}(t) \tag{3.3}$$

$$\frac{O}{F} = \frac{\dot{m}_{ox}}{\dot{m}_f} \tag{3.4}$$

The integrated equations hold if the mass flow rate of oxygen is held constant throughout the burn. Rearranging into more useful form, these become:

$$t_b = \left[\left(\frac{D_o}{D_i} \right)^{2n+1} - 1 \right] \frac{\pi D_i^{2n+1}}{(2n+1)2^{2n+1} a \dot{m}_o x^n} \tag{3.5}$$

$$\frac{L}{D_i} = \frac{4 \dot{m}_{ox} t_b}{\pi \rho_f \left(\frac{\bar{O}}{F} \right) \left[\left(\frac{D_o}{D_i} \right)^2 - 1 \right]} \tag{3.6}$$

$$\left(\frac{\bar{O}}{F} \right) = \frac{\int_0^{t_b} \dot{m}_{ox} dt}{\int_0^{t_b} \dot{m}_f dt} = \frac{M_{ox}}{M_f} \tag{3.7}$$

Note that in Equations 3.1 - 3.7, L refers to the length of the fuel grain, D refers to the diameter of the fuel grain, t_b refers to the burn time, $\dot{m}_{ox}$ refers to the oxidizer mass flow rate, $\dot{m}_f$ refers to the mass flow rate of fuel, G_{ox} is the mass flux of oxygen through the port, $\dot{r}$ is the regression rate, and ρ_f refers to the fuel density.

It has been found in the lab that a good starting condition for L/D_i is around 10. For paraffin fuels, D_o/D_i is generally chosen to be limited to two for structural reasons, although this limit is an active research topic in lab.

A sizing study was performed based on these design considerations and the regression rate of the fuel. A decent burn time was desired along with a reasonably sized fuel grain diameter and length. The final sizing parameters for the nominal design of are listed in Table 3.2.

As this research required operating the motor at various O/F ratios, the flow rates were adjusted for various conditions. This in turn also limited the maximum burn time allowed for the tests. The maximum burn times for all testing conditions are listed in Table 3.3. The burn times achieved for every test can be found in Appendix J. Note that the desired burn time was difficult to achieve because of timing and ignition issues related to the feed system, which was corrected at the end of this research. Note that it was desired to have some leftover fuel (to better estimate O/F ratios), so maximum burn-time tests were purposely not performed.

Table 3.2: The final sizing parameters used for the nominal conditions of the experimental motor.

Parameter	**Value**
Oxygen flow rate	50 g/s
Max. burn time	6 s
Fuel Grain OD	3.96 cm
Fuel Grain ID	1.98 cm
Fuel Grain Density	930 kg/m^3
Fuel Grain Length	15.88 cm
Initial L/D	8.0
Final L/D	4.0
Average O/F Ratio	2.2
Initial Ox. Mass Flux	162 kg/m^2s
Final Ox. Mass Flux	40 kg/m^2s

Table 3.3: The burn times were limited by the fast regression rates of the paraffin-based fuel.

Ox. Flow Rate (g/s)	**Max. Burn Time** (s)
25	8.6
50	5.5
90	4.0

3.2.1 The O/F Shift Effect

Conventional single and multi-port hybrid rocket motors suffer from O/F shift, where the O/F ratio varies slightly with time. This problem is caused by the varying fuel mass generation rate depending on the size of the port. To illustrate the losses when accounting for O/F shift, first consider the change in O/F ratio.

$$\Delta O/F = \frac{\dot{m}_{ox}^{1-n}}{4^n a \pi^{1-n} \rho L \; D_i^{1-2n}} - \frac{\dot{m}_{ox}^{1-n}}{4^n a \pi^{1-n} \rho L \; D_o^{1-2n}} \tag{3.8}$$

Here, it is immediately recognized that the O/F shift is independent of chamber pressure and that the O/F shift is zero if the n exponent is equal to one half. Because paraffin fuels can be tailored to meet specifications, certain additives could be found such that the O/F shift is eliminated altogether. Consider the motor design used in this research. Table 3.4 lists the relevant values for the nominal design conditions.

Note the outer fuel grain diameter listed in Table 3.4 is smaller than the fabricated grain, as it is desired to leave a small sliver of unburned fuel for better overall O/F approximation. The change in O/F ratio predicted by Equation 3.8 is roughly 0.20. That means the O/F ratio at the start of the burn is roughly 2.0 and at the end of the burn is roughly 2.2. Note that at this small scale of a motor, the uncertainty in the regression rate constants, burn time, and oxidizer flow rates

Table 3.4: The values used to estimate the theoretical O/F shift at the nominal design condition.

Parameter	**Value**	**Units**
L	0.159	m
D_i	0.019	m
D_o	0.030	m
ρ	932	kg/m^3
$\dot{m}_{ox}$	0.05	kg/s

Table 3.5: The theoretical change in O/F values for the various oxidizer flow rate conditions.

Ox. Flow Rate (g/s)	**O/F Shift** $(\pm)$	C^* **Loss** (%)
25	0.09	2
50	0.11	2
90	0.14	3

make it difficult to approximate the average O/F ratio to within plus or minus 0.1. Therefore, the uncertainty of the overall O/F ratio is around the same size as the O/F shift.

In terms of overall performance, the average C^* between the three conditions is 1767 m/s, only a reduction of 2.3% from the original optimal 1808 m/s. Although these are small performance losses associated with the O/F shift, it is recognized that the O/F shift does place some uncertainty in the reported nozzle erosion data. It is nonetheless difficult to quantify the exact uncertainty introduced by the O/F shift because of the uncertainty in the fuel grain geometry makes it difficult to estimate the true O/F shift experienced during each test. This issue can be resolved by using a larger-scale motor, as larger fuel grains are easier to measure because their larger ports allow easier access for measurement tools.

3.3 Motor Design Features

The fabricated motor is shown in Figures 3.3 and 3.4. Several design choices give the motor the capability for future studies. The modular design allows for drastic changes to any section without the need for a completely new motor. Some of the main features include:

- All standard fittings
- Optional sapphire window at fore end
- Ability to use several pressure transducers or other sensors
- Modular design allows for various internal geometry configuration
- Dual ignition ports with each port angled to face fuel grain

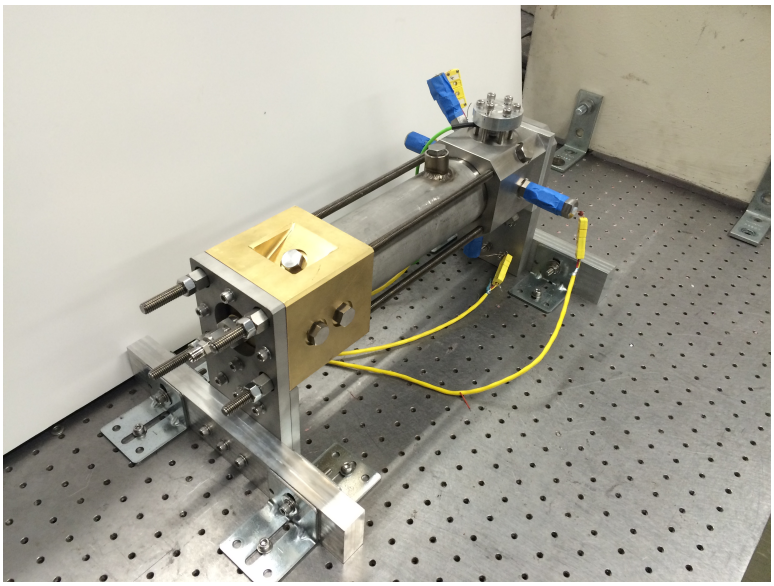

Figure 3.3: A view of the overall experimental motor. Note that the feed lines and pressure transducers are not shown here. The motor was designed to be mounted onto an optics table for easy adjustment.

- Mixer, fore end, and post combustion chamber elements
- Aft end allows for a sealed delay line and ultrasound transducer to be placed at the nozzle throat plane
- Aft end allows for up to 7 thermocouples in the nozzle

The standard fittings used in the motor are SAE J1926-6 fittings everywhere except for the pressure transducer port in the post combustion chamber region, which utilizes a SAE J1926-4 fitting [47]. Six of these fittings are on the fore end of the motor (including the two angled ignition ports) in the configuration with the sapphire window. Without the sapphire window, a seventh port is available on the axial injector block. The aft end is fitted with seven of these fittings for the thermocouple feedthroughs. The aft end is also fitted with a 0.79cm (0.31 in) hole for an ultrasound delay line at the nozzle throat plane. This hole is fitted with an o-ring to create a seal between the graphite nozzle and the outside of the motor. The nozzle remains sealed within the aft end despite being fitted with up to 7 thermocouples and an ultrasound transducer. The combustion chamber has one J1926-4 fitting that is used as a pressure tap to measure chamber pressure just upstream of the nozzle.

In addition to the use of standard fittings all around the motor, bolts and nuts are consistently sized for convenience. This allows for the motor to be completely assembled and disassembled

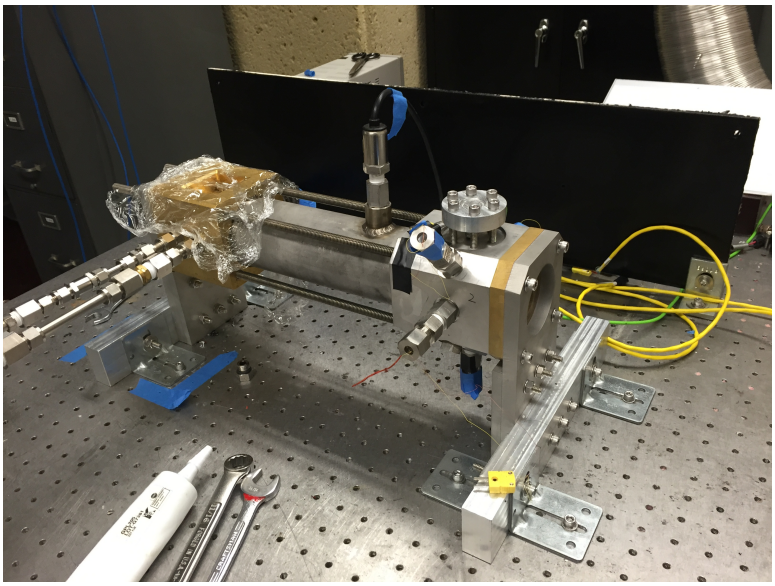

Figure 3.4: A view of the fully instrumented motor before a test. Note that the fore end is covered to prevent particles from entering through the open ignition port and to keep the sapphire window clean.

with just a few tools. Furthermore, the overall modularity of the motor allows for future research potential.

Before fabrication, the motor design was subjected to several finite element analysis (FEA) stress tests to find the weak points and verify that the motor could indeed withstand at least 4.1 MPa (600 psi) with a safety factor of two. The results of these simulations are shown in Figures 3.5 and 3.6.

The sapphire window was a point of concern in the design of the fore-end. Achieving a good seal and protecting the window from heat were the most challenging aspects. The final design choice included a female bore seal in the brass for a radial seal. Additionally, the window was pressed against EPDM spacer sheets of 1.6 mm (0.06 in.) thickness on each side to prevent contact with metal. The final design choice was considered successful as only one window had a minor crack after 20 hot fires.

Before the first fire, the motor was subjected to a hydrotest of 4.1 MPa (600 psi). Recall that the highest chamber pressure tested was 2.4 MPa (350 psi), which was significantly lower than the hydrotest. This gave confidence that the motor would not fail during testing because of chamber pressure. It also showed that the window seal was good and that the window was strong enough to withstand nominal chamber pressures.

A small problem experienced with the hydrotest was with the nozzles. Water seamed to be leaking out of the nozzle material and into the aft end section. The thermocouple feedthroughs did seal the water in, but water was not expected to seep through the graphite. Upon further inspection,

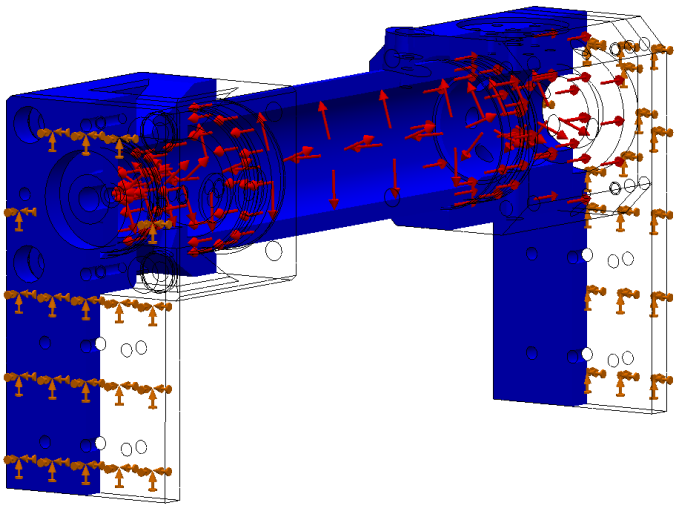

Figure 3.5: A simple finite element study shows that at a pressure of 6.89 MPa (1000 psi), the safety factor of the structural components is greater than 2. Having a relatively large safety factor at a pressure far greater than the expected testing conditions ensures that the motor will remain intact.

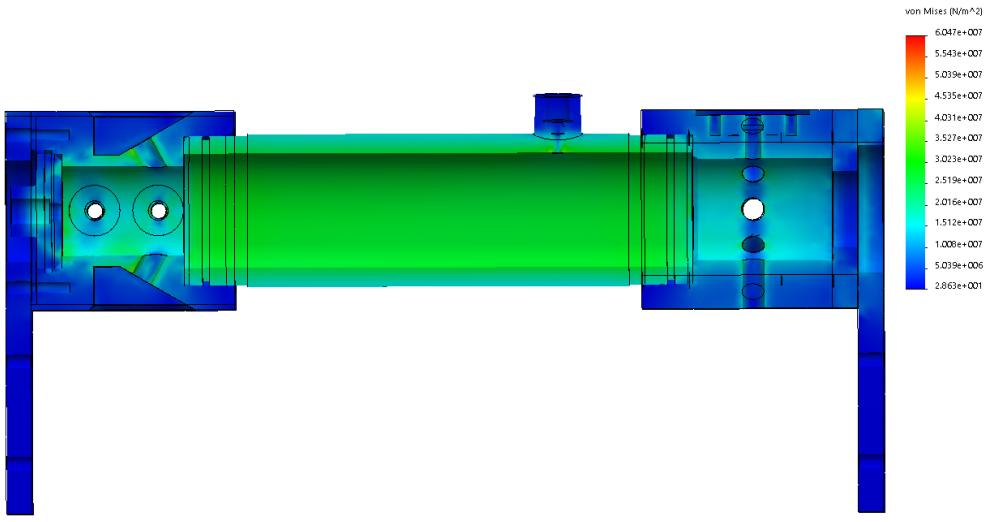

Figure 3.6: The structural members of the motor are designed to withstand more than twice the expected combustion pressures (6.89 MPa). The highest stress point is the aft end pressure measurement hole, which maintains a factor of safety above two.

it was determined that the porosity of the graphite allows for pressurized water to flow through very slowly. The manufacturer of the graphite confirmed that the same grade of graphite has been used successfully as rocket motor nozzles and that the porosity is a non-issue in terms of the material properties and the rocket nozzle application. In this research, although water flowed through the graphite, there was no evidence of combustion gases flowing through the graphite and the nozzles did not have any issues during the hot fires. For anyone designing rocket motors, it is recommended to not have any graphite in the motor during a hydrotest, as the graphite must be thoroughly baked to remove all water content before a hot fire.

3.3.1 The Fore End

A cross section view of the fore end is shown in Figures 3.7 and 3.8. This configuration is shown with the window installed (which was used for all tests). In this configuration, the window allows for an unobstructed view down the port of the motor. The video results from this view are discussed in Chapter 7. The fore end block was manufactured from a large block of brass. Brass was chosen for the fore end as its high density and thermal conductivity would protect the internal surfaces during the short burns. Typically with rocket motor designs, exposing metal to combustion products is not recommended. In order to have a window, some exposed metal would be required, and brass seemed to be the best option because the material conducts heat very well.

For the experiments run in this research, the bottom ignition port and one of the four ports were capped off and remained unused. A side injection scheme was used to introduce both gaseous oxygen and the nitrogen purge gases. Although this side injection scheme might be problematic for other oxidizers such as liquid oxygen and nitrous oxide, the results were great for gaseous oxygen. Ignition was problematic at times with this side injection scheme, but the straight-views down the port were worth the penalties associated with using side injection. A top-down cross section view of the forend is shown in Figure 3.7. Here, the feed system components are shown.

The fore end is fitted with a graphite tube to protect the inner channel of the brass. For the first test, this tube was made out of paper phenolic, which nearly completely burned away during the first test. During this test, the plume had several visible instabilities and was very smokey. However, the performance of the motor was notably higher and this concept of a burning precombustion chamber might provide a means for improving efficiencies [40]. This concept needs to be further explored.

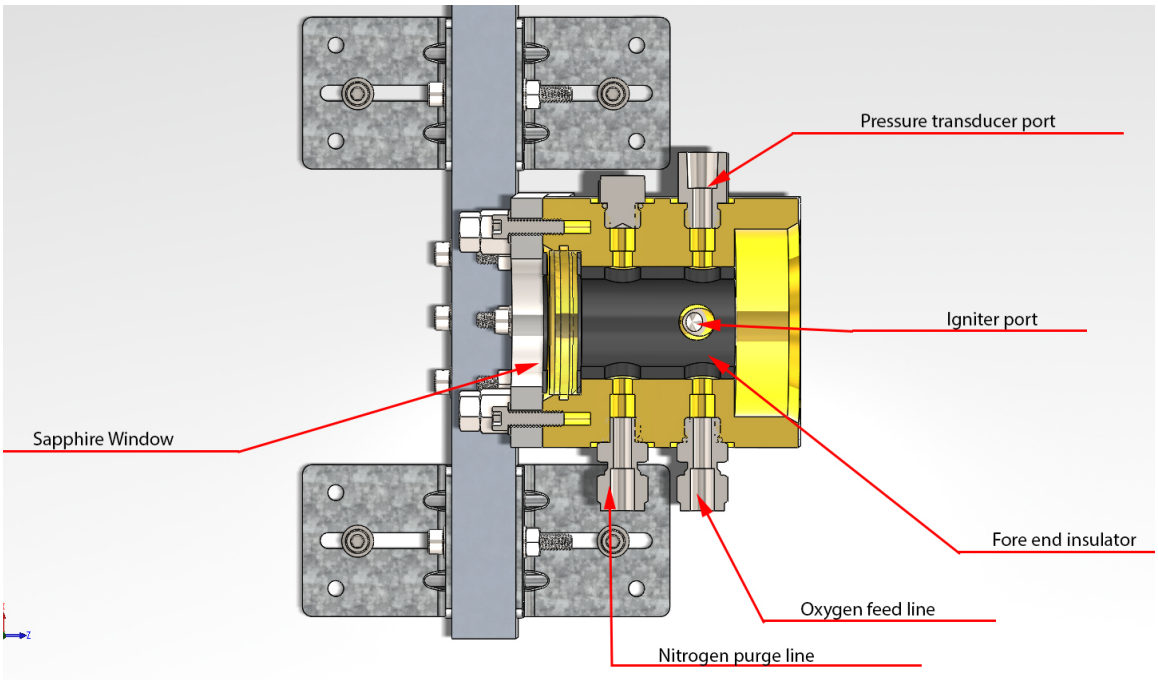

Figure 3.7: A top-down view of the CAD model of the fore end of the experimental motor highlights the side-injection scheme used to provide the motor with gaseous oxygen. Note that the fore end retains the capability of adding up to two more sensors or fittings for future research.

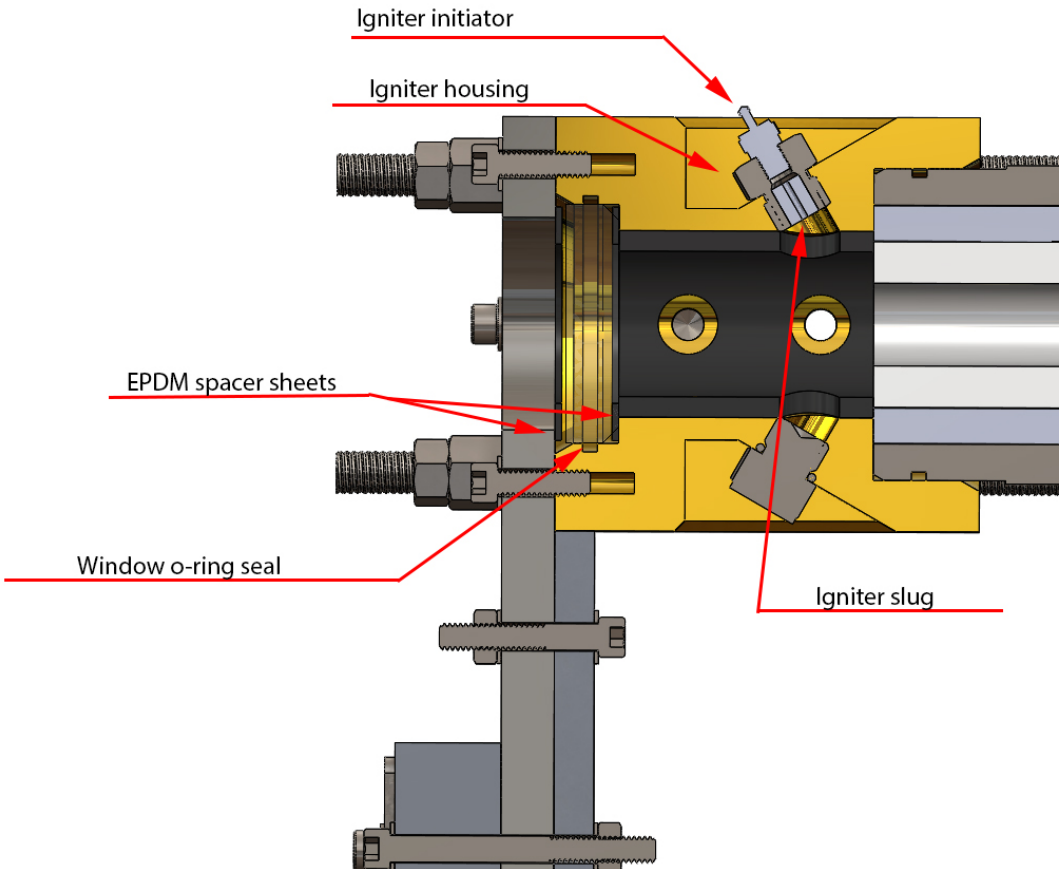

Figure 3.8: A side section of the CAD model of the fore end of the experimental motor shows the sapphire window and the sealing components as well as the igniter components. Note that the igniter assembly is pointed directly at the fuel grain.

3.3.2 The Combustion Chamber

A section view of the combustion chamber is shown in Figure 3.9. The insulator walls in the combustion chamber are made of thick paper phenolic. The insulators were designed to be thick so that the stainless steel chamber could have a larger inner diameter. Although not used for this research, this larger diameter might be needed for the combustion of lower regression rate fuels, which require more mass generation for performance.

To save on time and machining costs, the insulator in the chamber is made from two parts with differing inner diameters. The thicker insulator is used to house the fuel grain while the thinner insulator is used to house the acrylic mixer, post combustion chamber, nozzle pre-ramp, and a portion of the nozzle.

For every test, the fuel grain, insulators, mixer, and EPDM spacers are consumed. Because of this, these components are designed with simplicity in mind and were manufactured in large batches. The acrylic mixers were laser cut from 6.4 mm (0.25 in) thickness sheets of acrylic. The fuel grains were made in lab with a spin-casting machine, and the EPDM spacers (1.6mm thick) were cut in lab with standard scissors.

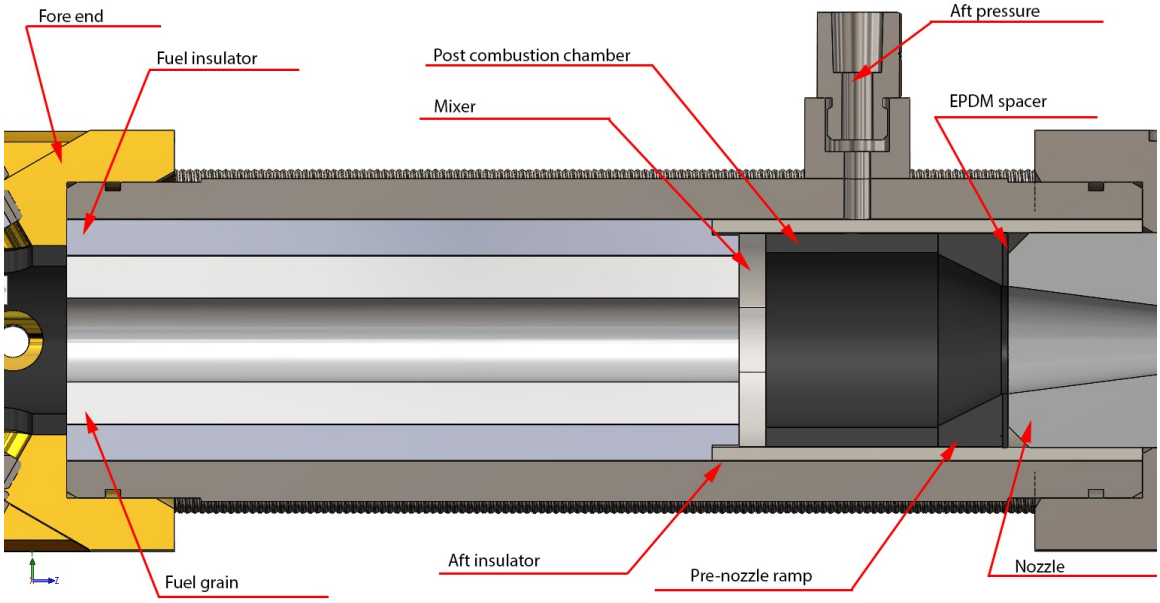

Figure 3.9: A side section of the CAD model of the combustion chamber of the experimental motor shows the internal elements of the combustion chamber. Note that the nozzle is shown in gray to clearly illustrate the flow path.

Figure 3.10: Most of the components used inside the combustion chamber are consumable. The only parts used in multiple tests are the graphite post combustion chamber and the graphite ramp, which transitions the flow from the combustion chamber diameter to the entrance diameter of the nozzle.

3.3.3 The Aft End

The aft end of the motor houses the nozzle and all related sensors. This includes 7 SAE J1926-6 fittings for attaching up to seven thermocouples to the nozzle as well as a delay line port for an ultrasound transducer. Each port is either blocked off or used with a feed through for the thermocouple wire. This ensures that the nozzle remains completely sealed with embedded sensors. The thermocouple wire feedthroughs used were manufactured by SpecTite with model number WFS-1/4"NPT-0.020"-2-T-A [48]. These feedthroughs have all Teflon (PTFE) internal packing components to reduce the likelihood of wires shorting. The delay line port, which includes a female o-ring grove to seal, allows for a 1-inch long delay line with a 0.30 inch diameter delay line. The 2.25 MHz ultrasound transducer model number is RDG022 from NDT Systems [49]. The transducer is secured in place by the transducer mounting block, which attaches to the aft end with 6 socket cap screws. Figure 3.11 shows a cross-section view of the nozzle throat plane. The seven SAE J1926-6 ports and delay line ports are clearly shown. The ultrasound transducer is fixed in place by a retaining plate with 6 bolts. This plate also has an o-ring grove so that the delay line port can be sealed if there is no ultrasound transducer used for a test. The aft end assembly is shown in Figure 3.12.

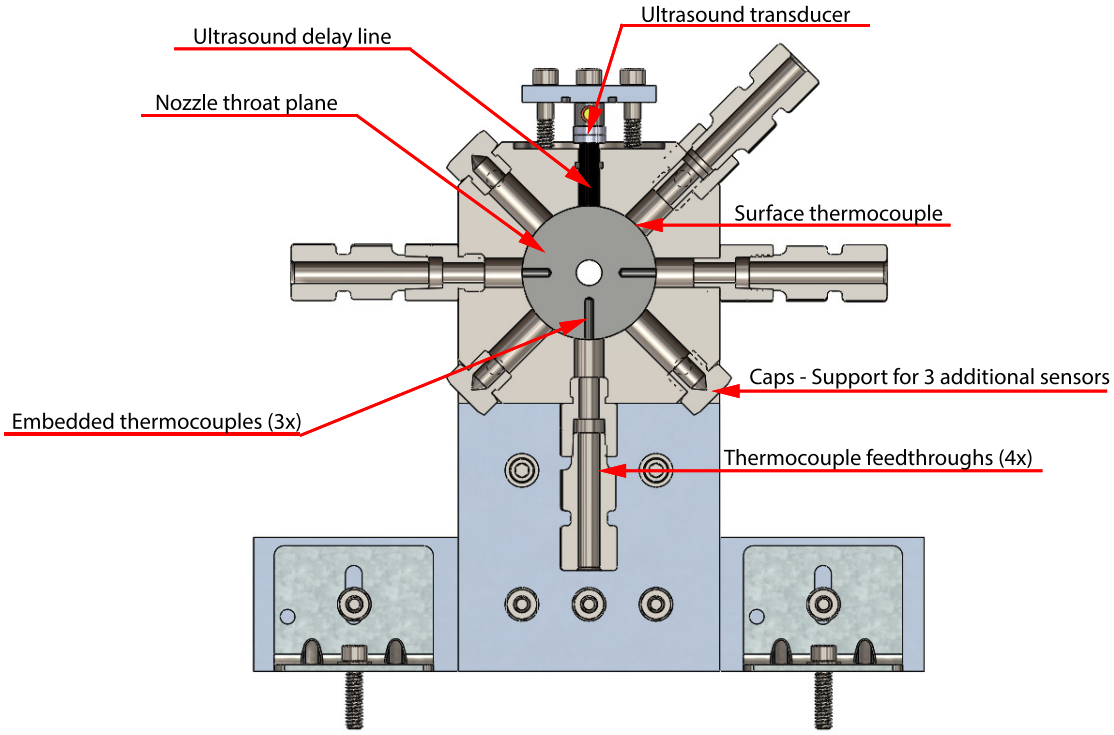

Figure 3.11: A section view of the CAD model of the nozzle throat section shows the paths for the embedded thermocouples, thermocouple feedthroughs, and the ultrasound transducer hardware.

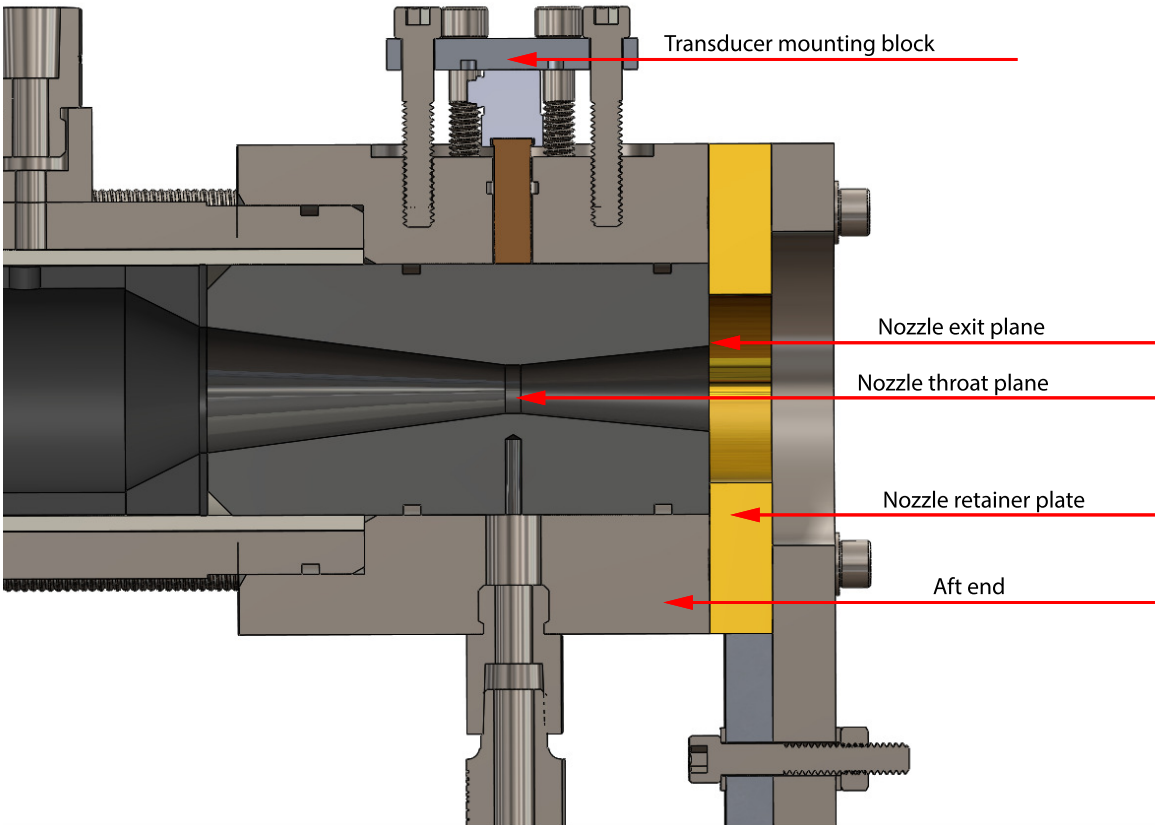

Figure 3.12: A side section view of the CAD model of the aft end of the experimental motor shows the design of the aft end components.

3.3.4 The Nozzle

A long nozzle design is utilized to simplify the thermal analysis. To reduce costs, a conical nozzle profile is used for both the converging and diverging sections. Nonetheless, the nozzle efficiency is estimated to be around 99%, based on textbook estimates given the nozzle geometry [2]. A measurement on the nozzle efficiency is not taken in this research as the thrust is not measured on the experimental motor. Table 3.6 lists the relevant diameters for each of the test cases. Note that in all cases, the outer diameter of the nozzle is 5.03 cm (1.98 inches). The overall length of each nozzle is 10.16 cm (4.0 inches), and the throat plane is located 3.97 cm (1.5625 in) upstream of the nozzle exit.

Each nozzle tested has three embedded thermocouples as well as a thermocouple placed on the outer surface. These thermocouples are placed inside the graphite nozzle, which has three holes drilled at various depths at the throat plane, as shown in Figure 3.11. The depths of the embedded thermocouples (as measured from the outer surface) are shown in Table 3.7. These depths were selected after several numerical testing studies. While these depths were not optimized for accuracy (the best accuracy would have thermocouples at the throat section, or maximum depth), their depths were based on the need for the nozzle to remain structurally sound throughout the burn and also took keep the thermocouples within their temperature limits [50]. The thermocouples used in this experiment were made from 50 μm wire, which is extremely delicate (See Section 4.4.1). This fine wire size was chosen as it would provide a good response time [41] yet still be stiff enough to handle. Upon installation, some thermocouples broke and provided no data. The data provided by the other thermocouples was enough to maintain accuracy and stability for the inverse solver. The maximum number of broken thermocouples was one for any given test. With more experience this number could be reduced to zero.

The thermocouples were embedded into the graphite nozzle with a high-conductivity ceramic paste, made by Cotronics Corporation (Resbond 906) [51]. This paste is electrically insulative, which reduces grounding problems as graphite is electrically conductive.

The ceramic paste is designed for use in much higher temperature applications and worked well. The thermocouple installation procedures are shown in Appendix H.4. Note that the response of the

Table 3.6: The relevant diameters for the nozzles used in the experiments for this research. Note that the inlet diameter (25.4 mm) is the same in all cases

Test Condition	**O/F**	**Pressure (Mpa)**	**Throat Diam (mm)**	**Exit Diam (mm)**
A	2.10	1.72	9.80	17.27
B	1.70	1.72	7.16	13.46
C	2.75	1.72	12.70	23.37
D	1.70	2.41	6.07	12.95
E	2.10	2.41	8.36	17.78
F	2.75	2.41	10.74	22.86

Table 3.7: The thermocouple depths for each of the nozzle configurations.

Test Condition	**TC Depth 1 (mm)**	**TC Depth 2 (mm)**	**TC Depth 3 (mm)**
A	16.26	14.22	11.18
B	15.49	13.46	11.43
C	12.70	1066.80	8.64
D	16.00	13.97	11.94
E	14.73	12.70	10.67
F	13.72	11.68	9.65

thermocouples are inherently reduced due to the fact that the thermal conductivities do not match. Unfortunately there is no easy way around this and there is some additional lag in the thermocouple response time. To somewhat alleviate this issue, the thermocouple sampling rate is limited to 10 Hz, which is still a relatively quick thermocouple measurement.

One point of concern when designing this experiment was the fact that the drilled holes for the embedded thermocouples might affect the heat transfer within the nozzle. Although nozzle erosion would not be affected by the insertion of thermocouples or an ultrasound transducer, the heat transfer would be affected nonetheless. A simple finite element analysis study was conducted to determine how much of an affect the drilled holes had on the temperature profile.

Figure 3.13 shows the results of the simulation at the throat plane of the nozzle when $30 MW/m^3$ of heat flux is applied on the inner surfaces of the nozzle for 5 seconds. Note that there seems to be no difference at the holes that are drilled for the embedded thermocouples. There also does not seem to be a hot spot at the tip of the drilled hole. This suggests that the introduction of the drilled hole might not have a large impact on the overall heat transfer within the nozzle.

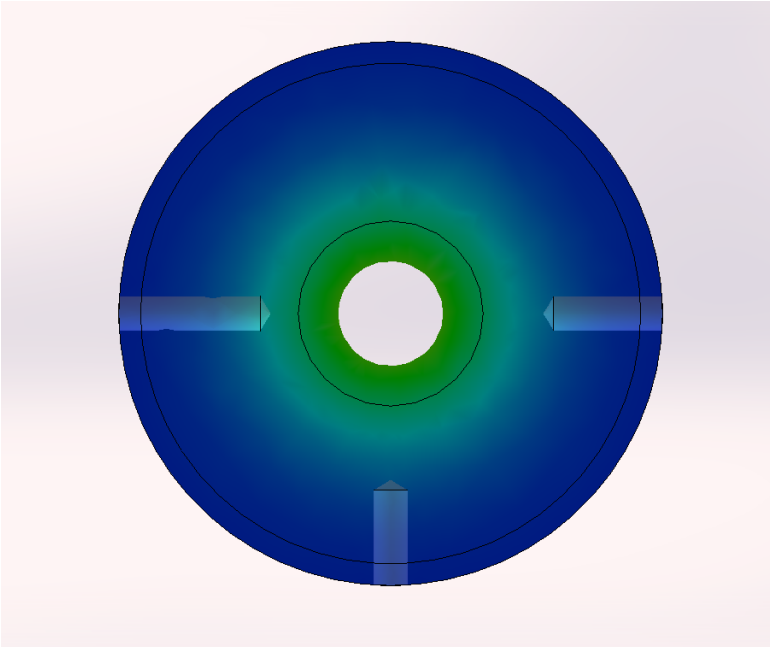

Figure 3.13: A simple nozzle thermal simulation shows that the temperature distribution remains symmetric despite the addition of holes for the embedded thermocouples.

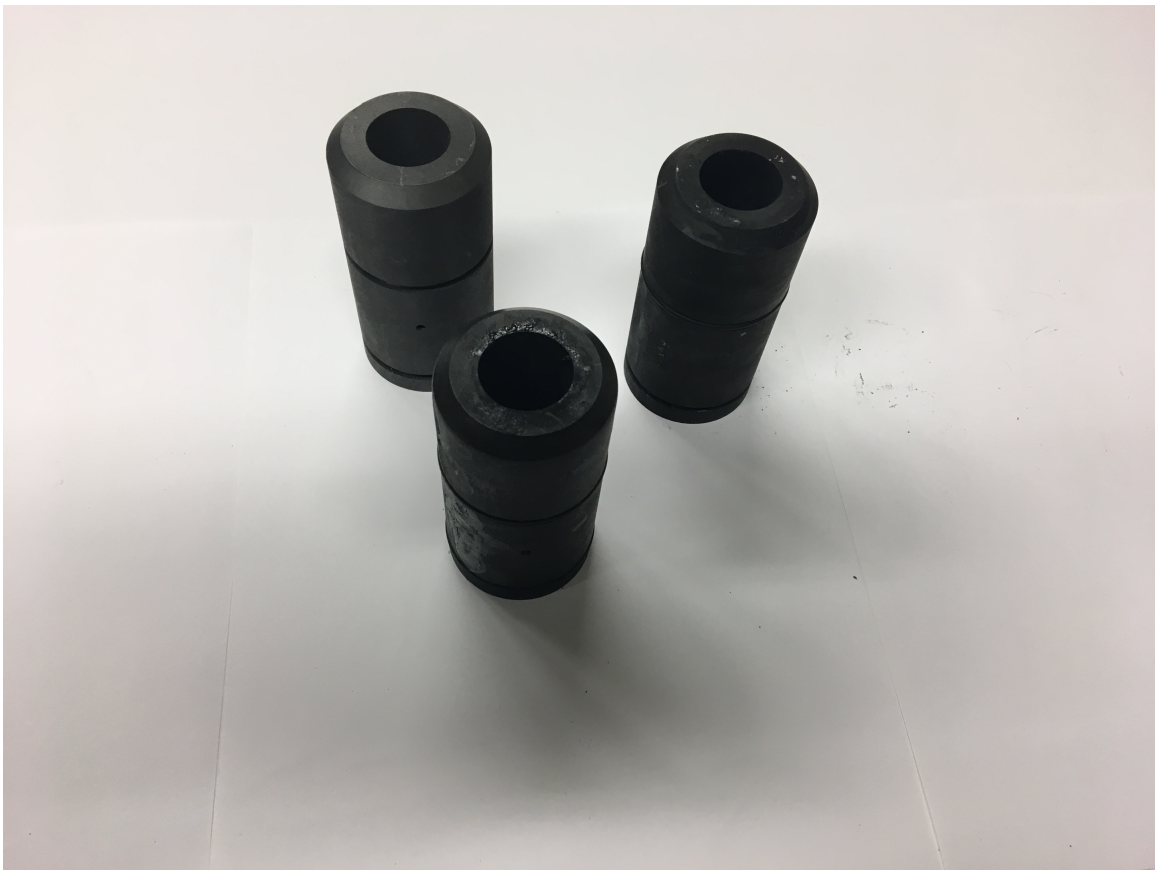

Figure 3.14: Three of nine total manufactured nozzles are shown here. The simple conical geometries of the nozzles allowed for variable geometries (between the nozzles) without large manufacturing costs.

Chapter 4

Experimental Setup

This chapter discusses the auxiliary equipment used with the experiment. This includes a quick discussion on the feed system and cold flow data. The fuel grain formulation, ignition system, data acquisition, and motor control systems are also described along with the most important sensors used in this research.

4.1 Feed System

The feed system utilized in this experiment was designed for the Stanford Combustion Visualization Facility [52], which provided some design limits for the motor sizing. The feed system was modified slightly so that one could select which experiment by opening and closing certain selector ball valves. The P&ID of the feed system is shown in Appendix D.2. Cold flow tests were run to determine the orifices and driving pressures required to obtain the desired flow rates, as shown in Table 4.1. The oxidizer for the motor is provided by two T-cylinders of oxygen mounted to a Dome-loaded regulator (Model 44-4019E212-108 from Tescom [53]). The driving pressure is selected by software.

For the cold flow tests, a pressure transducer was mounted just upstream of the orifice with a tee fitting so that the upstream pressure could be verified to be above a factor of two above the highest chamber pressure of 1.72 MPa (350 psi). Recall that in order for an isentropic flow of ideal gas, such as oxygen (with ratio of specific heats, γ, of 1.4) to be choked at an orifice, it must be a

Table 4.1: Driving pressure and orifice sizes for desired flow rates based on cold flow data.

Flow Rate, g/s	**Orifice Size, cm (in)**	**Driving Pressure, MPa (psi)**
25	0.18 (0.07)	5.7 (830)
50	0.22 (0.086)	6.2 (900)
90	0.32 (0.125)	6.6 (950)

Table 4.2: The average time required to actuate the main oxidizer valve.

Command	**Average Response Time**
Open	0.5 seconds
Close	1.2 seconds

factor of at least 1.89 greater than the back pressure][54]. For all cold flow tests, the pressure just upstream of the orifice was higher than 5.52 MPa (800 psi). Because chamber pressures were always below 2.25 MPa (400 psi), this suggested that the flow was choked at the orifice, which was located just upstream of the motor.

The only addition to the feed system for this research was the addition of a pneumatically actuated ball valve, some tubing, and the orifice as mentioned above. The ball valve is placed close to the motor so that start-up and shut-down transients remain short and pressurized oxidizer can quickly enter the chamber upon valve actuation. The approximate actuation times of this ball valve are listed in Table 4.2.

4.2 Ignition System

The igniter system used to start the motor is known as the Stanford Initiator. It consists of a modified McCoy MC59 glow plug and a secondary slug, commonly called the igniter slug. The combination of these two are thought to be an affordable and reliable method of igniting a hybrid rocket motor.

Unfortunately, a batch was most likely incorrectly made and this research was plagued by failed ignitions. In the lab, this was no big deal as a new igniter could be put in within minutes and the mass of lost oxidizer was negligible. Because this research does not utilize a traditional oxidizer tank, no time was needed to fill tanks to pressure again.

In the field, a failed ignition has drastically higher costs both in time and materials. Because of this, every step must be taken to reduce potential for failed ignitions. The Stanford Initiator was developed roughly 10 years ago with very little documentation surviving the years [55].

For obvious reasons, after testing was complete, it was desired to manufacture a correct batch of the initiator and igniter slug combination in the proper manner. A detailed set of procedures was also desired so that the components can be fabricated in the future when the lab stock runs low. In making the new batch, proper notes were taken and the procedures were made. Appendix H.1 contains the procedures and some other relevant notes in fabricating the Stanford Initiator. To date, the new batch of igniters has not failed and has proven successful for several hot fires in several hybrid rocket motors.

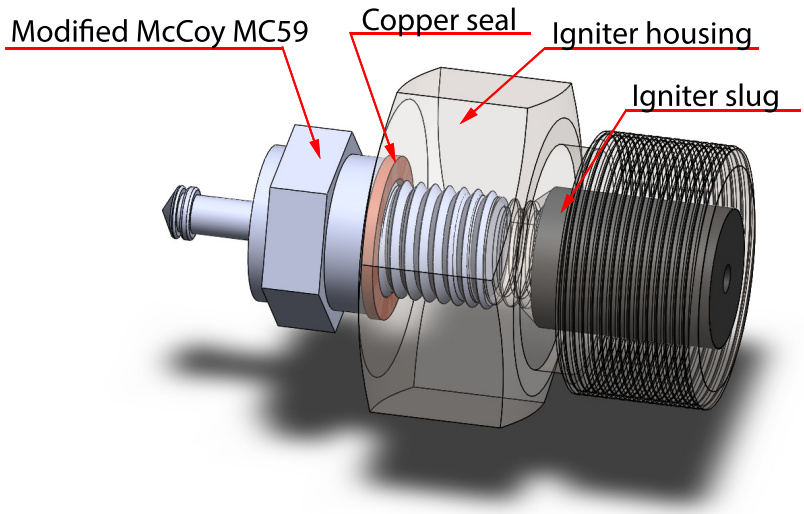

Figure 4.1: The igniter assembly contains four parts. Note that the only non-consumable part of the igniter system is the igniter housing, which is thoroughly cleaned between tests.

4.3 Fuel Grain Formulation

The motor was originally intended to burn pure (neat) paraffin without any additives or blackening agents. Therefore, the first set of tests were run with pure, unblackened paraffin. The early tests, which were run at 1.72 MPa (250 psi) at the lower flow rates of 50 g/s and 25 g/s showed no evidence of fuel grain-related issues.

However, with the higher flow rate of 90 g/s, there were some indicators that the fuel was cracking and exiting the motor unburned. In one particular test (Test #13), the fuel grain left the motor during the burn and only insulator was left burning for almost a second. It was clear that the insulator was burning as the chamber pressure was significantly reduced (the insulator has a low regression rate), as shown in Figure 4.2. Because of this, a new formulation was desired.

Because the paraffin used is essentially a high temperature candle wax, some guidelines were taken from the supplier of the paraffin. The paraffin part number in all of this research is 160 Melt Point Wax - 5560 (Model 2052) from The Candlewic Company [56]. The manufacturer recommends mixing stearic acid to the melted wax to increase the structural characteristics of the solidified wax. It is suggested to add up to 8% stearic acid by mass in increments of 2% until the desired properties are achieved [57]. The addition of 2% stearic acid by mass was enough to solve the cracking issues for the remainder of the tests. It was then decided to keep the new recipe for the rest of the tests and

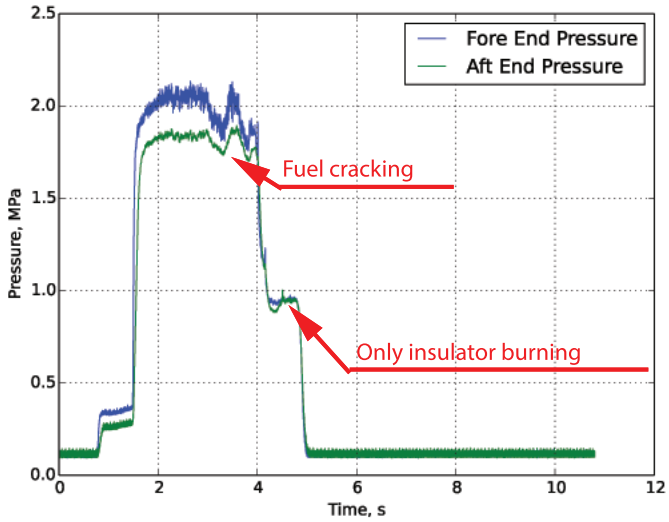

Figure 4.2: Test 13 suffered from a cracked fuel grain that was expelled from the motor relatively early. The insulator burned for nearly a second after the fuel was ejected, as shown by the lower chamber pressure.

Table 4.3: The mass fractions of the custom fuel blend used after Hot Fire 13. This blend did not seem to exhibit cracking for the rest of the campaign.

Ingredient	**Mass Fraction (%)**	**Ideal Molecular Formulation**
Paraffin Wax	98.0	$C_{32}H_{66}$ [59]
Stearic Acid	2.0	$C_{18}H_{36}O_2$ [60]

perhaps for other motors in the future. It was also attempted to add 0.1% iodized table salt to the blend as well. The thought behind the addition of salt was an attempt to color the flame a deeper yellow in hopes to detect the salt through a spectroscopic measurement [58]. However, the table salt did not mix into the liquid wax and ultimately did not make it into the fabricated fuel grains. For this research, each fuel grain was fabricated using a spin casting technique with machinery in the lab. The procedures for operating the spin casting hardware are given in Appendix H.2.

If one needed salt in the fuel grain, a different fabrication technique would need to be used. The major benefit of the spin casting technique for paraffin wax is that with proper speeds, the maximum density of paraffin wax can be achieved. However, certain additives, such as salt and aluminum, require alternative fabrication techniques. One such technique is a drip casting technique, where the liquid mixture is continuously dripped into a mold. This technique takes practice to master, as just the right dripping speed is needed. At this point, the achievable fuel grain densities when using a drip casting technique are unknown.

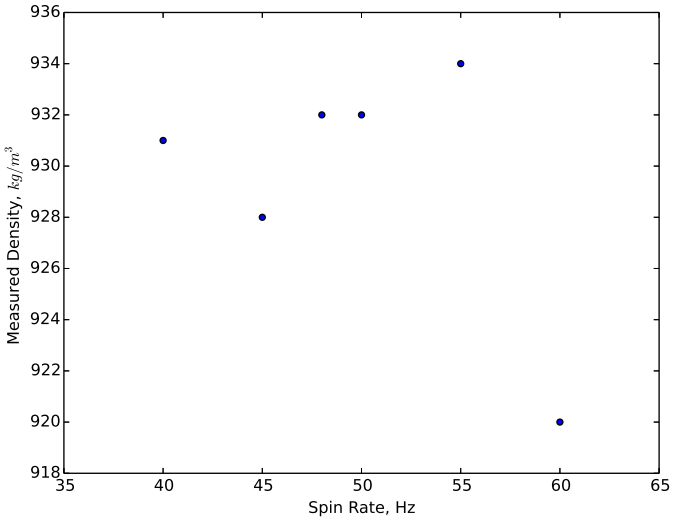

Figure 4.3: The measured densities of fuel grains vs. the spin-casting speed used to fabricate them. A constant fuel density value of 932 kg/m^3 was used in the analysis.

The fuel grains in this research were all manufacturing using a spin-casting technique. The casting machine in this lab was made a number of years ago and rebuilt by Edward Momanyi, a summer undergraduate student. In rebuilding the system, several full size fuel grain samples were made at various spin rates to optimize the fuel grain properties. Some of these samples were intentionally broken and inspected for internal defects, such as air bubbles, voids, and cracks. Six samples were machined down to size and their densities were measured in Professor Tiziana Vanorio's (from the Stanford School of Earth, Energy, and Environmental Sciences) lab using a helium pycnometer with the aid of Dr. Anthony Clark. The results of these tests are shown in Figure 4.3. A surprising find in these measurements was that the measured density of the fuel grains was actually *higher* than the 924 kg/m^3 generally used for paraffin wax. All grains were cast at a spin rate of 55 Hz, and a density of 932 kg/m^3 was used in all analysis for this research.

4.4 Data Acquisition and Control

The motor data was obtained via two different computers and acquisition systems. The nozzle thermocouple data was acquired using an MCCDAQ USB2408 device from the Measurement Computing Corporation [61]. This 24-bit DAQ is temperature compensated and can collect data at up to 1 kHz. This DAQ was connected to a laptop under the optics table that the motor was mounted on. This reduced the wiring lengths and helped to reduce noise and signal losses on the thermocouple measurements.

A Raptor ultrasound machine (manufactured by NDT Systems in Huntington Beach, California [49]) was connected to the ultrasound transducer on the motor. This machine was also placed under the optics table. The ultrasound machine was connected to the same laptop used for logging the temperature data. In order to align the thermocouple and ultrasound data to the data logged by the control computer, a digital input was used on the USB2408 device. This input was connected to the main oxygen valve power line through a relay for isolation. With this setup, the thermocouple and ultrasound data was easy to sync with the pressure data.

The feed system data, pressure transducer data, and motor control were all managed from another computer. This computer was located in the control room and wires were fed across into the testing room. The control and DAQ settings were all built for the Stanford Combustion Visualization Facility and only minor changes were allowed for this research.

The data acquisition and control hardware was manufactured by National Instruments. The part numbers are NI cDAQ-9174 for the hub [62], NI 9205 for the pressure data [63], NI 9237 for the differential pressure data [64], NI 9213 for the temperature data [65], and NI 9401 for the digital data [66]. A major drawback of this setup was that the control hardware was on the same USB line as the acquisition hardware and this proved to be buggy, as at times the system would crash. Additionally, the Labview software was in charge of collecting data at a high frequency (1600 Hz) as well as controlling the motor timing sequences. It is likely that this is too much for the hardware as the Labview control seems to be inconsistent (the main oxygen valve was open for up to 1 second longer than commanded at times, and sometimes ignition would fail, despite successful burning of the ignition hardware). Because of this, a new scheme was developed after this research concluded. See Appendix K. See Appendix E.3 for a schematic of the general layout of the test stand and control hardware.

Ignition Timing Sequence

The ignition timing sequence was determined based on trial and error along with the knowledge of ignition timings for previous experiments and previous knowledge. Initially, the the initiator was lit at the same time the main oxygen valve was opened. However, with some failed ignitions, a small delay was added between the two events. The finalized sequence involved commanding the main oxygen valve, waiting 0.2 seconds, and then powering the Stanford Initiator glow plug. Note that this timing sequence needs additional study as reliable ignition was not attained.

Figure 4.4 shows an image of the initial igniter tests that were performed before the first fire of the motor. These tests proved that the igniter was sufficient to start the motor and also that the feed system was behaving as expected. During the ignition testing, an LED was placed on top of the motor. This LED was powered by the oxidizer valve signal, so an accurate timing could be determined from when the oxidizer valve had signal and when the igniter gave out its first light. This helped in determining the response time of the system, but in the end, the ignition timing

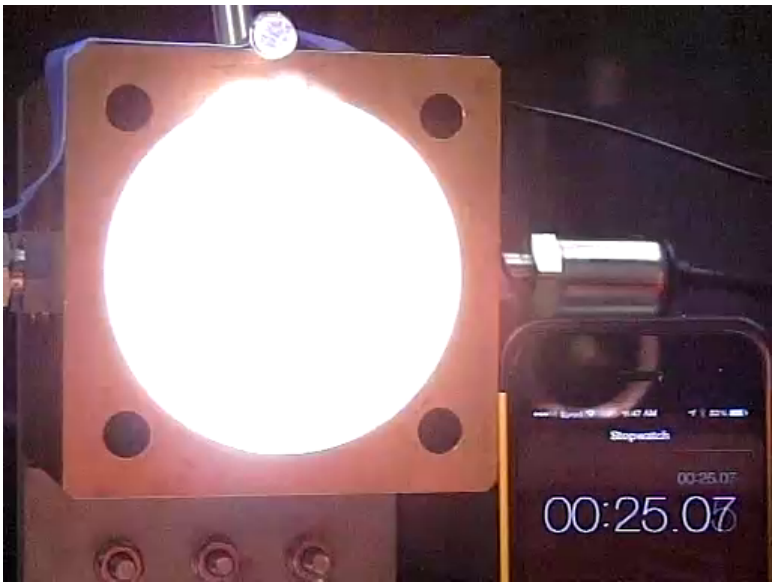

Figure 4.4: The ignition timing tests were run before the first hot fire of the motor. These tests proved that the feed system worked as predicted. These tests also showed that the igniters would be able to start the motor. Note the LED on top of the fore end and an iPhone provide some rough timing measurements.

sequence was empirically determined.

4.4.1 Sensors in the Motor

The experimental motor is fitted with sensors to measure several important hybrid rocket parameters. These include pressure measurements (used to estimate efficiency, thrust, stability, and burn time) as well as temperature measurements in the nozzle to estimate heat transfer. Arguably the most important sensor in this research is the 2.25 Mhz ultrasound transducer fitted on the nozzle at the throat plane.

Pressure Transducers

The pressure transducers on the motor are made by SSI Technologies (Model #P51-1000-A-A-I36-20MA-000-00) [67]. These transducers output 4-20mA signals depending on the load pressure. These were converted to voltage using a 250 Ohm resistor at the DAQ. Additionally, an analog first order low-pass filter is implemented with a 250 Ohm resistor and a 1 μF capacitor. This filter has a cut-off frequency of approximately 640 Hz. Because of this, only frequencies lower than this will be discernible.

The pressure transducers are located in the fore end and aft end of the motor. Because of the internal geometries of the motor, the aft end pressure readings are usually about 5% lower than

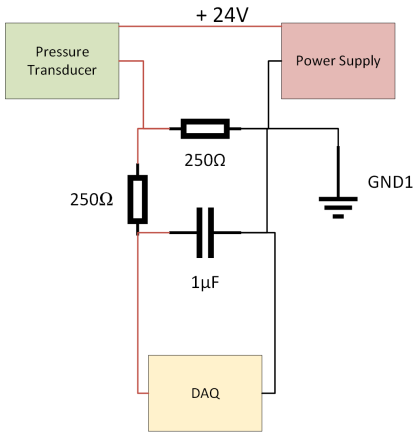

Figure 4.5: The circuit used to power and low-pass filter the pressure transducer data. The filter was applied to prevent both aliasing and capacitance issues with the pressure transducers.

the fore end measurements. The aft end measurements are used for all performance computations as these are likely the parameters that would determine the thrust of the motor. The aft end measurement is additionally filtered by the complicated flow path the hot gasses must take to reach the sensor. This protects the sensor and extends the lifetime of the sensor, which operates outside the recommended conditions. Because of this, spectral analysis must be done with the fore end pressure data. Each of these pressure transducers are connected to the feed system control DAQ. Note that as a safety feature, the feed system control DAQ performs an automatic emergency shutdown if chamber pressures exceed a certain predetermined value.

Temperature Sensors

Recall that the nozzle is equipped with embedded thermocouples and a surface thermocouple at the outer surface. All the thermocouples for this research were manufactured using a fine-wire welder (HotSpot II Thermocouple Welder from DCC Corporation [68]). The thermocouples were welded from 50 μm (0.002 in) uninsulated K-type thermocouple wire from Omega Engineering [69]. These wires had special limits of error with listed uncertainty of the greater of 1.1K and 0.4% error [42]. The full thermocouple assembly is shown in Figure 4.6.

Note that for each thermocouple, three fine welds are required. One for the thermocouple junction, and one each for stepping up the wire diameter from uninsulated 50 μm wire to insulated 75 μm wire. The ceramic tube protects the thermocouple wire from the high temperatures in the graphite nozzle and also prevents the thermocouple wire from shorting. The ceramic tube was purchased from McMaster-Carr (part number 87175K71) [70].

The thermocouples were each verified by placing in an ice water bath, boiling water, and exposing to room temperature. These tests also helped to detect thermocouples with weak joints, as those

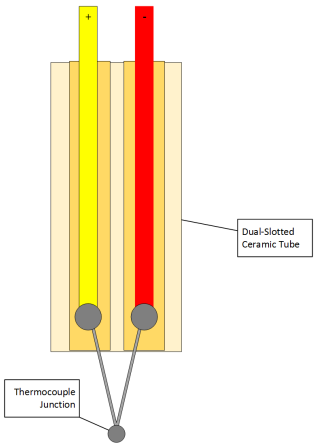

Figure 4.6: The thermocouple assembly diagram shows that each K-type thermocouple manufactured includes three welds. Each lead of the thermocouple junction is protected by a double-bored ceramic tube.

broke upon verification testing and were not desired to be used in the nozzles. In this research, the thermocouple sampling rate was 10 Hz.

Although 10 Hz may seem very slow for data acquisition, it is actually a very fast acquisition for thermocouples (assuming the thermocouples are propely sized). Very few affordable data acquisition systems are available that can sample thermocouples at 10 Hz at 24-bits resolution. In terms of inverse heat conduction solvers, as long as the thermocouples are properly sized, the inverse solution is generally gets better with faster acquisition rates. However, faster acquisition rates generally requires more computing time for a converged solution.

For this project, the limiting factor was the size of the thermocouples. It became increasingly difficult to make thermocouples with wires smaller than 50 μm in diameter. This limited the maximum sampling rate to 10 Hz.

Figure 4.7: Two thermocouple junctions are shown on top of a penny. The penny is used as a scale reference to illustrate how small the fabricated sensors really are. These sensors are made by welding two 50 μm wires together.

4.4.2 Important Sensors in the Feed System

The most critical sensors in the feed system are the sensors used to compute the mass flow rate of oxidizer flow. These sensors are a K-type thermocouple placed just upstream of a calibrated Venturi, a pressure measurement upstream of the Venturi, and a differential measurement across the Venturi. The equations used to compute mass flow rate are shown in Appendix D.3.

Chapter 5

Experimental Data

This chapter describes all of the important and relevant data for this research. It includes the pressure traces, stability, heat flux approximations, nozzle erosion measurements, and a brief discussion on the uncertainty in the nozzle erosion data. The chapter concludes with a observation made during the first test that lead to a performance boost. With further work, this boost could be fully understood and predictable, which would ultimately lead to even better performing hybrid rockets.

To date, 22 tests have been conducted for this research. The motor has since been used by other students for research involving spectrometers. A full test summary with key data points are listed in Appendix J.

5.1 Test Conditions

The motor was run at three different flow rates (to vary the overall O/F ratio) at two different chamber pressures. The flow rates and chamber pressures were chosen as they were realistic parameters one would expect out of a hybrid rocket. Although chamber pressure might be higher in many LOX-Paraffin hybrid motors, this quantity was limited to what was achievable in the lab. The lab limits were set because of the limits of the oxidizer feed system and the fact that these tests were run indoors (basement of Durand).

Table 5.1: Summary of the test conditions.

Test Condition	**Ox. Flow Rate** (g/s)	**Avg.** O/F	**Starting Ox. Mass Flux** $\left(kg/m^2s\right)$	**Chamber Pressure** (MPa)
A	50	2.10	162	1.72
B	25	1.70	81	1.72
C	90	2.75	291	1.72
D	25	1.70	81	2.41
E	50	2.10	162	2.41
F	90	2.75	291	2.41

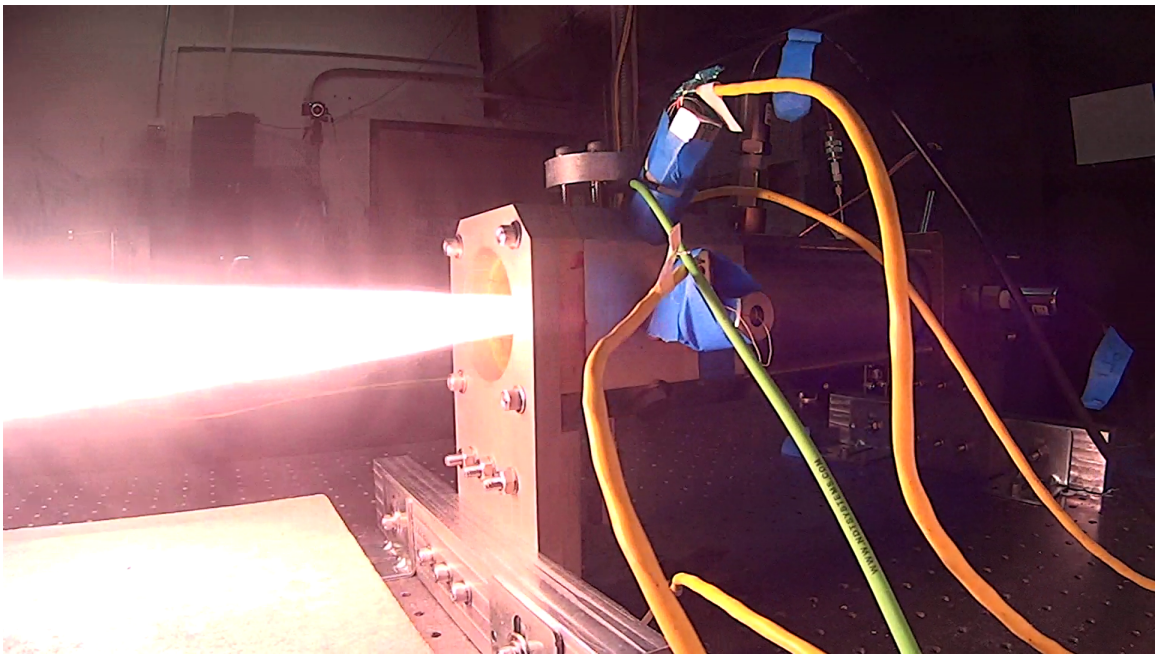

Figure 5.1: A still image from Test 4 shows the plume exiting the motor. This image shows how bright and intense the combustion process is within the combustion chamber.

5.2 Pressure Traces and Stability

The motor seemed to burn very stably in most tests. It was expected that stability might be problematic due to the side injection scheme used. However, only two of the six testing conditions showed some instability. Recall that the motor has two pressure transducers, one located at the fore end and the other located at the aft end. The pressure transducer in the aft end has a narrow complicated flow path to the transducer (to protect the sensor), which results in filtered data. However, this aft measurement is utilized in computing the combustion efficiency of the motor, as it is more indicative of the stagnation pressure entering the nozzle, which is the relevant pressure for C^*.

Figure 5.2 shows the pressure trace from Test 5. Note that the aft end measurement is smoothed out compared to the fore end measurement and that the aft measurement is generally lower. The aft pressure is lower due to the stagnation pressure loss across the combustion chamber.

Test 5 was run at the design condition of the motor, which was 1.72 MPa (250 psi) at an oxidizer flow rate of 50 g/s. The O/F ratio achieved in this test was 2.11, which was very close to the design condition. Note that at this small scale, it is difficult to achieve exact O/F ratios as the uncertainties in the mass measurements and burn times are relatively higher.

The Test 5 pressure trace displays the excellent stability of the motor. During the testing under stable conditions, the sound of the motor firing seemed stable and the videos of the plume indicated little unsteadiness as well. At lower oxidizer flow rates (lower O/F ratios) the motor was unstable compared to the other test conditions. Figure 5.3 shows the pressure trace obtained from Test 11, which was run with an oxidizer flow rate of 25 g/s and achieved an O/F ratio of 1.51. Compare the stability at this condition with Test 5.

Note that in the lower flow rate tests, the pressure drop across the combustion chamber is significantly less. This is expected as the flow rates are significantly lower in these cases, resulting in lower Mach numbers in the chamber.

Although stability was not a concern in this research, it was desired to understand the instability characteristics. The Fast Fourier Transform (FFT) [71] was computed on the fore end pressure measurements and the results were rather interesting. The unstable test data showed relatively low frequency peaks above 20 Hz. The stable test cases only showed extremely low frequency peaks (near 0 Hz). Figures 5.4 and 5.3 show the fore end pressure measurements and their spectral data for Tests 5 and 11. Note that Test 11 was the unstable test.

Four tests were run at the unstable flow condition of 25 grams per second. These tests were run at 1.72 MPa (Test 10 and 11) and 2.41 MPa (Test 20,21). Although all of these tests showed unstable behavior with large oscillations in the pressure data, the FFT data had some differences, as shown in Figure 5.6.

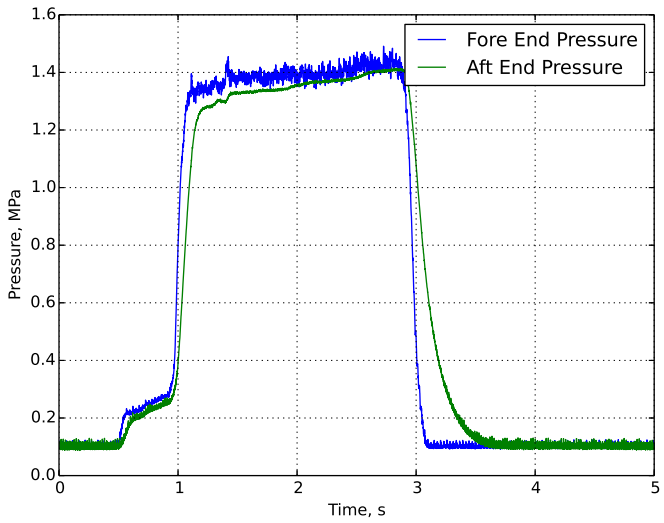

Figure 5.2: The pressure trace from Test 5 shows that the motor is stable at an oxidizer flow rate of 50 g/s. The average O/F ratio through the burn is 2.1.

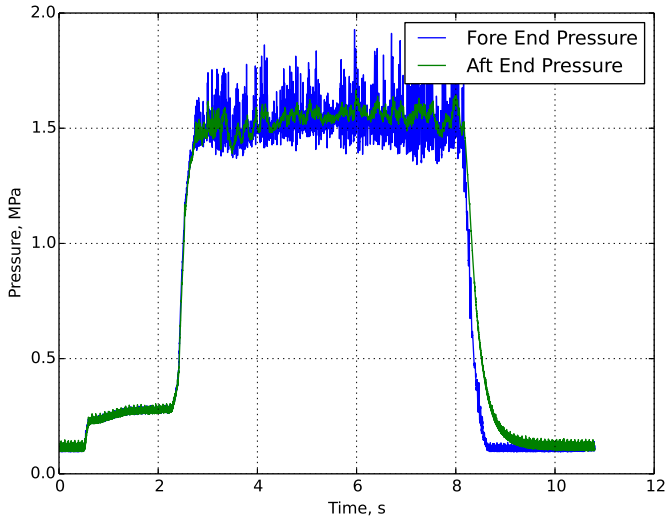

Figure 5.3: The pressure trace from Test 11 shows that the motor is relatively unstable at an oxidizer flow rate of 25 g/s. The average O/F ratio in this test was 1.51.

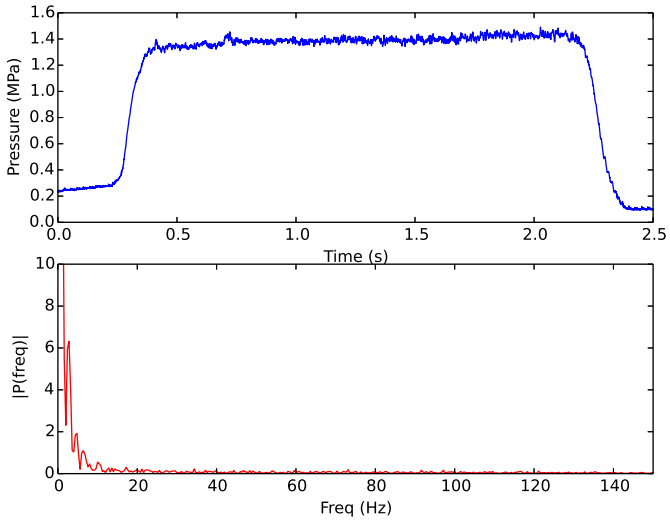

Figure 5.4: The frequency response of Test 5. This test showed the motor can behave in a very stable manner with only 5% peak to peak oscillations when compared to the average chamber pressure.

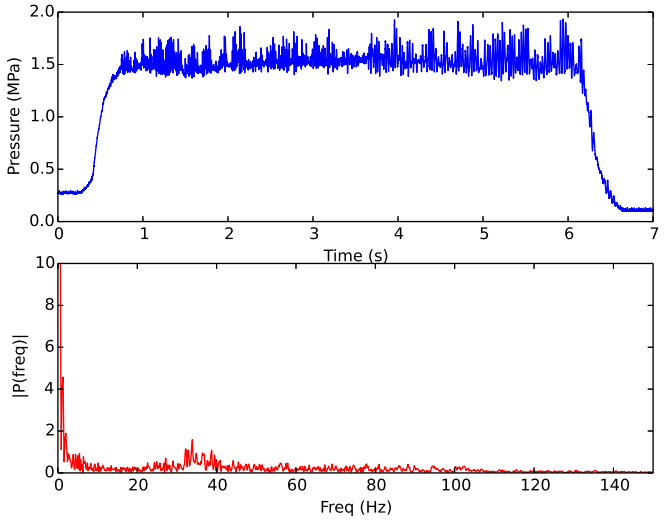

Figure 5.5: The frequency response of Test 11, which had some unstable behavior. The 35 Hz low-frequency oscillations were about 25% peak to peak when compared to the average chamber pressure.

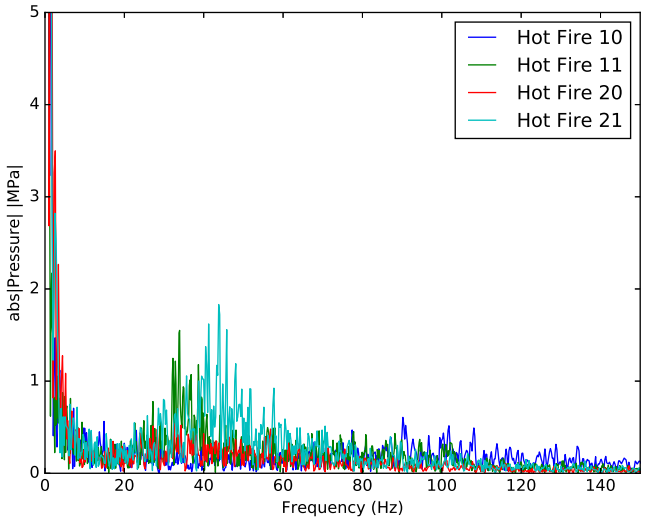

Figure 5.6: The FFT data for all unstable tests. None that although the tests did not have consistent peak locations, the unstable tests all showed elevated spectral levels up to about 100 Hz.

5.3 Heat Flux Estimations

Heat flux was estimated for Tests 2-22 with the embedded thermocouples and the inverse heat conduction solver as discussed in Section 2.3.8. Test 1 and Test 6 did not have thermocouples installed (and hence heat flux estimates were not computed). The time-varying heat flux data was consistent between the same test conditions (and different nozzles). Figure 5.7 shows the heat flux data for all data collected at 50 g/s at 1.72 MPa. Tests 2-5 were run with a single nozzle, and Tests 7-9 were run with another (same size). Note that the heat fluxes are similar.

For tests 2-5 and 7-9, the average surface heat flux estimates were relatively consistent between 30 MW/m^2 and 37 MW/m^2. Interestingly, these are very close to the heat flux estimate computed using Bartz' Equation [34], reprinted below for convenience, from Equation 2.8.

$$\begin{aligned} h_g &= \left[\frac{0.026}{D_*^{0.2}}\left(\frac{\mu^{0.26}C_p}{Pr^{0.6}}\right)\left(\frac{P_0 g}{c^*}\right)\left(\frac{D^*}{r_c}\right)^{0.1}\right]\left(\frac{A^*}{A}\right)^{0.9}\sigma \\ \sigma &= \left[\left(\frac{\rho_{ref}}{\rho}\right)\left(\frac{\mu_{ref}}{\mu_0}\right)^{0.2}\right] = \frac{1}{\left[\frac{1}{2}\left(\frac{T_w}{T_0}\right)\left(1+\frac{\gamma-1}{2}M^2\right)+\frac{1}{2}\right]^{0.8-m/5}\left[1+\frac{\gamma-1}{2}M^2\right]^{m/5}} \end{aligned} \tag{5.1}$$

For this testing condition, Bartz' Equation estimates a heat flux of 33.9 MW/m^2. Table 5.2 lists the inputs to generate this estimate. Bartz' Equation provides a remarkably accurate estimate for this condition. The average heat fluxes for all test conditions as well their Bartz' predictions are

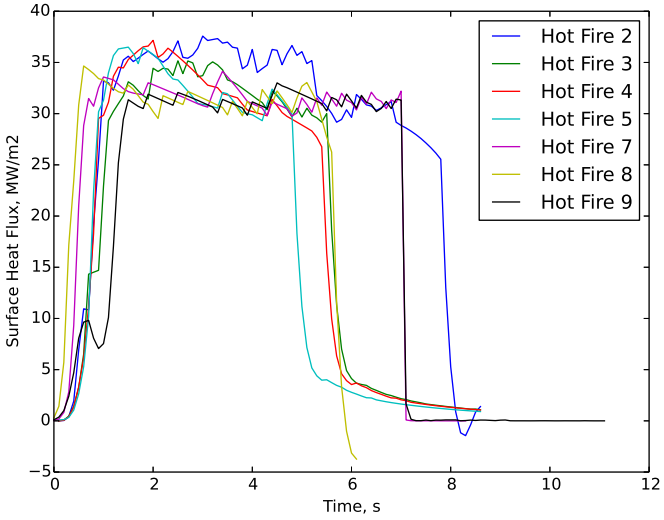

Figure 5.7: The heat flux estimates were consistent between nozzles for the same test conditions. The heat flux profiles shown were collected through seven tests using two different nozzles.

Table 5.2: Values used in determining the approximate heat flux given by Bartz' Equation.

Term	**Value**	**Units**
D_*	0.0099	m
μ	1.0669×10^{-4}	kg/ms
c_p	7.885	kJ/kgK
Pr	0.4582	–
P_0	1.7237	MPa
g	9.81	m/s^2
c^*	1807	m/s
r_c	.005	m
A^*/A	1	–
T_w/T_0	0.85	–
γ	1.1309	–
M	1	–

Table 5.3: The measured average and Bartz' Equation [34] estimates for the estimated heat flux at the nozzle throat plane.

Condition	**Avg Heat Flux** (MW/m^2)	**Bartz' Estimate** (MW/m^2)
A	33.11	33.9
B	33.49	36.0
C	29.30	42.7
D	51.60	58.6
E	47.76	54.9
F	50.37	54.5

listed in Table 5.3.

In addition to providing the estimated heat flux at the nozzle surface, the inverse heat conduction analysis also provided time-varying temperature profiles in the nozzle throat plane. These profiles seemed to match with the thermocouple data quite well. Figure 5.8 shows thermocouple data matched to the computed profiles for Test 3.

Note that at time = 6.00 seconds in Figure 5.8, the thermocouple data points do not match the computed profile very well. At this point in the experiment, the burn has already completed and the motor is in the purge phase. In this phase of the experiment, the 1D heat equation does not apply, as thermal soaking is taking place. Because of this, it is expected that the data points do not match the profile very well. Furthermore, as the 1D heat equation is not representative of the underlying physics, it is likely that the inverse heat equation may fail and go unstable. The end result is the temperature measurements and the output of the inverse solver are not used for data captured after the burn has completed. This would be problematic for motors that require multiple restarts (as the inverse code requires a known starting condition), and this nozzle measurement technique would require some changes. However, for this research, only a single burn is considered, and nozzle erosion is only expected to occur during the burn. Therefore, the only necessary thermal data is the data captured while the motor is burning. This data is expected to be accurate. This also means that unfortunately the nozzle throat area cannot be tracked as the motor cools.

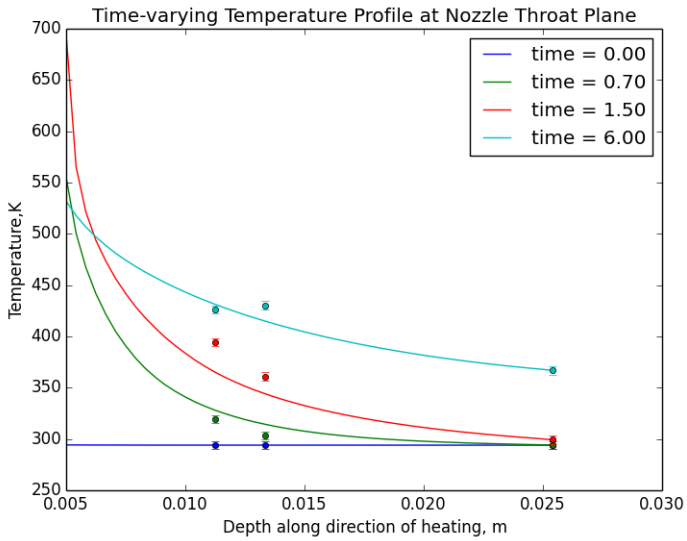

Figure 5.8: The thermocouple data matches well with the computed profile data. The only profile that does not match the trend of the thermocouple data is the final temperature profile, which is computed after the shutdown sequence. Because of thermal soaking, the underlying assumptions in the heat transfer development break down and the temperature profiles after the shutdown are expected to not follow the thermocouple trends.

5.4 Nozzle Erosion Measurements

The nozzle erosion measurements were the most sought after measurements in this research. In addition to the ultrasound technique, a visual measurement technique was employed for all tests starting with Test 7.

5.4.1 Visual Measurements

The visual measurement technique involved a parabolic mirror with focal length 143cm. A 10W Cree XML T6 LED light source was placed one focal length away from the mirror next to the experiment, pointed directly at the mirror. This light source proved successful in another visualization experiment where Schlieren videos were taken with the Stanford Combustion Visualization Facility [72].

The LED light reflecting from the mirror was now collimated and the mirror was oriented to point the collimated light through the nozzle from the aft side of the motor. A 12 megapixel (MP) iPhone 6s camera was used to capture the collimated light from the other side of the nozzle. A thin paper was used as a screen to prevent the collimated light from blinding the camera. Figure 5.10 shows a sample image captured for throat area measurement. Using a known scaling distance (the ultrasound transducer has a width of 12.5mm at the nozzle throat plane), it is possible to compute

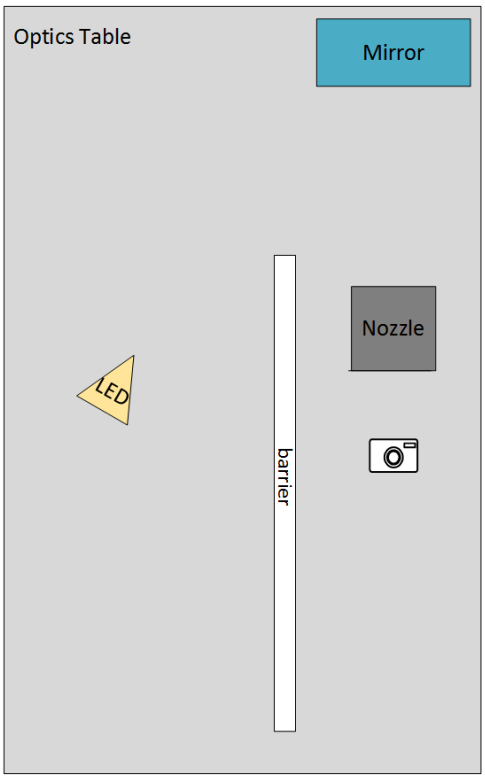

Figure 5.9: The LED was pointed at the parabolic mirror (of focal length 143cm) from one focal length away. The mirror collimated the light and pointed it through the nozzle. The resulting beam was captured with a digital camera and later analyzed.

the width of the nozzle throat section with basic image processing.

In developing this visual measurement scheme, many test images were taken. It was determined that the estimated uncertainty in the nozzle throat diameter was approximately 0.12 mm. The spatial resolution was generally about 0.05 $mm/pixel$, depending on the distance from the camera to the nozzle. This resolution was very high and allowed for precise and repeatable throat area measurements. To understand the consistency of the visual measurement scheme, a repeatability test was run after Hot Fire 8.

In this test, the LED, mirror, and camera were physically put away and then replaced back onto the optics table. The components were then realigned and a measurement was taken. This process was repeated twenty times and the measured results were compared. The standard deviation of the data was about 0.08 mm, which was considered a good result. This meant that the hardware was easy enough to align to provide repeatable results.

With the temperature profiles computed using the inverse heat conduction solver, it was possible to compute the time-varying speed of sound, using Equation 2.4 and Figure 2.5.

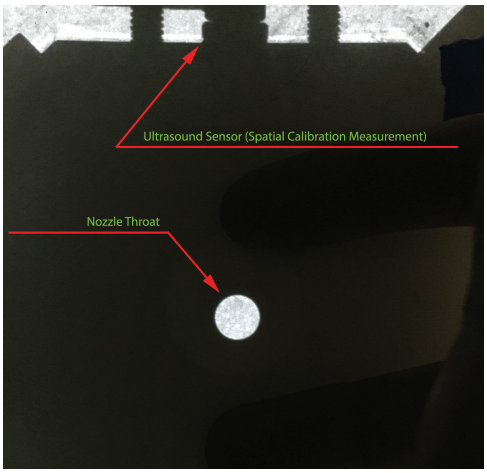

Figure 5.10: Raw image taken as the visual measurement of the nozzle throat area before Test 18. The throat area was determined by measuring the width of the ultrasound sensor in pixels.

Figure 5.11 shows the corrected ultrasound measurements for Test 18. Note that this measurement is the wall thickness. The nozzle throat area is simply a constant (referring to the outer diameter of the nozzle) minus the wall thickness. The desired metric is sought after is the slope of the regression section, as shown in Figure 5.11. This slope is directly related to nozzle erosion (by a factor of -1).

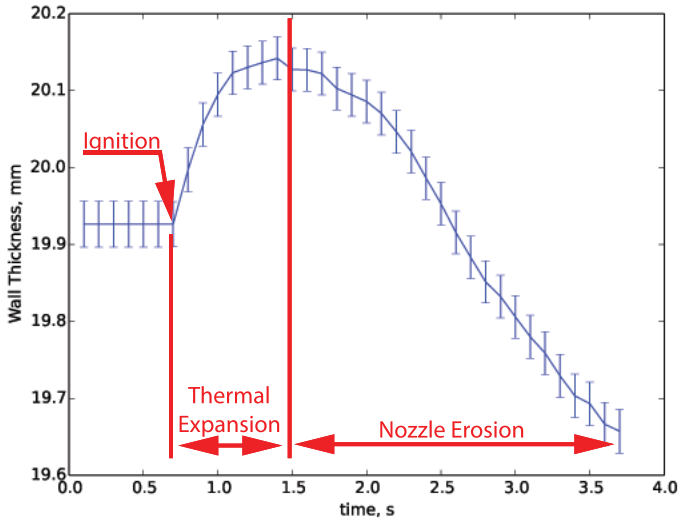

Figure 5.11: The wall thickness data clearly shows that there was nozzle erosion for Test 18. Note the distinct region where the nozzle expands due to heating and the region where nozzle erosion dominates.

Note that the ultrasound data contains two distinct regions. The first region after ignition is the nozzle expansion phase. As the nozzle gets hot from the exhaust gases of the motor, the graphite expands. Due to the large initial transients, the thermal expansion dominates over the nozzle erosion, and for a short period in time, the nozzle area actually shrinks. After the nozzle starts to get hot, the thermal expansion slows and the nozzle erosion begins to overtake the expansion. In this region, the slope of the nozzle wall thickness clearly shows a decrease. The slope of this decrease is the rate of increase of the nozzle radius.

Of interesting note, the ultrasound data and visual measurements are not consistent. This is partly due to two reasons. The first reason is error introduced in the time-averaging technique. The visual measurements are divided by the complete burn time to determine an average erosion rate. This does not take into account the expansion period, as this can only be estimated using the ultrasound measurement technique. The second reason is that the graphite thermal expansion likely has hysteresis. The hysteresis in the elasticity data (See Figures 2.3 and 2.4 in Chapter 2) strongly suggests that there is hysteresis in the thermal expansion as well. Therefore, the thermal expansion is not fully recovered upon cooling, and the nozzle is thought to be permanently deformed. Evidence of this is seen in the fuel rich test cases (25 g/s), where the ultrasound measurements did not indicate sensible nozzle erosion, and the visual measurements indicated slightly decreased nozzle areas (negative nozzle erosion). Figure 5.12 shows the ultrasound data Test 11, a fuel rich case. Note that there is no clear transition from the thermal expansion region to the nozzle erosion region

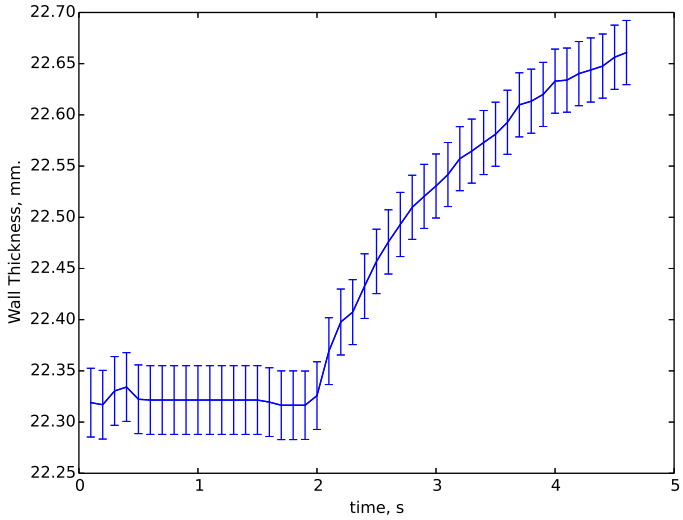

Figure 5.12: The ultrasound data for Test 21 (and the other fuel-rich tests) did not show evidence of nozzle erosion.

and there is no clear nozzle erosion.

Other than the fuel rich tests cases, the data made intuitive sense. The tests with higher oxidizer flow rates had higher nozzle erosion, and nozzle erosion increased with chamber pressure. Note however that for every test condition, the nozzle area was different, so more parameters vary between tests than just flow rates and chamber pressures. Table 5.4 lists the average nozzle erosion measurements from both the visual and ultrasound techniques.

The data is quite surprising. The fact that no nozzle erosion is detectable for fuel rich cases may drive future designs where nozzle erosion needs to be minimized. Furthermore, the magnitude of the nozzle erosion measurements are of interest as well. These estimates show that nozzle erosion is not negligible and that the conservative estimate of 0.00254 mm/s used in Section 1.3 is quite a bit

Table 5.4: Summary of nozzle erosion measurements.

Test Condition	**Avg. Fore End Pressure** (MPa)	**O/F Ratio**	**Nozzle Mass Flux** (kg/m^2s)	**Avg. Visual Regression Rate** (mm/s)	**Avg. Ultrasound Regression Rate** (mm/s)
A	1.49	2.00	906	0.030	0.069
B	1.48	1.60	1008	-0.008	-
C	1.73	2.40	1051	0.081	0.102
D	2.32	1.41	1595	-0.018	-
E	2.30	1.85	1321	0.051	0.127
F	2.28	2.36	1397	0.130	0.203

smaller than those measured in this research. Although the estimate used in Section 1.3 assumed different propellants, the measured nozzle erosion at the nominal condition was on the order of 0.1 mm/s, nearly 50 times larger than the "conservative" value previously used (see page 11)!

This means that for long burning missions, nozzle erosion is indeed important and for some missions it may be advisable to burn at a fuel rich condition. The consequence of burning fuel rich is reduced performance, but for some missions, the savings of avoiding nozzle erosion may overcome the performance losses associated with fuel rich O/F ratios.

Overall system benefits are also achieved when intentionally burning a motor fuel rich. When burning fuel rich, less oxidizer mass is needed, which results in smaller (high-pressure) oxidizer tanks. The additional fuel, if any, is stored in a lower pressure combustion chamber, which has minimal mass penalties. When lower mass flow rates are needed, the diameter of the feed system piping can be reduced, which reduces structural mass (and costs) and allows for the use of lower performing valves. The combination of these changes reduces overall system cost and structural mass fractions, which could ultimately be used to increase payload capacity.

For small motors, such as cubesats, which are likely to gain popularity in the hybrid rocket community in the near future, nozzle erosion may be equally important. Recall for small motors the percentage of area change for a small change in radius is significantly higher (Equation 1.6 on page 9). Because of this, even a small amount of nozzle erosion could result in significantly increased nozzle throat area. To avoid this, it would again be advised to burn fuel rich.

5.5 Thermal Expansion

Thermal expansion was witnessed in the ultrasound test data. Because the nozzle was heated from the inside out (and the fact that the outer dimension was relatively constrained), the throat area was forced to *decrease* due to thermal expansion.

It was desired to account for the thermal expansion in the ultrasound data so that thermal expansion could be decoupled from nozzle erosion in the wall thickness measurements taken by the ultrasound transducer. By decoupling the thermal expansion from the nozzle erosion measurements, it would be possible to detect when nozzle erosion first started.

Figure 5.13 shows the temperature-corrected ultrasound data compared against the same ultrasound data with the thermal expansion portion removed, based on the variable CTE estimated by Tsang (as shown on Page 24) [32]. From this data, it is clear that the estimated CTE is grossly underestimated. A better estimate is about 10 times larger than that estimated by Tsang. However, the ultrasound data decoupled from the thermal expansion varies significantly depending on the particular CTE value used, as shown in Figure 5.14. Because of this, the ultrasound data cannot be decoupled from the thermal expansion data without accurate knowledge of the CTE value of the graphite used in this research.

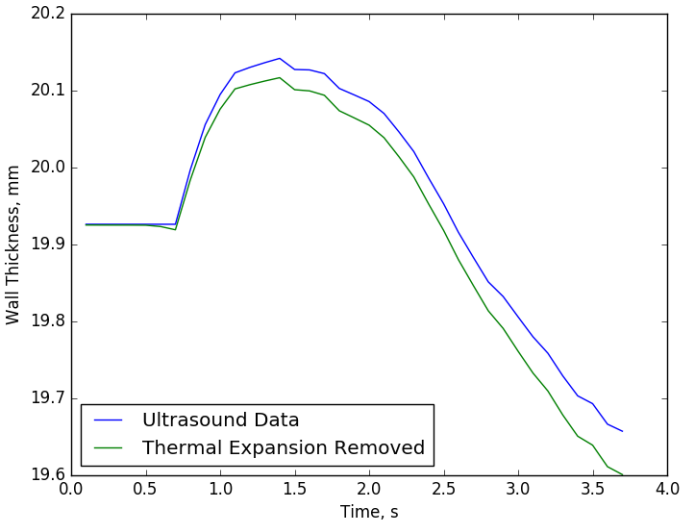

Figure 5.13: The attempt to decouple the thermal expansion from the ultrasound data requires a more accurate estimate of the CTE than that provided by Reference [32].

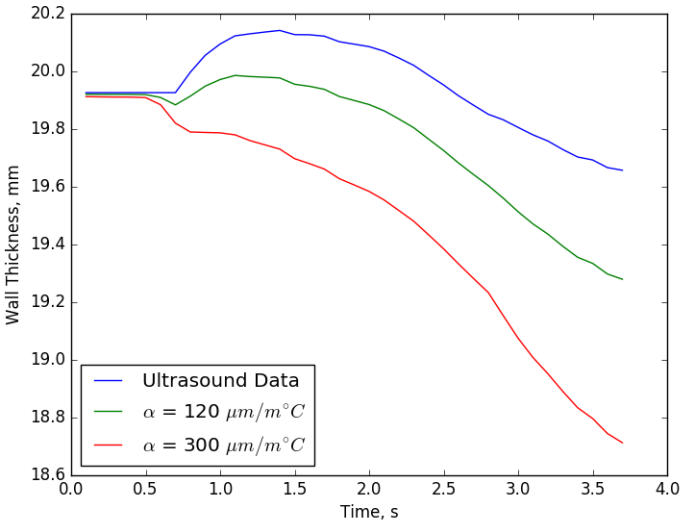

Figure 5.14: The ultrasound data decoupled from the thermal expansion data varies drastically depending on the CTE values used. This highlights the necessity of having an accurate estimate of the CTE for the sample of graphite material used.

5.6 Uncertainty Analysis

Uncertainty analysis was performed in this study to compute the size of the error bars on the ultrasound data. Because the ultrasound data is dependent on the temperature history of the nozzle, analytically determining the sensitivity coefficients would be a difficult task. Instead, the sensitivity coefficients are computed numerically by modeling a typical experiment and computing the overall variation of the computed integral average speed of sound based on the uncertainty of each element individually [73]. Because this problem is nonlinear, each element's uncertainty (plus and minus), are computed as individual sensitivity coefficients. The elements modeled include the thermocouples, modulus measurements, thermocouple locations, graphite density, graphite conductivity, and others. A full list of each element and its corresponding uncertainty is shown in Table 5.5.

With each of the sensitivity coefficients, the overall uncertainty could be computed as shown in Equation 5.2.

$$\delta R = \sqrt{\sum_{i=1}^{n} \left(\frac{\partial R}{\partial X_i} \delta X_i \right)^2} \tag{5.2}$$

The overall uncertainty computed in this manner for an experiment running five seconds with an input heat flux of 50 MW/m^2 was time varying with the worst case at the final time of 5 seconds. At this worst case condition, the estimated uncertainty in the speed of sound was roughly 1%. While this may seem opportunistic, note that these values are based on an assumption that the speed of sound profile is correct, which is a difficult assumption to verify. However, based on the data presented by Ref. [22], the moduli for other grades of graphite follow similar trends and the estimated speed of sound profile for the particular grade of graphite used in this research, GR001CC, is likely a good estimate.

One reason why the uncertainty computation of the overall speed of sound is very low is the

Table 5.5: A list of variables and their uncertainties used in determining the sensitivity coefficients and the overall uncertainty in the data.

Symbol	**Term**	**Uncertainty (%)**
E	Young's Modulus	3 [22]
G	Shear Modulus	3 [22]
ρ	Density	1 [18]
α	Thermal Diffusivity	2.2 [18]
K	Thermal Conductivity	5 [18]
D_i	Throat Diameter	1 (mm)
D_o	Outer Diameter	1 (mm)
χ_i	Thermocouple Location	1
τ_i	Thermocouple Error	0.4 [42]

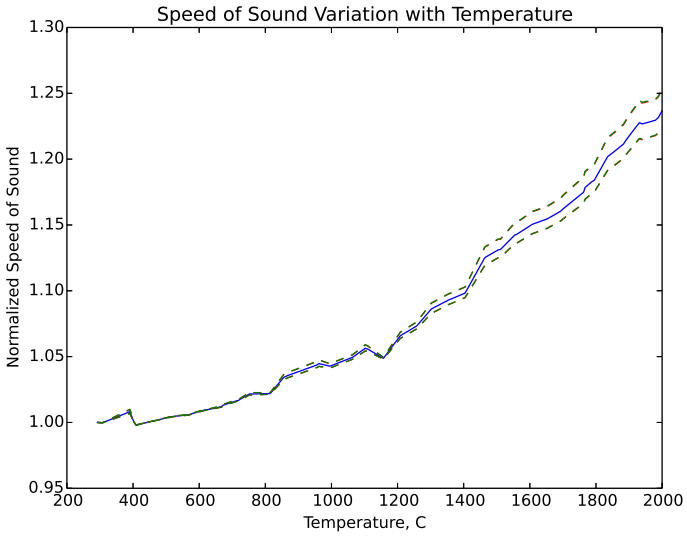

Figure 5.15: The normalized sound speed profile in graphite vs. temperature. The speed of sound increases by about 25% between room temperature and 2000 Celsius.

fact that the speed of sound profile has a small slope. If the computed integral average temperature was off by 2000C, the error would be just 25%. This would not be the error even if no thermal analysis was computed, as the highest integral average temperature estimated was around 800K. If no thermal analysis was computed, the error would then be about 5%. Therefore, with a robust estimate of the temperature profile, and an assumption that the speed of sound profile is correct, a 1% uncertainty on the computed speed of sound is very reasonable. The speed of sound profile is shown in Figure 2.5 and repeated in Figure 5.15 for convenience.

The uncertainty terms in the speed of sound profile were computed with just the terms relating to the speed of sound equation (Equation 2.4), which are density, Young's Modulus, and shear modulus. Note that these uncertainties grow with temperature.

5.7 Possibility of Boosting Hybrid Performance

The first hot fire of any rocket motor is a significant milestone. It also involves a lot of stress and the person in charge of the operation of the test has an extremely difficult job. When the experimental motor was first fired, it was no exception. Thankfully, the motor behaved well and the test was successful.

However, a couple of unexpected discoveries were made after the test when the motor was being disassembled for inspection. First was the large amount of soot on the outside of the fuel grain

insulator. Oxidizer managed to get in between the fuel grain insulator and stainless steel combustion chamber. The result of this was that the stainless steel chamber was slightly damaged from the heat and the outside of the fuel grain insulator was charred quite a bit, as seen in Figure 5.16. It was later determined that the stainless steel was still structural and could continue use, provided it be protected from the heat in the future tests. The burning of phenolic insulator was particular undesirable because it left a pungent odor that remained in the lab for several days. This problem was solved by placing silicone RTV between the insulator and stainless steel combustion chamber for all subsequent tests.

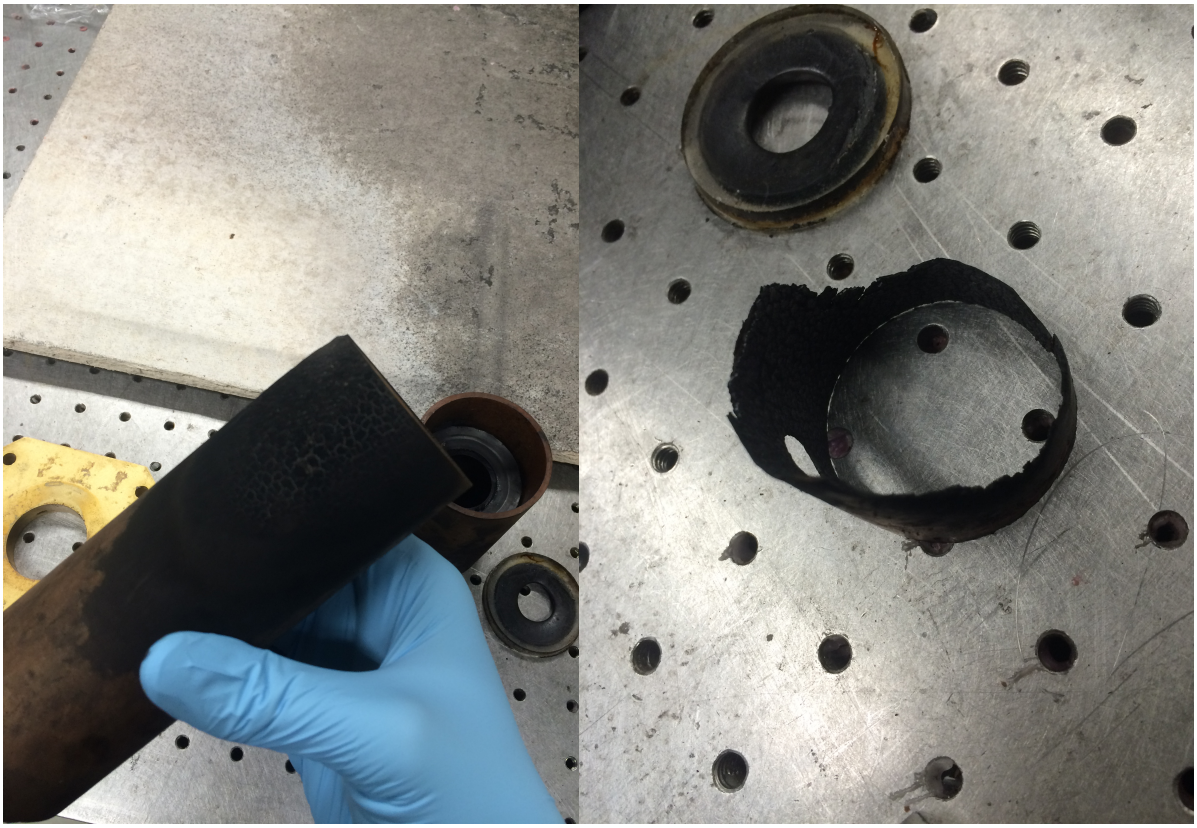

Figure 5.16: The outside of the fuel grain insulator (left) was accidentally burned as well as the fore end insulator (right). The pre-burning of the oxidizer with the fore-end insulator likely led to increased efficiency of the burn.

Secondly, the fore end insulator, which was fabricated out of phenolic material, nearly completely burned away during the first test. While this was also a source of the lingering pungent odor in the lab, it is thought that this was also a source of a performance boost. For the second hot fire, this phenolic insulator was replaced with graphite insulator that did not burn. This removed the pungent odor from the motor, increased stability, and also reduced the smokey plume. However, the

average combustion chamber pressure was about 10% less than the first test.

The 10% pressure increase of the first test is not predicted even if five grams of extra fuel (mass of insulator) was burned. Therefore, the performance gain of 10% cannot be attributed solely to the fact that extra material was burned.

This accidental discovery needs to be further studied, as pre-heating or pre-combusting the oxidizer may lead to higher C^* efficiency between the main propellants. The realization of a 10% increase in chamber pressure would be a significant boost that could ultimately increase the capability of hybrid rocket propulsion systems.

Chapter 6

Nozzle Erosion Model

In this chapter, all of the nozzle erosion data from Chapter 5 is combined and a dimensionless nozzle erosion is proposed. The relevant terms and dimensionless quantities are also briefly discussed along with some words of caution when using this model. The chapter then concludes with a discussion on possible techniques to reduce nozzle erosion.

This chapter concludes with a sample prediction calculation for nozzle erosion in the long burning hybrid rocket motor discussed in Chapter 1.

6.1 Relevant Parameters

Nozzle erosion in hybrid rockets can generally be considered a different problem than when compared to solid rocket motors [74]. This is because of the mass fractions of oxidizing species in the flow can be much higher depending on the throttling condition of the motor. Because of this, it should be noted that the dominant oxidizing species should be of importance in any nozzle erosion model for hybrid rockets and the mass fractions of the oxidizing species may also be related to how well the flow is mixed. The mass fractions for several oxidizing species when combustion the customized propellant used in this research and gaseous oxygen are shown in Figure 6.1.

It is thought that hybrid rocket motors without post combustion chambers and mixing elements experience less nozzle erosion. However, they also achieve lower efficiencies [75]. In these lower performance designs, nozzle erosion is reduced because a fuel rich boundary forms over the nozzle throat walls, which mimics the film cooling that is typically used in liquid engines. This phenomena could be exploited by placing a small sliver of slowly burning fuel just upstream of the nozzle throat section. This fuel, which would be of very small mass compared to the fuel grain, would protect the nozzle throat by the film cooling effect. Furthermore, as this small sliver of fuel would have very low mass, the overall flow would be generally very well mixed and a reduction in efficiency would not be witnessed.

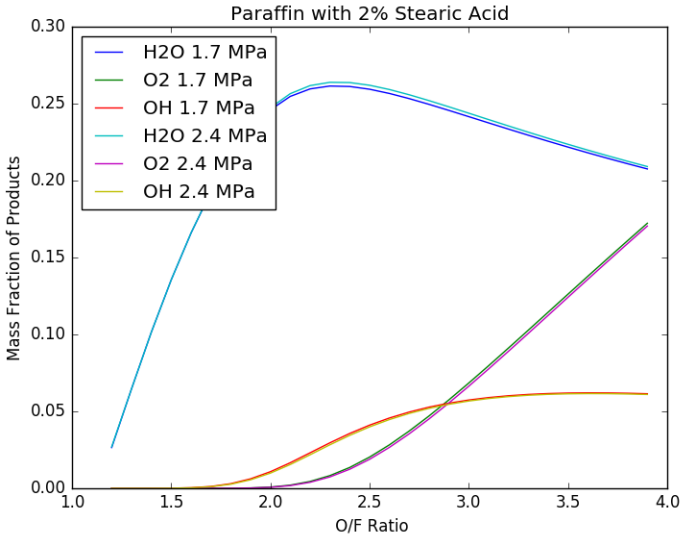

Figure 6.1: The theoretical mass fractions at the nozzle throat when combusting the customized fuel blend and oxygen at various O/F ratios based on a shifting equilibrium calculation. Note that the data remains relatively unchanged between the low and high pressure data sets.

The nozzle erosion problem itself is similar to a hybrid combustion problem. The oxidizer is in the gas phase and the fuel (the nozzle) is stored in the solid phase. The hot oxidizer mixture flows over a vaporizing fuel which is remarkably similar to the hybrid rocket fuel problem. Because of this, it is expected that a nozzle erosion model would appear to be similar to the commonly used hybrid fuel regression rate equation, as shown previously in Equation 3.1. Equation 3.1 is rewritten in Equation 6.1 for convenience.

$$\dot{r}(t) = aG_{ox}^{n} \tag{6.1}$$

Heat transfer is also thought to be a dominant factor in nozzle erosion. Graphite is one of very few materials that can withstand the intense heating experienced at the nozzle throat location. However, it is not always the ideal material choice. In some designs, phenolic or other materials are used instead. In those designs, the phenolic is intended to burn away to keep the heat away from the rest of the motor. Obviously in this instance nozzle erosion is higher, but sometimes the weight savings offset the performance losses associated with nozzle erosion. Nonetheless, the maximum temperature rating of a material, or a melt temperature, is expected to be relatively important in the nozzle erosion phenomena. The heat transfer rates are also expected to play a critical role in the nozzle erosion phenomena.

Significant work has been done in modeling the convective heat transfer coefficients in rocket nozzles [34] and this research has shown that the Bartz' Equation is valid for use in hybrid rockets. Additionally, significant work has been done in modeling the heat transfer in circular pipe flows [76],

Table 6.1: A list of relevant quantities for predicting nozzle erosion in hybrid rockets.

Term	Equation	Description	Notes
G_T	$G_T = 4\frac{\dot{m}_f + \dot{m}_o}{\pi D_t^2}$	Mass Flux throat nozzle throat	
ρ_{nozzle}		Density of Nozzle Material	
χ_i		Mass fraction of oxidizing species i	
C^*	$C^* = \frac{P_c A_t}{\dot{m}}$	Characteristic Exhaust Velocity	
C^*_{meas}	m/s	$MeasuredC^*$	Typically between 70% and 95% of ideal C^*
Reynolds Number	$Re_L = \frac{\rho U L}{\mu}$	Ratio between inertial forces and viscous forces	
Prandtl Number	$Pr = \frac{C_p \mu}{K}$	Ratio between momentum diffusivity and thermal diffusivity	
Stanton Number	$St = \frac{h_{conv}}{\rho u c_p}$	Ratio between heat transferred and thermal capacity	
Mixing Length	$\frac{L}{D_T}$	Ratio between length of post combustion chamber and nozzle diameter	
Temperature Ratio	$\frac{T_f}{T_{melt}}$	Ratio between flame temperature and temperature capability of nozzle	
Nusselt Number	$Nu \sim Re_L^{0.8} Pr^{0.5}$	Ratio between total heat transfer and conductive heat transfer	Correlation for turbulent flow in circular pipes [76]

and all of these play an important role in nozzle erosion.

Because it is expected that all of these factors play an important role in the nozzle erosion phenomena, they are all incorporated into the proposed dimensionless model.

6.2 Nozzle Erosion Model

A dimensionless model can be generated from the parameters listed in Table 6.1. The proposed model in a dimensional form is written in Equation 6.2.

$$\dot{r} = B\left[\frac{G_T}{\rho_{nozzle}} max\left(0, -0.06 + 0.27\chi_{H_2O} + \chi_{O_2} + 0.33\chi_{OH}\right)\right]^n \left(C^*_{meas}\right)^{1-n} \frac{Re_L^{0.8} Pr^{0.5}}{St^{0.6}} \left(\frac{L}{D_T}\right)^m \left(\frac{T_f}{T_{melt}}\right) \tag{6.2}$$

Where

$$B = 2 \cdot 10^{-11}$$

$$n = \frac{1}{2}$$

$$m = \frac{1}{2}$$

It should be noted that the Reynolds Number, Prandtl Number, and Stanton Numbers are computed from the fluid properties at the throat section. A simple method of computing the convective heat flux, h_g is by applying Bartz' Equation [34]. The fluid properties are also simple to obtain as CEA [15] provides the option to output the fluid properties at the throat section. The completely dimensionless model equation can be written out as:

$$\frac{\dot{r}}{\left(\frac{G_T}{\rho_{nozzle}}\right)^n \left(C^*_{meas}\right)^{1-n}} = B\left[max\left(0, -0.06 + 0.27\chi_{H_2O} + \chi_{O_2} + 0.33\chi_{OH}\right)\right]^n \frac{Re_L^{0.8} Pr^{0.5}}{St^{0.6}} \left(\frac{L}{D_T}\right)^m \left(\frac{T_f}{T_{melt}}\right) \tag{6.3}$$

This dimensionless model utilizes all of the critical parameters that are thought to play a major role in the nozzle erosion phenomena. In solid rockets, nozzle erosion has been studied extensively and some trends may be applicable to the hybrid rocket problem as well. For example, it has been found that nozzles fabricated out of exotic 3DCarbon-Carbon materials typically have significantly reduced nozzle erosion in solid rocket motors [2]. The major differences between the graphite used in this research and an exotic 3DCarbon-Carbon material are the material strength, density, and the resistance to oxidation at high temperatures. The 3DCarbon-Carbon material is more dense and can withstand higher temperatures than graphite. For these reasons, the proposed dimensionless model would predict reduced nozzle erosion than when compared to graphite.

Although 3DCarbon-Carbon is more dense that graphite, it makes for a better nozzle material as it can be manufactured in practically any geometry desired. While graphite is easily machined, it easily cracks and thick walls are almost always required. The biggest reason why 3DCarbon-Carbon is not always used in rocket motors is because the cost is currently too high.

The proposed dimensionless model captures all of the trends that were seen in the captured data in this research. The model forces zero nozzle erosion when O/F ratios are too low (based on the mass fractions of the oxidizing species), and also predicts increased nozzle erosion with increased O/F ratios. The model also predicts nozzle erosion to increase with increased chamber pressure.

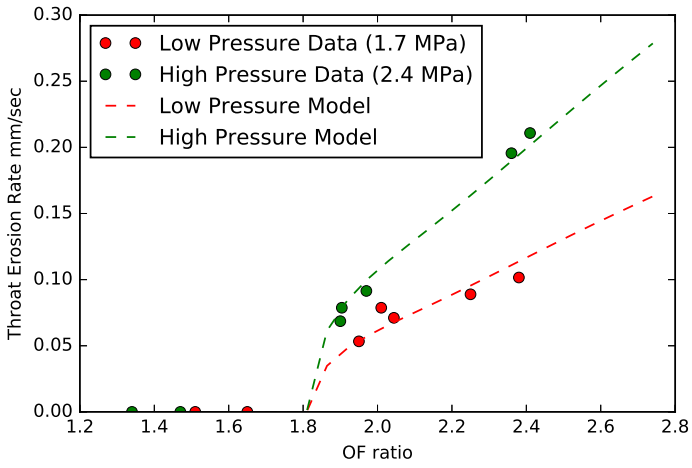

Figure 6.2: The proposed model generally captures the trend of the experimental data. Both the model and the measured data suggest no nozzle erosion at the lower O/F ratios (below 1.7) and increasing nozzle erosion at high O/F ratios (above 2.2). Note that more data is needed to verify the increasing nozzle erosion trends at even higher O/F ratios.

It should be noted that this model was generated based solely on the data collected for this research. This is an unfortunate shortcoming that could not be avoided because nozzle erosion data for hybrid rockets is extremely scarce. Because of this, the proposed model should be used with caution. As this model was generated based on data provided by a single motor with a single propellant combination, it may not behave well with other propellant combinations. It is likely that the C and n values may need to be adjusted based on propellant combinations and design conditions (as is customary for the hybrid fuel regression rate equation). Furthermore, it is likely that the dominant oxidizing species may change when considering other propellants.

It should also be noted that the nozzle erosion model predicts zero erosion at a somewhat arbitrary point. Enough data points were not collected to accurately predict the exact O/F ratio where nozzle erosion is likely to be eliminated. Nonetheless, the experimental data suggests that nozzle erosion is eliminated at an O/F ratio somewhere between 1.6 and 1.9 for this set of propellants.

6.3 Reducing Nozzle Erosion

The proposed model provides insight into some of the important sources of nozzle erosion in hybrid rockets. In this research, nozzle erosion was eliminated at low O/F ratios on a test motor. Although lower O/F ratios are commonly associated with lower performance, this is not necessarily always the case. The fact that nozzle erosion can be eliminated at low O/F ratios can be exploited in a hybrid rocket motor that still provides great performance.

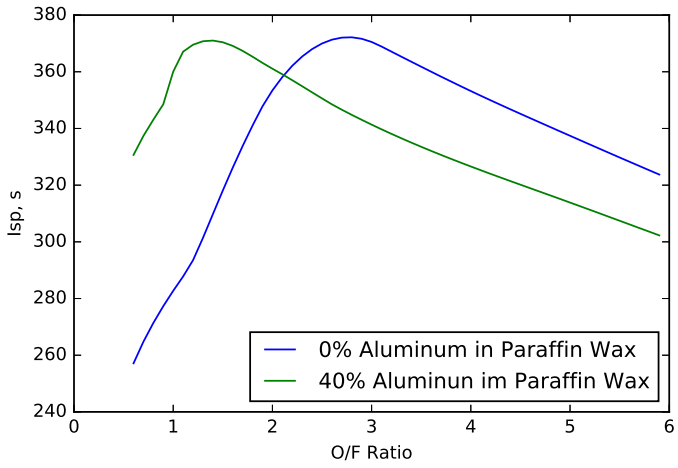

Figure 6.3: Addition of aluminum particles in paraffin wax shifts the optimal Isp to lower O/F ratios. This results in lower mass fractions of oxidizing species at the throat which could ultimately reduce nozzle erosion. These were computed in CEA using oxygen with shifting equilibrium calculations at 1.72 MPa at a nozzle expansion factor of 200.

Aside from performance benefits, paraffin wax also has one major feature that other classical hybrid fuels lack. It is well known that additives can be added to paraffin candles to alter their physical properties [57]. In terms of hybrid fuel design, this means that various additives can be added to paraffin to allow for a tailored regression rate. This means that a fuel grain can be manufactured to exactly fulfill a specific mission. For other classical hybrid fuels, typically the design process is the other way around; the mission must be specified according to what the propellants offer. Moreover, certain additives, such as aluminum powders, are known to enhance low O/F performance characteristics in hybrid rockets.

The major benefits of adding aluminum to a fuel grain include lower O/F ratio requirements for optimal performance and increased fuel density. In terms of system design, operating at a lower O/F ratio allows for a smaller oxidizer tank, which typically results in a motor that costs less to manufacture. With increased fuel density, the overall package of the grain can be reduced and the combustion chamber can realize some cost savings as well. With the results of this research, it is possible that another major benefit of adding aluminum powders to a fuel grain may include the reduction of nozzle erosion.

It should be noted that although the addition of aluminum powders to a fuel grain reduces the required O/F ratio and the oxidizing species present at the optimal O/F ratios, which in turn reduces the predicted nozzle erosion based on the proposed model, it is possible that another nozzle erosion phenomena is being overlooked. Recall that the nozzle erosion model does not include any terms relating to physical abrasion of the nozzle throat section. The aluminum particles in a fuel grain

would likely wear the surface of the nozzle away in a manner not predicted by the model. Also, it is likely that two-phase flow would reduce the overall velocities in the nozzle, thereby reducing the overall nozzle efficiency by a small amount. Nonetheless, a paraffin fuel grain loaded with aluminum would likely benefit from the reduction of nozzle erosion.

Additional methods can also be employed to reduce nozzle erosion. Recall that the proposed nozzle erosion model has a term intended to account for mixing. This L/D term, which accounts for a mixing region in the motor, increases the nozzle erosion rate. It would then seem to be a bad design choice to have mixing elements in hybrid rocket motors. However, these elements increase overall performance of the motor by increased C* efficiencies.

It would be possible to achieve mixing and high performance while still minimizing nozzle erosion. If a sliver of slow burning fuel was placed on the nozzle section just upstream of the throat, it would create a fuel-rich boundary layer that could protect the surface of the nozzle at the throat section. Mixing geometries could still be used in this design and the performance penalty associated with the fuel rich boundary layer and the sliver of slow burning fuel would be minimal.

One technique of minimizing nozzle erosion could be through the use of multiple restarts. Note that in all of the test data with nozzle erosion, erosion did not begin to occur until about one second into the test. Prior to that, the nozzle was thought to be heating up. This "heating up" portion of the burn can be taken advantage of.

A motor can be designed with multiple restart capability that would do short burns of up to one second and then wait until the nozzle was cool. Although this type of mission is not practical for launch missions, this type of a system could work well for in-space missions. Multiple restarts for hybrid rockets are an exciting area of active research and minimizing nozzle erosion could be a criteria used to limit the burn times in a future study.

6.4 Estimated Nozzle Erosion Rate for a Long Burning Hybrid Rocket Motor

Recall in Chapter 1 the nozzle erosion problem was a point of concern for the preliminary design of a long burning hybrid rocket motor. At the time, a conservative nozzle erosion rate of 0.00254 mm/s was used. This estimate comes from an estimated nozzle erosion rate of a nozzle made from 3D carbon-carbon in a solid rocket motor. It is desired to compute a better estimate of nozzle erosion for this system.

The preliminary design parameters are first observed, as printed in Table 6.2.

Upon inspection, according to the nozzle erosion model, the mass fractions of oxidizing species at an O/F ratio of 2.18 are not high enough to cause detectable erosion. The mass fractions of the relevant oxidizing species for N_2O_4 and paraffin with 40% aluminum additive is shown in Figure 6.4.

Table 6.2: Some basic design parameters for a long burning hybrid rocket mission.

Design Parameter	**Value**	**Units**
Chamber Pressure	1.03	Mpa
Nozzle Throat Diameter	0.482	m
Nozzle Material	3D Carbon-Carbon	
Fuel	Paraffin+ 40	
Oxidizer	N2O4	
O/F Ratio	2.18	
$Cmeas^*$	1121	m/s
Oxidizer Flow Rate	0.804	kg/s

The term involving the oxidizing mass fractions is equal to 0.

$$max\left(0, -0.06 + 0.27\chi_{H_2O} + \chi_{O_2} + 0.33\chi_{OH}\right) = 0$$

This forces the erosion rate to be zero. Although this is great news for the design of the long burning system, the word of caution with the proposed nozzle erosion model should be taken. The model was developed for the use of oxygen as the oxidizer, and the presence of nitrogen in N_2O_4 likely reduces the mass fractions of the oxidizing species, which should reduce nozzle erosion. It is currently unknown if the nozzle erosion rate would be zero or not for this propellant combination.

For the sake of research, the $max\left(0, -0.06 + 0.27\chi_{H_2O} + \chi_{O_2} + 0.33\chi_{OH}\right)$ term is temporary modified so that nozzle erosion is not forced to zero at this condition. The replacement term is:

$$max\left(0, -0.04 + 0.27\chi_{H_2O} + \chi_{O_2} + 0.33\chi_{OH}\right)$$

With this modification, the nozzle erosion is not forced to zero and should still remain relatively reasonable.

To continue along in the analysis, a few assumptions of the nozzle material must be made. These are:

- Density of the 3D carbon-carbon is 2100 kg/m^3
- Temperature limit of the nozzle material is 5000 K
- The radius of curvature at the nozzle throat is approximately 0.24 m
- The post combustion chamber length is 0.3 m

With these assumptions and the given parameters, it is possible to compute an estimated nozzle erosion rate. First, CEA [15] is used to compute the values shown in Table 6.3.

With the CEA outputs, the Re_L term can be computed to be $Re_L = \rho UL/\mu = 1.85E6$. It is also possible to compute the estimated heat transfer coefficient from Bartz Equation [34]. It should

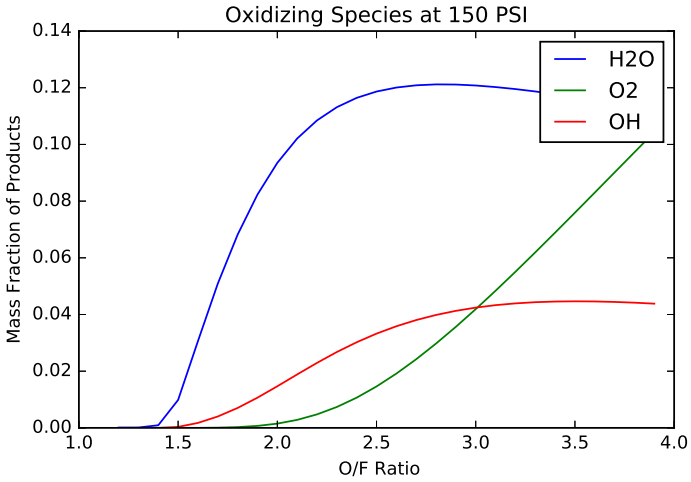

Figure 6.4: Mass fractions of oxidizing species for N_2O_4 and paraffin with 40% aluminum additive.

Table 6.3: Some important CEA output values for estimated nozzle erosion rate.

Parameter	**Value**	**Units**
X_{O_2}	0.0043	
X_{OH}	0.022	
X_{H_2O}	0.11	
γ	1.12	
flow density	0.57	kg/m^3
Velocity	1090	m/s
Viscosity	0.0001	PaS
Specific Heat	6360	J/KgK
Flame Temperature	3550	K
Flow Temperature at Throat	3390	K
Prandtl Number	0.35	

be noted that the Bartz Equation requires all units to be converted to English units.

The Bartz Equation provides an estimated convective heat transfer coefficient $h_{conv} = 11.6kW/m^2K$. From there, the Stanton number can be computed to be $St = h_{conv}/\rho UC_p = 0.003$.

Finally, the estimated nozzle erosion rate can be computed from Equation 6.2 to be 0.04 mm/s, which is roughly the same regression rate that was seen in the motor used in this research. However, there is a key finding that is worth discussing.

The proposed model in its original form had to be slightly modified for this application. While the modification was slight, the reason behind the modification is noteworthy. The nitrogen molecules in the oxidizer seem to reduce the presence of oxidizing species in the equilibrium composition of the combusting flow. This could drastically reduce nozzle erosion and the original finding of zero nozzle erosion might actually be reasonable for the system. Further research will need to be conducted to verify this finding.

For this long burning hybrid rocket motor, the computed erosion rate (according to the model), would be somewhere between zero and 0.04 mm/s, which is a wide range for this application. This research would need to be extended into other propellant combinations, such as nitrous oxide, nitric acid, high density polyethylene (HDPE), hydroxyl-terminated polybutadiene (HTPB), and poly methyl methacrylate (PMMA), in order to better predict the nozzle erosion in a system utilizing propellants other than oxygen and paraffin. Nonetheless, this model is a powerful tool that can provide a quick nozzle erosion estimate for a hybrid rocket designer.

Chapter 7

Visualization of Fast Burning Fuels

In this chapter, the measurements taken from the viewing window at the fore end of the motor are discussed. The published regression rate constants for paraffin fuels are verified by comparing against the visual data.

7.1 Overview

Recall that the experimental motor was designed with a sapphire window at the fore end. This window allowed a camera to capture the view down the port of the motor while the motor was burning. This was the first time that a view inside of a conventional hybrid rocket motor was available. Initially, it was thought that the images recorded by the high speed cameras would be saturated and not enough data would be extractable for meaningful results. Nonetheless, the motor was fitted with the window mostly out of curiosity and a general interest in the lab to visualize the combustion processes, as done previously by other members of the lab [44] [45].

One of the obvious goals for this secondary research topic was to visualize the paraffin burning, which is known to have a very fast regression rate in a conventional system at conventional conditions. A metric of this would be to track the port area with time and compute the regression rates and verify the measured rates with published data. Previous work in this manner has been done by De Luca et al, where port area measurements were taken on a micro-scale burner utilizing HTPB and Paraffin fuels [77]. That particular setup remains unclear. Nonetheless, that research led to very successful fuel regression rate measurements and proved that the published data was quite accurate. This showed that it might be possible to measure the fuel regression rates inside of a conventional hybrid rocket motor at the lab-scale size at relevant chamber pressures.

Table 7.1: Published average regression rate measurements for a paraffin fuel [78]

Parameter	Value	Units
a	$9.27x10^{-5}$	$m^{1-m}/s\left(kg/m^2s\right)^n$
n	0.62	-
m	0.09	-

7.2 Methodology

The first goal of the visual measurements is to track the fuel grain boundary and estimate the port area while the motor is burning. With time-varying estimates of the port area and the hydraulic diameter of the fuel grain boundaries, the published regression rates could be verified by comparing to the space-time coupled hybrid fuel regression rate equations [46], as shown in Equations 7.1 and 7.2.

$$\frac{\partial r(x,t)}{\partial t} = \frac{a}{x^m}\left(\frac{\dot{m}_{port}}{\pi r^2}\right)^n \tag{7.1}$$

$$\frac{\partial \dot{m}_{port}(x,t)}{\partial x} = \rho_f(2\pi r)\frac{a}{x^m}\left(\frac{\dot{m}_{port}}{\pi r^2}\right)^n \tag{7.2}$$

Note that the mass flux, which varies along the port length, can still be computed:

$$G = \frac{\dot{m}_{port}(x,t)}{\pi r(x,t)^2} = \frac{\dot{m}_{ox}(t) + \dot{m}_f(x,t)}{\pi r(x,t)^2} \tag{7.3}$$

The unknown terms, a, n, and m are usually published for ranges of average O/F ratios and oxidizer mass fluxes. The regression rate equation, as shown in Equation 7.1, can be numerically integrated quite easily. A first order scheme is explicitly provided in Ref. [79].

With the regression rate equation integrated throughout the burn time, it is possible to track the fuel grain profile at any given time within the burn, the O/F ratio through the burn, and the flux at any given axial location at any given time. Note that Equation 7.1 is markedly different than Equation 3.1 on Page 51 in that he simplified space-time averaged regression rate equation does not consider the mass flow rate of fuel. The regression rate dependence on the axial coordinate is generally small, as m usually has low values.

While ignoring the fuel mass flow rate undoubtedly makes the regression rate easier to solve, it is inherently incorrect. Regression rate constants reported for the space-time averaged equation generally have very strict limits on the average O/F ratio and the oxidizer mass flux uses. Unfortunately, these limits are rarely published along with the data, which often leads to large differences between published regression rates and regression rates achieved in motors. The ideal method of reporting these regression rate constants is based on the space-time coupled equations, as shown in Equation 7.1. This equation inherently accounts for the variable O/F ratios and is valid on a wider

range of conditions. In the data below, the reader will find that the achieved regression rates match the published regression rates within 3% when using the space-time coupled equations.

7.2.1 Visual Analysis

OpenCV [80] and Python [81] are chosen as the packages of choice for this research. These packages are open source, compatible on a variety of computing platforms, and most importantly, free. These packages made it easy to load and analyze the high speed data.

The preliminary analysis of the visual data was to determine a calibration for estimating the fuel grain geometry. A test video of the fore-end of the motor was taken prior to each hot fire. In this video, the same frame rate setting was used, but the f-stop and ISO settings were adjusted so that an image was visible when a bright CREE XML T6 LED was pointed at the motor to provide illumination. Because the fuel grain was not visible in this video, the fore end view port was used as a calibration reference. Because of the limited resolutions offered by the camera for high-speed recording, the images were upscaled by a factor of 2 in post processing. This doubled the resolution of the recorded images. Lanczos resampling [82] was applied in all of the upscaling tasks in this research. Along with the knowledge that the viewport has a diameter of 50.7mm, it is possible to determine the width of each pixel, which is roughly 0.317 $mm/pixel$ for each test. Note that because the fore-end view port reference and the front of the fuel grain are not located in the same plane, another correction factor must be applied to adjust for perspective losses. To determine this, a still photograph of the fore-end of the motor was taken with a high-resolution camera. In this image, (shown in Figure 7.1), both the view port on the fore end block and the front of the fuel grain are visible, which allows for a correct calibration factor to be determined. The scaling factor required to correct for the perspective losses turned out to be 1.039, so the correct calibration would be 0.329 $mm/pixel$.

The measured calibration factor indicates that a higher resolution camera might be desired. Compare this calibration term to the term used in measuring the nozzle throat area, which was around 0.05 $mm/pixel$ for each measurement. Higher resolution video data might improve the processed data.

With the calibration complete, the high-speed videos were analyzed. For every video, each frame was upscaled by a factor of two in an effort to improve resolution and clarity. The images were then copied. One of the copied images was subjected to a gray-scale color conversion, while the other was converted into the HSV color format (Hue-Saturation-Value) [83]. The HSV color format is a format similar to RGB (Red-Green-Blue), but is easier to process color images due to the color definitions.

A blur is then applied to the gray-scale images to filter out noise and small particles in the port. This also has the effect of removing particles stuck on the sapphire window. After the blurring process was completed, a threshold of the image was taken such that only the port area remained. From there it was relatively easy to take the port area and hydraulic diameter measurements.

Figure 7.1: The fuel grain can clearly be seen when looking down the sapphire window.

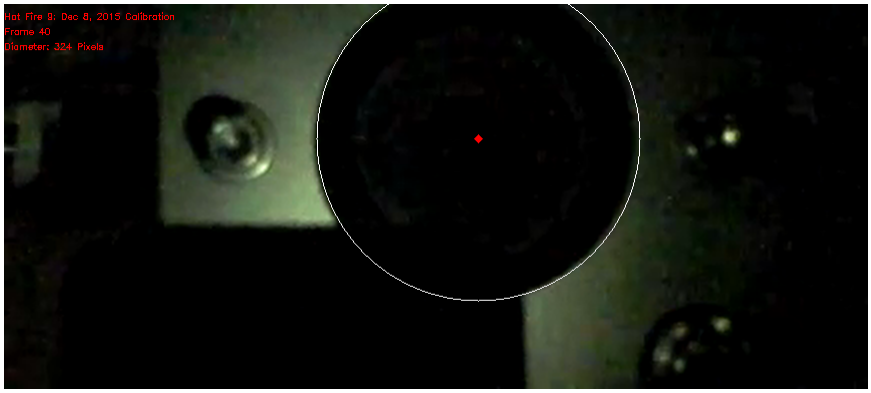

Figure 7.2: The upscaled calibration image shows that the fore end support block of the motor has a viewport diameter of 324 pixels, which corresponds to 5.07 cm. To measure the fuel grain diameter, a correction factor of 1.039 is applied to account for perspective losses because the fuel grain is further away from the camera lens.

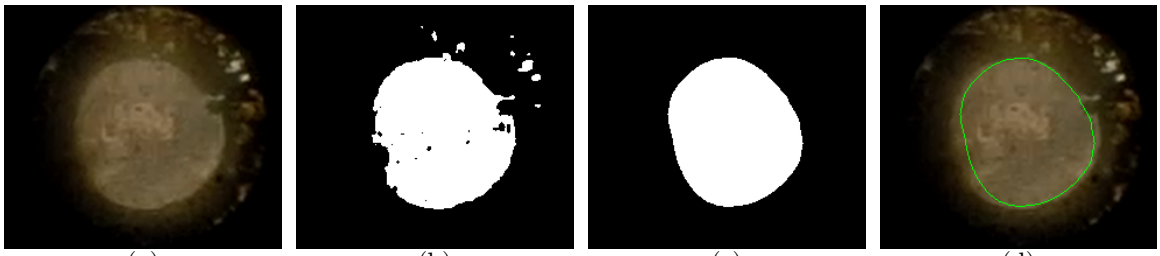

(a) (b) (c) (d)

Figure 7.3: The image processing sequence is shown for the HSV-based filtering method. (a) The image is first upscaled and converted to the HSV color-space. (b) The image is then filtered, allowing only a yellowish color to pass through. (c) The image is blurred to reduce noise. (d) The port area can be detected and the hydraulic diameter can be computed.

The color image in the HSV space was filtered based on the color of the image. Only a reddish-yellow color (defined by the range from [0,0,90] through [40,145,255] in HSV space) was allowed through the filter. After the filtering, a blur was again applied to remove noise and small particles. After these processes, only the port area remained in the image, which was easy to track.

7.2.2 Camera and Settings

The Casio Exilim EX-1 allowed for recording high-speed video of the port while the motor was fired. Unfortunately, the camera was limited to low resolution videos for high speed capture. The resolution and frames per second (FPS) limits are listed in Table 7.2. For this research, the data was recorded at 300 FPS (with unsuccessful results) and 600 FPS (with some successful results). The 1200 FPS setting was avoided because it offered severely reduced resolutions that likely would not cover the port area. A list of all of the settings used to record the images for the successful test data is shown in Table 7.3. In addition to the camera settings, an ND4 neutral density filter was attached to the lens of the camera, which was used to help reduce the intensity of the light at the camera's sensor.

Table 7.2: Recording data at high frame rates reduced the resolution of the captured images.

Frame Rate (FPS)	**Maximum Resolution**
300	512x384
600	432x192
1200	336x96
30-300	512x384

Table 7.3: The settings used to record the calibration of the high speed port area measurements.

Parameter	**High Speed Value**	**Calibration Value**	**Units**
Frame Rate	600	600	(FPS)
Shutter Speed	1/40,000	1/30	Hz
ISO	100	1600	
F Stop	7.5	7.5	

7.3 Data

Most of the high-speed video data captured was unfortunately not usable, as midway into the burn, the fuel grain surface became blurry and out of focus. In most of the tests, the front of the fuel grain burned away by a small amount. The settings on the camera allowed for a very small depth of field, which meant that the fuel grain surface was only clearly defined for a very narrow range of depths. Moving the camera further back (to increase the depth of field) was considered, but ultimately abandoned because of the inability for the camera to accept a larger zoom lens, in addition to the resolution problem. If the camera was moved back, the pixel resolution would be significantly diminished, and accurate data would not be obtainable. Figure 7.4 shows a cut of a fuel grain after Test 2. This shows that the front surface of the fuel grain regressed about 10mm. This likely was the cause of the captured image getting blurry after some time into the burn.

Another problem with most of the high speed data was the saturation problem. In some tests, the entire view port was filled with bright light and it was impossible to obtain port area measurements. Figure 7.5 shows sample frames collected from Test 7, where the fuel surface was only visible in the early portions of the burn. A faster shutter speed would likely fix this problem.

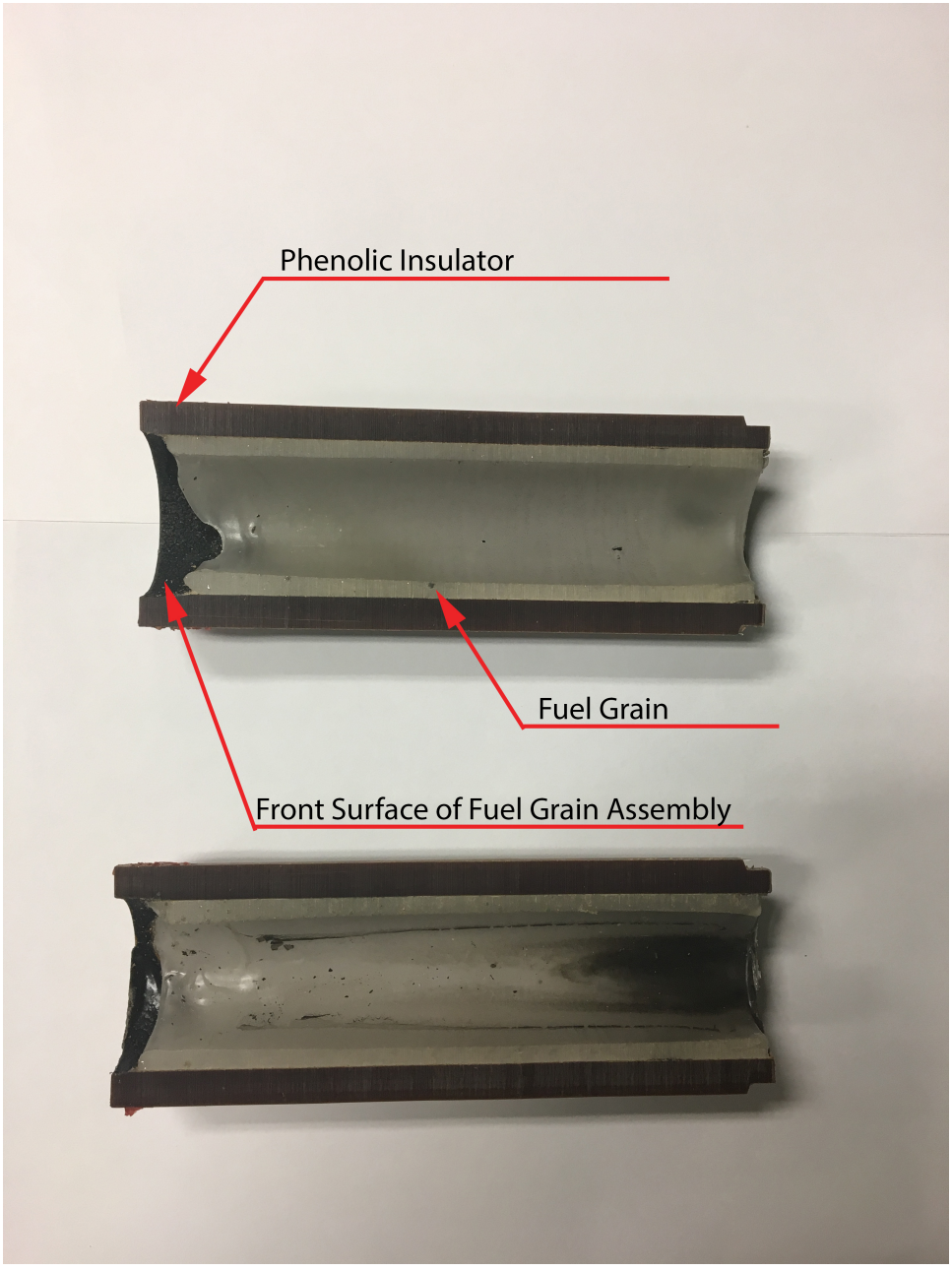

Figure 7.4: A slice of the fuel grain after Test 2 shows that the front surface of the fuel grain regressed by about 10mm. This was likely the cause of the image becoming blurry towards the end of the burn.

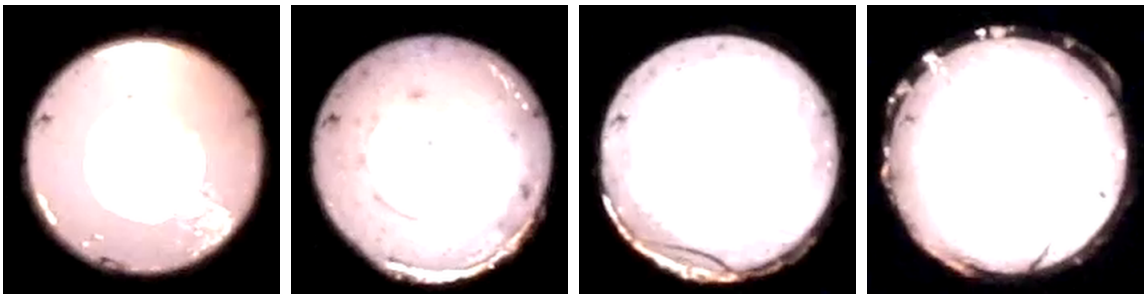

Figure 7.5: The images were saturated and out of focus for many of the tests. Focus was lost due to the fuel burning from the front surface.

While many of the high speed recordings did not provide usable data, two tests in particular provided excellent data. For most of the duration of the burns, the high speed videos collected from Tests 9 and 10 provided clear images throughout the burn. These tests were run at conditions A and B, respectively (see Table 5.1 on Page 82). Figure 7.6 shows a series of stills captured from Test 9. These stills show that the hydraulic diameter was tracked for much of the duration of the burn, although the time-varying port area and diameter measurements are quite noisy, as seen in Figure 7.7. Note that the tracked port area was a bit smaller than the port area shown in the videos and also that in some frames the port area was not captured. In this case, zero was logged for both the area and hydraulic port area measurements. Care was taken to avoid dividing by zero in the subsequent operations. The under-captured port area was later measured and corrected for by using a few stills and tracking the port area manually. This procedure is described later in this chapter.

Although the captured port area and diameter measurements are noisy, the general trend of the data can easily be seen. The same algorithm would possibly produce less noise with data from a camera with faster shutter speeds and higher resolution. Nonetheless, these images are the first look inside of a burning hybrid rocket motor in a conventional layout and at relevant chamber pressures.

The fuel grains were physically measured before and after the burn. At the beginning of the burn, the fore end port diameter of the fuel grains were measured (and it was assumed that the grains had a constant port diameter to begin with).

After the burn, only the aft end of the grain was measurable. This is because the front surface of the fuel grain tended to burn away, leaving bare insulator exposed. Because of the scale of this motor, it was difficult to get measurement calipers far enough into the insulator such that the fuel grain had reasonable thickness. It was much easier to measure the aft surface of the fuel grain after the burn, which did not burn away because it was protected by the mixer during the burn.

The early port area measurements of the fuel grain were underestimated, as a thin layer of fuel residual was left on the aft face from the shutdown sequence. Once this issue was discovered, the residual fuel was chipped away and the grain was slightly pushed out of the insulator housing, so that an average wall thickness measurement could be made. Table 7.4 lists the initial and final port

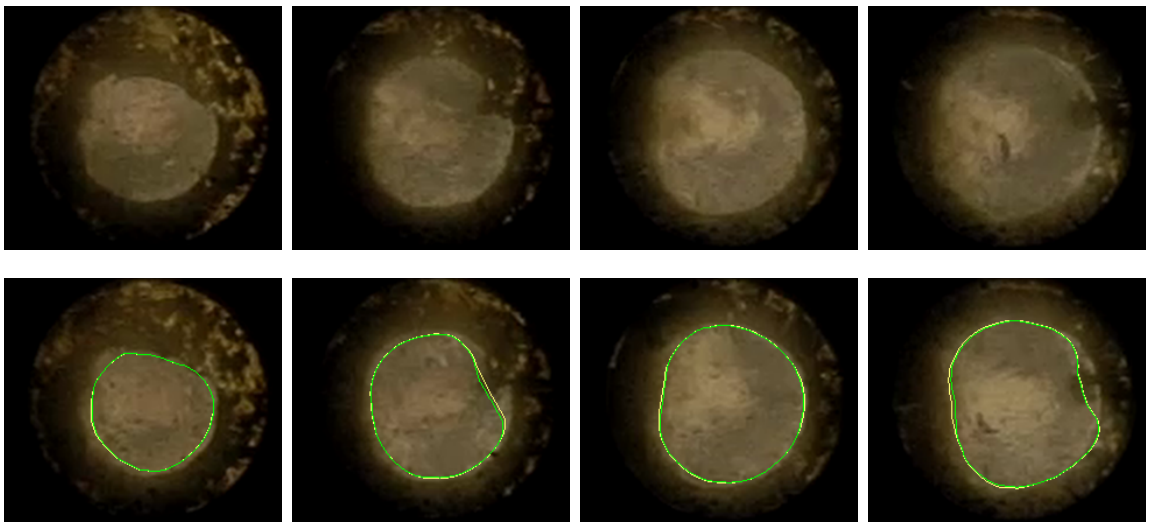

Figure 7.6: Some still images from Test 9 indicate that the image processing algorithm tracked the port area fairly well for the test. The top row of images are the raw stills, while the bottom row of images include the detected port area. Note that the tracked area is slightly smaller than the actual visible port area. A correction is later applied for this nearly constant offset.

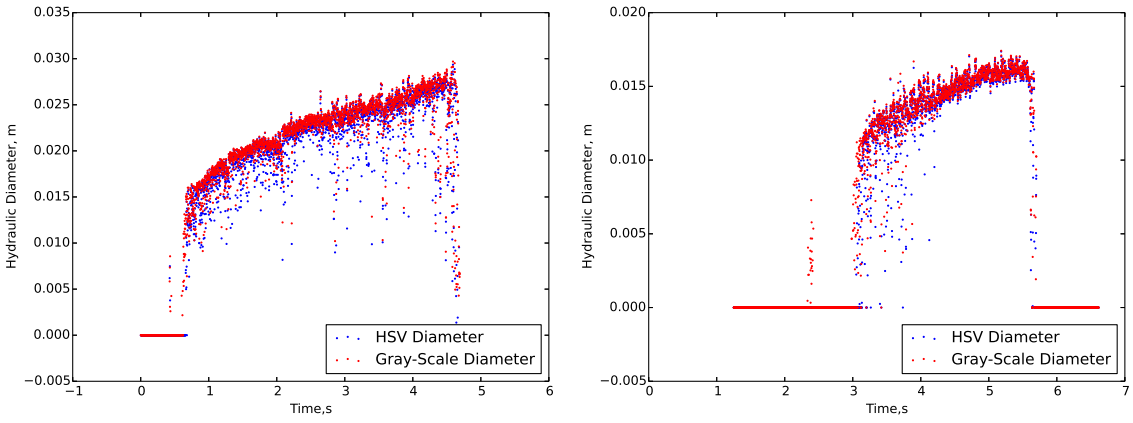

Figure 7.7: The tracked hydraulic diameters for Test 9 (left) and Test 10 (right) correctly show increasing port diameters with time.

Table 7.4: Data used to compute the regression rate of paraffin fuels from Tests 9 and 10.

Test	**Initial Port Diameter** (m)	**Final Port Diameter** (m)	**Burn Time** (s)	**Avg. Ox. Mass Flow Rate** (kg/s)
9	0.0184	0.0366	4.22	0.0501
10	0.0163	0.0281	3.37	0.0244

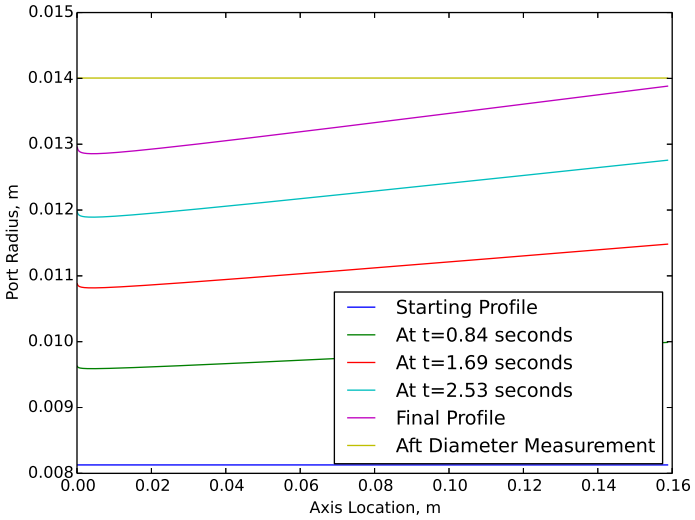

Figure 7.8: The numerical solution to the regression rate equation shows that the port radius varies down the length. The minimum port area occurs slightly downstream of the front surface of the grain. The regression rate is determined based on fitting the numerical estimate of the aft diameter at the end of the burn matching to the physical measurement. The profiles shown are taken from Test 10.

diameters for Tests 9 and 10.

Note that a estimates for Test 9 and 10 were very similar to the published regression rate constant, which confirmed the previously measured regression rate of paraffin fuels. This was a surprising find, as the published regression rate constants were determined on a much larger-scale system.

There was good agreement between the regression rate equation and the initial and final port diameter measurements. However, note that this is by design. The a constant was chosen such that the measured final aft diameter matches the numerical solution. It just so happened that the a constant was nearly identical to that found previously. It was desired to understand how well the regression rate equation predicted the port geometry *while the motor was burning*. The comparison between visual data and the regression rate equation validates that the regression rate equation captures the fuel burning behavior quite well, as shown in Figure 7.9.

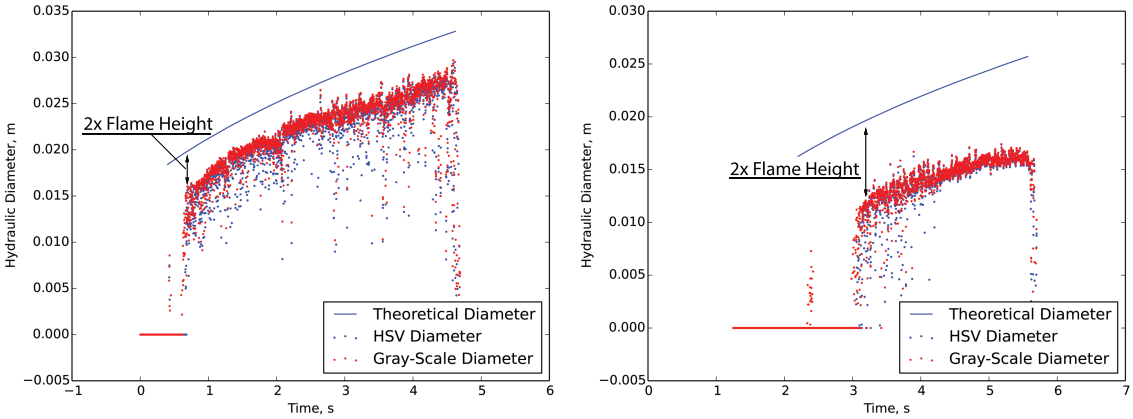

Figure 7.9: The tracked hydraulic diameters for Test 9 (left) and Test 10 (right) along with the theoretical values. Note that in Test 10 the image processing could not detect the port area early in the burn. Because of this, the theoretical curve starts before the image processing has detected a port area.

Note that there is an offset between the theoretical port diameter and the measured hydraulic diameters. This offset is partially caused by the algorithm consistently tracking a port area smaller that the port area, as seen in Figure 7.6. This offset was estimated to be about 1 mm based on fine tuning of the image processing parameters for select frames for each test. Accounting for this 1 mm offset does not fully account for the difference between the visual plots and the regression rate equation. Recall that the image processing scheme searches for a bright edge boundaries (or color boundaries), which may not correspond to the true fuel grain geometries. Instead, the bright edge could possibly be the flame location. In Test 9, the flame height was about 0.75 mm above the fuel grain surface. In Test 10, the flame height was approximately 2.70 mm. The difference in flame heights in the test could be attributed to the difference in oxidizer mass flow rates (hence the flux and velocities in the motor) as well as the low resolution problem. The uncertainty in the calibration image (roughly 3 pixels in diameter), results in the uncertainty of the flame height of roughly 1 mm. These measured flame heights have general agreement with those measured from Reference [84], where the flame location was estimated using an OH* chemiluminescence technique. In that study, flame heights were observed from the side of a fuel grain to be up to 5mm above the fuel grain surface. Those tests were done on the Stanford Combustion Visualization Facility [44].

If the measured visual data points are shifted to account for the diameter offset, the numerical regression rate data agrees with the measured visual data remarkably well. This validates the hybrid fuel regression rate equation with visual confirmation.

It should be noted that the original (simplified space-time averaged) regression rate constants were determined through a series of nearly 70 tests. The visual scheme used in this research could

determine these regression rate constants to relatively good accuracy with just a few tests. Although the regression rate constants were roughly well known to begin with for this study, it is likely that the same set of regression rate constants could be determined with just a few more tests if they been unknown from the start.

The reader should be reminded that running even a single ground test of a hybrid rocket motor requires a significant amount of time, effort, and resources. A testing requirement reduction of this magnitude could have large (and beneficial impacts) in the hybrid rockets community, as this visual method could greatly improve the published regression rate constants for a variety of fuels.

7.4 The Average Regression Rate

Because the fuel regression rate data matched the visual data very well for Tests 9 and 10, it was desired to estimate the fuel regression rate data for the full range of tests performed. The regression rate constant a was determined for each test point and an average regression rate was computed.

The average a constant was $9.58x10^{-5}$ $\left(m^{1-m}/s\left(kg/m^2s\right)^n\right)$. This is only 3% larger than the the published regression rate constants. As seen in Table 7.5, there is some discrepancy between the mass burned computed by the regression rate equation and the mass burned that was physically measured. This discrepancy is likely caused by the sometimes violent ignition and shutdown characteristics of the motor. Furthermore, upon shutdown, the fuel is still very hot and vaporizing during the purge phase. This is evident as most tests had a very smokey plume during the nitrogen purge after shutdown. Furthermore, the total mass burned in the motor accounts for other burning components, such as the various EPDM spacers, the mixer, and sometimes the insulators. The regression rate model additionally does not account for the front edge of the fuel grain burning away, which for some tests is estimated to be up to 15 grams.

This mass discrepancy does highlight some uncertainty of the O/F ratio *during the burn.* This is a very difficult quantity to estimate on such small scale of a motor. On a larger scale motor, the uncertainty remains roughly constant, meaning that the relative accuracy of the masses and physical measurements greatly improves. Nonetheless, all data reported in the research is used based on mass-based computed O/F ratios. Note that in some tests, the fuel grain was completely burned away from the chamber. After the stearic acid was added to the fuel grains, there were no indications of fuel grain cracking (from the pressure traces) during the burn. However, in tests 12,13,14,18, and 22, the fuel grains either melted away during the purge or were ejected during shutdown.

Table 7.5: The regression rates measured during the tests and the mass discrepancies between the measured mass burned and the theoretical mass burned based on Equation 7.1.

Test	$a\ x\ 10^5$**,** $(m^{1-m}/s\left(kg/m^2s\right)^n)$	**Mass Discrepancy** (g)
1	9.51	8.4
2	9.23	13.2
3	9.97	11.3
4	9.94	10.3
5	9.69	10.0
6	9.81	5.6
7	9.93	12.9
8	9.26	12.9
9	9.10	14.8
10	9.50	1.0
11	9.57	8.9
12	-	-
13	-	-
14	-	-
15	9.99	12.3
16	9.49	9.8
17	9.73	13.9
18	-	-
19	9.32	3
20	9.51	7.6
21	9.93	13.1
22	-	-

Chapter 8

Conclusions

In this research, a conventional hybrid rocket motor was built with an emphasis on performance and a conventional internal design that might be used in a flight system. This was chosen so that the data obtained from the fabricated motor would be useful to others and would be applicable to future motor designs. This motor was outfitted with a variety of sensors mainly on the nozzle throat plane. These sensors allowed for a time-varying measurement of the heat flux applied to the nozzle surface from the combustion of the propellants as well as a an ultrasound measurement used to measure the nozzle throat area variation during the burn. These are thought to be the first measurements of their kind. Additionally, the fuel regression rates were directly measured with a high-speed camera pointed directly down the port of the motor.

The original goals of this study were all met and a short summary of their results are listed below.

1. *Design and build a hybrid rocket motor with the ability to track the nozzle throat area while the motor burns. The throat area measurements would ideally be affordable, and would not present safety hazards. The motor design should also be conventional such that the data collected on the motor would be expected to be similar to the data collected on other motors intended to fly missions.*

   A hybrid rocket motor was built with the desired ability to measure the throat area without affecting the performance of the motor. The tracking of the nozzle throat area was a novel approach, as two independent measurements (the thermal measurements along with the raw ultrasound measurements) were combined to compute the throat area accurately. Furthermore, the internal motor geometries proved to provide stable combustion over a wide range of flow conditions. The stability of the motor was better than expected and it would be difficult to provide suggestions for improvement.

   The motor also utilized a converging-diverging nozzle geometry. This is typical for flight and

high performance motors as supersonic exhausts are known to dramatically improve performance. Furthermore, the tested nozzles were all fabricated using a fine grade of graphite that the manufacturer confirmed other customers regularly use as nozzles in rocket engines.

The ultrasound scheme utilized to measure the throat area also met the initial goals of the study. While still considered expensive, the ultrasound method is far less expensive than x-ray methods used by other groups to measure nozzle throat area in solid rocket motors. Furthermore, while the use of x-ray machines poses safety concerns and requires lengthy training (and proper licenses), ultrasound machines used in engineering applications do not pose safety risks and neither safety training nor certification is required. The ultrasound technique can also be used in a variety of other studies and now that the lab has experience with ultrasound, a few other projects have already begun to use the technique to scan fuel grains and to measure the regression rates of fuels.

2. *Track the nozzle throat area as a function of time while a hybrid rocket motor is burning.*

   The nozzle throat area was measured as a function of time for six different test conditions. Several important observations were made from the recorded data. These included the fact that at the beginning of the burn, while the nozzle heats up, the nozzle throat area shrinks because of thermal expansion. Furthermore, nozzle erosion does not overcome thermal expansion until about a second after motor ignition. Notably, nozzle erosion was not witnessed during fuel-rich test conditions.

   An additional result of this study was that an estimate of the nozzle heating was determined. This heating estimate could be very useful to future designers of hybrid rocket motors. Furthermore, this heating estimate was generally very close to that predicted by Bartz' Equation, a simple equation originally developed to predict heating in liquid engines (and later found to estimate the heating of solid motors as well). This research proved that Bartz Equation works well for the hybrid configuration and it is likely that design considerations developed for liquid and solid rocket motors apply to hybrids as well.

3. *Propose a model for nozzle erosion.*

   A dimensionless model for nozzle erosion in hybrid rocket applications was proposed in Chapter 6 of this thesis. The research found that nozzle erosion was heavily dependent on the chamber pressure and O/F ratio. Most interestingly, nozzle erosion was eliminated when running at fuel rich test conditions. This surprising observation could influence the design of future long-burning motors.

In addition to the three goals that this research set out to accomplish, working on this research project led to other accomplishments as well. The port of a hybrid motor was visualized. Although the Stanford Propulsion and Space Exploration (SPaSE) lab has experience with combustion visualization inside of hybrid motors, this was the first time that visualization was done in a conventional

set up and in a motor that delivered reasonable performance and high chamber pressures. Furthermore, the chamber pressures achieved were higher than ever tested previously in the lab. The fast regression rate of paraffin was verified visually, and the regression rate constants could possibly be determined with just a few tests with the visual scheme used in this research. Although just two successful measurements were taken, it should be reiterated that images from *inside* of a conventional and high-pressure hybrid rocket motor were taken and usable data was extracted. This accomplishment is individually very exciting and worthwhile as a topic on its own. However, I feel extremely lucky that I had the opportunity to work on this topic as secondary research project in addition to my main research.

8.1 Suggestions Based on Findings

Based on the findings of this research, nozzle erosion can indeed be an issue for small-scale hybrid rockets or hybrid rockets requiring extended burn times. Although the nozzle erosion problem can be a roadblock in the development of these systems, this research also luckily identified a solution to eliminate nozzle erosion altogether.

For missions where nozzle erosion poses a significant challenge, operating the motor at fuel rich conditions has shown, at least from the experimental motor results, that nozzle erosion can be eliminated. For some particular mission designs, the losses associated with burning fuel rich could likely be overcome by the savings gained by avoiding nozzle erosion. Additionally, the act of burning fuel rich has numerous system benefits as well. Particularly, when burning fuel rich, less oxidizer is needed. Therefore, the oxidizer storage tank mass can be significantly reduced, and the additional fuel required is easier to store, as the combustion chamber can usually be rated for lower pressures than the oxidizer tank. Furthermore, when operating fuel rich, the feed system can be sized for lower flow rates, which can reduce pipe diameters and valve masses, thereby increasing the propellant mass fraction or allowing for a larger payload. The combination of these system-wide changes would ultimately reduce the cost of a mission.

Additionally, other possible nozzle erosion reduction techniques were also identified. One could passively control the boundary layer at the nozzle throat section by placing a sliver of slow burning fuel upstream of the nozzle section. Alternatively, one could consider the addition of aluminum particles in the fuel, or consider a different oxidizer altogether. It is likely that some oxidizers inherently cause less nozzle erosion than others.

For any hybrid rocket designer, it is strongly suggested to use the proposed model to, at the very least, have an understanding of what the nozzle erosion model predicts for any future hybrid design. While this may not lead to any design changes for most cases, it may highlight a potential problem early in the design stage of a future mission.

8.2 Future Work

As this research is thought to be first of its kind, it can hardly be classified as "complete". The nozzle erosion problem in hybrid rockets is still considered an unsolved one (although it has now finally been studied and a potential solution has been identified). The proposed model needs to be adjusted to account for various propellants and physical abrasion.

These upgrades to the model cannot occur until more data is acquired. Unfortunately, testing with other propellants and additives is cost prohibitive, as a new feed system and motor would likely need to be fabricated. Operating a hybrid rocket motor utilizing any other oxidizer would not be feasible in the lab. A new facility would need to be obtained so that various propellants could be tested on a regular basis. This is not feasible in the near future.

Many possible follow on projects to this research exist. The affects of scale are yet to be determined (although nozzle erosion is less of an issue for larger systems), so nozzle erosion data for large scale systems would be incredibly valuable. Also, the potential nozzle erosion reduction techniques discussed in Chapter 6 need to be tested to see if any of those actually work.

Additionally, the data reduction used in this research takes an incredible amount of time to process. A future project can be undertaken to reduce the time required to solve the inverse heat conduction problem by programming in a more efficient fashion. Also, a newer objective function could be found that does not require future time-steps. Without looking at future data, the inverse analysis could potentially be done in real time, which would allow for the ability to track the nozzle throat area in real time. This improvement would not be limited to only hybrid rocket engines.

The first time the motor was tested, a phenolic insulator was used to protect the fore-end from exposure to the flame. This insulator nearly completely burned away and likely was the cause of the smokey and unstable-looking plume. However, the chamber pressure was also a bit higher than the subsequent tests, which used a graphite insulator that did not burn. It is likely that the pressure gain was experienced because oxidizer was pre-heated before combusting with the paraffin fuel grain. This accidental discovery needs attention as this could increase efficiency and performance of other hybrid propulsion systems.

The preliminary visual scheme discussed in Chapter 7 provided fantastic results and with some enhancements, the scheme could drastically reduce the amount of effort required to deduce the full set of regression rate constants for any propellant combination.

Appendix A

Exact Solutions of the Heat Equation

This section of the appendix goes through the derivation of three similarity solutions of the heat equation. The first is the semi-infinite slab with a constant heat flux applied at the surface, the second is a semi-infinite cylinder with a given inner radius and constant temperature where $x/\sqrt{4\alpha t}$ is constant. The third solution is a semi-infinite slab with variable thermal properties.

A.1 Semi-infinite Slab with Constant Properties

For this problem, a semi-infinite slab of material is subjected to a constant heat flux starting at time t=0. The initial temperature of the slab is a constant T_i. The infinite boundary condition is given by the relation

$$T(x \to \infty) = T_i \tag{A.1}$$

and the constant flux boundary condition is given by:

$$q_s = -k \frac{\partial T}{\partial x}\bigg|_{x=0} \tag{A.2}$$

The heat equation for a semi-infinite slab is given by:

$$\alpha \frac{\partial^2 T}{\partial x^2} = \frac{\partial T}{\partial t} \tag{A.3}$$

Firstly, T is transformed such that the initial temperature is subtracted out.

$$\theta = T(x,t) - T_i \tag{A.4}$$

The PDE is then given by:

$$\alpha \frac{\partial^2 \theta}{\partial x^2} = \frac{\partial \theta}{\partial t} \tag{A.5}$$

It is desired to find nondimensional variables such that the partial differential equation is reduced to an ordinary differential equation. We search for a dilation group such that the differential equation remains invariant. Let

$$\tilde{x} = e^a x$$
$$\tilde{t} = e^b t$$
$$\tilde{\theta} = e^c \theta$$

The relevant differentials are then:

$$\frac{\partial \tilde{\theta}}{\partial \tilde{x}} = e^{c-a} \frac{\partial \theta}{\partial x}$$
$$\frac{\partial^2 \tilde{\theta}}{\partial \tilde{x}^2} = e^{c-2a} \frac{\partial^2 \theta}{\partial x^2}$$
$$\frac{\partial \tilde{\theta}}{\partial \tilde{t}} = e^{c-b} \frac{\partial \theta}{\partial t}$$

With this dilation group, the PDE is then given by:

$$\alpha \frac{\partial^2 \tilde{\theta}}{\partial \tilde{x}^2} = \frac{\partial \tilde{\theta}}{\partial \tilde{t}}$$
$$\alpha e^{c-2a} \frac{\partial^2 \theta}{\partial x^2} = e^{c-b} \frac{\partial \theta}{\partial t}$$

The original differential equation is clearly invariant if $a = 2b$. c is chosen as unity for simplicity. The characteristic equations are then given by Equation A.6

$$\frac{dx}{x} = \frac{dt}{2t} = \frac{d\theta}{\theta} \tag{A.6}$$

Integrating the left set of equations in the characteristic equations yield the first independent variable.

$$ln\,(x) = ln\left(t^{\frac{1}{2}}\right) + ln\,(\eta)$$
$$\eta = \frac{x}{\sqrt{t}}$$

The variable is nondimensionalized with the introduction of $\sqrt{\alpha}$ and is shown in Equation A.7. Note the introduction of $\sqrt{4}$ for later convenience.

$$\eta = \frac{x}{\sqrt{4\alpha t}} \tag{A.7}$$

This variable is related to the Fourier number, $Fo = \alpha t / L^2$.

The derivatives of this first variable are then:

$$\frac{\partial \eta}{\partial x} = \frac{1}{\sqrt{4\alpha t}}$$
$$\frac{\partial \eta}{\partial t} = \frac{-\frac{1}{2}x}{\sqrt{4\alpha t}^3} 4\alpha = -\frac{\eta}{2t}$$

The second set of equations in the characteristic equations yield the second dependent variable.

$$ln\left(F\left(\eta\right)\right) + ln\left(t^{\frac{1}{2}}\right) = ln\left(\theta\right)$$
$$F\left(\eta\right) = \frac{\theta}{\sqrt{t}}$$

This variable is nondimensionalized with the factor $k/q_s\sqrt{4\alpha}$. Note again that the factor of $\sqrt{4}$ is introduced for later convenience. The second variable is then given by Equation A.8.

$$F\left(\eta\right) = \frac{k\theta}{q_s\sqrt{4\alpha t}} \tag{A.8}$$

Solving for θ yields the similarity form of the solution.

$$\theta = \frac{q_s}{k}\sqrt{4\alpha t}F\left(\eta\right) \tag{A.9}$$

Equation A.9 can now be differentiated. The relevant derivatives are:

$$\frac{\partial \theta}{\partial x} = \frac{q_s}{k}\sqrt{4\alpha t}F'\frac{\partial \eta}{\partial x} = \frac{q_s}{k}F'$$
$$\frac{\partial^2 \theta}{\partial x^2} = \frac{q_s}{k}F''\frac{\partial \eta}{\partial x} = \frac{q_s\sqrt{4\alpha t}}{2kt}\left(\frac{F''}{2\alpha}\right)$$
$$\frac{\partial \theta}{\partial x} = \frac{1}{2}\frac{q_s}{k}\left(4\alpha t\right)^{\frac{-1}{2}} 4\alpha F + \frac{q_s}{k}\sqrt{4\alpha t}F'\frac{\partial \eta}{\partial t} = \frac{q_s\sqrt{4\alpha t}}{2kt}\left(F - F'\eta\right)$$

Where F' is $\frac{dF}{d\eta}$.

The derivatives can now be substituted back into Equation A.5 to convert into an ordinary differential equation.

$$\frac{F''}{2} = F - F'\eta \tag{A.10}$$

Recall the boundary conditions given by Equations A.1 and A.2. These boundary conditions are transformed into the new variables and are given in Equation A.11.

$$\begin{aligned} F\left(\eta \to \infty\right) &= 0 \\ F'\left(0\right) &= -1 \end{aligned} \tag{A.11}$$

The ordinary differential equation (Equation A.10) can then be integrated. The solution is given in Equation A.12.

$$F = \frac{1}{\sqrt{\pi}} exp\left(-\eta^2\right) - \eta\, erfc\left(\eta\right) \tag{A.12}$$

Where $erfc\left(\eta\right) = 1 - erf\left(\eta\right)$.

The solution is shown in Figure A.1. Note that the boundary conditions are satisfied.

The solution can then be transformed back into the original variables with Equations A.7 and A.8.

$$T - T_i = \frac{2q_s}{k}\sqrt{\frac{\alpha t}{\pi}}\, exp\left(\frac{-x^2}{4\alpha t}\right) - \frac{q_s x}{k}\, erfc\left(\frac{x}{\sqrt{4\alpha t}}\right) \tag{A.13}$$

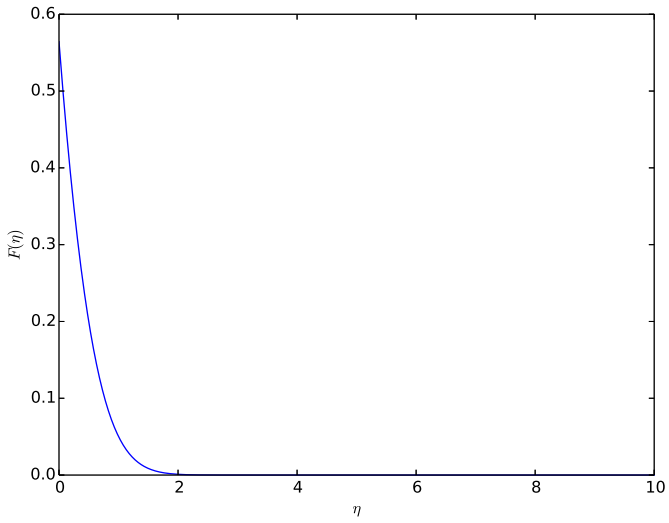

Figure A.1: The similarity solution for the heating of a semi-infinite slab with constant heat flux at the left boundary.

A.2 Semi-infinite Cylinder

In this problem a semi-infinite cylinder with an inner radius of r_i is applied with a constant temperature of T_s at a varying position with time. While this condition seems arbitrary, it avoids having to specify a condition at the singularity where r=0. The heat equation for a cylinder is given by Equation A.14.

$$\alpha\frac{\partial^2 T}{\partial r^2}+\frac{\alpha}{r}\frac{\partial T}{\partial r}=\frac{\partial T}{\partial t} \tag{A.14}$$

The boundary conditions are specified as:

$$\begin{aligned} T\left(r\rightarrow\infty\right)&=T_i\\ T\left(r=\sqrt{4\alpha t}\right)&=T_s\\ T\left(r,0\right)&=T_i \end{aligned} \tag{A.15}$$

The equation is transformed such that the initial temperature is subtracted out.

$$\theta=T(r,t)-T_i \tag{A.16}$$

The partial differential equation is then:

$$\alpha\frac{\partial^2\theta}{\partial r^2}+\frac{\alpha}{r}\frac{\partial\theta}{\partial r}=\frac{\partial\theta}{\partial t} \tag{A.17}$$

This differential equation is invariant under the same dilation group as the equation from Section A.1. Therefore the first dimensionless variable is:

$$\eta=\frac{r}{\sqrt{4\alpha t}} \tag{A.18}$$

This variable is enough to solve the problem. The relevant derivatives are then given by Equation A.19.

$$\begin{aligned} \frac{\partial\theta}{\partial r}&=\frac{\partial\theta}{\partial\eta}\frac{\partial\eta}{\partial r}=\frac{1}{\sqrt{4\alpha t}}\frac{\partial\theta}{\partial\eta}\\ \frac{\partial^2\theta}{\partial r^2}&=\frac{\partial}{\partial r}\left(\frac{\partial\theta}{\partial\eta}\frac{1}{\sqrt{4\alpha t}}\right)=\frac{\partial^2\theta}{\partial\eta^2}\frac{1}{4\alpha t}\\ \frac{\partial\theta}{\partial t}&=\frac{-r}{2t\sqrt{4\alpha t}}\frac{\partial\theta}{\partial\eta}=\frac{-\eta}{2t}\frac{\partial\theta}{\partial\eta} \end{aligned} \tag{A.19}$$

The partial differential equation is converted into an ordinary one by substituting the dimensionless variable and the relevant derivatives into Equation A.17. The resultant ordinary differential equation

is shown in Equation A.20.

$$\frac{\partial^2\theta}{\partial\eta^2} + \frac{1}{\eta}\frac{\partial\theta}{\partial\eta} + 2\eta\frac{\partial\theta}{\partial\eta} = 0 \tag{A.20}$$

The transformed boundary conditions are:

$$\theta\left(\eta \to \infty\right) = 0$$
$$\theta|_{\eta=1} = T_s - T_i$$

The solution to the ordinary differential equation is given by Equation A.21. Note the use of the exponential integral function, which is defined as:

$$Ei(x) = -\int_{-x}^{\infty} \frac{e^{-t}}{t} dt$$

$$\theta\left(\eta\right) = \frac{\left(T_s - T_i\right)}{Ei(-1)} Ei(-\eta^2) \tag{A.21}$$

$\theta\left(\eta\right)$ is plotted for $T_s - T_i = 1$ in Figure A.2. Note that the boundary conditions are satisfied.

Equation A.21 can be transformed back into a function of the original variables by using Equations A.18 and A.16.

$$T(r,t) - T_i = \frac{T_s - T_i}{Ei(-1)} Ei\left(\frac{-r^2}{4\alpha t}\right) \tag{A.22}$$

The time-varying flux at $r = r_i$ can then be determined by differentiating Equation A.22.

$$\left.\frac{\partial T}{\partial r}\right|_{r=r_i} = \frac{2\left(T_s - T_i\right)}{r_i\, Ei(-1)} e^{-\frac{{r_i}^2}{4\alpha t}}$$

$$q_s = -k\left.\frac{\partial T}{\partial r}\right|_{r=r_i} = \frac{-2k\left(T_s - T_i\right)}{r_i Ei\left(-1\right)} e^{\frac{-r_i^2}{4\alpha t}} \tag{A.23}$$

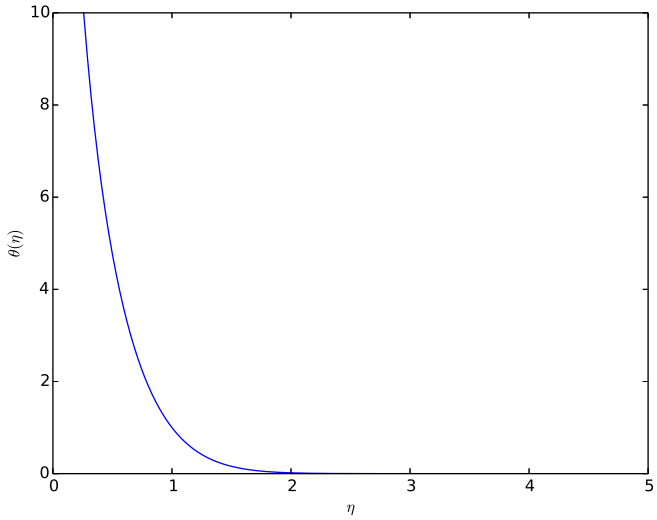

Figure A.2: The similarity solution for the heating of a semi-infinite cylinder.

A.3 Variable Thermal Diffusivity

Consider the heat equation in a thick slab of material with variable thermal diffusivity. Allow $\alpha = cT^{-\sigma}$, where $c = 1$ with units such that α is in the desired scale. When expanding the derivative term, it becomes clear that the heat equation is nonlinear.

$$\frac{\partial T}{\partial t} - \frac{\partial}{\partial x}\left(\alpha \frac{\partial T}{\partial x}\right) = 0$$

$$\frac{\partial T}{\partial t} + \sigma T^{-\sigma-1}\left(\frac{\partial T}{\partial x}\right)^2 - T^{-\sigma}\frac{\partial^2 T}{\partial x^2} = 0 \tag{A.24}$$

Using the "IntroToSymmetry" package for Mathematica from Reference [85], two dilation groups can be identified:

$$\chi^1 : \begin{cases} \zeta & = x \\ \tau & = 0 \\ z & = \frac{-2T}{\sigma} \end{cases} \qquad \chi^2 : \begin{cases} \zeta & = 0 \\ \tau & = t \\ z & = \frac{T}{\sigma} \end{cases}$$

We now superpose the two dilation groups,

$$\chi^3 = \chi^1 + \gamma\chi^2$$

It can be shown that the original equation remains invariant under this new group. The characteristic equation for this group is:

$$\frac{dx}{x} = \frac{dt}{\gamma t} = \frac{\sigma dz}{(\gamma - 2)z} \tag{A.25}$$

The first independent similarity variable can be determined by integrating the x and t terms in A.25.

$$\eta = \frac{x}{t^{\frac{1}{\gamma}}} \tag{A.26}$$

The second similarity variable can also be generated.

$$\theta(\eta) = \frac{T}{t^{\frac{\gamma-2}{\gamma\sigma}}} \tag{A.27}$$

Rearranging A.27 for T,

$$T = t^{\frac{\gamma-2}{\gamma\sigma}}\theta(\eta) \tag{A.28}$$

For convenience, the relevant derivatives are listed below:

$$\frac{\partial T}{\partial t} = \frac{\gamma-2}{\gamma\sigma} t^{\frac{\gamma-2}{\gamma\sigma}-1}\theta - \frac{\eta t^{\frac{\gamma-2}{\gamma\sigma}-1}}{\gamma}\frac{\partial\theta}{\partial\eta}$$
$$\frac{\partial T}{\partial x} = t^{\frac{\gamma-2}{\gamma\sigma}-\frac{1}{\gamma}}\frac{\partial\theta}{\partial\eta}$$
$$\frac{\partial^2 T}{\partial x^2} = t^{\frac{\gamma-2}{\gamma\sigma}-\frac{2}{\gamma}}\frac{\partial^2\theta}{\partial\eta^2}$$

These can be substituted back into Equation A.24, which results in the conversion from the partial differential equation to an ordinary differential equation.

$$\frac{\gamma-2}{\gamma\sigma}\theta - \frac{\eta}{\gamma}\frac{\partial\theta}{\partial\eta} + \sigma\theta^{-\sigma-1}\left(\frac{\partial\theta}{\partial\eta}\right)^2 - \theta^{-\sigma}\frac{\partial^2\theta}{\partial\eta^2} = 0 \tag{A.29}$$

The value of σ is open for the user to best fit material property data. For this example, $\sigma = 1$ captures the trend of the measured thermal diffusivity fairly well. The value of γ must then be selected so that the desired boundary condition remains invariant. For the case of an impulsively imposed wall temperature, $\gamma = 2$.

For this example, the reduced differential equation must be numerically solved.

$$\theta'' = -\frac{\eta}{2}\theta'\theta + \frac{(\theta')^2}{\theta} \tag{A.30}$$

The following boundary conditions are applied:

$$\theta(\eta \to \infty) = 1$$
$$\theta(0) = 3$$

This differential equation can easily be solved numerically, as shown in Figure A.3.

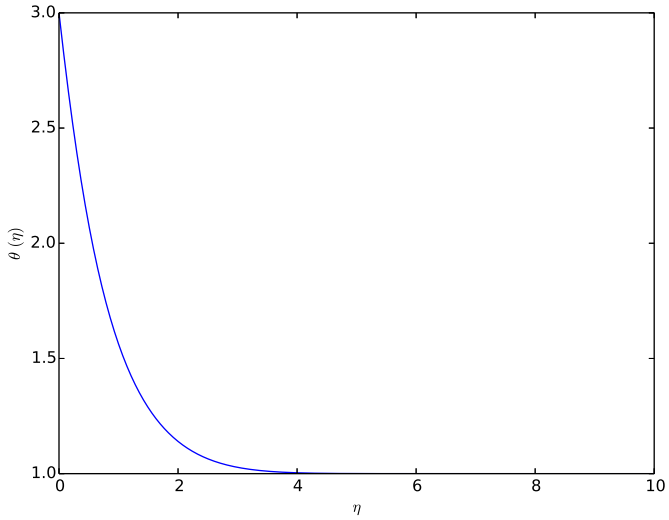

Figure A.3: The similarity solution for the nonlinear heat equation.

Appendix B

Derivation of Bartz' Equation

This section provides the derivation of the Bartz Equation from Reference [34].

The heat transfer coefficient is first thought to be of the form

$$h_g \sim (\rho' U)^m \tag{B.1}$$

where ρ' is the free stream value of the local gas density. Equation B.1 can be rewritten in a more familiar nondimensional form.

$$Nu = C\,(Re)^m\,(Pr)^n \tag{B.2}$$

It can be shown that $m = 0.8$ and n is selected to be 0.4. The arithmetic mean (am) of the properties are evaluated between the bulk temperature T and the wall temperature T_w. Then,

$$h_g = \frac{C}{D^{0.2}} \left(\frac{\mu^{0.2} C_p}{Pr^{0.8}} \right)_{am} (\rho_{am} U)^{0.8} \tag{B.3}$$

It is assumed that C_p and Pr do not vary much with temperature. They can then be evaluated at stagnation temperature conditions and held constant. The ρ_{am} and μ_{am} can be evaluated in terms of stagnation and static values. Equation B.3 can then be written as:

$$h_g = \frac{C}{D^{0.2}} \left(\frac{\mu^{0.2} C_p}{Pr^{0.8}} \right)_{0} (\rho' U)^{0.8}\,\sigma \tag{B.4}$$

Where $\sigma \equiv (\rho_{am}/\rho')^{0.8}\,(\mu_{am}/\mu_0)^{0.2}$. Noting that $T_{am} = 1/2\,(T + T_w)$, that $\rho \sim (1/T)$ and that $\mu \sim T^w$, the σ can be evaluated in terms of T_0, T_w and M.

$$\sigma = \frac{1}{\left[\frac{1}{2}\left(1 + \frac{\gamma-1}{2}M^2\right) + \frac{1}{2}\right]^{0.8-(w/5)} \left[1 + \frac{\gamma-1}{2}M^2\right]^{w/5}} \tag{B.5}$$

Bartz suggests using $w = 0.60$. The equation can then be rewritten in a more convenient form by evaluating $\rho' U$ in terms of C^* and A_*/A.

$$h_g = \left[\frac{C}{D_*^{0.2}} \left(\frac{\mu^{0.2} C_p}{Pr^{0.6}} \right)_0 \left(\frac{P_c g}{C^*} \right)^{0.8} \right] \left(\frac{A_*}{A} \right)^{0.9} \sigma \tag{B.6}$$

Note that A_*/A and σ can be evaluated at any location within a nozzle. $C = 0.026$ based on measured data. The radius of curvature is introduced based on similarity considerations. The final equation can then be written as shown in Equation B.7.

$$h_g = \left[\frac{0.026}{D_*^{0.2}} \left(\frac{\mu^{0.2} C_p}{Pr^{0.6}} \right)_0 \left(\frac{P_c g}{C^*} \right)^{0.8} \left(\frac{D_*}{r_c} \right)^{0.1} \right] \left(\frac{A_*}{A} \right)^{0.9} \sigma \tag{B.7}$$

This equation was developed by D. R. Bartz in Reference [34]. It was originally based on data from a liquid engine that burned Red-Fuming Nitric Acid (RFNA) and Hydrazine (N_2H_4). This research has shown that the equation provides a decent prediction for the heat transfer coefficient in hybrid propulsion systems.

Appendix C

Derivation of Thrust Coefficient

This section goes through the derivation of the Thrust Coefficient, C_f, from the general thrust equation, as shown in Equation 1.3, reprinted as Equation C.1 for convenience.

$$T = \dot{m}_e u_e + (P_e - P_a) A_e \tag{C.1}$$

The definition of C_f is first applied.

$$C_f = \frac{T}{P_c A_t} \tag{C.2}$$

So

$$C_f = \frac{\dot{m} U_e}{P_c A_t} + \frac{(P_e - P_a)}{P_c} \frac{A_e}{A_t} \tag{C.3}$$

Assuming frozen flow (constant γ), an ideal gas, and isentropic flow, the isentropic flow relations hold anywhere within the nozzle. For convenience, they are printed in Equations C.4 - C.6.

$$f(M) = \frac{A^*}{A} = \left(\frac{\gamma+1}{2}\right)^{\frac{\gamma+1}{2(\gamma-1)}} \frac{M}{\left(1 + \frac{\gamma-1}{2} M^2\right)^{\frac{\gamma+1}{2(\gamma-1)}}} \tag{C.4}$$

$$\frac{T_t}{T} = 1 + \frac{\gamma - 1}{2} M^2 \tag{C.5}$$

$$\frac{P_t}{P} = \left(1 + \frac{\gamma - 1}{2} M^2\right)^{\frac{\gamma}{\gamma-1}} \tag{C.6}$$

Now, recall that the mass flow rate in a nozzle is conserved. Then, $\dot{m} = \dot{m}_e$. Also, recall the mass flow rate of any fluid flow can be evaluated as $\dot{m} = \rho U A$. Therefore,

$$C_f = \frac{PUA}{RTP_c A_t} U_e + \frac{(P_e - P_a)}{P_c} \frac{A_e}{A_t} \tag{C.7}$$

Where the ideal gas law is used, $P = \rho RT$.

Now, recall that the flow velocity is related to the speed of sound and Mach number, $U = \sqrt{\gamma RT}M$. Therefore,

$$C_f = \frac{P}{P_c T}\sqrt{\gamma RT}M\frac{A}{A_t}\frac{U_e}{R} + \frac{(P_e - P_a)}{P_c}\frac{A_e}{A_t} \tag{C.8}$$

Now, substituting in the isentropic flow relations and evaluating the P, T, M, A terms at the exit plane of the nozzle, the equation becomes:

$$C_f = \frac{P_e}{P_c T_e}(\gamma T_e) M_e^2 \frac{1}{f(M_e)} + \frac{(P_e - P_a)}{P_c}\frac{A_e}{A_t} \tag{C.9}$$

With some algebra, this can be shown to be:

$$C_f = \frac{P_e}{P_c}\gamma M_e \left(\frac{2}{\gamma+1}\right)^{\frac{\gamma+1}{2(\gamma-1)}} \left(1 + \frac{\gamma-1}{2}M_e^2\right)^{\frac{\gamma+1}{2(\gamma-1)}} + \frac{(P_e - P_a)}{P_c}\frac{A_e}{A_t} \tag{C.10}$$

Now, solving for M_e in Equation C.6,

$$M = \sqrt{\frac{2}{\gamma-1}\left[\left(\frac{P_t}{P_e}\right)^{\frac{\gamma-1}{\gamma}} - 1\right]} \tag{C.11}$$

Substituting Equation C.11 into Equation C.10 and performing some algebraic manipulations finally results in the well-known specific thrust equation.

$$C_f = \sqrt{\frac{2\gamma^2}{\gamma-1}\left(\frac{2}{\gamma+1}\right)^{(\gamma+1)/(\gamma-1)}\left[1 - \left(\frac{P_e}{P_t}^{(\gamma-1)/\gamma}\right)\right]} + \left(\frac{P_a - P_e}{P_c}\right)\frac{A_e}{A_t} \tag{C.12}$$

Appendix D

Feed System Analysis

This chapter of the appendix describes the oxygen feed system and how the mass flow rate computations were conducted.

D.1 Major Feed System Features

The oxidizer feed system provides pressurized oxygen and nitrogen to two motors. The oxygen line is rated to 6.9 MPa and has provided flow rates up to 130 grams per second (for much lower chamber pressures). In this research, the highest flow rate used was 90 grams per second with a chamber pressure of 2.4 MPa, which the highest chamber pressure tested in the lab to date.

The oxygen is supplied by two T-type oxygen cylinders (part number OX-T from Praxair, purchased from the Stanford SmartMart system). The line pressure is regulated by a dome-loaded pressure regulator (Model 44-4019E212-108 from Tescom [53]). The dome-loaded pressure regulator actively controls the line pressure with a PID-type controller. The gains were experimentally determined with a previous student and are listed in Table D.1. In addition to the main valves that supply the motor, oxygen line also contains a vent valve, check valve, and a relief valve. These valves ensure that the system can safely be pressurized and can withstand an over-pressurization event. The check valve additionally protects the feed system components because it restricts the flow to only go in one direction.

Additionally, the feed system contains an E-stop button, which physically breaks the power connection to the main valve feeding the motor. In case of a fire in the motor, the E-stop would cut the oxygen to the motor and the fire would be starved of oxygen. Although the E-stop cuts the oxygen valve power, the rest of the system is still active and the system can safely be vented and depressurized in case of emergency.

The feed system itself is controlled through a LabView interface. For safety, all valves also have a manual switch that overrides the LabView interface. This ensures that control authority is present

Table D.1: The PID gains used for the dome-loaded pressure regulator.

Gain	**Value**
K_P	600
K_D	40
K_I	400

even if the computer or LabView software crashes.

Nitrogen is also supplied by the feed system. Although nitrogen is not used as a propellant in the motor, it is used to distinguish any residual flames in the motor after shutdown. The nitrogen line also has a vent valve, check valve, and a relief valve. However, the E-stop does not shut down the main valve for the nitrogen. This allows for the flow of nitrogen into the motor in case of emergency.

Figure D.1: The cylinders that supply the feed system are placed in the control room.

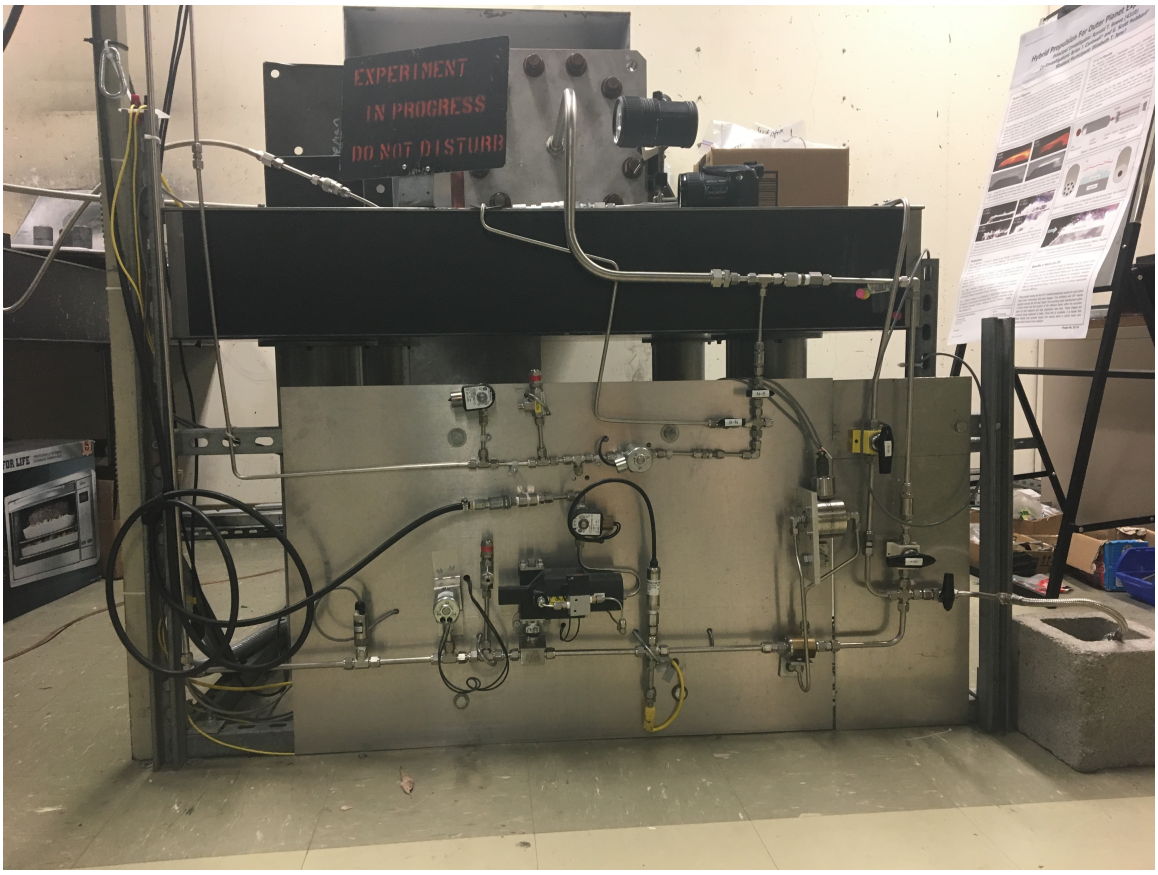

Figure D.2: The main feed system components are placed on a control panel in the test room.

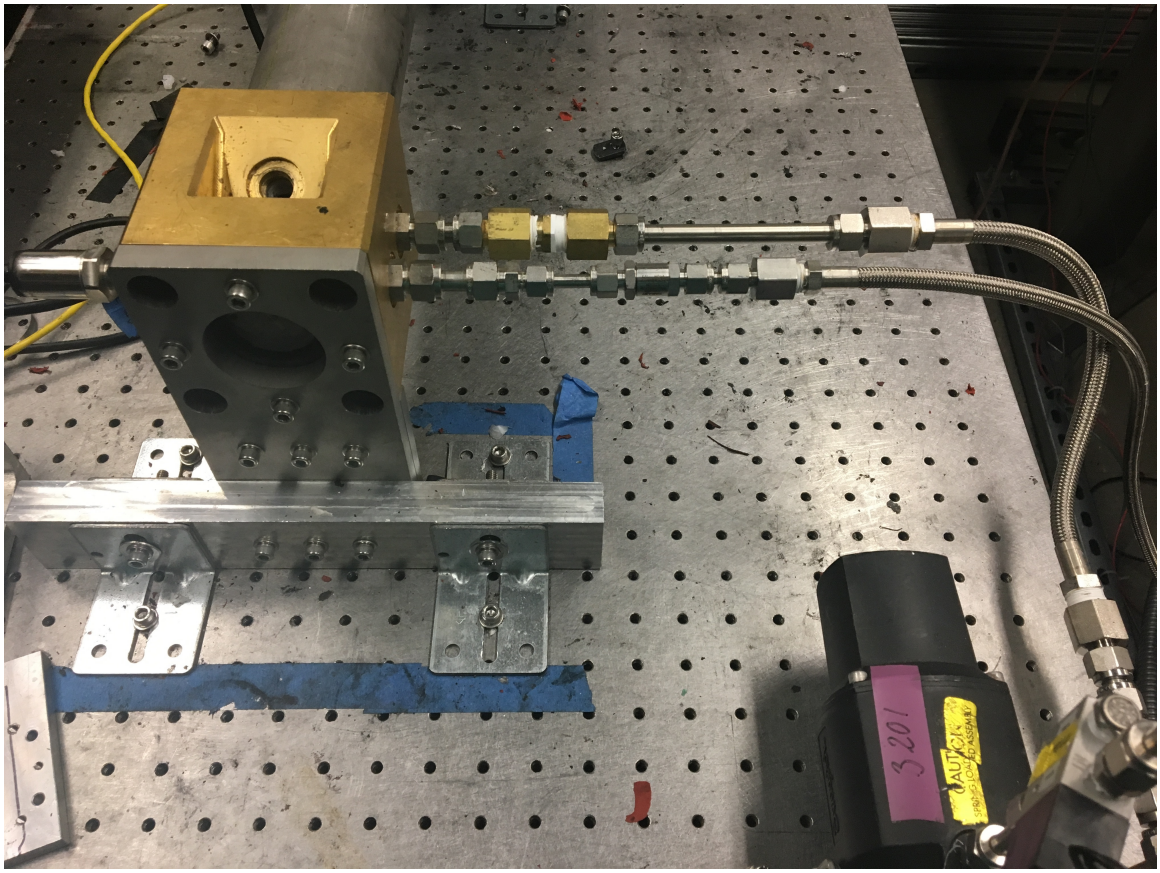

Figure D.3: The feed system supplies oxygen and nitrogen to the motor through two separate lines. The downstream line supplies oxygen, while the upstream line supplies nitrogen.

D.2 Feed System PID

The P&ID for the feed system is shown in Figure D.4 below. Note that the experimental motor is shown as Test 2.

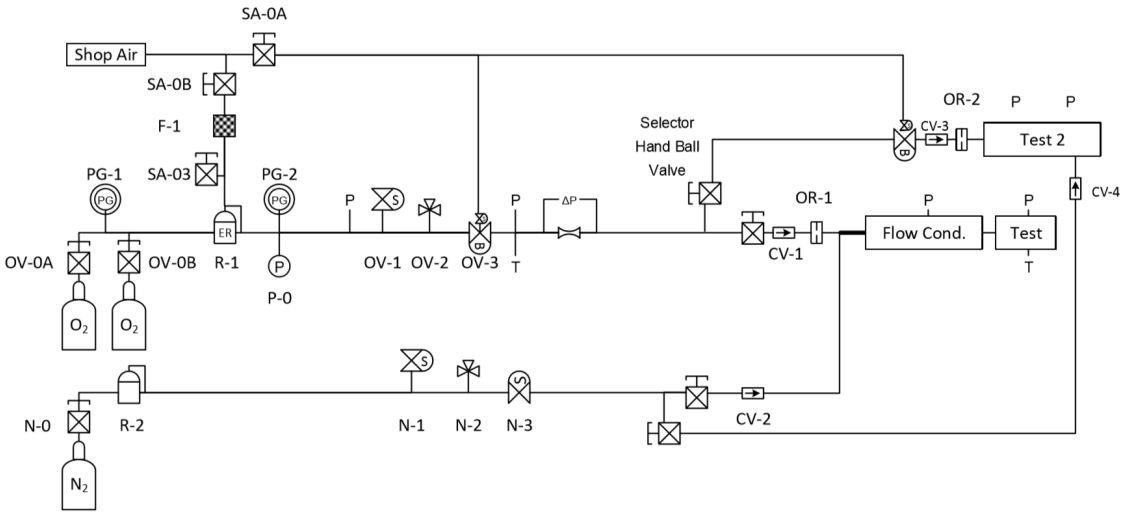

Figure D.4: P&ID of the feed system.

Table D.2: The feed system components and their descriptions.

Item	Description
OV-0A	Valve on oxygen cylinder
OV-0B	Valve on oxygen cylinder
R-1	Dome-loaded regulator for oxygen
R-2	Nitrogen regulator
OV-1	Oxygen vent valve
OV-2	Oxygen relief valve
OV-3	Main oxygen valve for visualization experiment
OV-4	Main valve for nozzle erosion motor
OR-1	Orifice in oxygen line for visualization experiment
OR-2	Orifice in oxygen line for nozzle erosion measurement
PG-1	Oxygen cylinder pressure gauge
PG-2	Feed line pressure gauge
P-O	Pressure transducer
P1	Pressure transducer upstream of OV-3
P2	Pressure transducer upstream section of Venturi
T2	Temperature sensor at upstream section of Venturi
DP-1	Differential pressure across Venturi
N-0	Valve on nitrogen cylinder
N-1	Nitrogen vent valve
N-2	Nitrogen relief valve
N-3	Nitrogen purge valve
CV-1	check valve for oxygen line on visualization experiment
CV-2	check valve for nitrogen line on visualization experiment
CV-3	check valve for oxygen line on nozzle erosion motor
CV-4	check valve for nitrogen line on nozzle erosion motor
SA-0A	Compressed air valve
F-1	Filter for shop air
SA-1	Compressed air valve
SA-2	Compressed air valve
SA-3	Compressed air valve

D.3 Mass Flow Rate calculations

The oxidizer mass flow rate through the feed system was computed using a flow Venturi that was originally made by previous students. This Venturi was made per ASME standards and calibration found that the discharge coefficient was 0.999 for the range of Reynolds numbers tested. The upstream diameter of the Venturi was 7.67mm and the throat section had a diameter of 5.97mm.

The mass flow rates were computed using the same equations as Reference [45]. They are reprinted here for convenience.

$$\dot{m} = C_d A_t \sqrt{\frac{\frac{2\gamma}{\gamma-1} P_u \rho_1 \left[\left(\frac{P_t}{P_u}\right)^{\frac{2}{\gamma}} - \left(\frac{P_t}{P_u}\right)^{\frac{\gamma+1}{\gamma}} \right]}{1 - \left(\frac{A_t}{A_u}\right)^2 \left(\frac{P_t}{P_u}\right)^{\frac{2}{\gamma}}}} \tag{D.1}$$

Here the subscript u denotes the upstream section of the Venturi, and the subscript t denotes the throat section of the Venturi. Alternatively, this could be written as:

$$\dot{m} = C_d Y A_t \sqrt{\frac{2\rho_1 \Delta P}{\left(1 - \frac{D_t}{D_u}\right)^4}} \tag{D.2}$$

Where

$$Y = \sqrt{\left(\frac{P_t}{P_u}\right)^{\frac{2}{\gamma}} \left(\frac{\gamma}{\gamma-1}\right) \left(\frac{1 - (\frac{P_t}{P_u})^{\frac{\gamma-1}{\gamma}}}{1 - \frac{P_t}{U_u}}\right) \left(\frac{1 - \left(\frac{D_t}{D_u}\right)^4}{1 - \left(\frac{D_t}{D_u}\right)^4 \left(\frac{P_t}{P_u}\right)^{\frac{2}{\gamma}}}\right)} \tag{D.3}$$

Appendix E

Experiment Manual

This section of the appendix provides all engineering drawings used to fabricated this experiment as well as instructions to assemble the parts as well. This appendix then concludes with a diagram showing the layout of the lab.

E.1 Experiment Drawings

Experiment drawings start on following page.

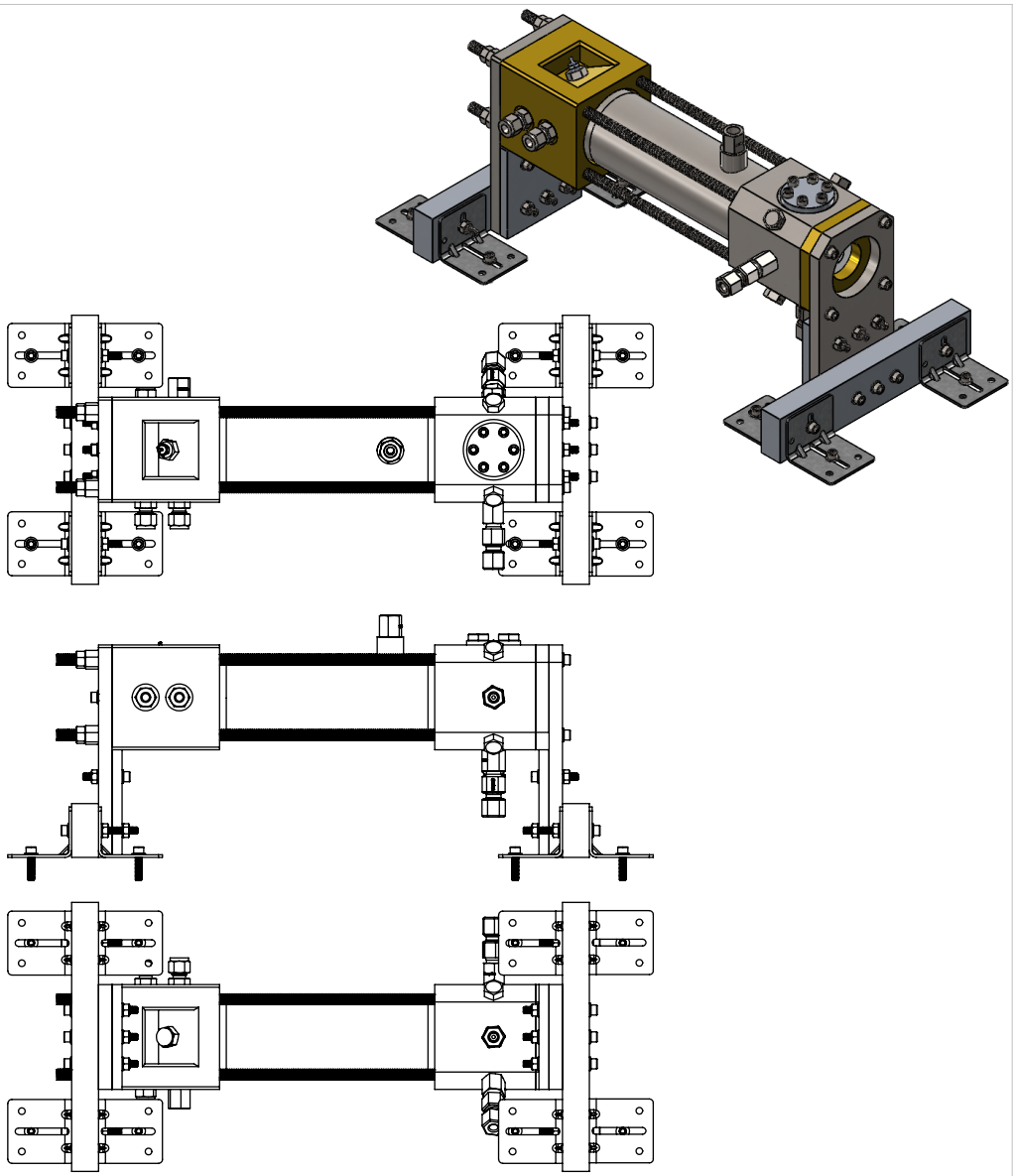

		UNLESS OTHERWISE SPECIFIED:		NAME	DATE
		DIMENSIONS ARE IN INCHES	DRAWN	PN	8/23/14
		TOLERANCES:	CHECKED		
		FRACTIONAL ±.005	ENG APPR.		
		ANGULAR: MACH ± BEND ±	MFG APPR.		
		TWO PLACE DECIMAL ±.005	Q.A.		
		THREE PLACE DECIMAL ±.0005	COMMENTS:		
		MATERIAL			
		FINISH			
NEXT ASSY	USED ON	Unfinished except where machined. Deburr all edges			
APPLICATION		DO NOT SCALE DRAWING			

Overall Assembly

SIZE	DWG. NO.	REV.
A		E
SCALE:1:5	WEIGHT:	SHEET 1 OF 4

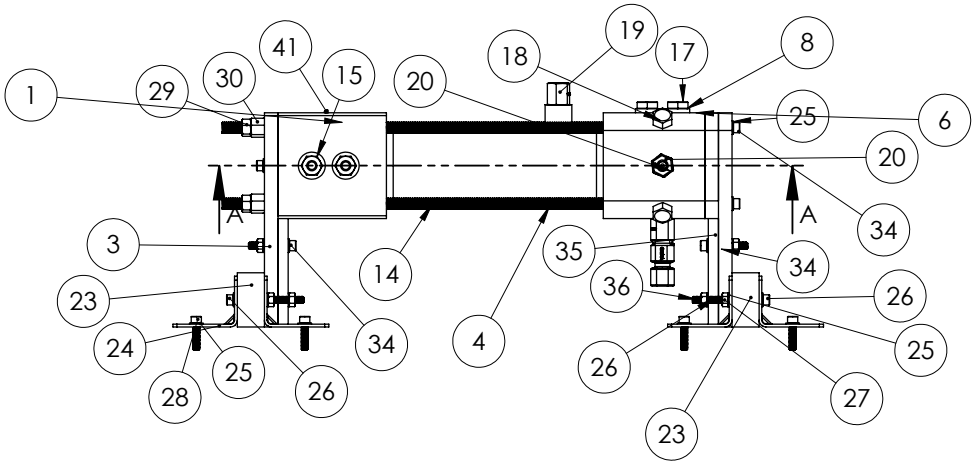

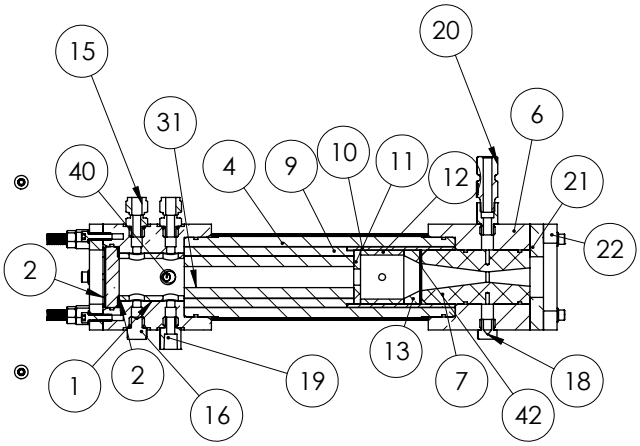

SECTION A-A

Raw Material Will be supplied.

		UNLESS OTHERWISE SPECIFIED:		NAME	DATE
		DIMENSIONS ARE IN INCHES	DRAWN	PN	8/23/14
		TOLERANCES:	CHECKED		
		FRACTIONAL ±.005	ENG APPR.		
		ANGULAR: MACH ± BEND ±	MFG APPR.		
		TWO PLACE DECIMAL ±.005	Q.A.		
		THREE PLACE DECIMAL ±.0005	COMMENTS:		
		MATERIAL			
NEXT ASSY	USED ON	FINISH Unfinished except where machined. Deburr all edges			
APPLICATION		DO NOT SCALE DRAWING			

Overall Assembly

SIZE	DWG. NO.	REV.
A		E
SCALE:1:5	WEIGHT:	SHEET 2 OF 4

ITEM NO.	PART NUMBER	DESCRIPTION	QTY.
1	ForeEnd	Alro Metals	1
2	siliconeWasher	McM 8525T41 in Lab	2
3	windowPlate	McM 8992K907	1
4	combustionChamber	McM 89495k83	1
5	bungFitting	McM 89325K24	1
6	aftEnd	Alro metals	1
7	Nozzle	Graphite Store GT001623	1
8	UltrasonicMountingBracketPlate	McM 8974K73	1
9	FuelInsulator	Franklin Fibre	1
10	AftInsulator	Franklin Fibre	1
11	mixer	McM 8560K355	1
12	postCombustionChamber	Graphite Store GT001646	1
13	preNozzle	Graphite Store GT001623	1
14	threaded rod	McM 93250A031	4
15	SS_600_1_6ST	SwageLok Fitting	2
16	SS_6_PST	SwageLok Fititng	2
17	92185A537	1/4"-20 x 1/2" Socket Cap Screw	6
18	ORBCapSS	Straight Thread Cap (-6)	4
19	ORBtoNPPF	Male MS Fitting to Female NPT	5
20	FeedThroughFitting	TCDirect.com	3
21	nozzleCoverPlate	Nozzle Hold Config, McM 8954K124	1
22	nozzleCoverPlate	Fixture Config, McM 8992K907	1
23	baseBlock	McM 8975K237	2
24	15275A63	L-Bracket	8
25	91525A117	SS. 1/4" Washer, .04-.06", 1/2" OD	48
26	92185A550	1/4"-20 x 2" Socket Cap Screw	4
27	94804A029	1/4"-20 Nut, 7/16" Width, 7/32" Height	16
28	92185A542	1/4"-20 x 1" Socket Cap Screw	8
29	94804A320	3/8"-16 Nut, 9/16" Width, 21/64 Height ,SS	4
30	91115A888	3/8"-16 Nut, 1" Long, 5/8" Hex Size	4
31	fuelGrain	Made in lab	1
32	91950A031	3/8" SS Washer, OD 13/16", .05.08" Thickn.	4
33	92185A541	1/4"-20 x 7/8" Socket Cap Screw	4
34	92185A546	1/4"-20 x 1+1/2" Socket Cap Screw	10
35	supportBlock	McMaster 8992K541	2
36	92185A555	1/4"-20 x 2+1/2" Socket Cap Screw	6
37	ForeEndInsulator	GraphiteStore GT001623	1
38	sapphireWindow	In Lab	1
39	IgniterFitting	Straight Thread Cap (-6)	1
40	secondarySlug	Made in Lab	1
41	Initiator	Modified From McCoy MC-59	1
42	combChamberSpacer	McMaster PN 8610K82	1

UNLESS OTHERWISE SPECIFIED:
DIMENSIONS ARE IN INCHES
TOLERANCES:
FRACTIONAL ± .005
ANGULAR: MACH ± BEND ±
TWO PLACE DECIMAL ± .005
THREE PLACE DECIMAL ± .0005
MATERIAL
FINISH
Unfinished except where machined. Deburr all edges
NEXT ASSY | USED ON
APPLICATION
DO NOT SCALE DRAWING

	NAME	DATE
DRAWN	PN	8/23/14
CHECKED		
ENG APPR.		
MFG APPR.		
Q.A.		
COMMENTS:		

Overall Assembly

SIZE A | DWG. NO. | REV. E
SCALE:1:5 | WEIGHT: | SHEET 3 OF 4

REVISIONS				
ZONE	REV.	DESCRIPTION	DATE	APPROVED
-	A	Creation	6/24/14	-
	B	Edited Entries for machine shops	7/23/14	
	C	Added annotation for hydrotest plate cover	8/18/14	
	D	Changed Name to overall assembly. Added descriptions for all components. Added all fixturing components.	9/17/14	
	E	Updated feed system components and igniters. Added combustion chamber spacer to assembly	5/10/16	

		UNLESS OTHERWISE SPECIFIED:		NAME	DATE
		DIMENSIONS ARE IN INCHES TOLERANCES: FRACTIONAL ±.005 ANGULAR: MACH ± BEND ± TWO PLACE DECIMAL ±.005 THREE PLACE DECIMAL ±.0005	DRAWN	PN	8/23/14
			CHECKED		
			ENG APPR.		
			MFG APPR.		
			Q.A.		
		MATERIAL	COMMENTS:		
		FINISH Unfinished except where machined. Deburr all edges			
NEXT ASSY	USED ON				
APPLICATION		DO NOT SCALE DRAWING			

Overall Assembly

SIZE	DWG. NO.	REV.
A		E
SCALE:1:5	WEIGHT:	SHEET 4 OF 4

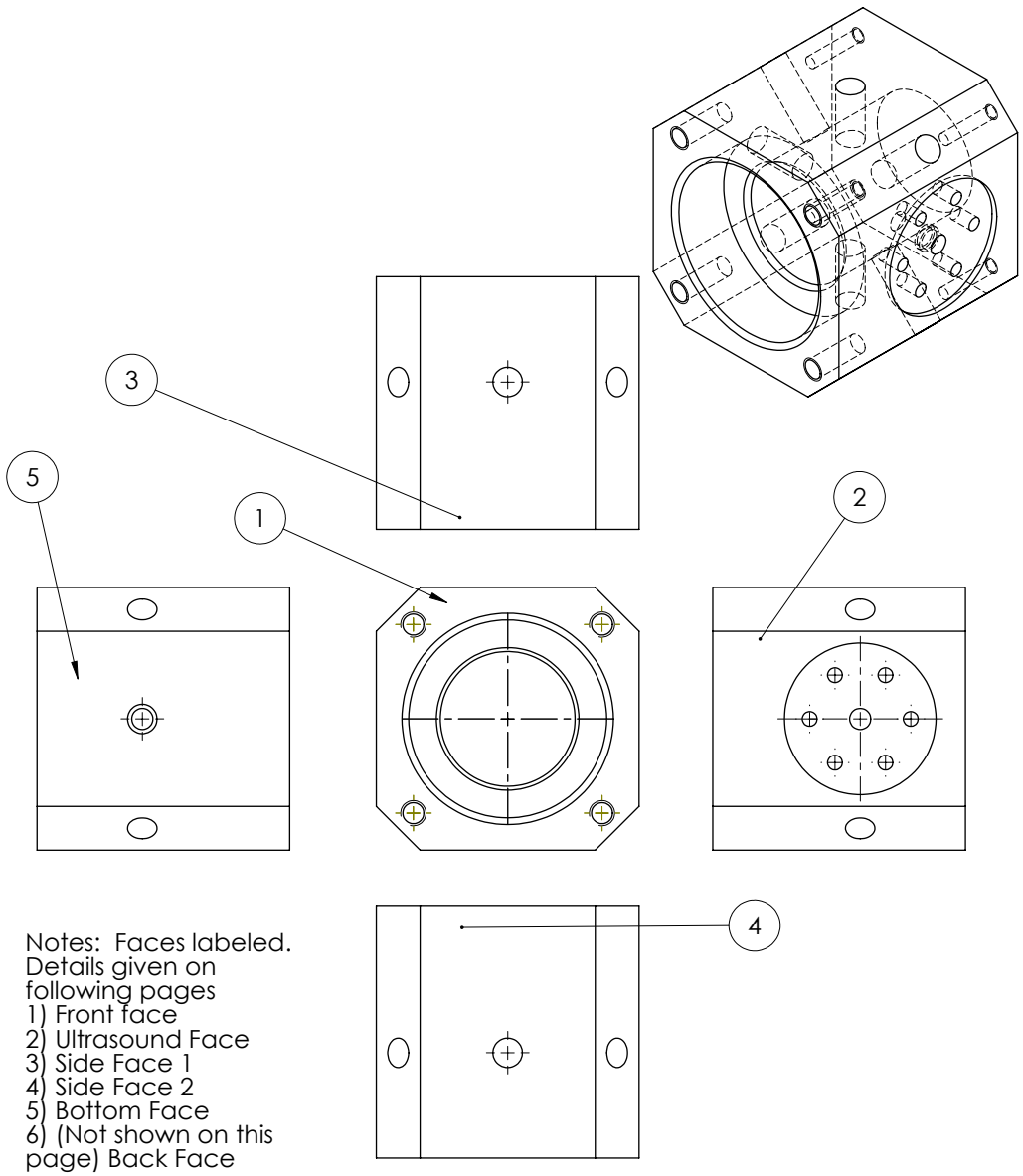

Notes: Faces labeled. Details given on following pages
1) Front face
2) Ultrasound Face
3) Side Face 1
4) Side Face 2
5) Bottom Face
6) (Not shown on this page) Back Face

				NAME	DATE
		UNLESS OTHERWISE SPECIFIED:			
		DIMENSIONS ARE IN INCHES	DRAWN	PN	6/24/2014
		TOLERANCES:	CHECKED		
		FRACTIONAL ± .005	ENG APPR.		
		ANGULAR: MACH ± BEND ±	MFG APPR.		
		TWO PLACE DECIMAL ± .005	Q.A.		
		THREE PLACE DECIMAL ± .0005	COMMENTS:		
		MATERIAL S.S. 316			
NEXT ASSY	USED ON	FINISH Unfinished except where machined. Deburr all edges			
APPLICATION		DO NOT SCALE DRAWING			

Aft End

SIZE	DWG. NO.	REV.
A		C
SCALE:1:2	WEIGHT:	SHEET 1 OF 7

(1) Front Face

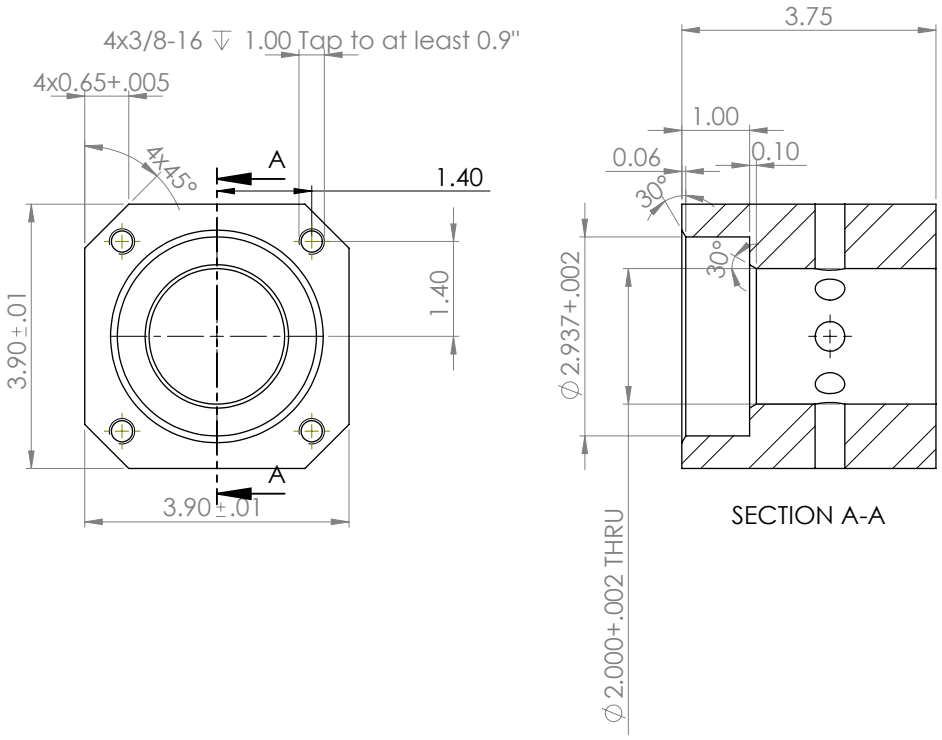

		UNLESS OTHERWISE SPECIFIED:		NAME	DATE
		DIMENSIONS ARE IN INCHES	DRAWN	PN	6/24/2014
		TOLERANCES:	CHECKED		
		FRACTIONAL ±.005	ENG APPR.		
		ANGULAR: MACH ± BEND ±	MFG APPR.		
		TWO PLACE DECIMAL ±.005	Q.A.		
		THREE PLACE DECIMAL ±.0005	COMMENTS:		
		MATERIAL S.S. 316			
NEXT ASSY	USED ON	FINISH Unfinished except where machined. Deburr all edges			
APPLICATION		DO NOT SCALE DRAWING			

Aft End

SIZE	DWG. NO.	REV.
A		C
SCALE:1:2	WEIGHT:	SHEET 2 OF 7

(2) Ultrasound Face

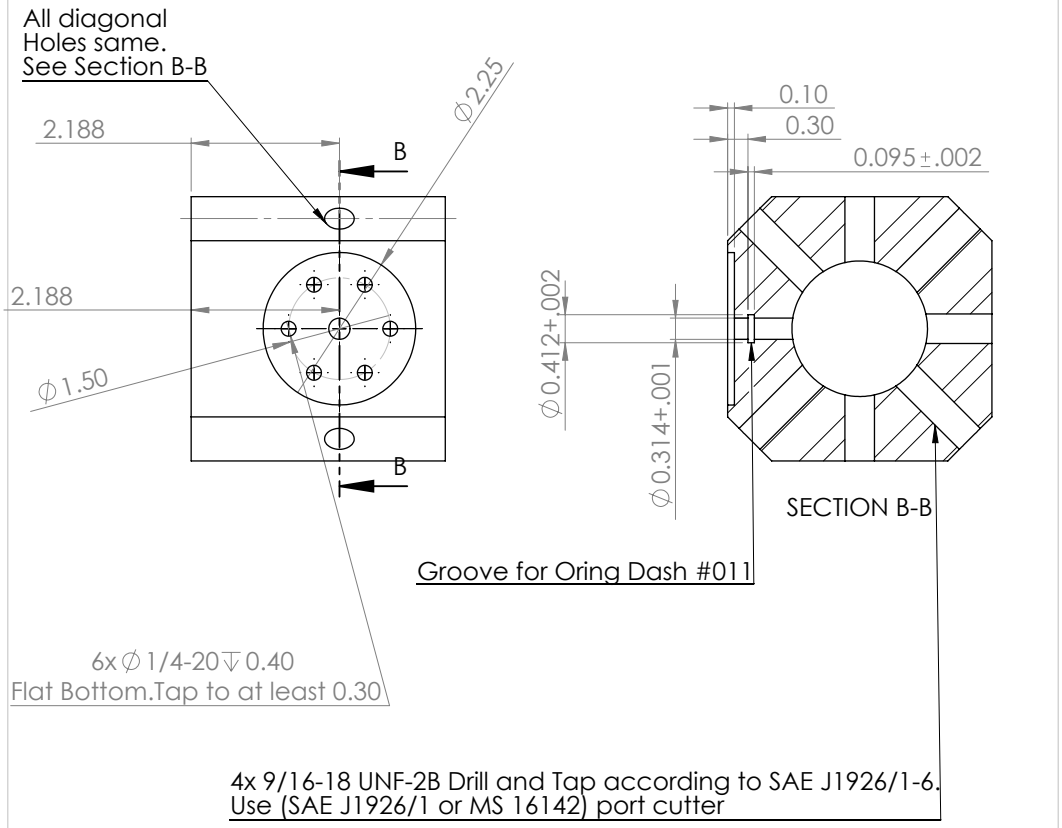

				NAME	DATE	
		UNLESS OTHERWISE SPECIFIED:				
		DIMENSIONS ARE IN INCHES	DRAWN	PN	6/24/2014	
		TOLERANCES:	CHECKED			
		FRACTIONAL ±.005	ENG APPR.			Aft End
		ANGULAR: MACH ± BEND ±	MFG APPR.			
		TWO PLACE DECIMAL ±.005	Q.A.			
		THREE PLACE DECIMAL ±.0005	COMMENTS:			
		MATERIAL S.S. 316				
NEXT ASSY	USED ON	FINISH Unfinished except where machined. Deburr all edges				SIZE A / DWG. NO. / REV. C
APPLICATION		DO NOT SCALE DRAWING				SCALE:1:2 / WEIGHT: / SHEET 3 OF 7

(3) Side Face 1

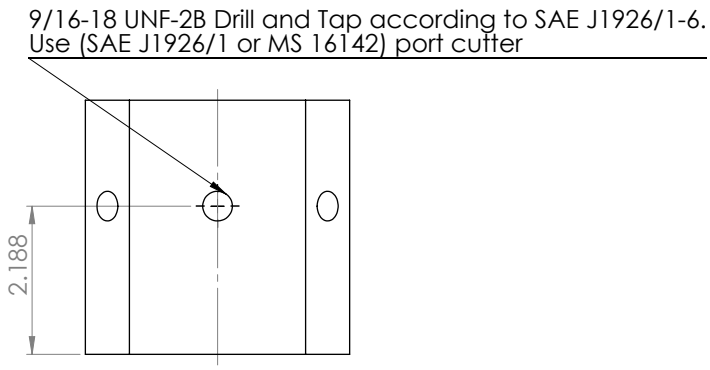

(4) Side Face 2

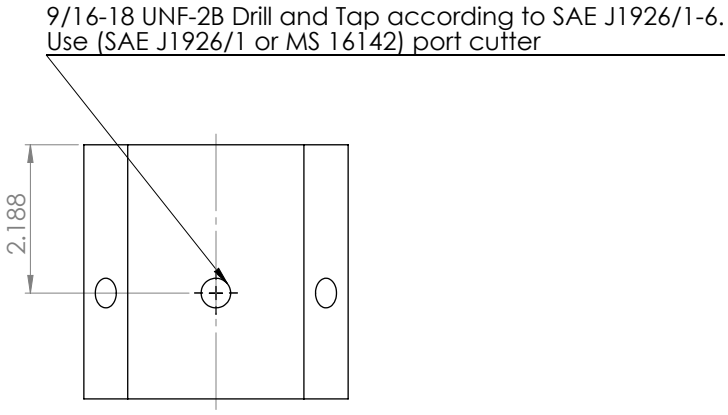

		UNLESS OTHERWISE SPECIFIED:		NAME	DATE
		DIMENSIONS ARE IN INCHES TOLERANCES: FRACTIONAL ±.005 ANGULAR: MACH ± BEND ± TWO PLACE DECIMAL ±.005 THREE PLACE DECIMAL ±.0005	DRAWN	PN	6/24/2014
			CHECKED		
			ENG APPR.		
			MFG APPR.		
			Q.A.		
		MATERIAL S.S. 316	COMMENTS:		
NEXT ASSY	USED ON	FINISH Unfinished except where machined. Deburr all edges			
APPLICATION		DO NOT SCALE DRAWING			

Aft End

SIZE	DWG. NO.	REV.
A		C
SCALE:1:2	WEIGHT:	SHEET 4 OF 7

(5) Bottom Face

9/16-18 UNF-2B Drill and Tap according to SAE J1926/1-6.
Use (SAE J1926/1 or MS 16142) port cutter

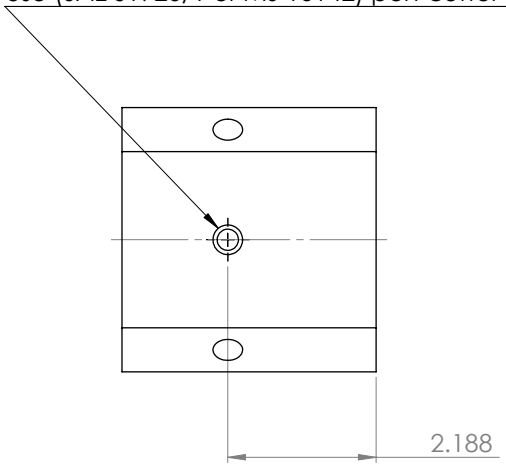

		UNLESS OTHERWISE SPECIFIED:		NAME	DATE
		DIMENSIONS ARE IN INCHES TOLERANCES: FRACTIONAL ±.005 ANGULAR: MACH ± BEND ± TWO PLACE DECIMAL ±.005 THREE PLACE DECIMAL ±.0005	DRAWN	PN	6/24/2014
			CHECKED		
			ENG APPR.		
			MFG APPR.		
			Q.A.		
		MATERIAL S.S. 316	COMMENTS:		
NEXT ASSY	USED ON	FINISH Unfinished except where machined. Deburr all edges			
APPLICATION		DO NOT SCALE DRAWING			

Aft End

SIZE	DWG. NO.	REV.
A		C
SCALE:1:2	WEIGHT:	SHEET 5 OF 7

(6) Back Face

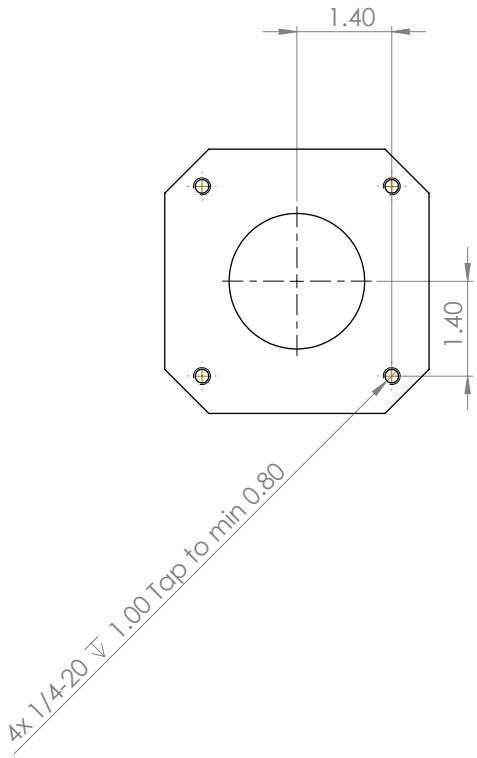

		UNLESS OTHERWISE SPECIFIED:		NAME	DATE
		DIMENSIONS ARE IN INCHES TOLERANCES: FRACTIONAL ± .005 ANGULAR: MACH ± BEND ± TWO PLACE DECIMAL ± .005 THREE PLACE DECIMAL ± .0005	DRAWN	PN	6/24/2014
			CHECKED		
			ENG APPR.		
			MFG APPR.		
			Q.A.		
		MATERIAL S.S. 316	COMMENTS:		
NEXT ASSY	USED ON	FINISH Unfinished except where machined. Deburr all edges			
APPLICATION		DO NOT SCALE DRAWING			

Aft End

SIZE	DWG. NO.	REV.
A		C
SCALE:1:2	WEIGHT:	SHEET 6 OF 7

REVISIONS				
ZONE	REV.	DESCRIPTION	DATE	APPROVED
-	A	Creation	6/24/14	-
	B	Added Chamfers for nozzle. Added thread lengths for blind holes	8/4/14	
	C	Removed back face, updated orings	8/18/14	
	D	Removed mounting holes	9/11/14	

		UNLESS OTHERWISE SPECIFIED:		NAME	DATE
		DIMENSIONS ARE IN INCHES TOLERANCES: FRACTIONAL ±.005 ANGULAR: MACH ± BEND ± TWO PLACE DECIMAL ±.005 THREE PLACE DECIMAL ±.0005	DRAWN	PN	6/24/2014
			CHECKED		
			ENG APPR.		
			MFG APPR.		
			Q.A.		
		MATERIAL S.S. 316	COMMENTS:		
NEXT ASSY	USED ON	FINISH Unfinished except where machined. Deburr all edges			
APPLICATION		DO NOT SCALE DRAWING			

Aft End

SIZE	DWG. NO.	REV.
A		C
SCALE:1:2	WEIGHT:	SHEET 7 OF 7

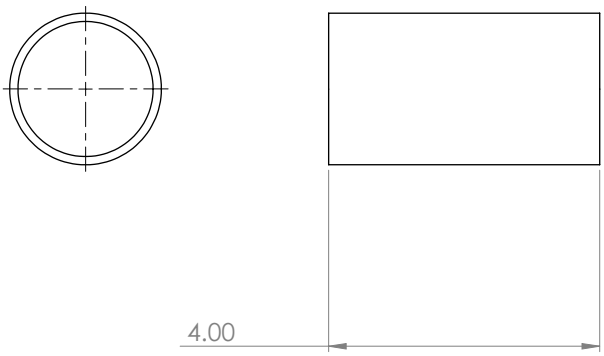

Note:
1) Self Machined
2) Raw Material from Franklin Fiber

		UNLESS OTHERWISE SPECIFIED:		NAME	DATE
		DIMENSIONS ARE IN INCHES TOLERANCES: FRACTIONAL ±.005 ANGULAR: MACH ± BEND ± TWO PLACE DECIMAL ±.005 THREE PLACE DECIMAL ±.0005	DRAWN	PN	9/18/14
			CHECKED		
			ENG APPR.		
			MFG APPR.		
			Q.A.		
		MATERIAL Phenolic	COMMENTS:		
NEXT ASSY	USED ON	FINISH Unfinished except where machined. Deburr all edges			
APPLICATION		DO NOT SCALE DRAWING			

Aft Insulator

SIZE	DWG. NO.	REV.
A		A
SCALE:1:2	WEIGHT:	SHEET 1 OF 1

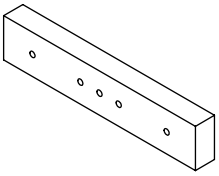

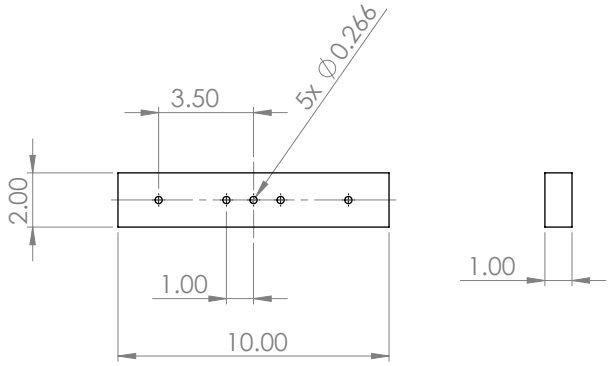

		UNLESS OTHERWISE SPECIFIED:		NAME	DATE
		DIMENSIONS ARE IN INCHES TOLERANCES: FRACTIONAL ± .005 ANGULAR: MACH ± BEND ± TWO PLACE DECIMAL ± .005 THREE PLACE DECIMAL ± .0005	DRAWN	PN	9/17/14
			CHECKED		
			ENG APPR.		
			MFG APPR.		
			Q.A.		
		MATERIAL Al 6061	COMMENTS:		
NEXT ASSY	USED ON	FINISH Unfinished except where machined. Deburr all edges			
APPLICATION		DO NOT SCALE DRAWING			

Base Block

SIZE	DWG. NO.	REV.
A		A

SCALE:1:5	WEIGHT:	SHEET 1 OF 1

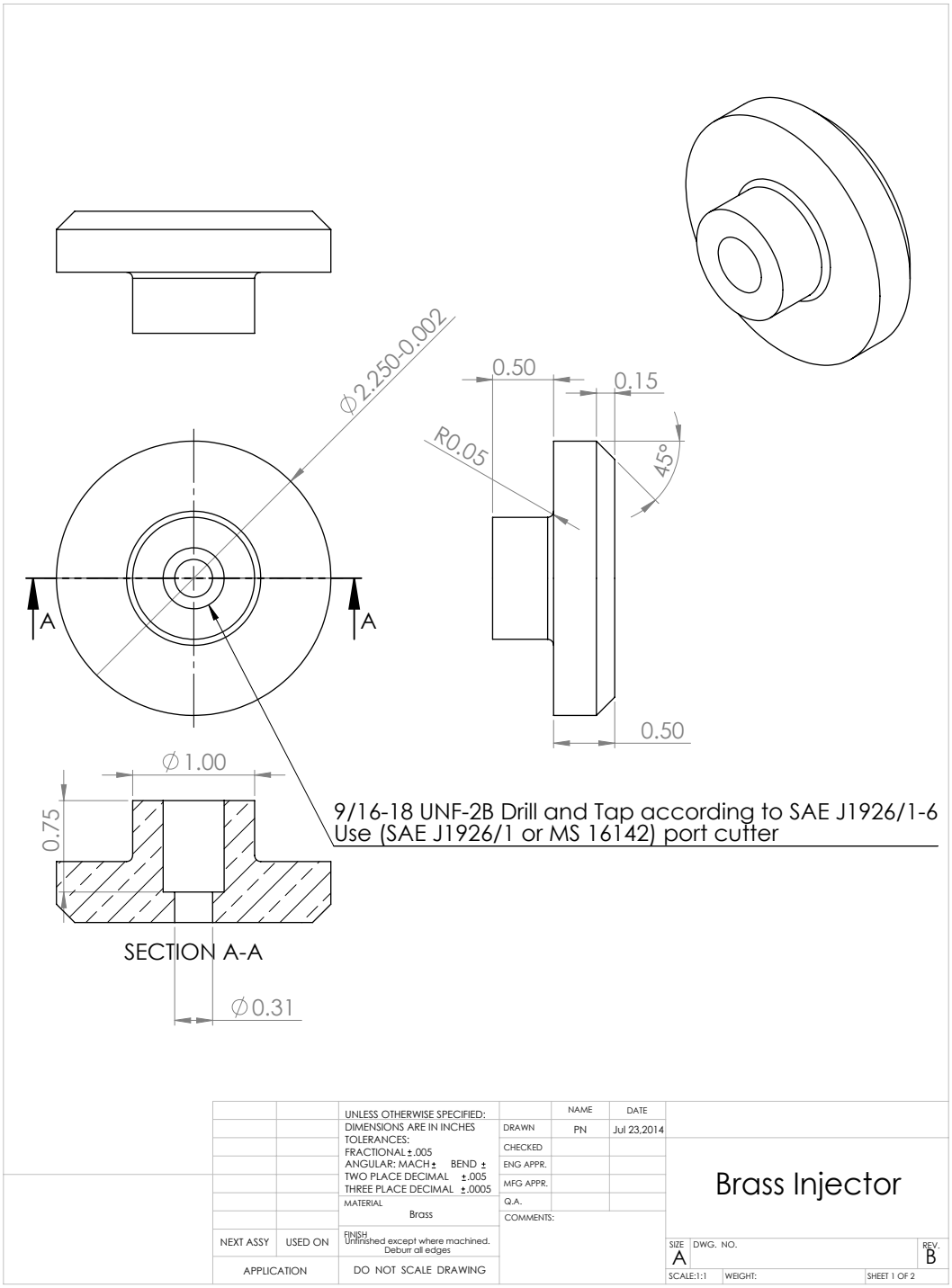

		UNLESS OTHERWISE SPECIFIED:		NAME	DATE
		DIMENSIONS ARE IN INCHES TOLERANCES: FRACTIONAL ±.005 ANGULAR: MACH ± BEND ± TWO PLACE DECIMAL ±.005 THREE PLACE DECIMAL ±.0005	DRAWN	PN	Jul 23,2014
			CHECKED		
			ENG APPR.		
			MFG APPR.		
			Q.A.		
		MATERIAL Brass	COMMENTS:		
NEXT ASSY	USED ON	FINISH Unfinished except where machined. Deburr all edges			
APPLICATION		DO NOT SCALE DRAWING			

Brass Injector

SIZE	DWG. NO.	REV.
A		B
SCALE:1:1	WEIGHT:	SHEET 1 OF 2

REVISIONS				
ZONE	REV.	DESCRIPTION	DATE	APPROVED
-	A	Creation	7/23/14	-
	B	Added Chamfer and Fillet	9/17/14	

		UNLESS OTHERWISE SPECIFIED:		NAME	DATE
		DIMENSIONS ARE IN INCHES TOLERANCES: FRACTIONAL ±.005 ANGULAR: MACH ± BEND ± TWO PLACE DECIMAL ±.005 THREE PLACE DECIMAL ±.0005	DRAWN	PN	Jul 23,2014
			CHECKED		
			ENG APPR.		
			MFG APPR.		
			Q.A.		
		MATERIAL Brass	COMMENTS:		
NEXT ASSY	USED ON	FINISH Unfinished except where machined. Deburr all edges			
APPLICATION		DO NOT SCALE DRAWING			

Brass Injector

SIZE	DWG. NO.	REV.
A		B
SCALE:1:1	WEIGHT:	SHEET 2 OF 2

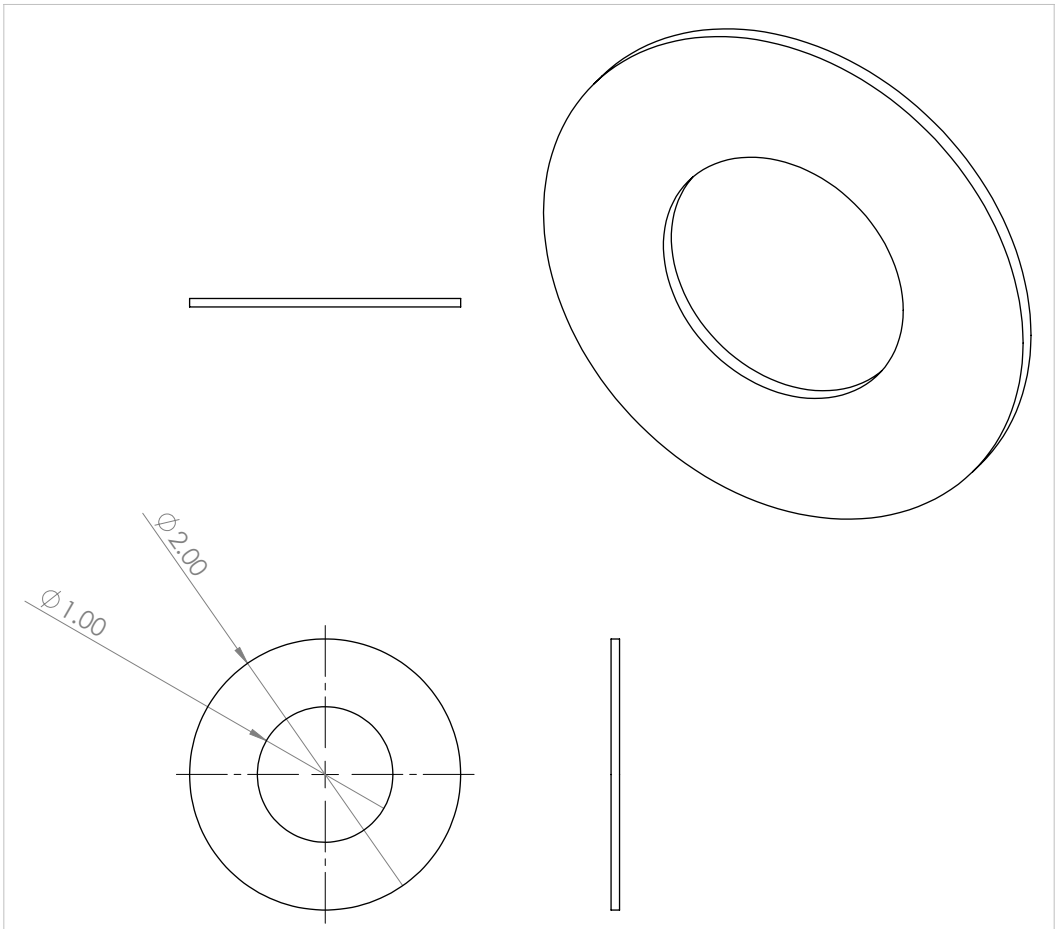

1) Made from McMaster P/N: 8610K82
2) Ok to cut with scissors

		UNLESS OTHERWISE SPECIFIED:		NAME	DATE
		DIMENSIONS ARE IN INCHES TOLERANCES: FRACTIONAL ±.005 ANGULAR: MACH ± BEND ± TWO PLACE DECIMAL ±.005 THREE PLACE DECIMAL ±.0005	DRAWN	PN	9/17/14
			CHECKED		
			ENG APPR.		
			MFG APPR.		
			Q.A.		
		MATERIAL EPDM	COMMENTS:		
NEXT ASSY	USED ON	FINISH Unfinished except where machined. Deburr all edges			
APPLICATION		DO NOT SCALE DRAWING			

ChamberSpacer

SIZE	DWG. NO.	REV.
A		A
SCALE:2:1	WEIGHT:	SHEET 1 OF 1

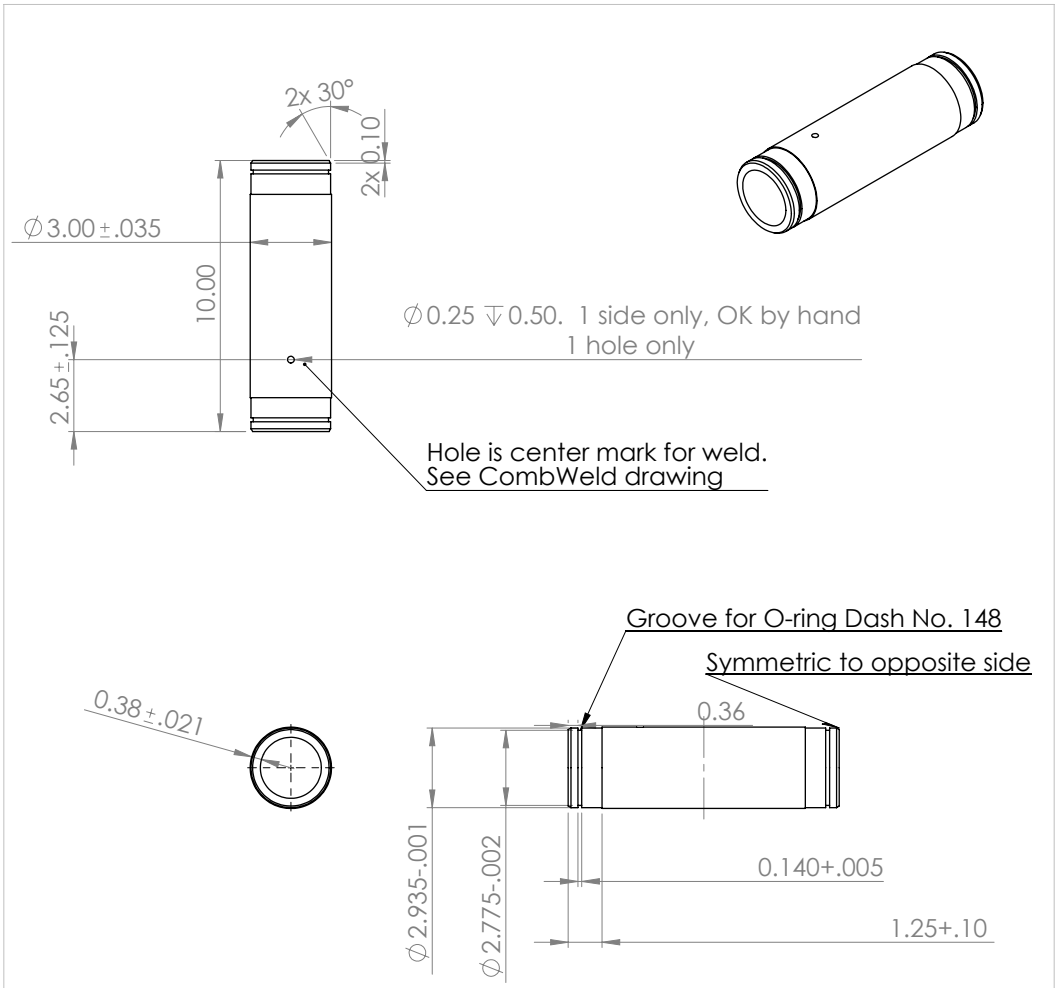

Notes:
1) Raw material sourced from McMasterCar. See below
2) Debur all edges
3) See "ChamberWeld" Drawing

		UNLESS OTHERWISE SPECIFIED:		NAME	DATE
		DIMENSIONS ARE IN INCHES TOLERANCES: FRACTIONAL ±.005 ANGULAR: MACH ± BEND ± TWO PLACE DECIMAL ±.005 THREE PLACE DECIMAL ±.0005	DRAWN	PN	6/24/14
			CHECKED		
			ENG APPR.		
			MFG APPR.		
			Q.A.		
		MATERIAL S.S. 316	COMMENTS:		
NEXT ASSY	USED ON	FINISH Unfinished except where machined. Deburr all edges			
APPLICATION		DO NOT SCALE DRAWING			

Combustion Chamber

SIZE	DWG. NO.	REV.
A		C
SCALE:1:5	WEIGHT:	SHEET 1 OF 2

REVISIONS				
ZONE	REV.	DESCRIPTION	DATE	APPROVED
-	A	Creation	6/24/14	-
	B	Changed material to S.S. 316	7/23/14	
	C	Added comment for one hole only	8/4/14	
	D	Updated grooves for orings	8/18/14	

		UNLESS OTHERWISE SPECIFIED:		NAME	DATE
		DIMENSIONS ARE IN INCHES TOLERANCES: FRACTIONAL ± .005 ANGULAR: MACH ± BEND ± TWO PLACE DECIMAL ± .005 THREE PLACE DECIMAL ± .0005	DRAWN	PN	6/24/14
			CHECKED		
			ENG APPR.		
			MFG APPR.		
			Q.A.		
		MATERIAL S.S. 316	COMMENTS:		
NEXT ASSY	USED ON	FINISH Unfinished except where machined. Deburr all edges	Combustion Chamber		
APPLICATION		DO NOT SCALE DRAWING	SIZE A	DWG. NO.	REV. C
			SCALE:1:5	WEIGHT:	SHEET 2 OF 2

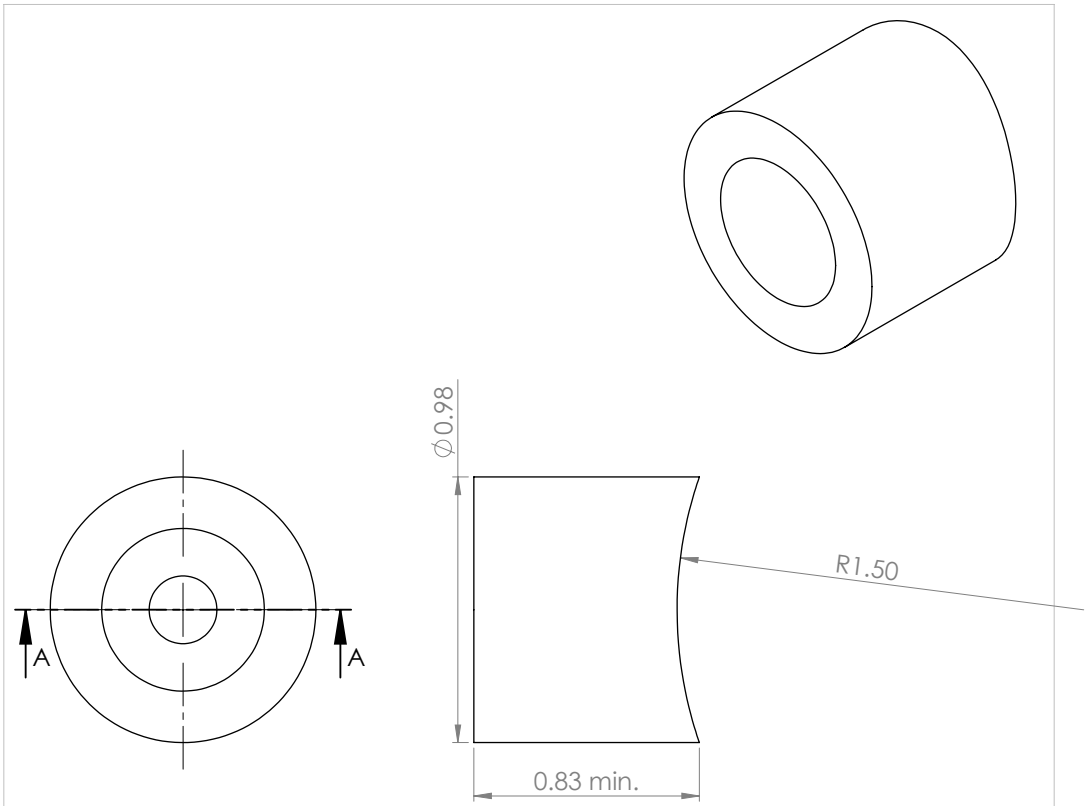

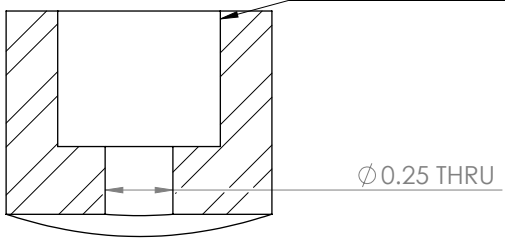

SECTION A-A

		UNLESS OTHERWISE SPECIFIED:		NAME	DATE
		DIMENSIONS ARE IN INCHES	DRAWN	PN	6/24/14
		TOLERANCES:	CHECKED		
		FRACTIONAL ±.005	ENG APPR.		
		ANGULAR: MACH ± BEND ±	MFG APPR.		
		TWO PLACE DECIMAL ±.005	Q.A.		
		THREE PLACE DECIMAL ±.0005	COMMENTS:		
		MATERIAL S.S. 316			
NEXT ASSY	USED ON	FINISH Unfinished except where machined. Deburr all edges			
APPLICATION		DO NOT SCALE DRAWING			

Bung Fitting

SIZE	DWG. NO.	REV.
A		C
SCALE:2:1	WEIGHT:	SHEET 1 OF 2

REVISIONS				
ZONE	REV.	DESCRIPTION	DATE	APPROVED
-	A	Creation	6/24/14	-
	B	Edited Material to S.S. 316	7/23/14	
	C	Added thread depth for MS port fitting	8/19/14	

		UNLESS OTHERWISE SPECIFIED:		NAME	DATE
		DIMENSIONS ARE IN INCHES TOLERANCES: FRACTIONAL ± .005 ANGULAR: MACH ± BEND ± TWO PLACE DECIMAL ± .005 THREE PLACE DECIMAL ± .0005	DRAWN	PN	6/24/14
			CHECKED		
			ENG APPR.		
			MFG APPR.		
			Q.A.		
		MATERIAL S.S. 316	COMMENTS:		
NEXT ASSY	USED ON	FINISH Unfinished except where machined. Deburr all edges			
APPLICATION		DO NOT SCALE DRAWING			

Bung Fitting

SIZE	DWG. NO.	REV.
A		C
SCALE:2:1	WEIGHT:	SHEET 2 OF 2

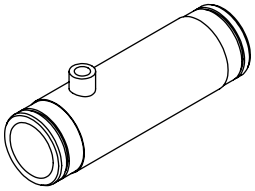

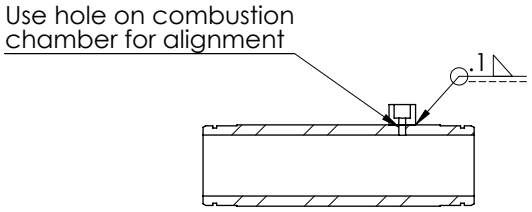

SECTION A-A

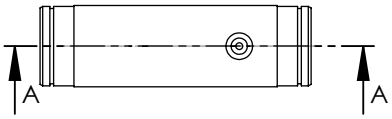

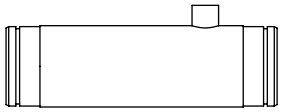

		UNLESS OTHERWISE SPECIFIED:		NAME	DATE
		DIMENSIONS ARE IN INCHES TOLERANCES: FRACTIONAL ± .005 ANGULAR: MACH ± BEND ± TWO PLACE DECIMAL ± .005 THREE PLACE DECIMAL ± .0005	DRAWN	PN	6/24/2014
			CHECKED		
			ENG APPR.		
			MFG APPR.		
			Q.A.		
		MATERIAL	COMMENTS:		
NEXT ASSY	USED ON	FINISH Unfinished except where machined. Deburr all edges.			
APPLICATION		DO NOT SCALE DRAWING			

combWeld

SIZE	DWG. NO.	REV.
A		A

SCALE:1:5 WEIGHT: SHEET 1 OF 1

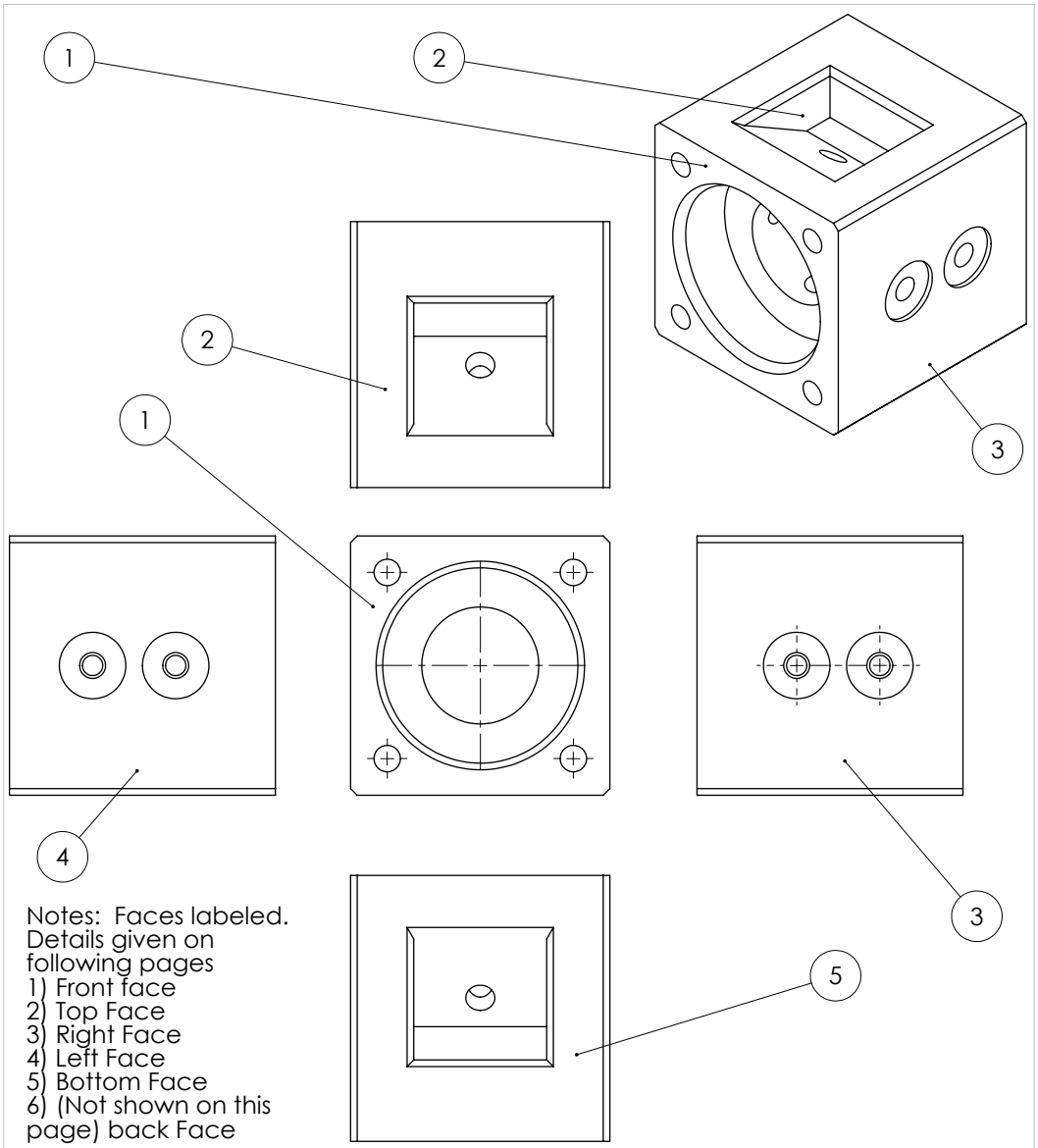

Notes: Faces labeled.
Details given on
following pages
1) Front face
2) Top Face
3) Right Face
4) Left Face
5) Bottom Face
6) (Not shown on this
page) back Face

All helicoils inserted are
S.S. 18-8 (Supplied)

		UNLESS OTHERWISE SPECIFIED:		NAME	DATE
		DIMENSIONS ARE IN INCHES TOLERANCES: FRACTIONAL ±.005 ANGULAR: MACH ± BEND ± TWO PLACE DECIMAL ±.005 THREE PLACE DECIMAL ±.0005	DRAWN	PN	6/24/14
			CHECKED		
			ENG APPR.		
			MFG APPR.		
			Q.A.		
		MATERIAL Brass	COMMENTS:		
NEXT ASSY	USED ON	FINISH Unfinished except where machined. Deburr all edges			
APPLICATION		DO NOT SCALE DRAWING			

Fore End Cap

SIZE	DWG. NO.	REV.
A		H
SCALE:1:2	WEIGHT:	SHEET 1 OF 8

(1) Front Face

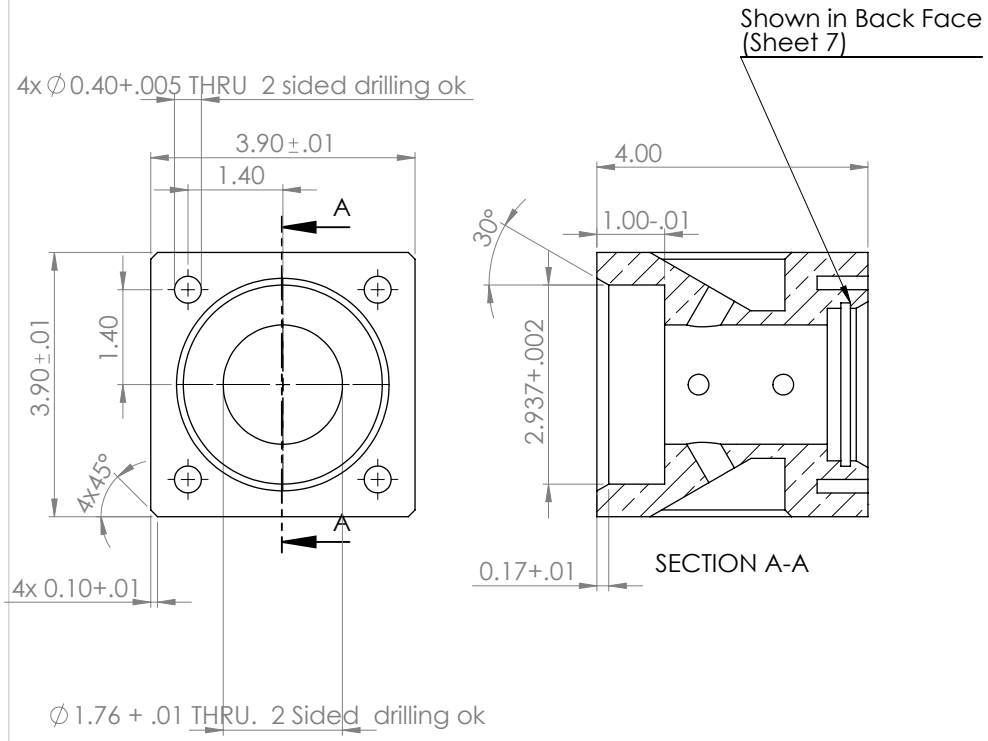

		UNLESS OTHERWISE SPECIFIED:		NAME	DATE
		DIMENSIONS ARE IN INCHES TOLERANCES: FRACTIONAL ± .005 ANGULAR: MACH ± BEND ± TWO PLACE DECIMAL ± .005 THREE PLACE DECIMAL ± .0005	DRAWN	PN	6/24/14
			CHECKED		
			ENG APPR.		
			MFG APPR.		
			Q.A.		
		MATERIAL Brass	COMMENTS:		
NEXT ASSY	USED ON	FINISH Unfinished except where machined. Deburr all edges			
APPLICATION		DO NOT SCALE DRAWING			

Fore End Cap

SIZE	DWG. NO.	REV.
A		H
SCALE:1:2	WEIGHT:	SHEET 2 OF 8

(2) Top Face

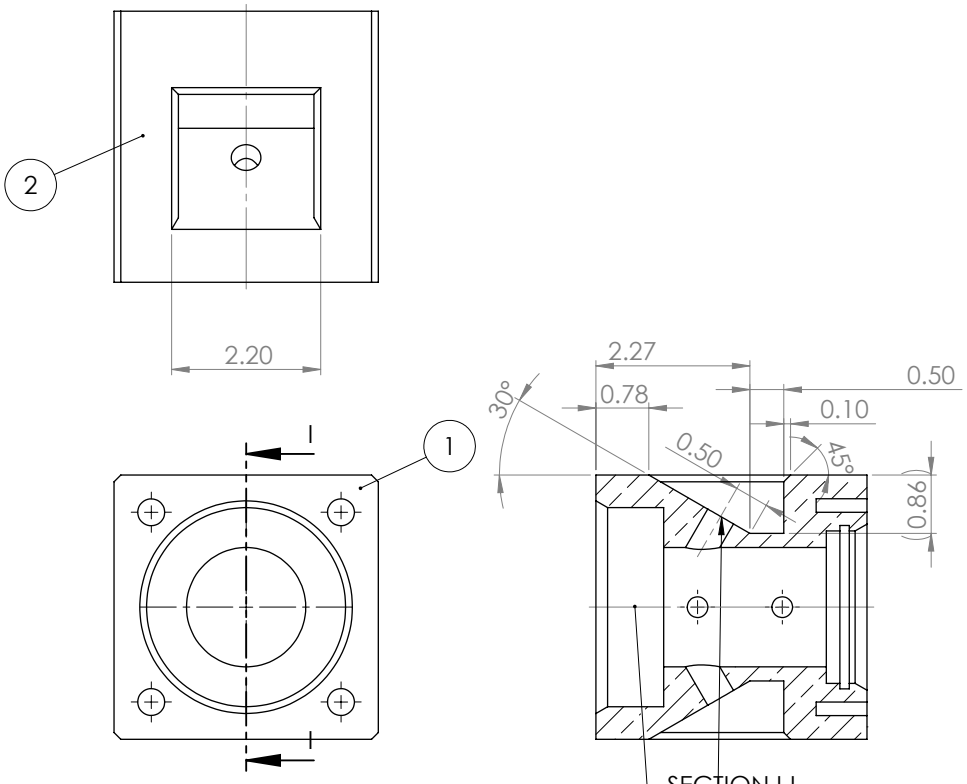

		UNLESS OTHERWISE SPECIFIED:		NAME	DATE
		DIMENSIONS ARE IN INCHES TOLERANCES: FRACTIONAL ±.005 ANGULAR: MACH ± BEND ± TWO PLACE DECIMAL ±.005 THREE PLACE DECIMAL ±.0005	DRAWN	PN	6/24/14
			CHECKED		
			ENG APPR.		
			MFG APPR.		
			Q.A.		
		MATERIAL Brass	COMMENTS:		
NEXT ASSY	USED ON	FINISH Unfinished except where machined. Deburr all edges			
APPLICATION		DO NOT SCALE DRAWING			

Fore End Cap

SIZE	DWG. NO.	REV.
A		H
SCALE:1:2	WEIGHT:	SHEET 3 OF 8

(3) Right Face

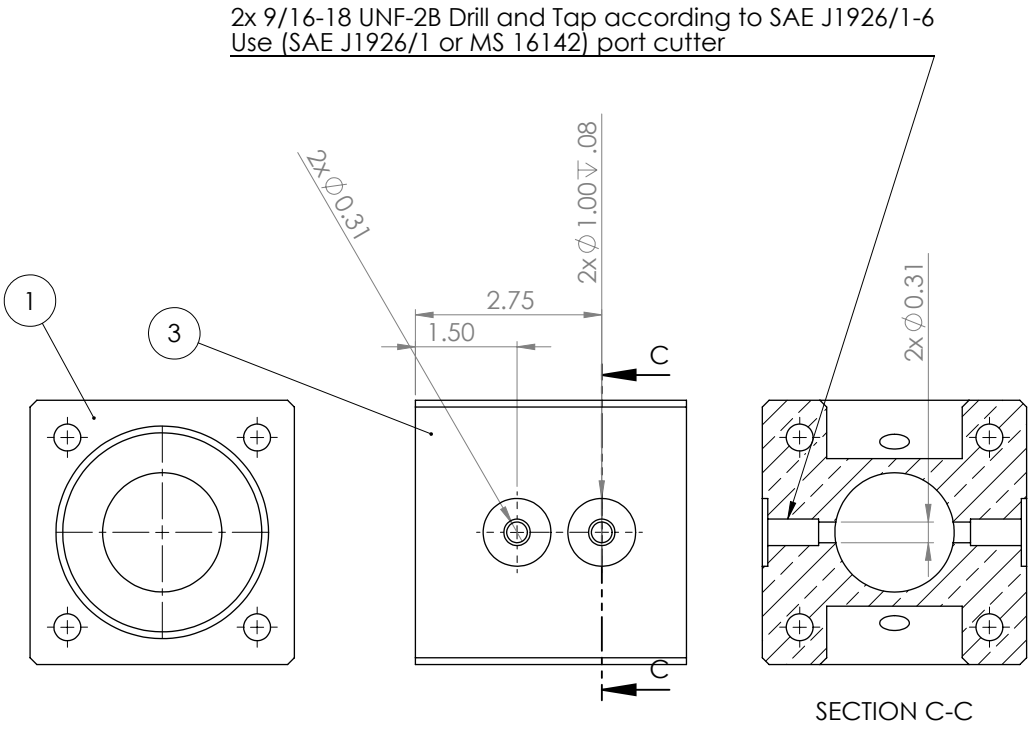

		UNLESS OTHERWISE SPECIFIED:		NAME	DATE
		DIMENSIONS ARE IN INCHES TOLERANCES: FRACTIONAL ±.005 ANGULAR: MACH ± BEND ± TWO PLACE DECIMAL ±.005 THREE PLACE DECIMAL ±.0005	DRAWN	PN	6/24/14
			CHECKED		
			ENG APPR.		
			MFG APPR.		
			Q.A.		
		MATERIAL Brass	COMMENTS:		
NEXT ASSY	USED ON	FINISH Unfinished except where machined. Deburr all edges			
APPLICATION		DO NOT SCALE DRAWING			

Fore End Cap

SIZE	DWG. NO.	REV.
A		H
SCALE:1:2	WEIGHT:	SHEET 4 OF 8

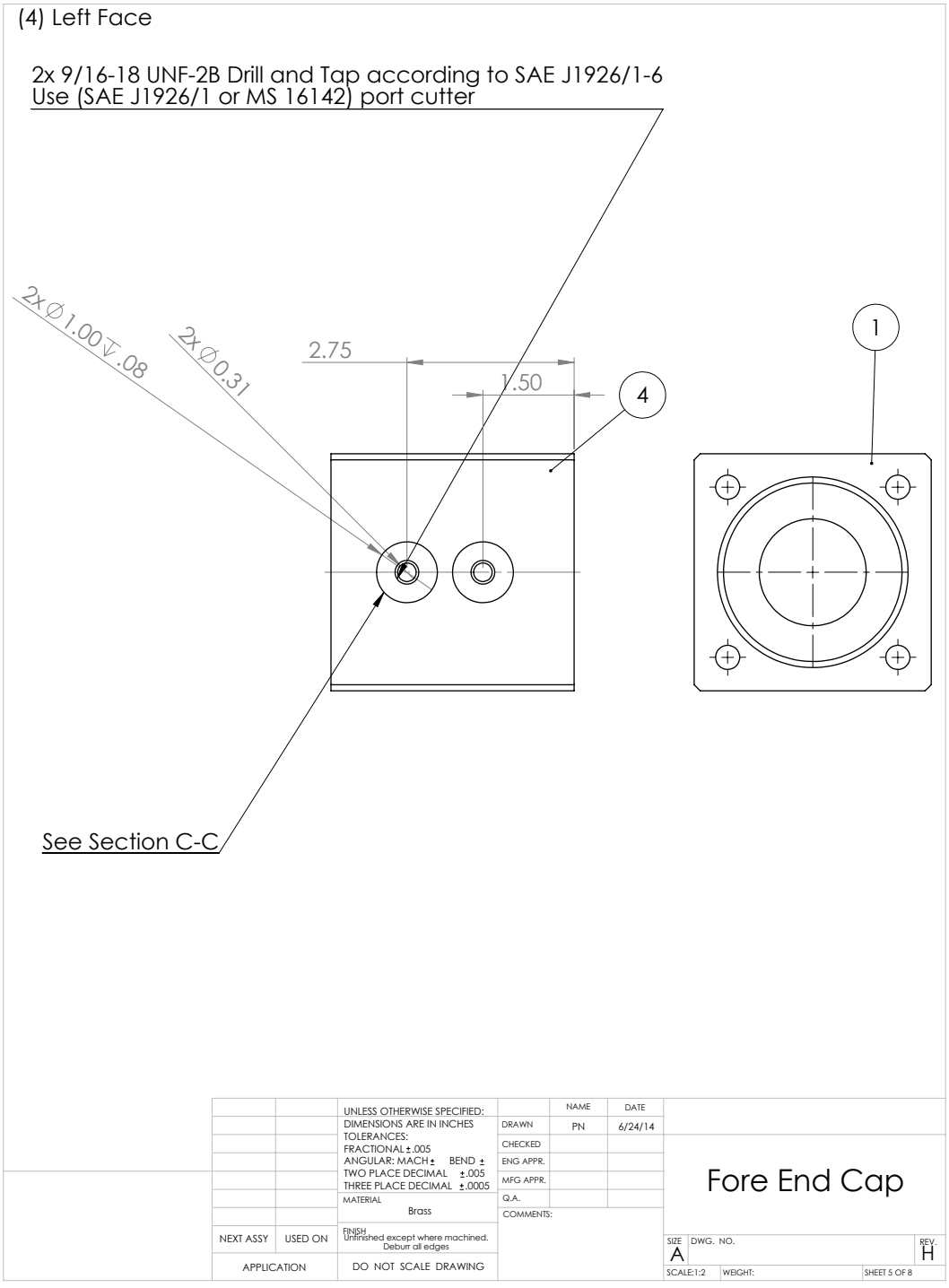
(4) Left Face
2x 9/16-18 UNF-2B Drill and Tap according to SAE J1926/1-6
Use (SAE J1926/1 or MS 16142) port cutter
2x⌀1.00⌽.08
2x⌀0.31
2.75
1.50
4
1
See Section C-C
UNLESS OTHERWISE SPECIFIED:
DIMENSIONS ARE IN INCHES
TOLERANCES:
FRACTIONAL ±.005
ANGULAR: MACH ± BEND ±
TWO PLACE DECIMAL ±.005
THREE PLACE DECIMAL ±.0005
MATERIAL
Brass
FINISH
Unfinished except where machined.
Deburr all edges
DO NOT SCALE DRAWING
NAME
DATE
DRAWN
PN
6/24/14
CHECKED
ENG APPR.
MFG APPR.
Q.A.
COMMENTS:
NEXT ASSY
USED ON
APPLICATION
Fore End Cap
SIZE
A
DWG. NO.
REV.
H
SCALE:1:2
WEIGHT:
SHEET 5 OF 8

(5) Bottom Face

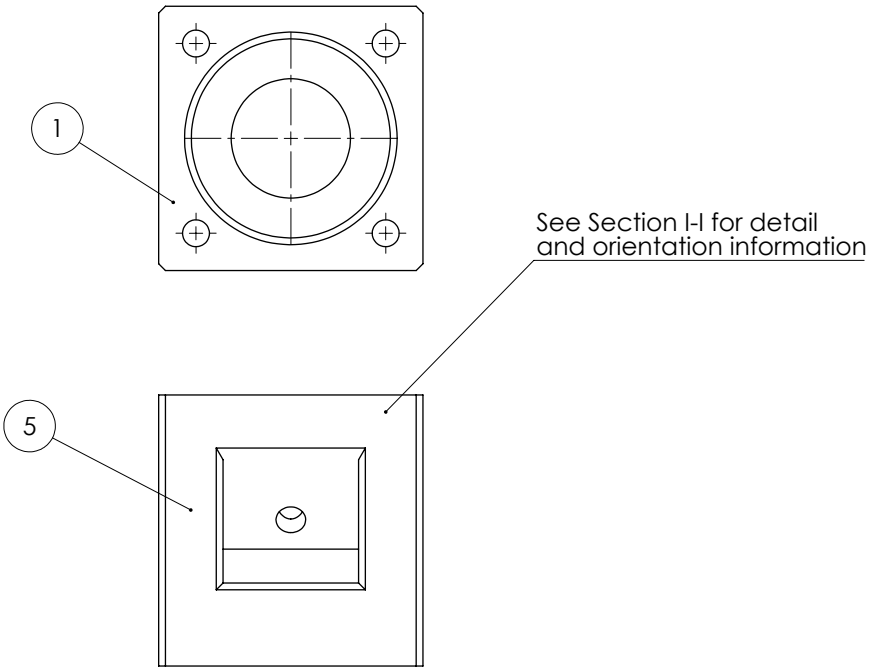

		UNLESS OTHERWISE SPECIFIED:		NAME	DATE
		DIMENSIONS ARE IN INCHES TOLERANCES: FRACTIONAL ±.005 ANGULAR: MACH ± BEND ± TWO PLACE DECIMAL ±.005 THREE PLACE DECIMAL ±.0005	DRAWN	PN	6/24/14
			CHECKED		
			ENG APPR.		
			MFG APPR.		
			Q.A.		
		MATERIAL Brass	COMMENTS:		
NEXT ASSY	USED ON	FINISH Unfinished except where machined. Deburr all edges			
APPLICATION		DO NOT SCALE DRAWING			

Fore End Cap

SIZE	DWG. NO.	REV.
A		H
SCALE:1:2	WEIGHT:	SHEET 6 OF 8

(6) Back Face

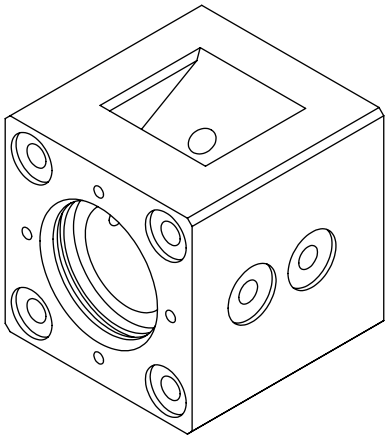

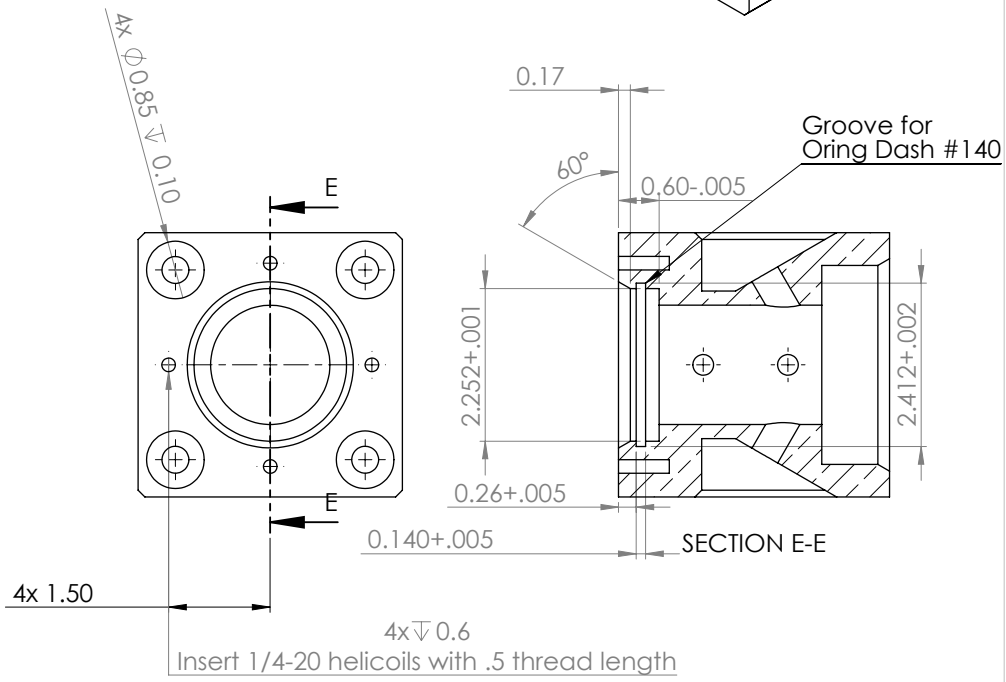

		UNLESS OTHERWISE SPECIFIED:		NAME	DATE
		DIMENSIONS ARE IN INCHES TOLERANCES: FRACTIONAL ±.005 ANGULAR: MACH ± BEND ± TWO PLACE DECIMAL ±.005 THREE PLACE DECIMAL ±.0005	DRAWN	PN	6/24/14
			CHECKED		
			ENG APPR.		
			MFG APPR.		
			Q.A.		
		MATERIAL Brass	COMMENTS:		
NEXT ASSY	USED ON	FINISH Unfinished except where machined. Deburr all edges			
APPLICATION		DO NOT SCALE DRAWING			

Fore End Cap

SIZE	DWG. NO.	REV.
A		H
SCALE:1:2	WEIGHT:	SHEET 7 OF 8

REVISIONS				
ZONE	REV.	DESCRIPTION	DATE	APPROVED
-	A	Creation	6/24/14	-
	B	Mirrored the two inlet holes to the left side	7/23/14	
	C	Added tolerance for overall geometry. Minor changes to tap depth and where they are called out. Added call outs for heli-coils	8/4/14	
	D	Removed excess mounting holes. No longer flat bottom. Updated window o-ring	8/18/14	
	E	Changed igniter holes to angled. Removed mounting holes.	9/11/14	
	F	Minor Changes.	9/20/14	
	G	Widened flow path for insulator. Minor drawing changes	9/26/14	
	H	Widened flow path to 1.76 to fit insulator		

		UNLESS OTHERWISE SPECIFIED:		NAME	DATE
		DIMENSIONS ARE IN INCHES TOLERANCES: FRACTIONAL ± .005 ANGULAR: MACH ± BEND ± TWO PLACE DECIMAL ± .005 THREE PLACE DECIMAL ± .0005	DRAWN	PN	6/24/14
			CHECKED		
			ENG APPR.		
			MFG APPR.		
			Q.A.		
		MATERIAL Brass	COMMENTS:		
NEXT ASSY	USED ON	FINISH Unfinished except where machined. Deburr all edges			
APPLICATION		DO NOT SCALE DRAWING			

Fore End Cap

SIZE	DWG. NO.	REV.
A		H
SCALE:1:2	WEIGHT:	SHEET 8 OF 8

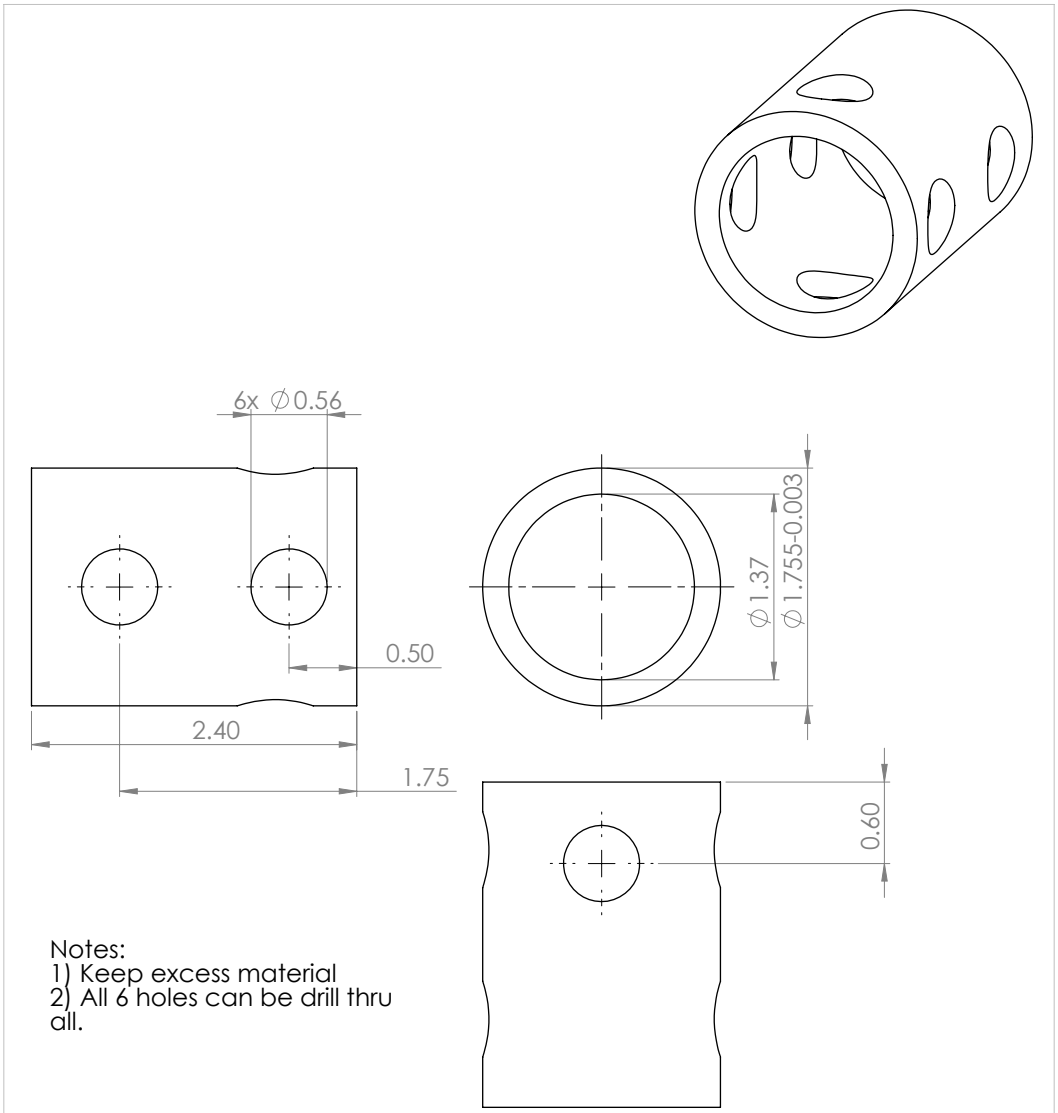

Notes:
1) Keep excess material
2) All 6 holes can be drill thru all.

		UNLESS OTHERWISE SPECIFIED:		NAME	DATE
		DIMENSIONS ARE IN INCHES	DRAWN	PN	5/6/15
		TOLERANCES:	CHECKED		
		FRACTIONAL ±.005	ENG APPR.		
		ANGULAR: MACH ± BEND ±	MFG APPR.		
		TWO PLACE DECIMAL ±.005	Q.A.		
		THREE PLACE DECIMAL ±.0005	COMMENTS:		
		MATERIAL Graphite			
NEXT ASSY	USED ON	FINISH Unfinished except where machined. Deburr all edges			
APPLICATION		DO NOT SCALE DRAWING			

Fore End Insulator

SIZE	DWG. NO.	REV.
A		A
SCALE:1:1	WEIGHT:	SHEET 1 OF 1

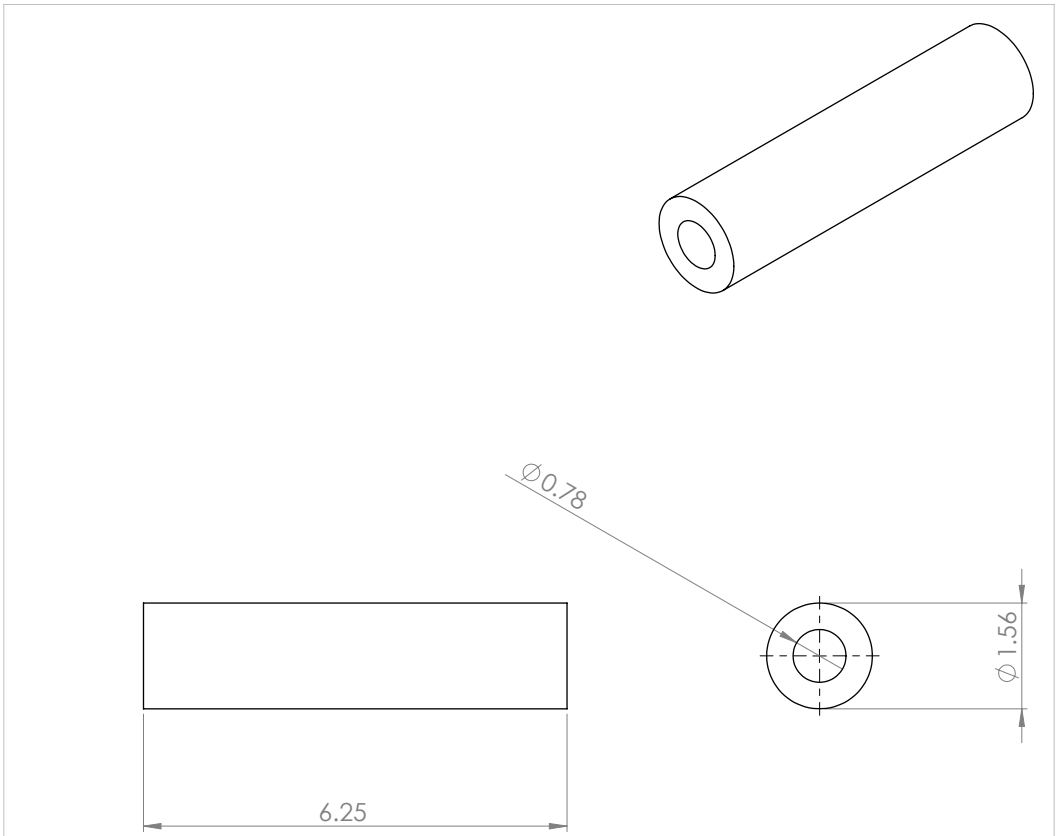

Spin Cast in lab. Settings TBD

		UNLESS OTHERWISE SPECIFIED:		NAME	DATE
		DIMENSIONS ARE IN INCHES TOLERANCES: FRACTIONAL ±.005 ANGULAR: MACH ± BEND ± TWO PLACE DECIMAL ±.005 THREE PLACE DECIMAL ±.0005	DRAWN	PN	6/24/14
			CHECKED		
			ENG APPR.		
			MFG APPR.		
			Q.A.		
		MATERIAL Paraffin Wax	COMMENTS:		
NEXT ASSY	USED ON	FINISH Unfinished except where machined. Deburr all edges			
APPLICATION		DO NOT SCALE DRAWING			

Fuel Grain

SIZE	DWG. NO.	REV.
A		A
SCALE:1:2	WEIGHT:	SHEET 1 OF 1

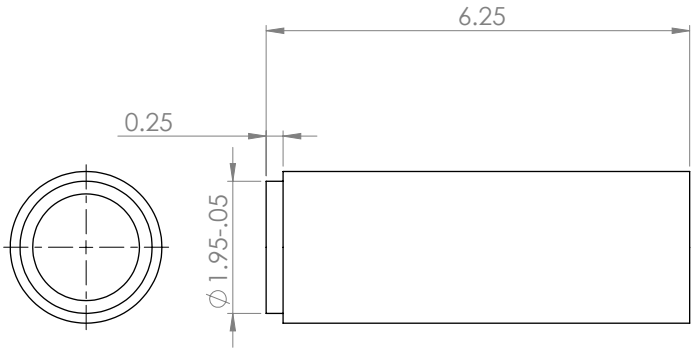

Notes:
1)Self Machined.
2) Raw Material from Franklin Fiber

		UNLESS OTHERWISE SPECIFIED:		NAME	DATE
		DIMENSIONS ARE IN INCHES TOLERANCES: FRACTIONAL ±.005 ANGULAR: MACH ± BEND ± TWO PLACE DECIMAL ±.005 THREE PLACE DECIMAL ±.0005	DRAWN	PN	9/18/14
			CHECKED		
			ENG APPR.		
			MFG APPR.		
			Q.A.		
		MATERIAL Phenolic	COMMENTS:		
NEXT ASSY	USED ON	FINISH Unfinished except where machined. Deburr all edges			
APPLICATION		DO NOT SCALE DRAWING			

Fuel Insulator

SIZE	DWG. NO.	REV.
A		A
SCALE:1:2	WEIGHT:	SHEET 1 OF 1

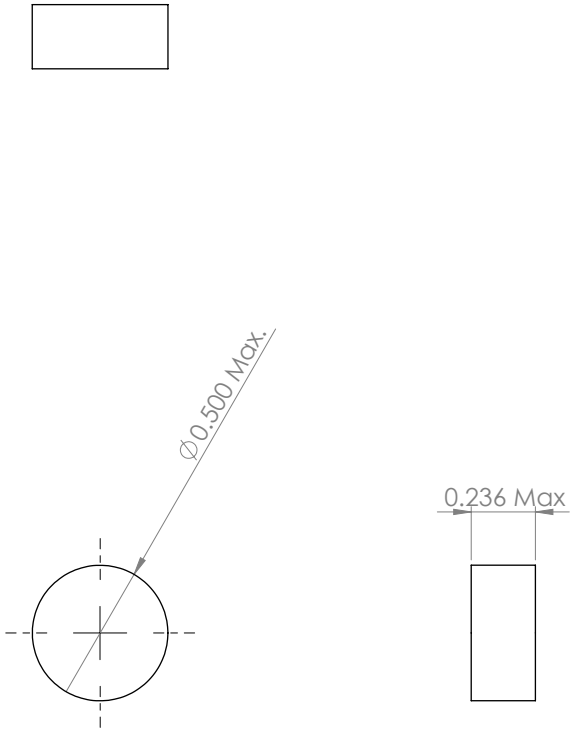

Use Raw Material from Graphite Store: P/N GT001623
Keep Excess Material

		UNLESS OTHERWISE SPECIFIED:		NAME	DATE
		DIMENSIONS ARE IN INCHES TOLERANCES: FRACTIONAL ±.005 ANGULAR: MACH ± BEND ± TWO PLACE DECIMAL ±.005 THREE PLACE DECIMAL ±.0005	DRAWN	PN	8/23/14
			CHECKED		
			ENG APPR.		
			MFG APPR.		
			Q.A.		
		MATERIAL Graphite, Superfine Isomolded	COMMENTS:		
NEXT ASSY	USED ON	FINISH Unfinished except where machined. Deburr all edges			
APPLICATION		DO NOT SCALE DRAWING			

LFA Block

SIZE	DWG. NO.	REV.
A		A
SCALE:5:1	WEIGHT:	SHEET 1 OF 1

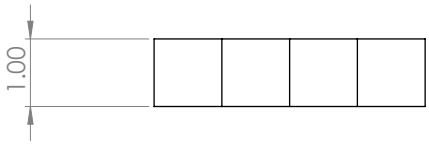

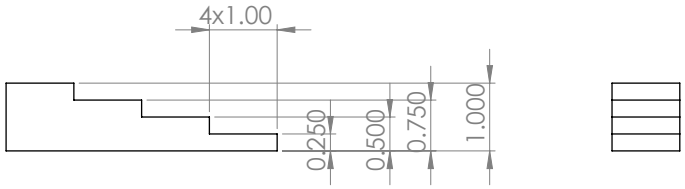

Use Raw Material from Graphite Store: P/N GT001623
Keep Excess Material

		UNLESS OTHERWISE SPECIFIED:		NAME	DATE
		DIMENSIONS ARE IN INCHES TOLERANCES: FRACTIONAL ±.005 ANGULAR: MACH ± BEND ± TWO PLACE DECIMAL ±.005 THREE PLACE DECIMAL ±.0005	DRAWN	PN	8/23/14
			CHECKED		
			ENG APPR.		
			MFG APPR.		
		MATERIAL Graphite, Superfine Isomolded	Q.A.		
			COMMENTS:		
NEXT ASSY	USED ON	FINISH Unfinished except where machined. Deburr all edges			
APPLICATION		DO NOT SCALE DRAWING			

Steps

SIZE	DWG. NO.	REV.
A		A
SCALE:1:2	WEIGHT:	SHEET 1 OF 1

Front Face

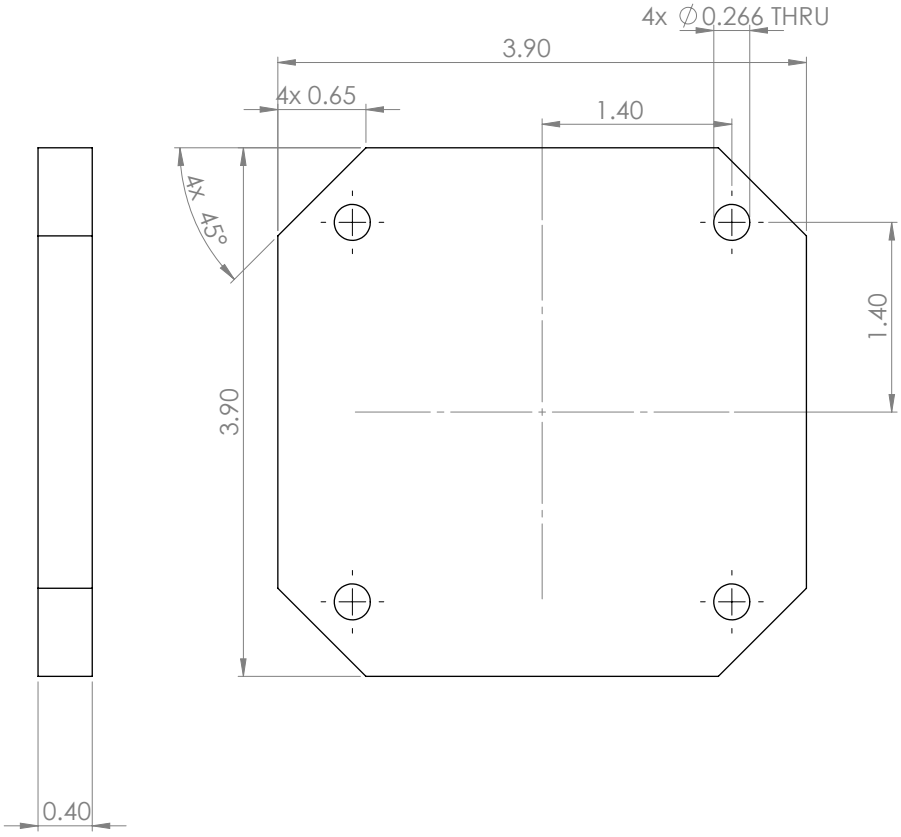

		UNLESS OTHERWISE SPECIFIED:		NAME	DATE
		DIMENSIONS ARE IN INCHES TOLERANCES: FRACTIONAL ±.005 ANGULAR: MACH ± BEND ± TWO PLACE DECIMAL ±.005 THREE PLACE DECIMAL ±.0005	DRAWN	PN	8/19/14
			CHECKED		
			ENG APPR.		
			MFG APPR.		
			Q.A.		
		MATERIAL Al 6061	COMMENTS:		
NEXT ASSY	USED ON	FINISH Unfinished except where machined. Deburr all edges			
APPLICATION		DO NOT SCALE DRAWING			

HyrdoTestCap

SIZE	DWG. NO.	REV.
A		A
SCALE:1:1	WEIGHT:	SHEET 1 OF 2

Back Face

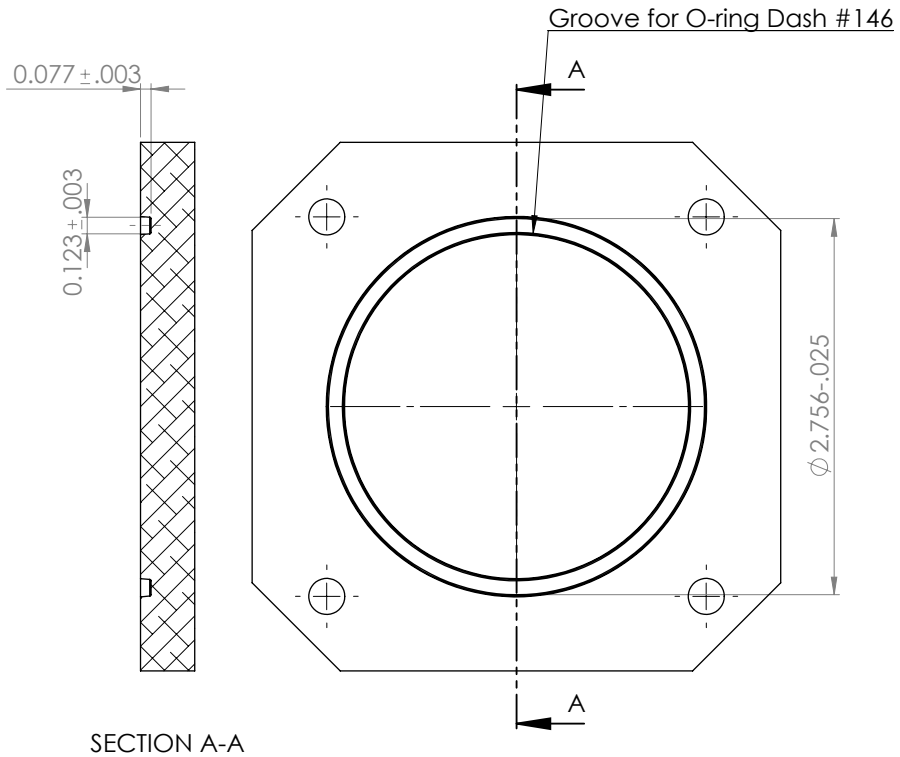

SECTION A-A

		UNLESS OTHERWISE SPECIFIED:		NAME	DATE
		DIMENSIONS ARE IN INCHES TOLERANCES: FRACTIONAL ±.005 ANGULAR: MACH ± BEND ± TWO PLACE DECIMAL ±.005 THREE PLACE DECIMAL ±.0005	DRAWN	PN	8/19/14
			CHECKED		
			ENG APPR.		
			MFG APPR.		
		MATERIAL Al 6061	Q.A.		
			COMMENTS:		
NEXT ASSY	USED ON	FINISH Unfinished except where machined. Deburr all edges			
APPLICATION		DO NOT SCALE DRAWING			

HyrdoTestCap

SIZE	DWG. NO.	REV.
A		A
SCALE:1:1	WEIGHT:	SHEET 2 OF 2

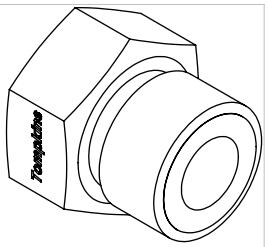

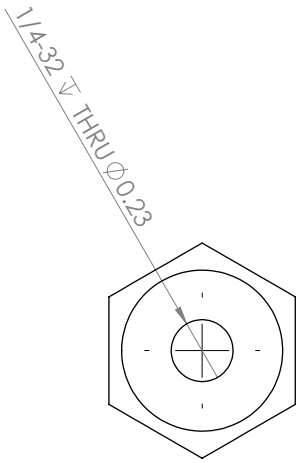

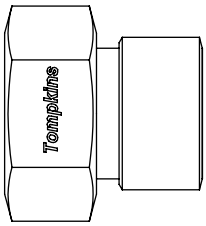

Notes:
1) Debur and face top surface for seal
2) Use drill size 1 (0.2280) for tap drill
3) Use 1/4-32 tap
4) Raw Material is SS-6408

		UNLESS OTHERWISE SPECIFIED:		NAME	DATE
		DIMENSIONS ARE IN INCHES TOLERANCES: FRACTIONAL ±.005 ANGULAR: MACH ± BEND ± TWO PLACE DECIMAL ±.005 THREE PLACE DECIMAL ±.0005	DRAWN	PN	1/30/14
			CHECKED		
			ENG APPR.		
			MFG APPR.		
			Q.A.		
		MATERIAL SS 316	COMMENTS:		
NEXT ASSY	USED ON	FINISH Unfinished except where machined. Deburr all edges			
APPLICATION		DO NOT SCALE DRAWING			

Igniter Fitting

SIZE	DWG. NO.	REV.
A		A
SCALE:2:1	WEIGHT:	SHEET 1 OF 1

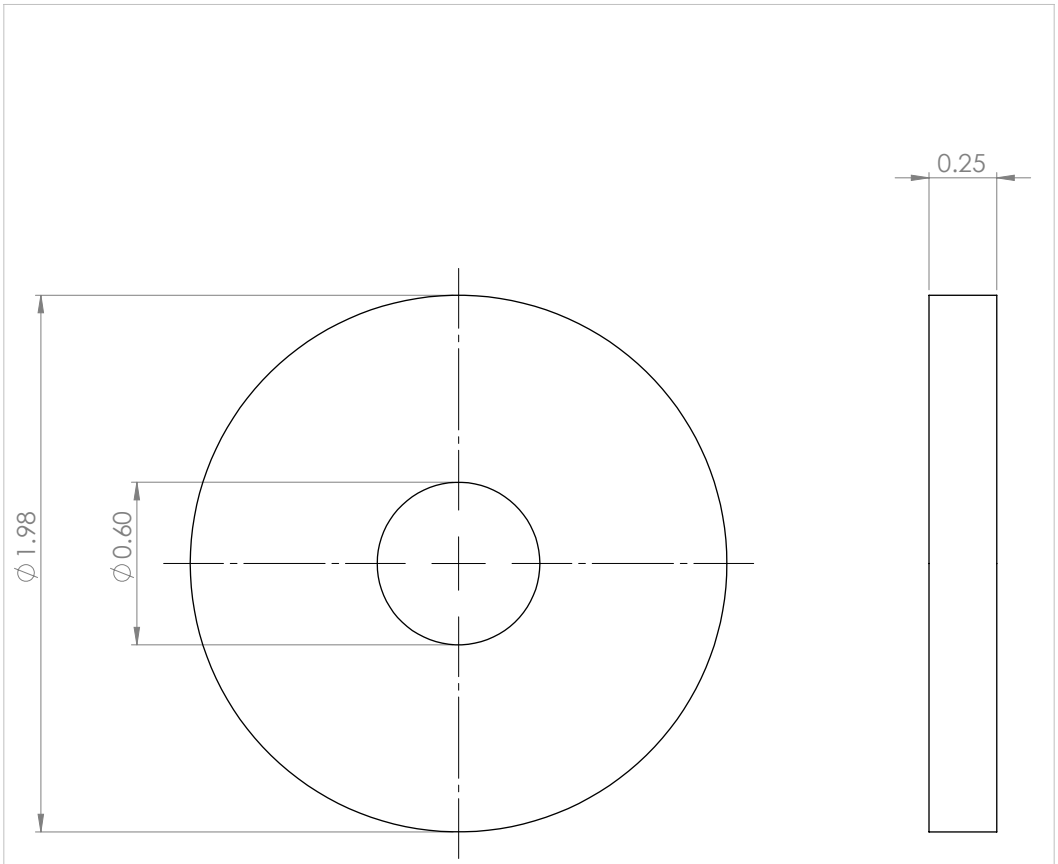

Ok if water-jet cut or laser cut.

		UNLESS OTHERWISE SPECIFIED:		NAME	DATE
		DIMENSIONS ARE IN INCHES TOLERANCES: FRACTIONAL ±.005 ANGULAR: MACH ± BEND ± TWO PLACE DECIMAL ±.005 THREE PLACE DECIMAL ±.0005	DRAWN	PN	6/24/14
			CHECKED		
			ENG APPR.		
			MFG APPR.		
			Q.A.		
		MATERIAL Acrylic	COMMENTS:		
NEXT ASSY	USED ON	FINISH Unfinished except where machined. Deburr all edges			
APPLICATION		DO NOT SCALE DRAWING			

Mixer

SIZE	DWG. NO.	REV.
A		B
SCALE:2:1	WEIGHT:	SHEET 1 OF 2

REVISIONS				
ZONE	REV.	DESCRIPTION	DATE	APPROVED
-	A	Creation	6/24/14	-
	B	Changed Material Properties to Acrylic (from Nylon)	7/23/14	

		UNLESS OTHERWISE SPECIFIED:		NAME	DATE
		DIMENSIONS ARE IN INCHES TOLERANCES: FRACTIONAL ±.005 ANGULAR: MACH ± BEND ± TWO PLACE DECIMAL ±.005 THREE PLACE DECIMAL ±.0005	DRAWN	PN	6/24/14
			CHECKED		
			ENG APPR.		
			MFG APPR.		
			Q.A.		
		MATERIAL Acrylic	COMMENTS:		
NEXT ASSY	USED ON	FINISH Unfinished except where machined. Deburr all edges			
APPLICATION		DO NOT SCALE DRAWING			

Mixer

SIZE	DWG. NO.	REV.
A		B
SCALE:2:1	WEIGHT:	SHEET 2 OF 2

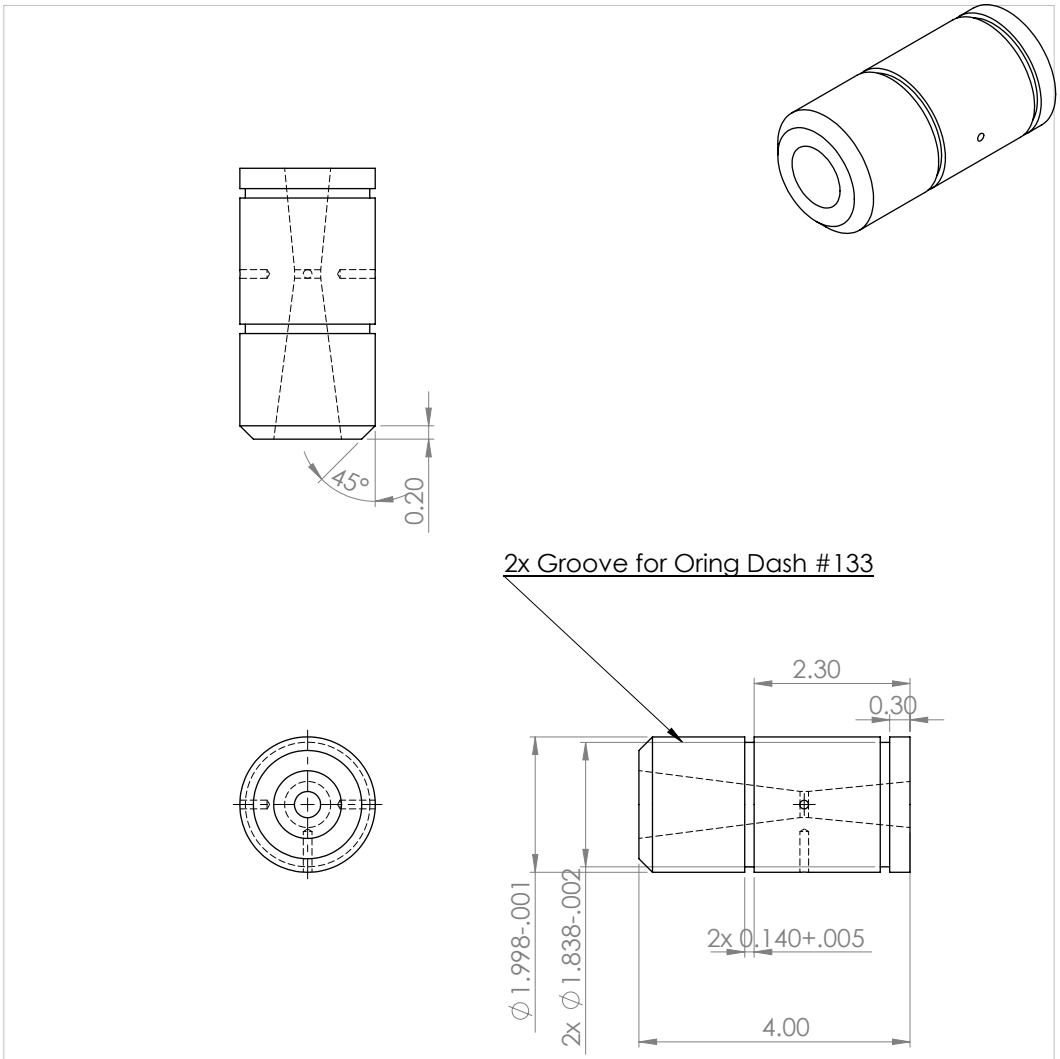

Use Raw Material from Graphite Store: P/N GT001623
Keep Excess Material

		UNLESS OTHERWISE SPECIFIED:		NAME	DATE
		DIMENSIONS ARE IN INCHES TOLERANCES: FRACTIONAL ±.005 ANGULAR: MACH ± BEND ± TWO PLACE DECIMAL ±.005 THREE PLACE DECIMAL ±.0005	DRAWN	PN	6/24/14
			CHECKED		
			ENG APPR.		
			MFG APPR.		
		MATERIAL Graphite, Superfine Isomolded	Q.A.		
			COMMENTS:		
NEXT ASSY	USED ON	FINISH Unfinished except where machined. Deburr all edges			
APPLICATION		DO NOT SCALE DRAWING			

Nozzle

SIZE	DWG. NO.	REV.
A	A-F	1
SCALE:1:2	WEIGHT:	SHEET 1 OF 4

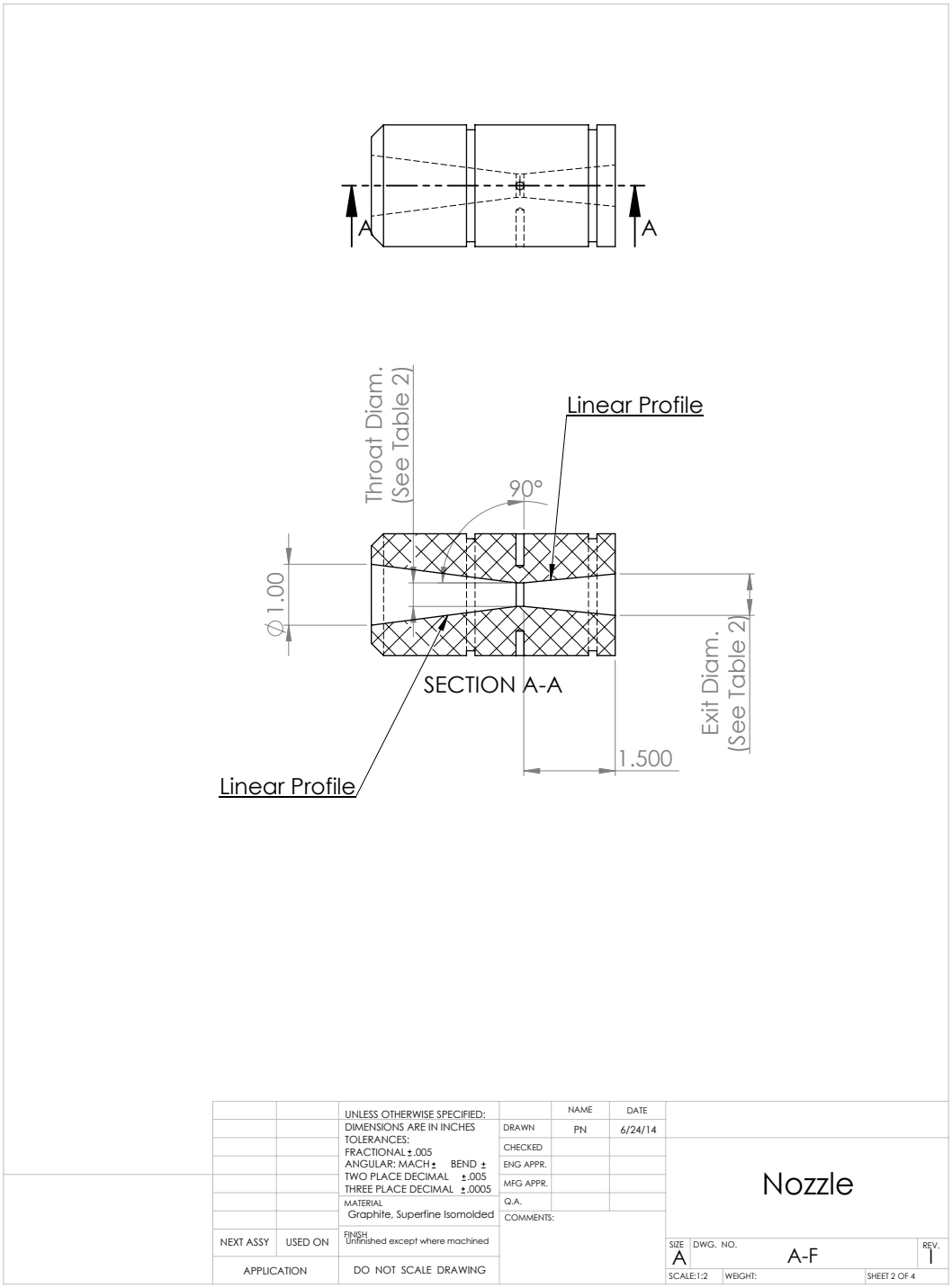

		UNLESS OTHERWISE SPECIFIED:		NAME	DATE
		DIMENSIONS ARE IN INCHES TOLERANCES: FRACTIONAL ±.005 ANGULAR: MACH ± BEND ± TWO PLACE DECIMAL ±.005 THREE PLACE DECIMAL ±.0005	DRAWN	PN	6/24/14
			CHECKED		
			ENG APPR.		
			MFG APPR.		
			Q.A.		
		MATERIAL Graphite, Superfine Isomolded	COMMENTS:		
NEXT ASSY	USED ON	FINISH Unfinished except where machined			
APPLICATION		DO NOT SCALE DRAWING			

Nozzle

SIZE	DWG. NO.	REV.
A	A-F	1
SCALE:1:2	WEIGHT:	SHEET 2 OF 4

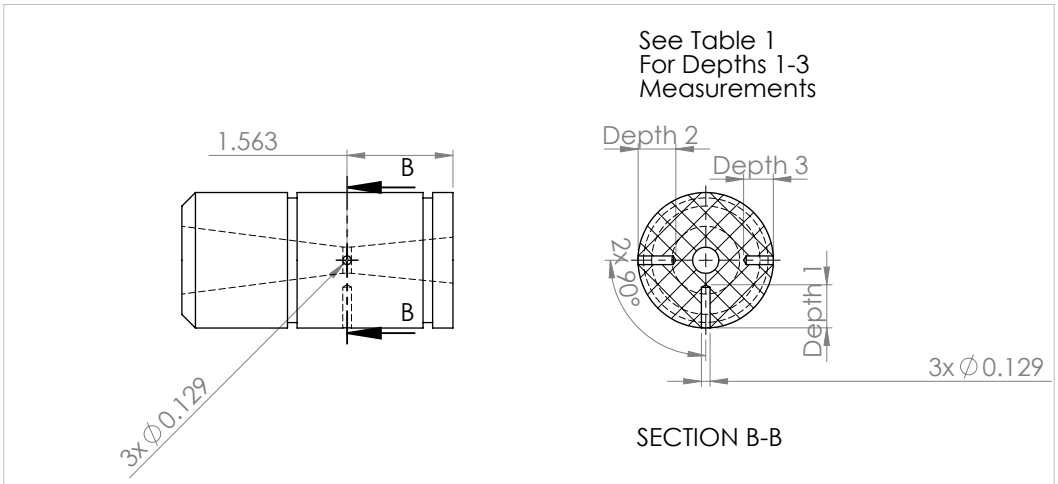

TABLE 1

Config	Depth 1	Depth 2	Depth 3
A	0.64	0.56	0.44
B	0.61	0.53	0.45
C	0.50	0.42	0.34
D	0.63	0.55	0.47
E	0.58	0.50	0.42
F	0.54	0.46	0.38

		UNLESS OTHERWISE SPECIFIED:		NAME	DATE
		DIMENSIONS ARE IN INCHES TOLERANCES: FRACTIONAL ± .005 ANGULAR: MACH ± BEND ± TWO PLACE DECIMAL ± .005 THREE PLACE DECIMAL ± .0005	DRAWN	PN	6/24/14
			CHECKED		
			ENG APPR.		
			MFG APPR.		
		MATERIAL Graphite, Superfine Isomolded	Q.A.		
			COMMENTS:		
NEXT ASSY	USED ON	FINISH Unfinished except where machined. Deburr all edges			
APPLICATION		DO NOT SCALE DRAWING			

Nozzle

SIZE	DWG. NO.	REV.
A	A-F	I
SCALE:1:2	WEIGHT:	SHEET 3 OF 4

TABLE 2

Config	O/F	Pres.	Throat Diam.	Exit Diam.
A	2.10	250	0.386	0.68
B	1.70	250	0.282	0.53
C	2.75	250	0.500	0.920
D	1.70	350	0.239	0.51
E	2.10	350	0.329	0.70
F	2.75	350	0.423	0.90

REVISIONS				
ZONE	REV.	DESCRIPTION	DATE	APPROVED
-	A	Creation	6/24/14	-
	B	Changed the TC Hole depths. 2 now correspond to inverse code, 25 and 35 %. The last is in between.	7/23/14	
	C	Changed hole diameter to #30 drill bit (.1285 inches). Also changed tolerances on drill bit hole.	7/24/14	
	D	Changed chamfer on faces of nozzle to fit aft end	8/4/14	
	E	Modified Oring dimensions. Added dimensions for nozzle profile	8/18/14	
	F	Removed combustion chamber o-ring	9/11/14	
	G	Added configurations for more test conditions	9/25/15	
	H	Updated TC Hole depths. Nozzles B-E now have 0.25 wall safety thickness. A, F have 0.17	9/25/15	
	I	Updated dimensions in both tables for 100% C* efficiency	10/15/15	

		UNLESS OTHERWISE SPECIFIED:		NAME	DATE
		DIMENSIONS ARE IN INCHES TOLERANCES: FRACTIONAL ±.005 ANGULAR: MACH ± BEND ± TWO PLACE DECIMAL ±.005 THREE PLACE DECIMAL ±.0005	DRAWN	PN	6/24/14
			CHECKED		
			ENG APPR.		
			MFG APPR.		
		MATERIAL Graphite, Superfine Isomolded	Q.A.		
			COMMENTS:		
NEXT ASSY	USED ON	FINISH Unfinished except where machined. Deburr all edges			
APPLICATION		DO NOT SCALE DRAWING			

Nozzle

SIZE	DWG. NO.	REV.
A	A-F	I
SCALE:1:2	WEIGHT:	SHEET 4 OF 4

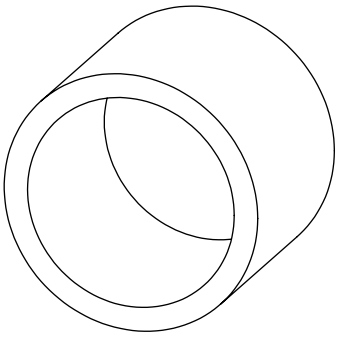

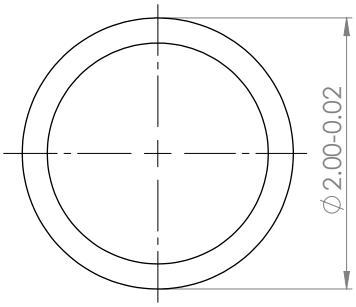

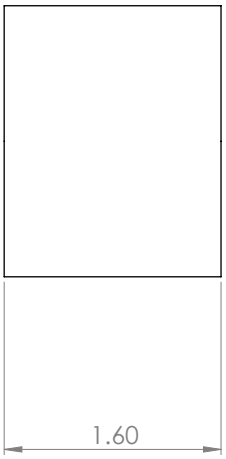

Notes:
1) Raw Material from Graphite Store. P/N: GT001656
2) Do not machine ID

		UNLESS OTHERWISE SPECIFIED:		NAME	DATE
		DIMENSIONS ARE IN INCHES TOLERANCES: FRACTIONAL ±.005 ANGULAR: MACH ± BEND ± TWO PLACE DECIMAL ±.005 THREE PLACE DECIMAL ±.0005	DRAWN	PN	2/17/15
			CHECKED		
			ENG APPR.		
			MFG APPR.		
			Q.A.		
		MATERIAL Graphite	COMMENTS:		
NEXT ASSY	USED ON	FINISH Unfinished except where machined. Deburr all edges			
APPLICATION		DO NOT SCALE DRAWING			

postCombustionChamber

SIZE	DWG. NO.	REV.
A		A
SCALE:1:1	WEIGHT:	SHEET 1 OF 1

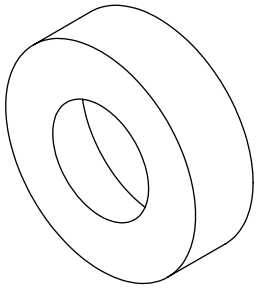

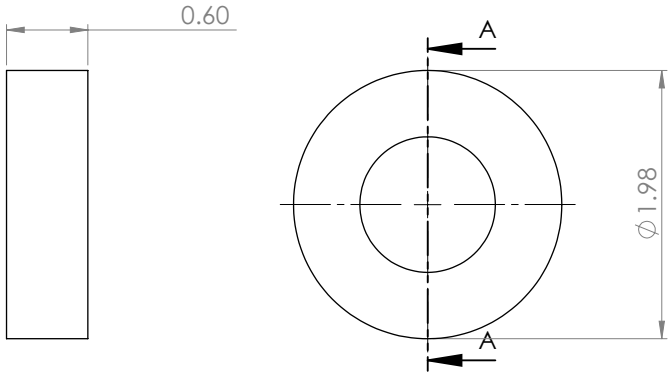

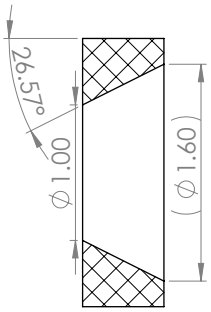

SECTION A-A

Notes:
1)Raw Material from Graphite Store, P/N: GT001623
2) Excess Material retained for Nozzle

		UNLESS OTHERWISE SPECIFIED:		NAME	DATE
		DIMENSIONS ARE IN INCHES TOLERANCES: FRACTIONAL ±.005 ANGULAR: MACH ± BEND ± TWO PLACE DECIMAL ±.005 THREE PLACE DECIMAL ±.0005	DRAWN	PN	6 /24/14
			CHECKED		
			ENG APPR.		
			MFG APPR.		
			Q.A.		
		MATERIAL Graphite	COMMENTS:		
NEXT ASSY	USED ON	FINISH Unfinished except where machined. Deburr all edges			
APPLICATION		DO NOT SCALE DRAWING			

preNozzle

SIZE	DWG. NO.	REV.
A		B
SCALE:1:1	WEIGHT:	SHEET 1 OF 2

REVISIONS				
ZONE	REV.	DESCRIPTION	DATE	APPROVED
-	A	Creation	6/14/14	-
	B	Minor Changes	8/18/14	

		UNLESS OTHERWISE SPECIFIED:		NAME	DATE
		DIMENSIONS ARE IN INCHES TOLERANCES: FRACTIONAL ± .005 ANGULAR: MACH ± BEND ± TWO PLACE DECIMAL ± .005 THREE PLACE DECIMAL ± .0005	DRAWN	PN	6 /24/14
			CHECKED		
			ENG APPR.		
			MFG APPR.		
			Q.A.		
		MATERIAL Graphite	COMMENTS:		
NEXT ASSY	USED ON	FINISH Unfinished except where machined. Deburr all edges			
APPLICATION		DO NOT SCALE DRAWING			

preNozzle

SIZE	DWG. NO.	REV.
A		B
SCALE:1:1	WEIGHT:	SHEET 2 OF 2

Notes:
1)Repair threads at cuts
2)Ends can be rounded
3) Raw Material P/N McM 93250A031

		UNLESS OTHERWISE SPECIFIED:		NAME	DATE
		DIMENSIONS ARE IN INCHES TOLERANCES: FRACTIONAL ±.005 ANGULAR: MACH ± BEND ± TWO PLACE DECIMAL ±.005 THREE PLACE DECIMAL ±.0005	DRAWN	PN	9/11/14
			CHECKED		
			ENG APPR.		
			MFG APPR.		
			Q.A.		
		MATERIAL S.S. 316	COMMENTS:		
NEXT ASSY	USED ON	FINISH Unfinished except where machined. Deburr all edges			
APPLICATION		DO NOT SCALE DRAWING			

Threaded Rod

SIZE	DWG. NO.	REV.
A		A

SCALE:1:5	WEIGHT:	SHEET 1 OF 1

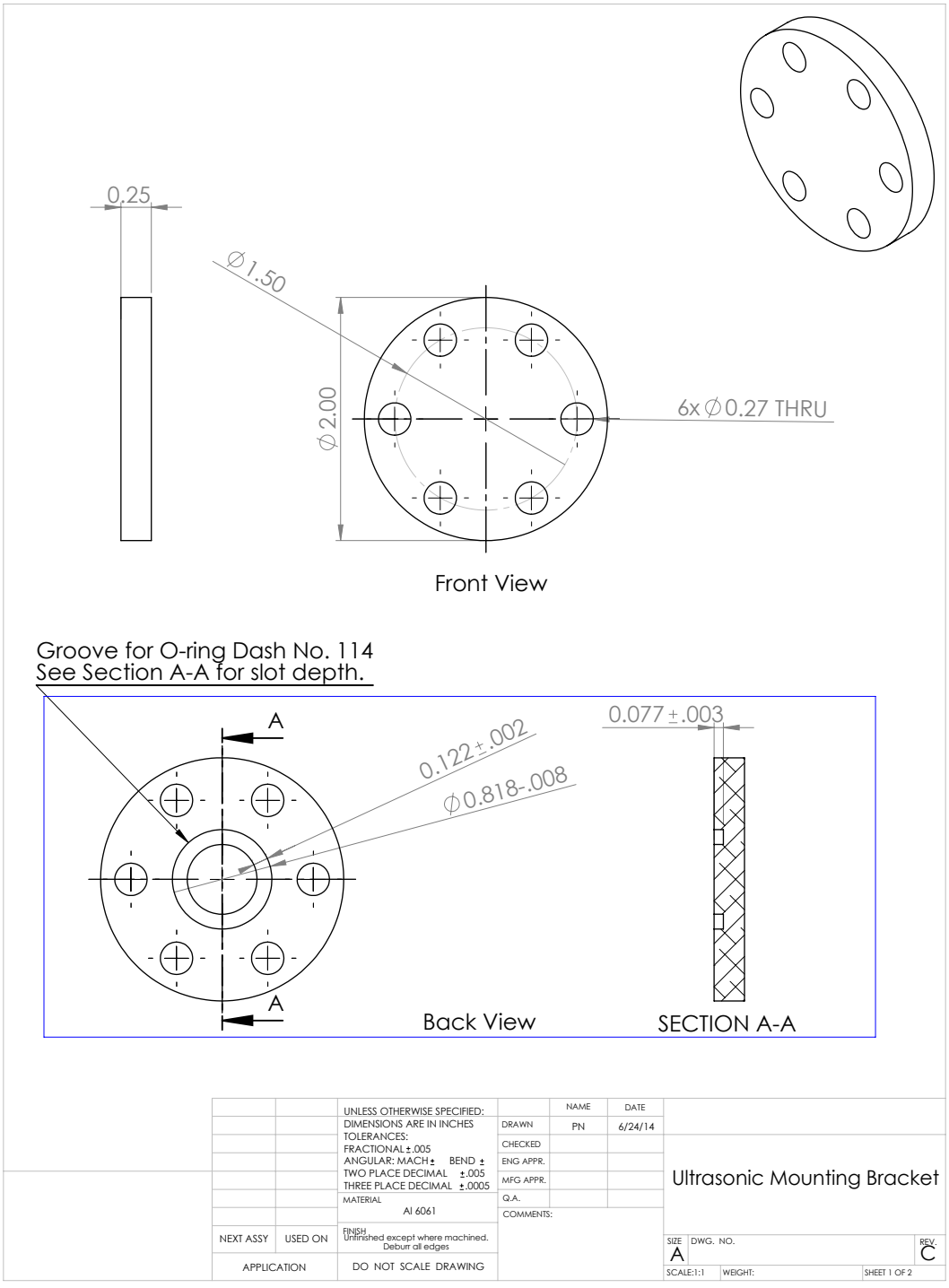
0.25
∅1.50
∅2.00
6x∅0.27 THRU
Front View
Groove for O-ring Dash No. 114
See Section A-A for slot depth.
A
A
0.122±.002
∅0.818-.008
0.077±.003
Back View
SECTION A-A
UNLESS OTHERWISE SPECIFIED:
DIMENSIONS ARE IN INCHES
TOLERANCES:
FRACTIONAL ±.005
ANGULAR: MACH ± BEND ±
TWO PLACE DECIMAL ±.005
THREE PLACE DECIMAL ±.0005
MATERIAL
Al 6061
FINISH
Unfinished except where machined.
Deburr all edges
DO NOT SCALE DRAWING
NEXT ASSY
USED ON
APPLICATION
NAME
DATE
DRAWN
PN
6/24/14
CHECKED
ENG APPR.
MFG APPR.
Q.A.
COMMENTS:
Ultrasonic Mounting Bracket
SIZE
A
DWG. NO.
REV.
C
SCALE:1:1
WEIGHT:
SHEET 1 OF 2

REVISIONS				
ZONE	REV.	DESCRIPTION	DATE	APPROVED
-	A	Creation	6/24/14	-
	B	Changed oring to #114	8/20/14	
	C	Changed material to Al 6061	9/20/14	

		UNLESS OTHERWISE SPECIFIED:		NAME	DATE
		DIMENSIONS ARE IN INCHES TOLERANCES: FRACTIONAL ±.005 ANGULAR: MACH ± BEND ± TWO PLACE DECIMAL ±.005 THREE PLACE DECIMAL ±.0005	DRAWN	PN	6/24/14
			CHECKED		
			ENG APPR.		
			MFG APPR.		
			Q.A.		
		MATERIAL Al 6061	COMMENTS:		
NEXT ASSY	USED ON	FINISH Unfinished except where machined. Deburr all edges			
APPLICATION		DO NOT SCALE DRAWING			

Ultrasonic Mounting Bracket

SIZE	DWG. NO.	REV.
A		C
SCALE:1:1	WEIGHT:	SHEET 2 OF 2

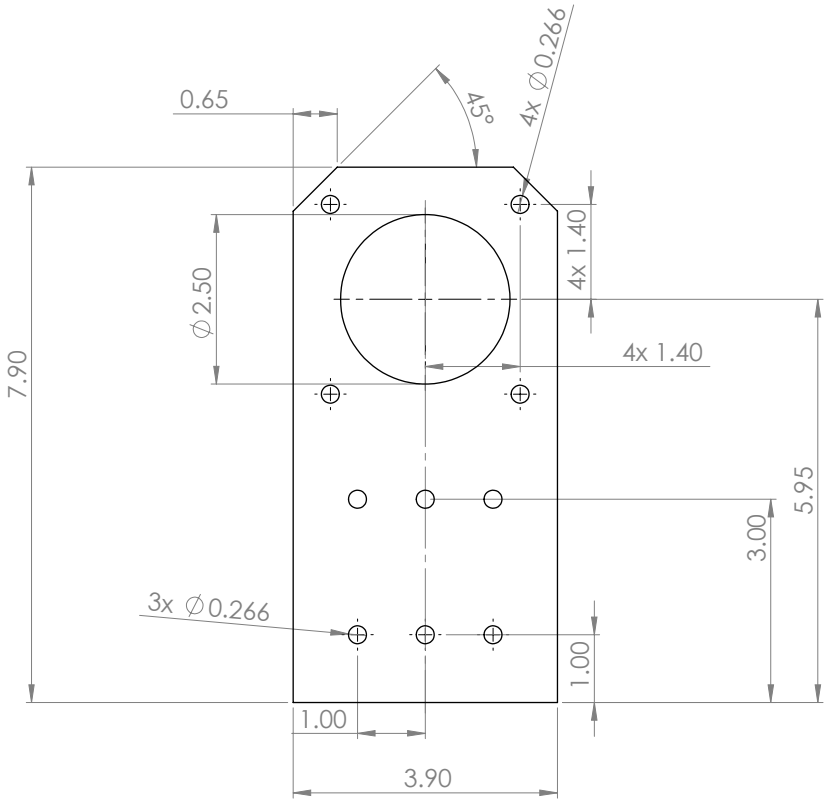

Notes:
1) Plate thickness is 0.5"
2) Ok if laser cut or water jet cut or machined
3) This is the Fixture Configuration (of nozzleCoverPlate)

				NAME	DATE	
		UNLESS OTHERWISE SPECIFIED:				
		DIMENSIONS ARE IN INCHES TOLERANCES: FRACTIONAL ± .005 ANGULAR: MACH ± BEND ± TWO PLACE DECIMAL ± .005 THREE PLACE DECIMAL ± .0005	DRAWN	PN	9/11/14	Aft Support Plate
			CHECKED			
			ENG APPR.			
			MFG APPR.			
			Q.A.			
		MATERIAL S.S. 304	COMMENTS:			
NEXT ASSY	USED ON	FINISH Unfinished except where machined. Deburr all edges				SIZE A · DWG. NO. · REV. A
APPLICATION		DO NOT SCALE DRAWING				SCALE:1:2 · WEIGHT: · SHEET 1 OF 1

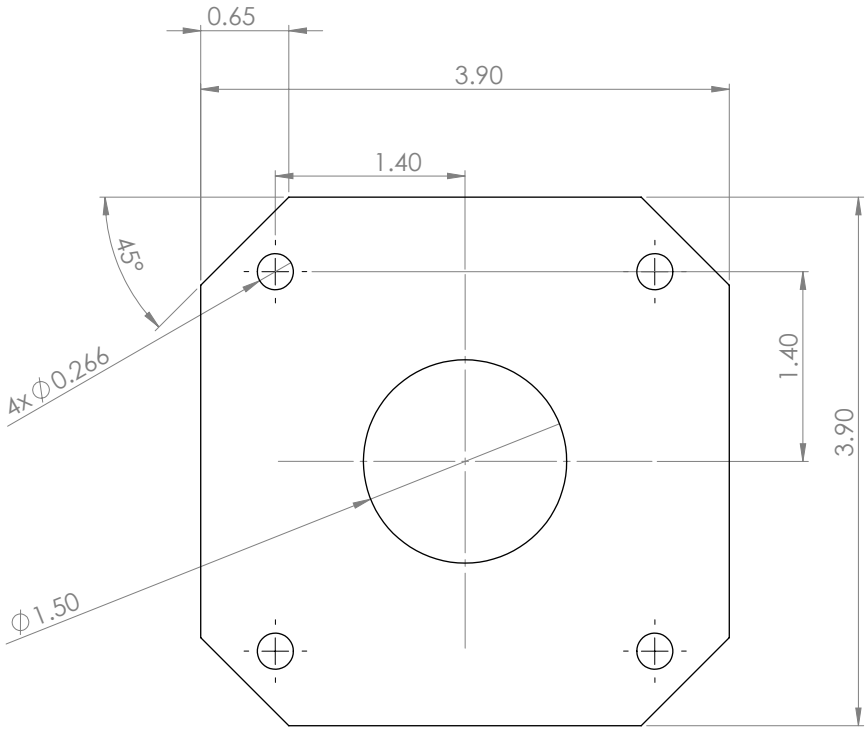

Note:
1) Thickness of plate is 1/2"
2) Can be laser cut or water jet cut or machined.
3) This is Nozzle Hold Configuration

		UNLESS OTHERWISE SPECIFIED:		NAME	DATE
		DIMENSIONS ARE IN INCHES TOLERANCES: FRACTIONAL ±.005 ANGULAR: MACH ± BEND ± TWO PLACE DECIMAL ±.005 THREE PLACE DECIMAL ±.0005	DRAWN	PN	6/24/14
			CHECKED		
			ENG APPR.		
			MFG APPR.		
			Q.A.		
		MATERIAL Brass	COMMENTS:		
NEXT ASSY	USED ON	FINISH Unfinished except where machined. Deburr all edges			
APPLICATION		DO NOT SCALE DRAWING			

Nozzle Cover Plate

SIZE	DWG. NO.	REV.
A		E
SCALE:1:1	WEIGHT:	SHEET 1 OF 2

REVISIONS				
ZONE	REV.	DESCRIPTION	DATE	APPROVED
-	A	Creation	6/24/14	-
	B	Minor Changes	8/4/14	
	C	Added hole for flow to pass	8/18/14	
	D	Added Nozzle Hold Configuration Note, changed to SS 304	9/14/14	
	E	Changed material for this config to Brass	10/1/14	

		UNLESS OTHERWISE SPECIFIED:		NAME	DATE
		DIMENSIONS ARE IN INCHES TOLERANCES: FRACTIONAL ± .005 ANGULAR: MACH ± BEND ± TWO PLACE DECIMAL ± .005 THREE PLACE DECIMAL ± .0005	DRAWN	PN	6/24/14
			CHECKED		
			ENG APPR.		
			MFG APPR.		
			Q.A.		
		MATERIAL Brass	COMMENTS:		
NEXT ASSY	USED ON	FINISH Unfinished except where machined. Deburr all edges			
APPLICATION		DO NOT SCALE DRAWING			

Nozzle Cover Plate

SIZE	DWG. NO.	REV.
A		E
SCALE:1:1	WEIGHT:	SHEET 2 OF 2

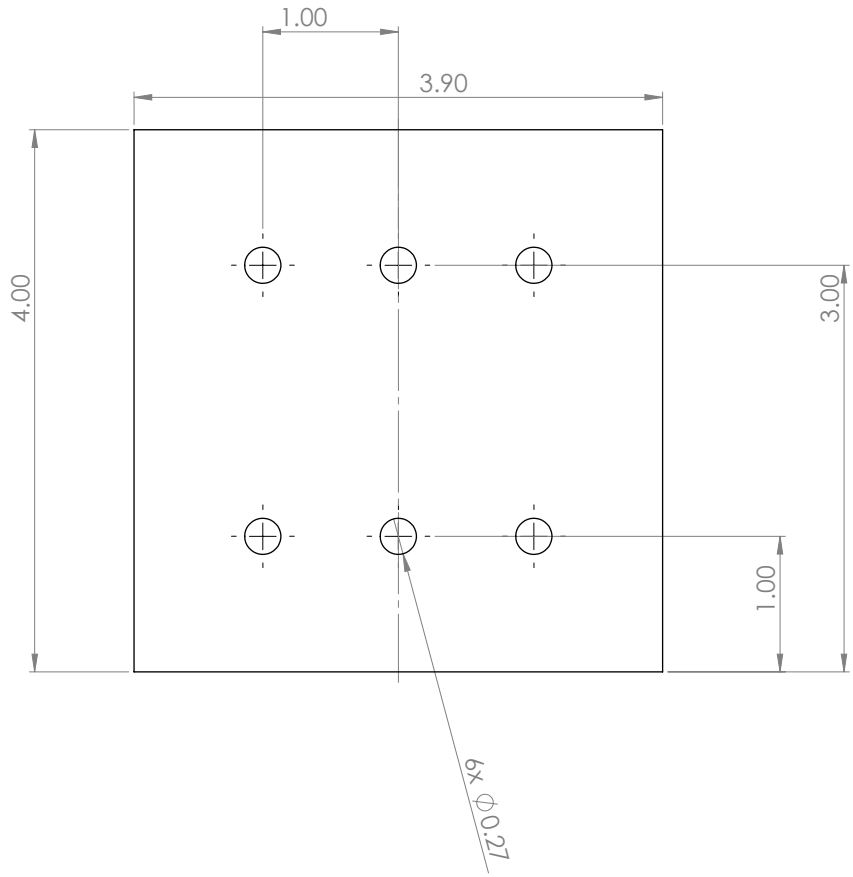

Notes:
1) Plate thickness is 3/8"
2) Ok if water jet cut or laser cut or machined

		UNLESS OTHERWISE SPECIFIED:		NAME	DATE
		DIMENSIONS ARE IN INCHES TOLERANCES: FRACTIONAL ±.005 ANGULAR: MACH ± BEND ± TWO PLACE DECIMAL ±.005 THREE PLACE DECIMAL ±.0005	DRAWN	PN	9/17/14
			CHECKED		
			ENG APPR.		
			MFG APPR.		
			Q.A.		
		MATERIAL SS 304	COMMENTS:		
NEXT ASSY	USED ON	FINISH Unfinished except where machined. Deburr all edges			
APPLICATION		DO NOT SCALE DRAWING			

Support Block

SIZE	DWG. NO.	REV.
A		A
SCALE:1:1	WEIGHT:	SHEET 1 OF 1

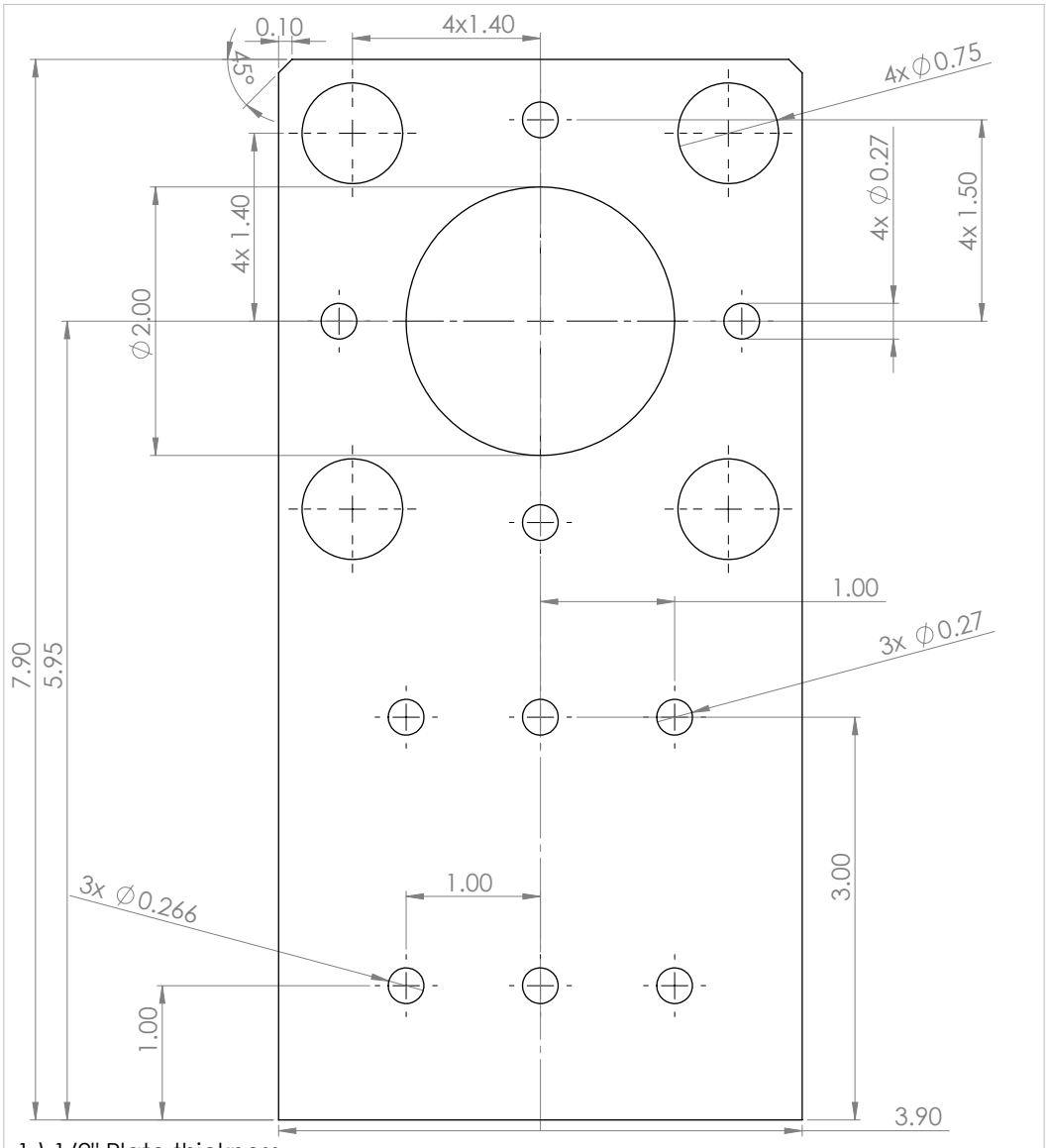

1.) 1/2" Plate thickness
2.) Can be water-jet cut or laser cut or machined.

		UNLESS OTHERWISE SPECIFIED:		NAME	DATE
		DIMENSIONS ARE IN INCHES TOLERANCES: FRACTIONAL ±.005 ANGULAR: MACH ± BEND ± TWO PLACE DECIMAL ±.005 THREE PLACE DECIMAL ±.0005	DRAWN	PN	6/24/14
			CHECKED		
			ENG APPR.		
			MFG APPR.		
			Q.A.		
		MATERIAL SS 304	COMMENTS:		
NEXT ASSY	USED ON	FINISH Unfinished except where machined. Deburr all edges			
APPLICATION		DO NOT SCALE DRAWING			

window Plate

SIZE	DWG. NO.	REV.
A		C
SCALE:1:1	WEIGHT:	SHEET 1 OF 2

REVISIONS				
ZONE	REV.	DESCRIPTION	DATE	APPROVED
-	A	Creation	6/24/14	-
	B	Made tie rod holes larger. Center referenced all holes	8/18/14	
	C	Changed thickness. Changed material to SS. Made part larger for supports	9/11/14	

		UNLESS OTHERWISE SPECIFIED:		NAME	DATE
		DIMENSIONS ARE IN INCHES TOLERANCES: FRACTIONAL ±.005 ANGULAR: MACH ± BEND ± TWO PLACE DECIMAL ±.005 THREE PLACE DECIMAL ±.0005	DRAWN	PN	6/24/14
			CHECKED		
			ENG APPR.		
			MFG APPR.		
			Q.A.		
		MATERIAL SS 304	COMMENTS:		
NEXT ASSY	USED ON	FINISH Unfinished except where machined. Deburr all edges			
APPLICATION		DO NOT SCALE DRAWING			

window Plate

SIZE	DWG. NO.	REV.
A		C
SCALE:1:1	WEIGHT:	SHEET 2 OF 2

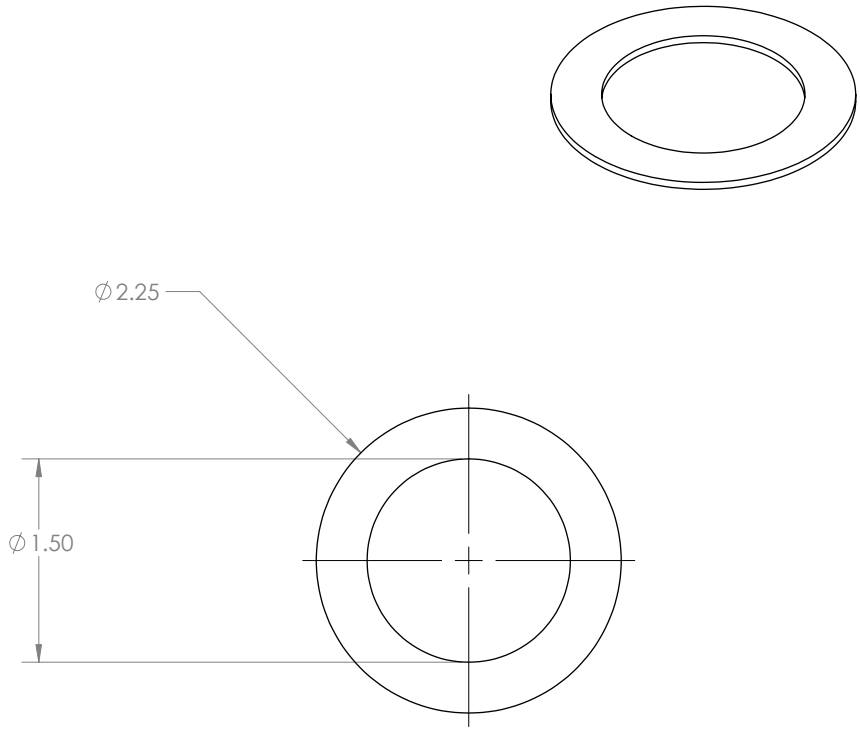

Notes:
1) Use 1/16" EPDM (pref.) or Silicone
2) Cut by hand.
3) Cut to fit.

		UNLESS OTHERWISE SPECIFIED:		NAME	DATE
		DIMENSIONS ARE IN INCHES TOLERANCES: FRACTIONAL ±.005 ANGULAR: MACH ± BEND ± TWO PLACE DECIMAL ±.005 THREE PLACE DECIMAL ±.0005	DRAWN	PN	4/17/16
			CHECKED		
			ENG APPR.		
			MFG APPR.		
			Q.A.		
		MATERIAL EPDM or Silicone	COMMENTS:		
NEXT ASSY	USED ON	FINISH Unfinished except where machined. Deburr all edges			
APPLICATION		DO NOT SCALE DRAWING			

siliconeWasher

SIZE	DWG. NO.	REV.
A		A

SCALE:1:1 WEIGHT: SHEET 1 OF 1

E.2 Instructions for building the experiment

An exploded view of the motor highlights the number of parts and complexity of the motor, as shown in Figure E.1. Although the experimental motor is still arguably simple, a set of assembly instructions would be extremely useful to anyone picking up this project in the future.

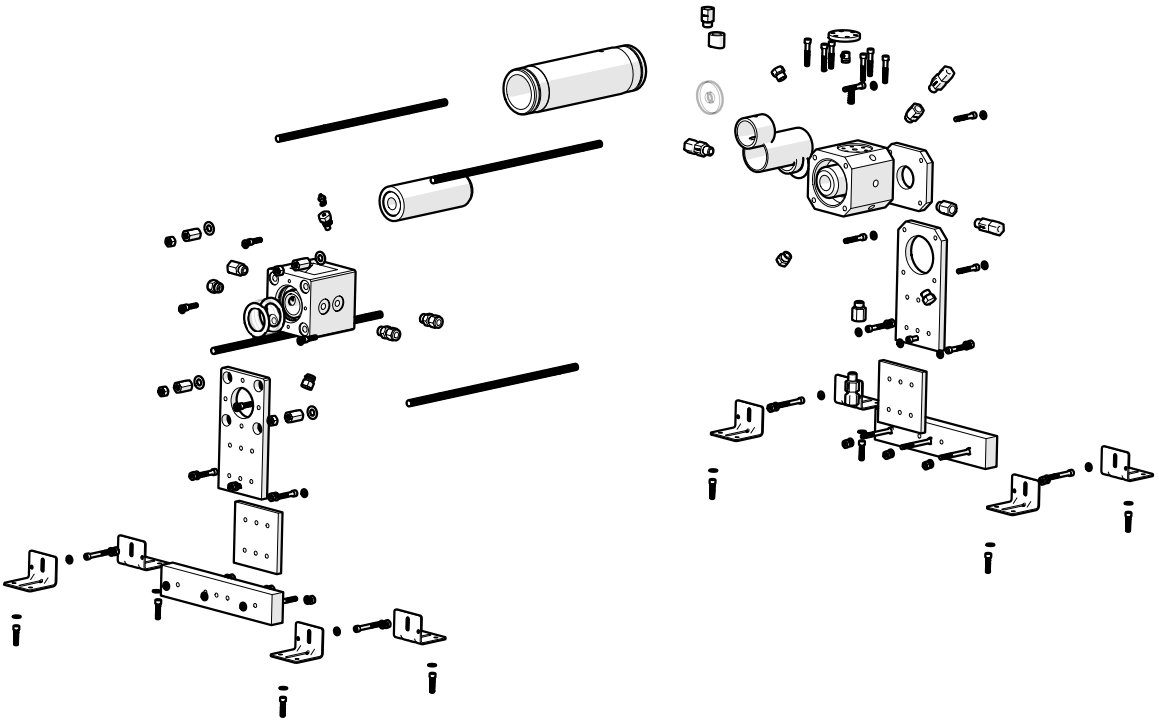

Figure E.1: An exploded view of all of the components of the motor.

E.2.1 Aft End Support Assembly

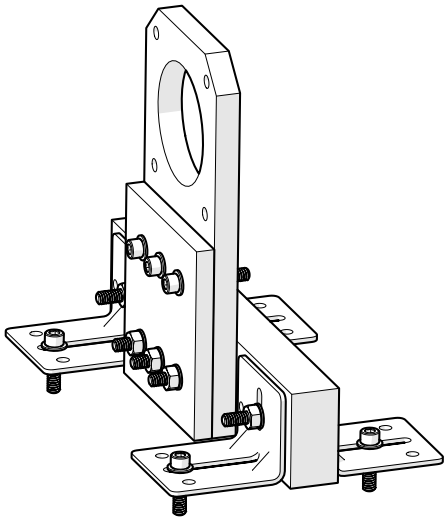

Final image of aft end support sub-assembly.

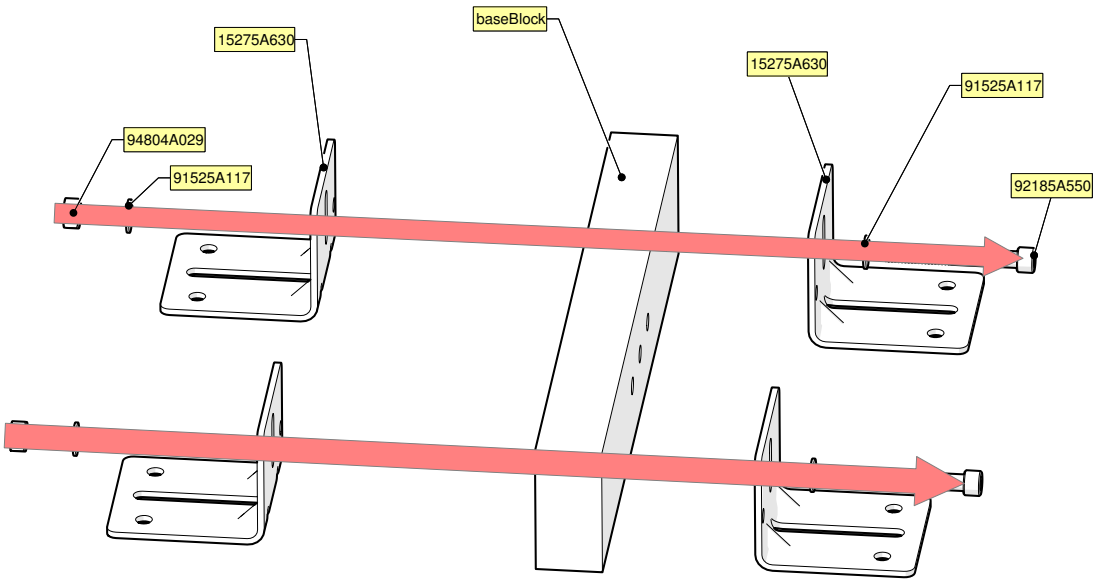

Step 1: Bolt the L-brackets to the base block using the bolts, washers, and nuts.

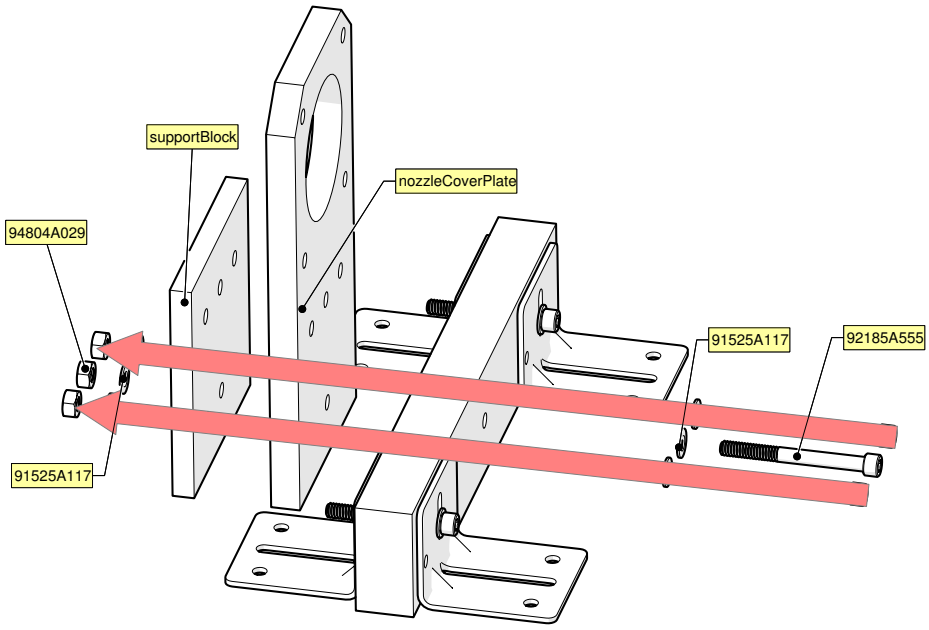

Step 2: Bolt the nozzle cover plate and support block onto the base block with the correct bolts, washers, and nuts.

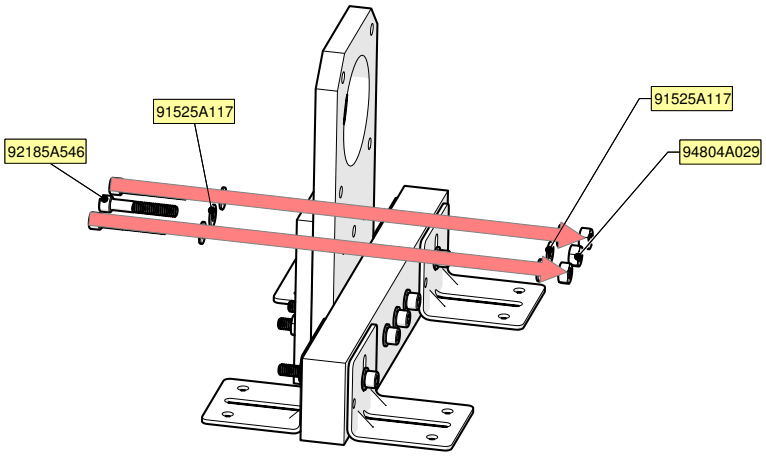

Step 3: Add more bolts, washers, and nuts to fully fix the nozzle cover plate and support blocks.

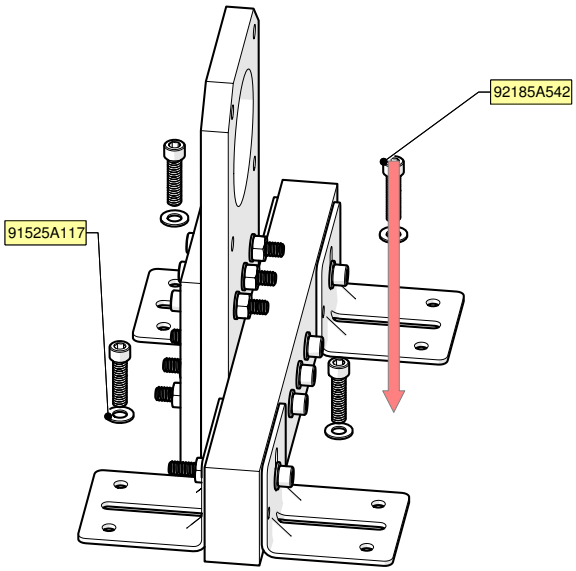

Step 4: Complete the sub-assembly by bolting the assembly onto the optics table.

E.2.2 Fore End Support Assembly

The fore-end sub-assembly is very similar to the aft end.

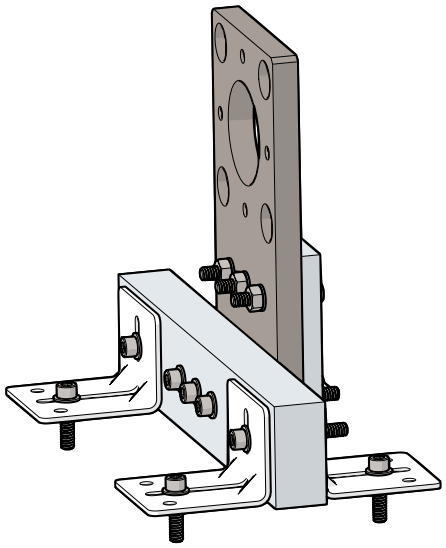

Final image of fore-end support sub-assembly.

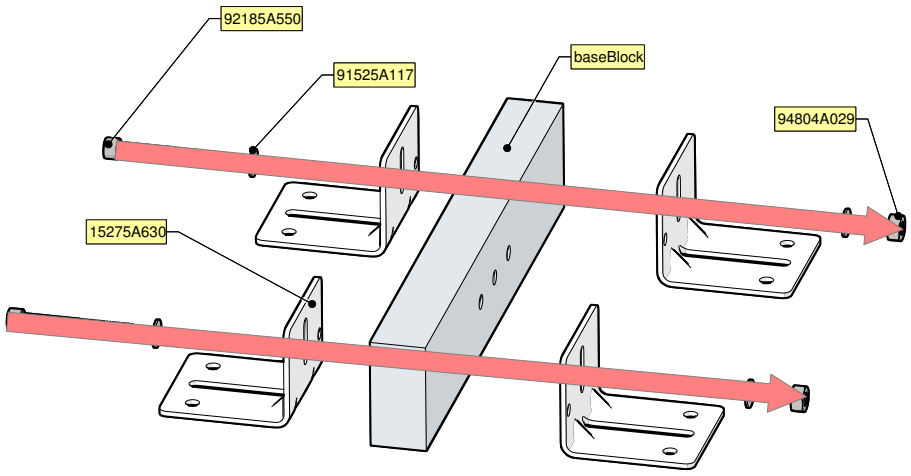

Step 1: Connect the L-brackets and the base block with the correct bolts, nuts, and washers.

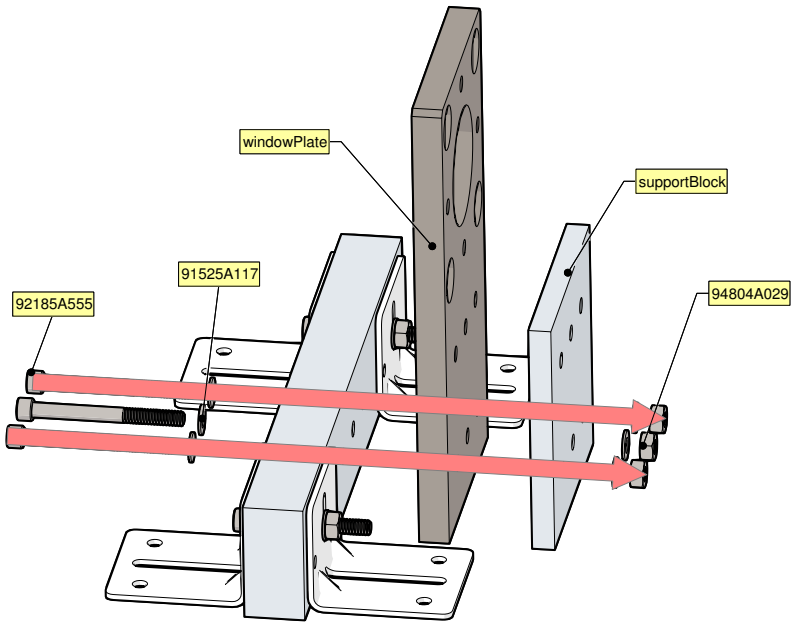

Step 2: Connect the support plate and window plate to the base block with the correct bolts, nuts, and washers.

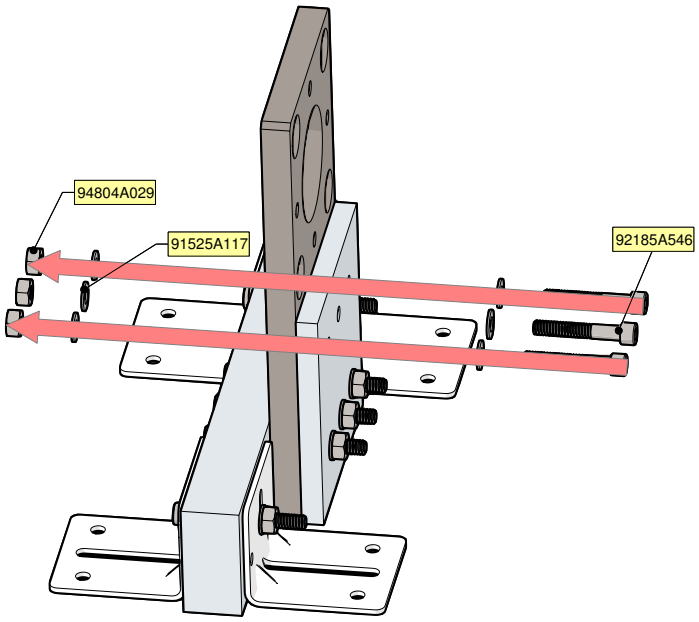

Step 3: Secure the support plate and window plate with additional bolts, washers, and nuts.

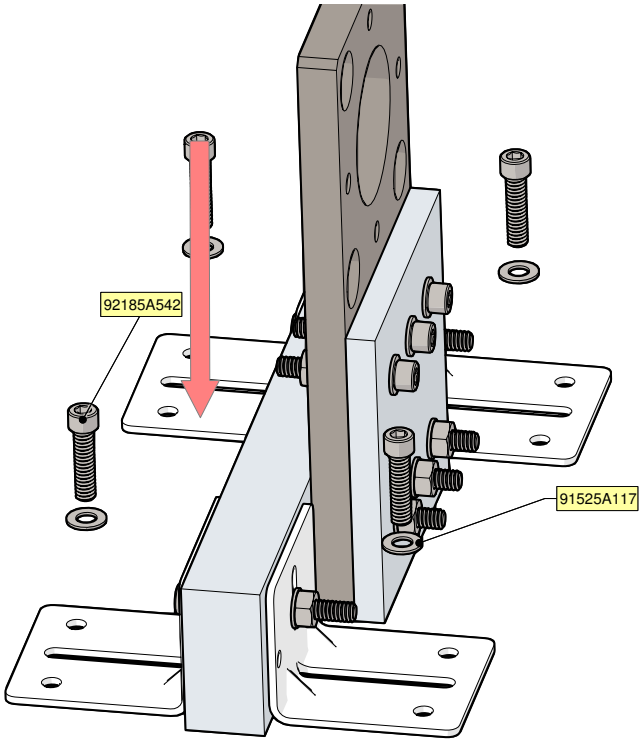

Step 4: Complete the subassembly by securing the L-brackets to the optics table with the correct bolts and washers.

E.2.3 Fore End Assembly

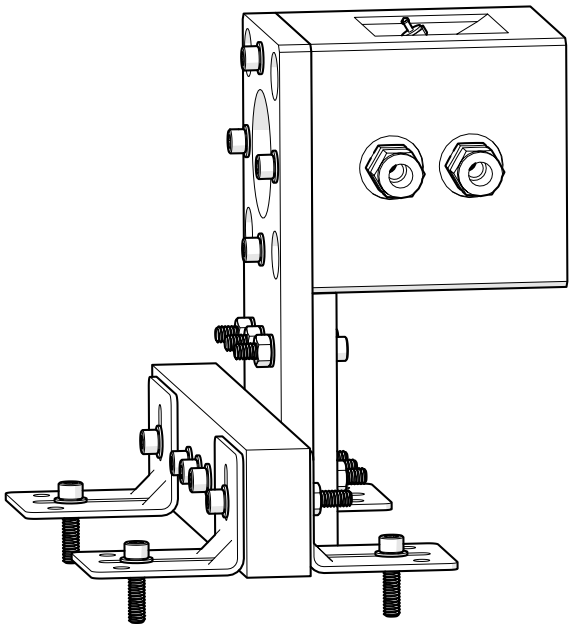

Final image of fore end sub-assembly.

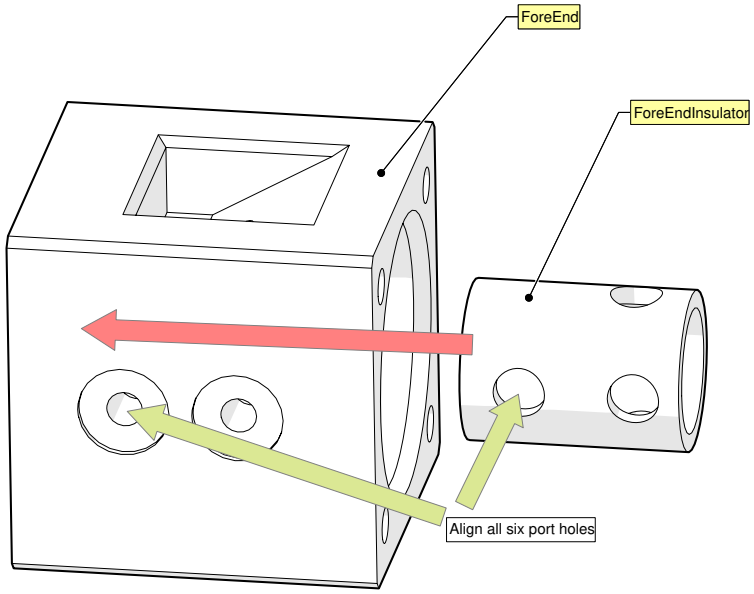

Step 1: Insert fore end insulator into fore end block. Note the alignment of the port holes.

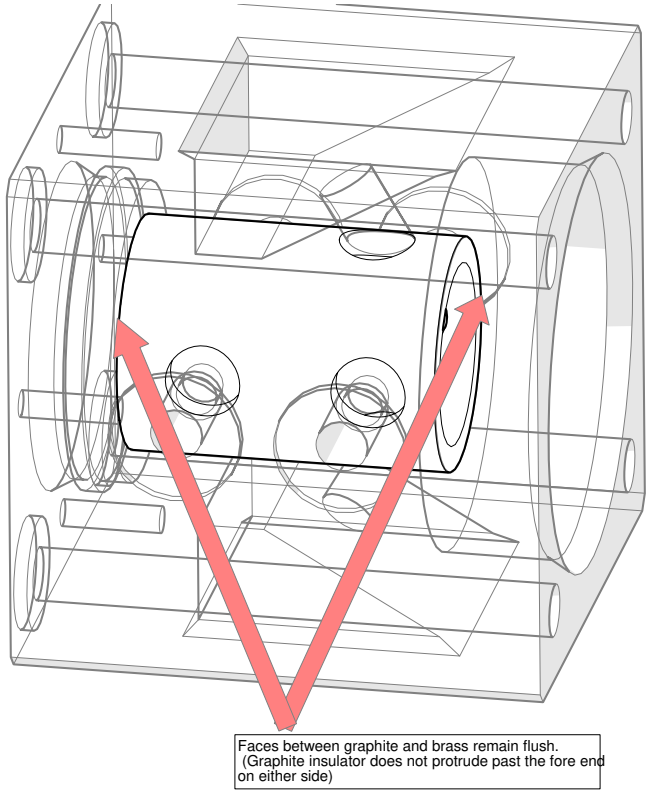

Step 1a: The insulator should remain flush on both faces.

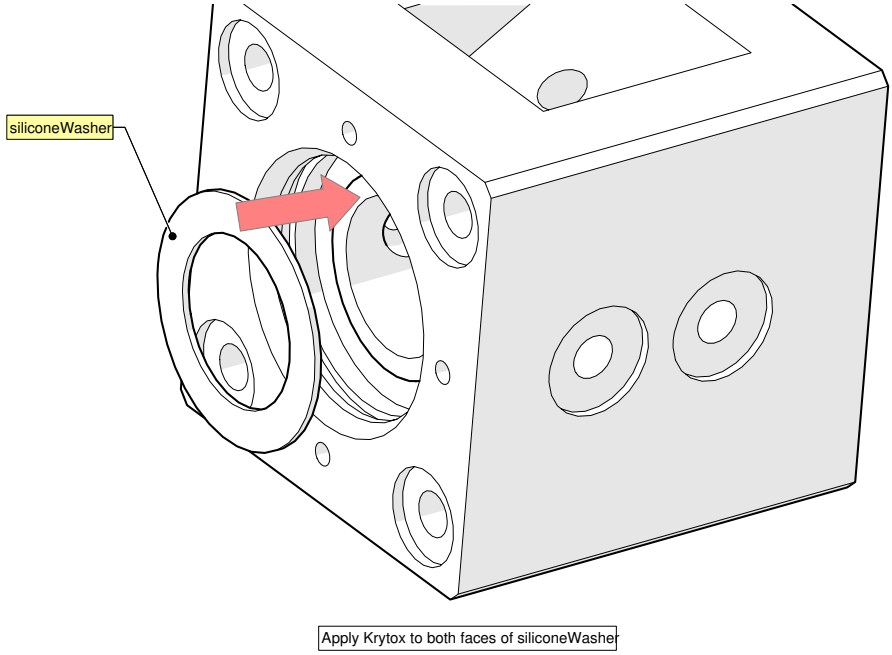

Step 2: Apply Krytox to silicone washer before installation.

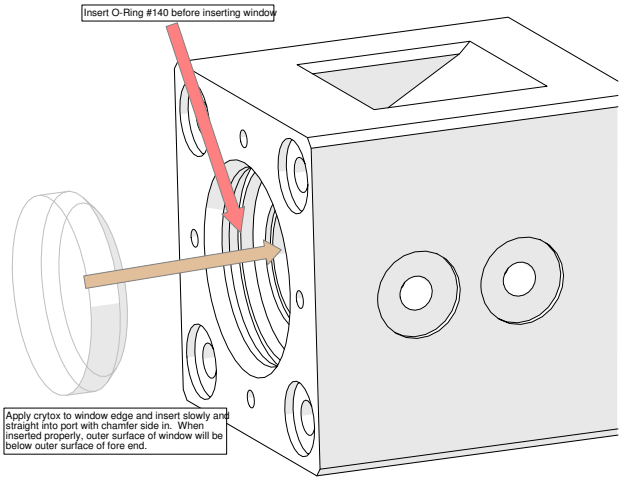

Step 3: Carefully install the sapphire window.

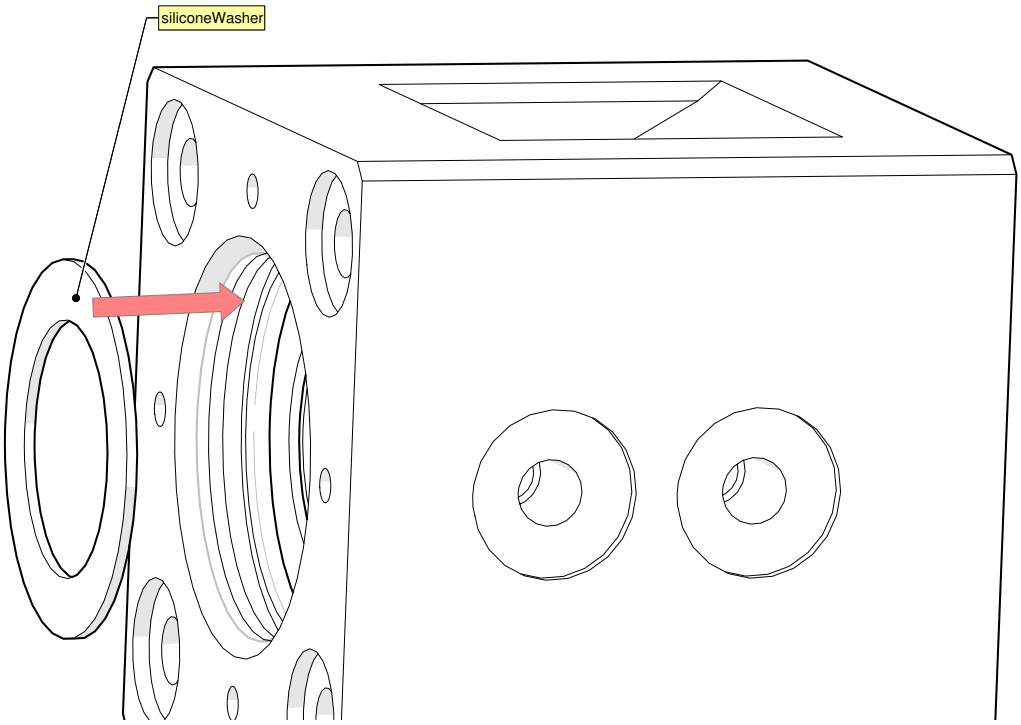

Step 4: Place the silicone washer on the sapphire window.

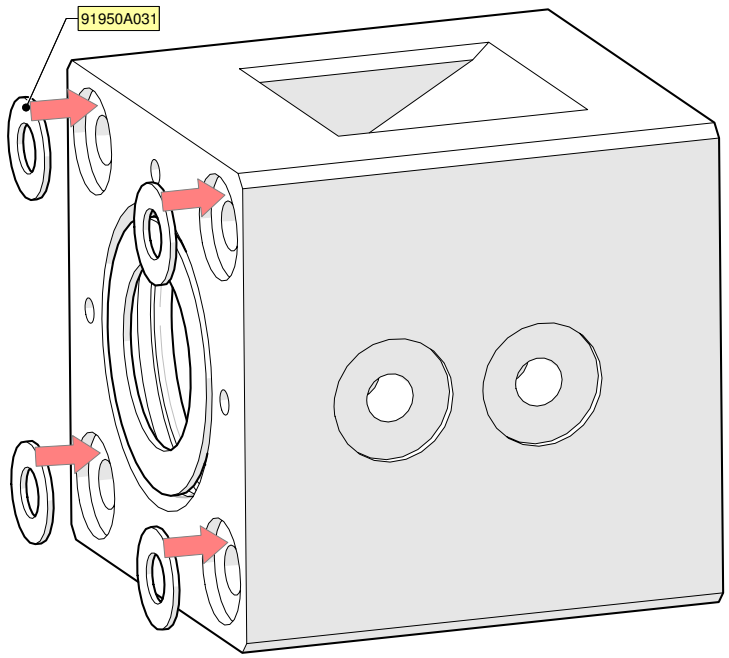

Step 5: Place the four washers in their grooves.

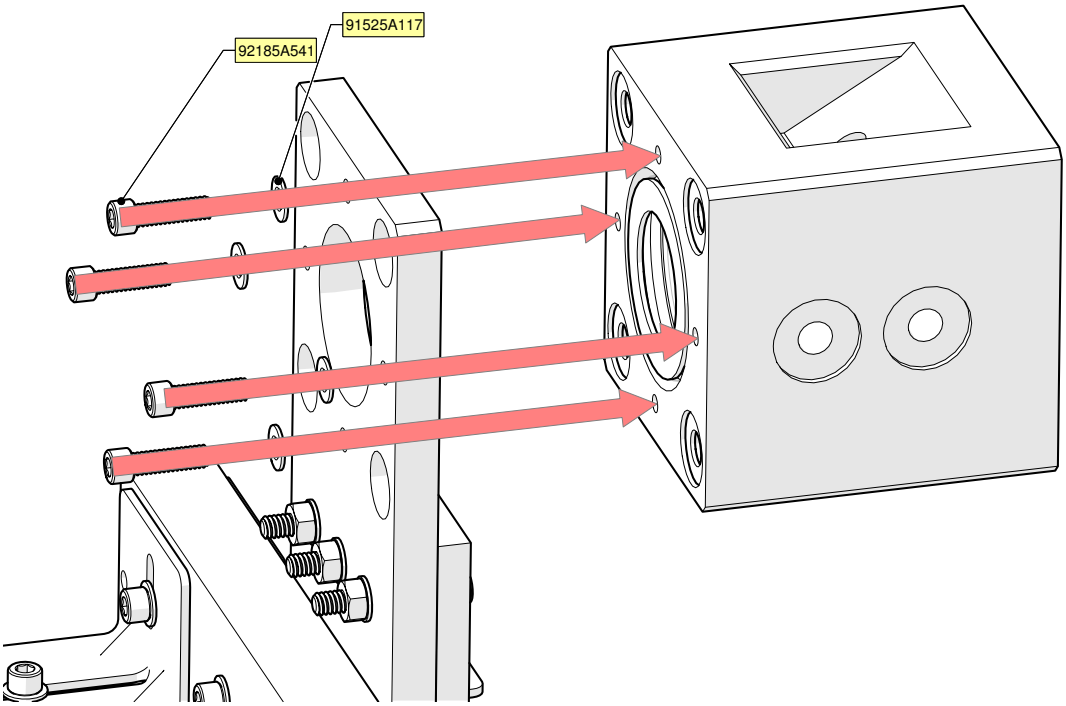

Step 6: Carefully and uniformly tighten the fore end block onto the fore end support sub assembly, making sure the washers stay in place.

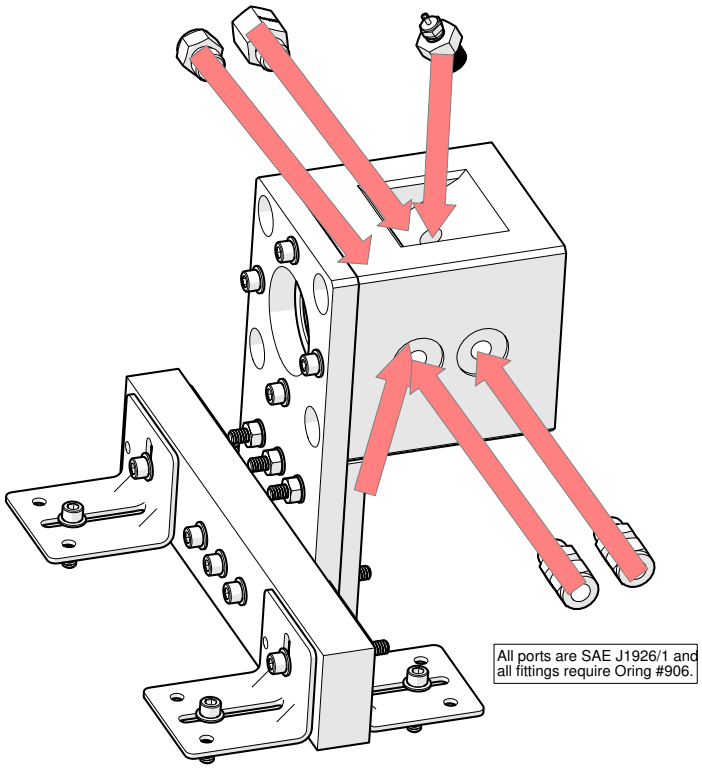

Step 7: To complete the assembly, insert all of the desired fittings on the port holes.

E.2.4 Aft End Assembly

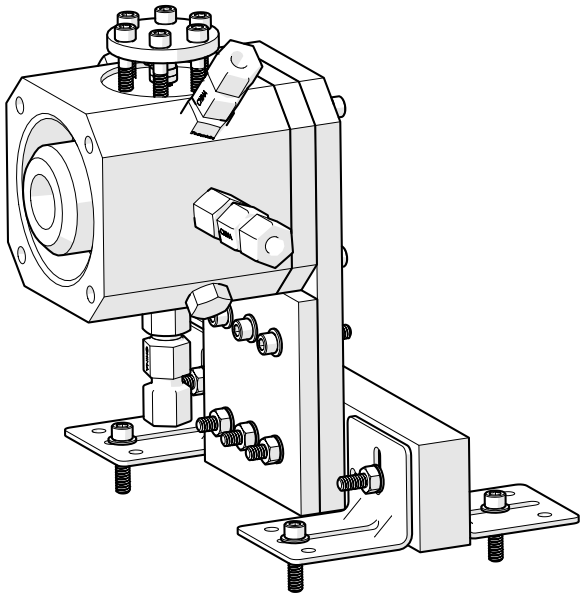

Final image of aft end support sub-assembly.

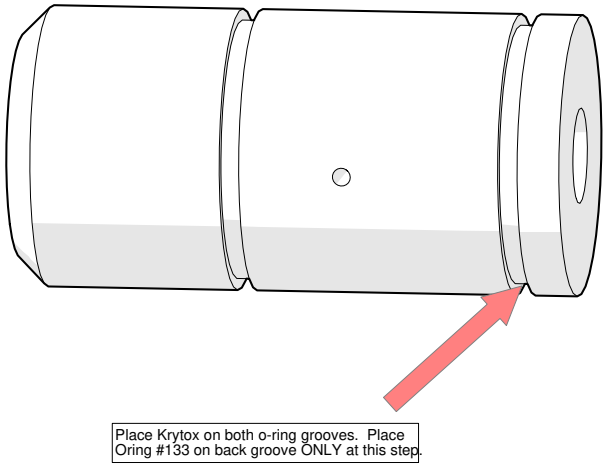

Step 1: Install back O-ring on the nozzle.

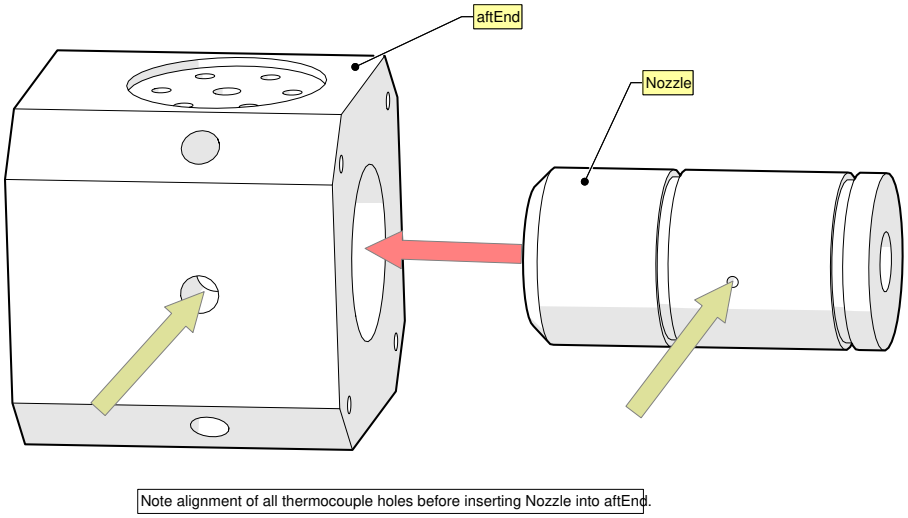

Step 2: Install nozzle through the back of the aft end. Be sure to align the port holes.

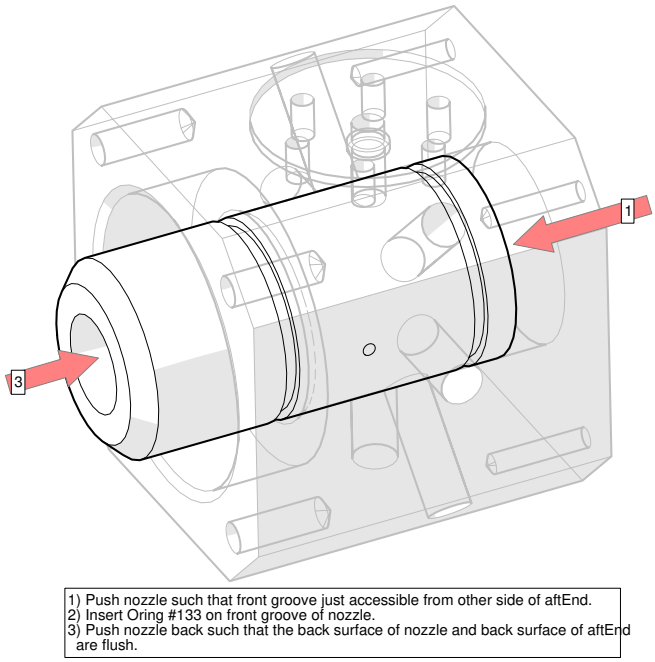

Step 3: Install O-ring and adjust nozzle.

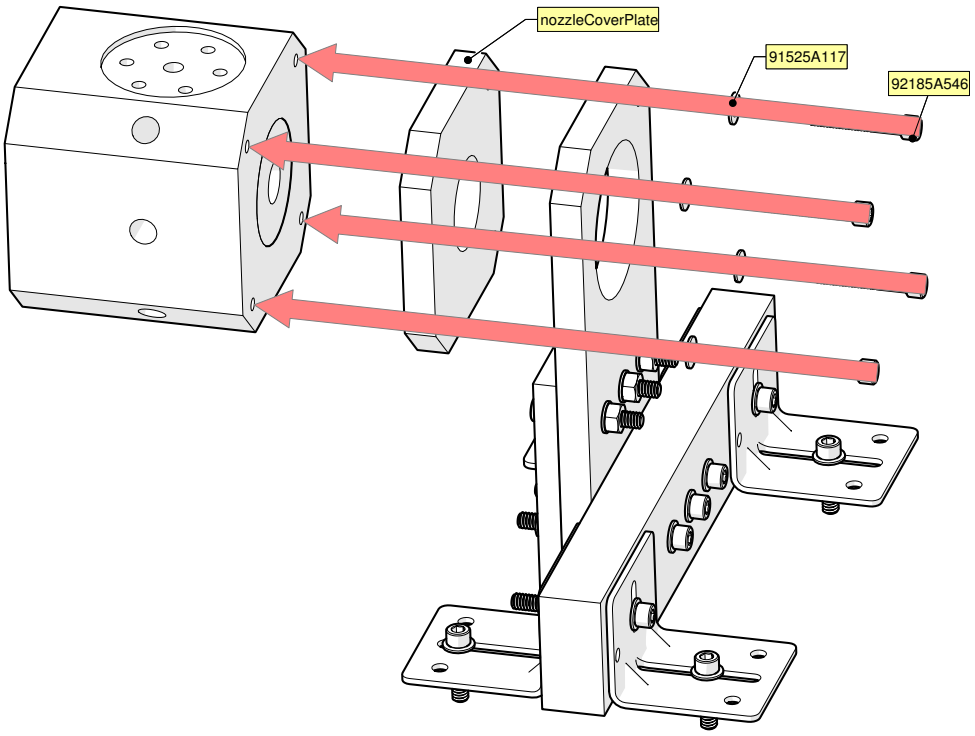

Step 4: Install aft end onto aft end support sub assembly.

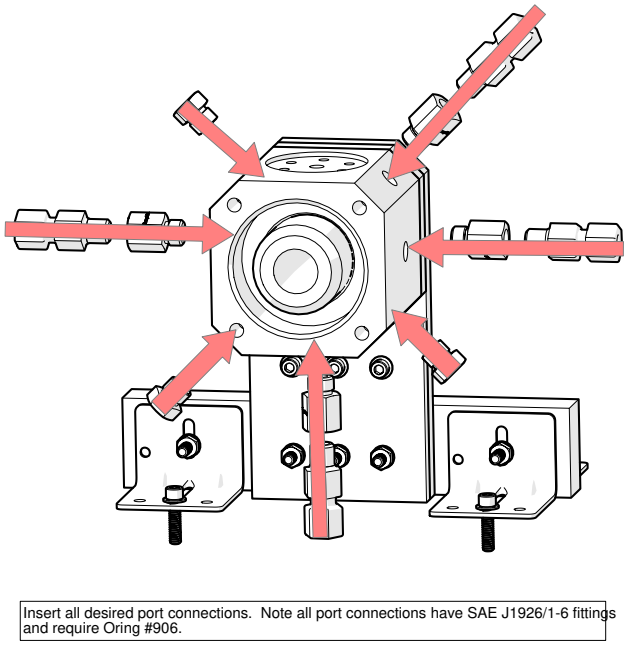

Step 5: Install desired fittings onto the seven port holes.

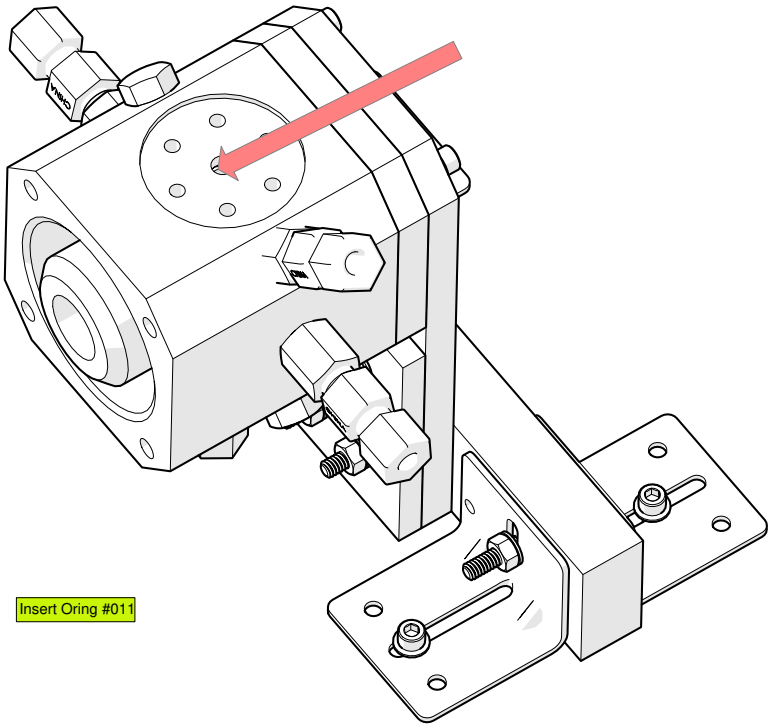

Step 6: Install O-ring to seal the ultrasound sensor.

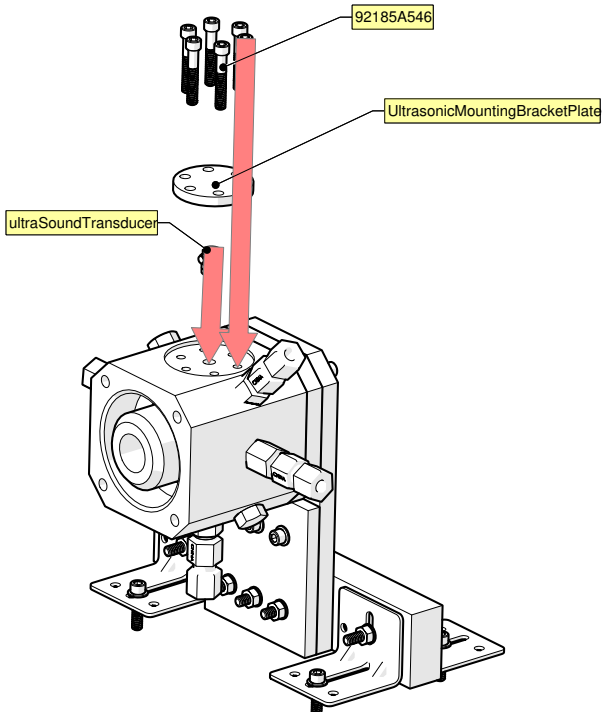

Step 7: Complete the sub assembly by installing the delay line and ultrasound transducer, along with the mounting bracket and bolts. The bolts are only finger-tight.

E.2.5 Combustion Chamber and Final Assembly

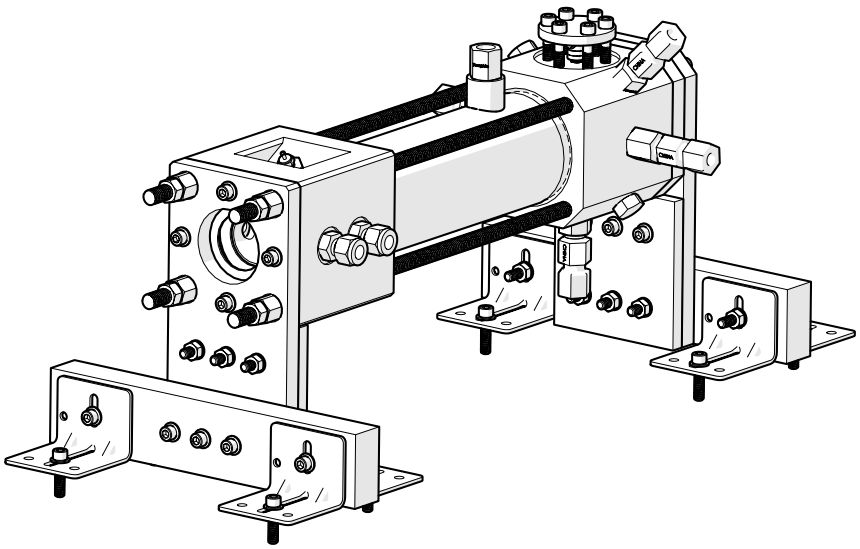

Image of assembled motor.

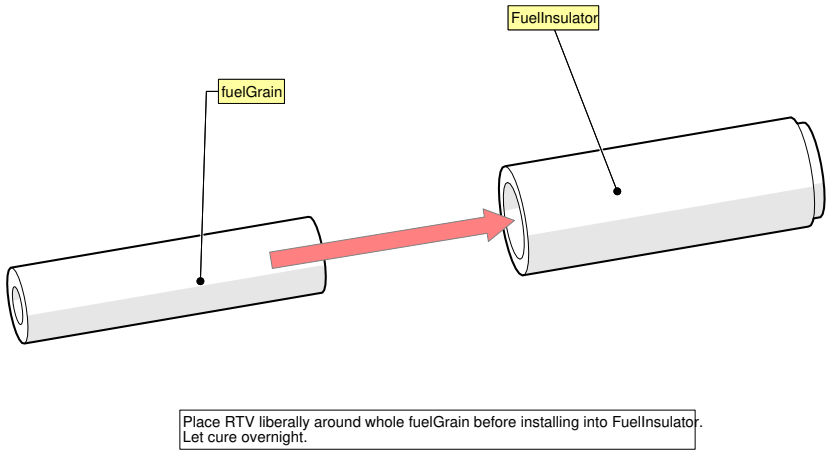

Step 1: Install fuel grain.

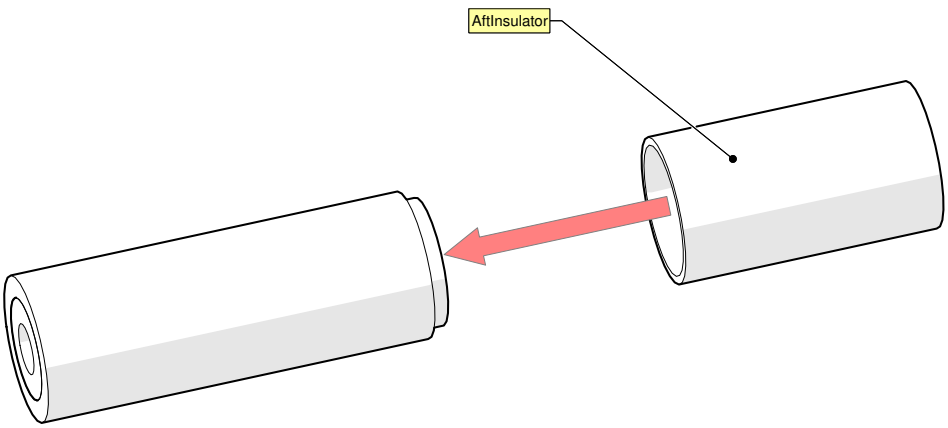

Step 2: Install aft insulator.

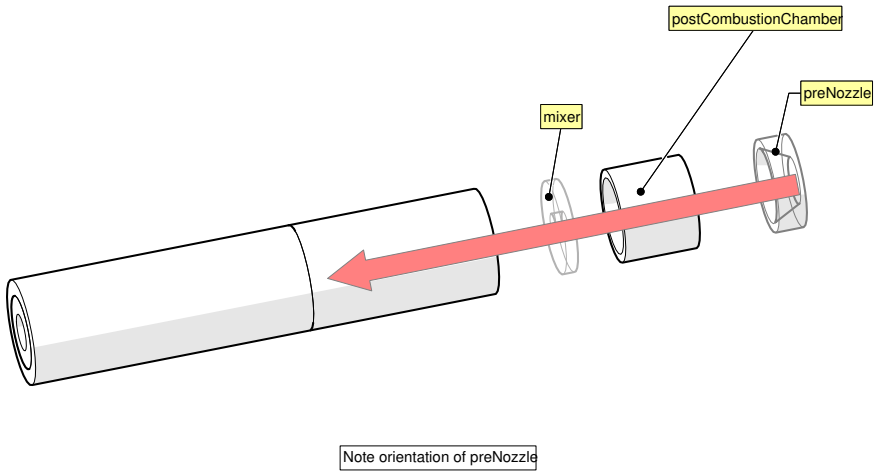

Step 3: Install internal geometry parts. Note orientation on the preNozzle (post combustion chamber ramp).

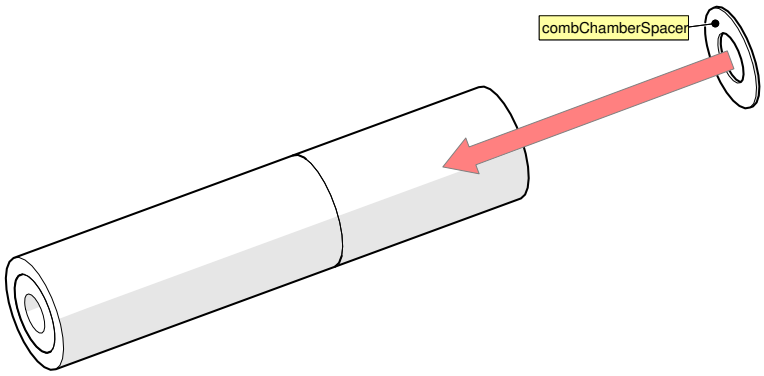

Step 3a: Carefully insert the spacer.

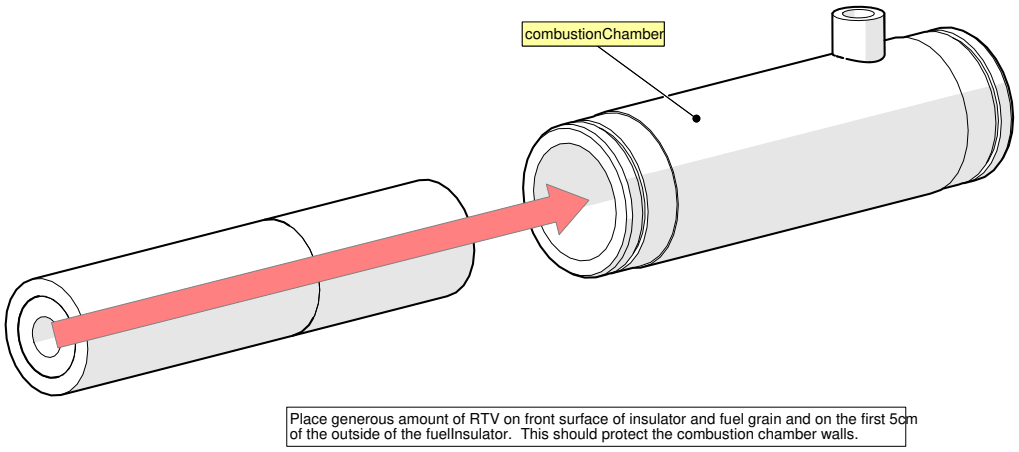

Step 4: Insert the combustion chamber elements into the stainless steel combustion chamber housing.

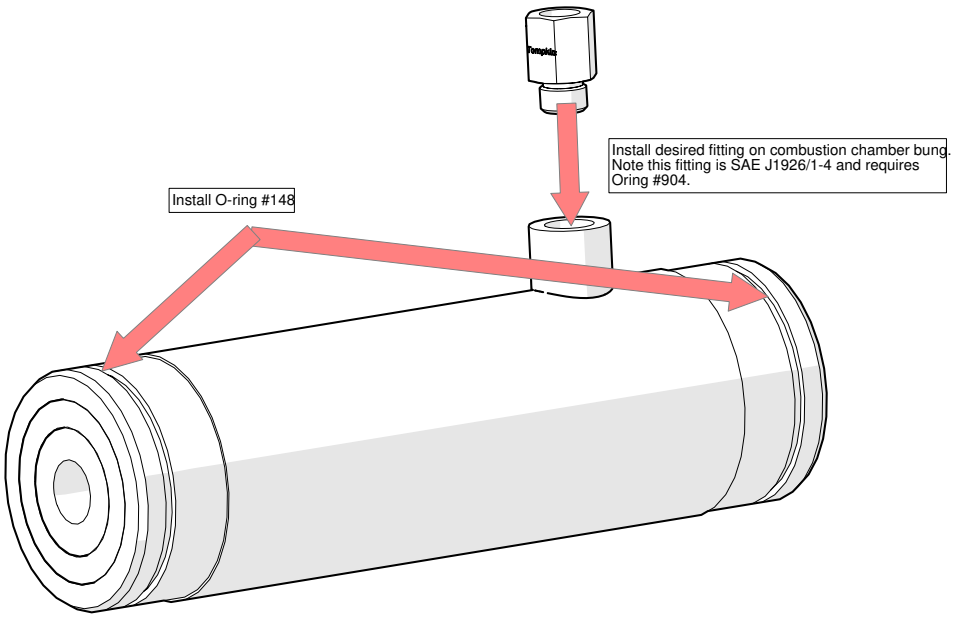

Step 5: Insert combustion chamber O-rings and desired combustion chamber sensor.

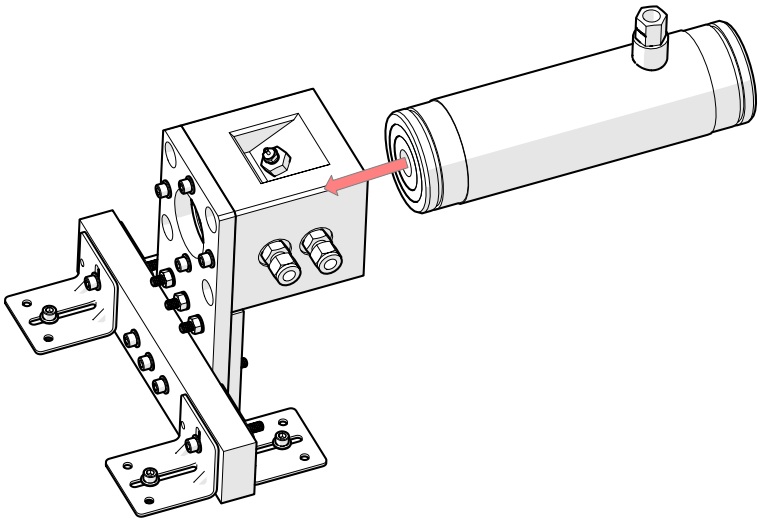

Step 6: Insert combustion chamber assembly onto fore end sub assembly.

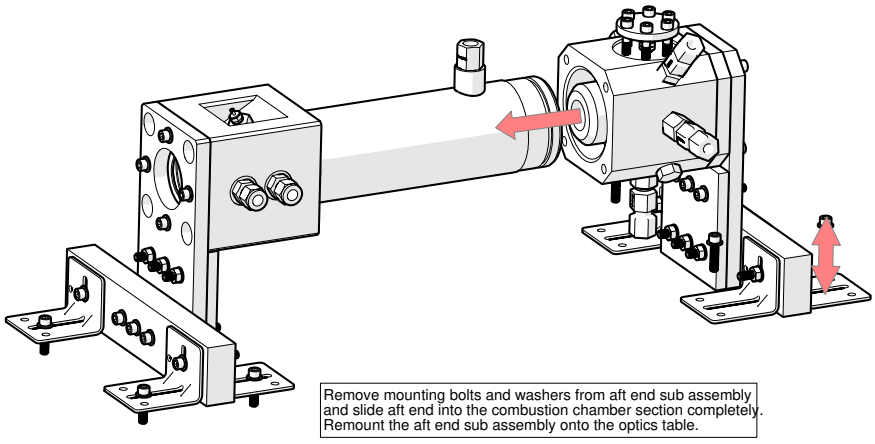

Step 7: Slide aft end sub assembly into place.

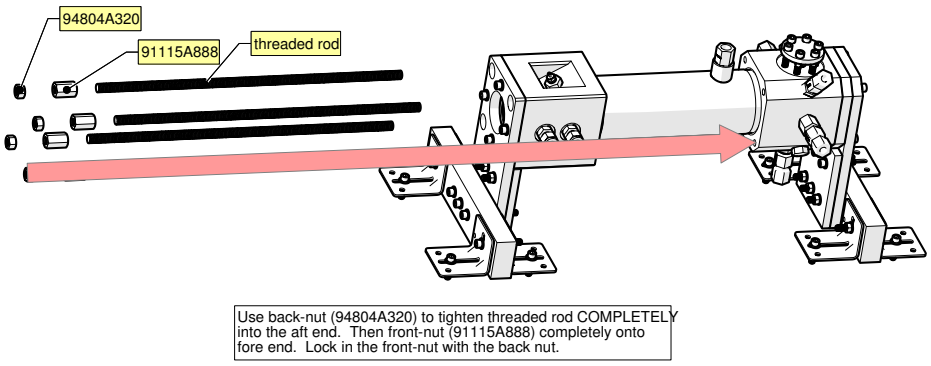

Step 8: Complete the assembly by securing motor with tie rods.

E.3 Lab Layout

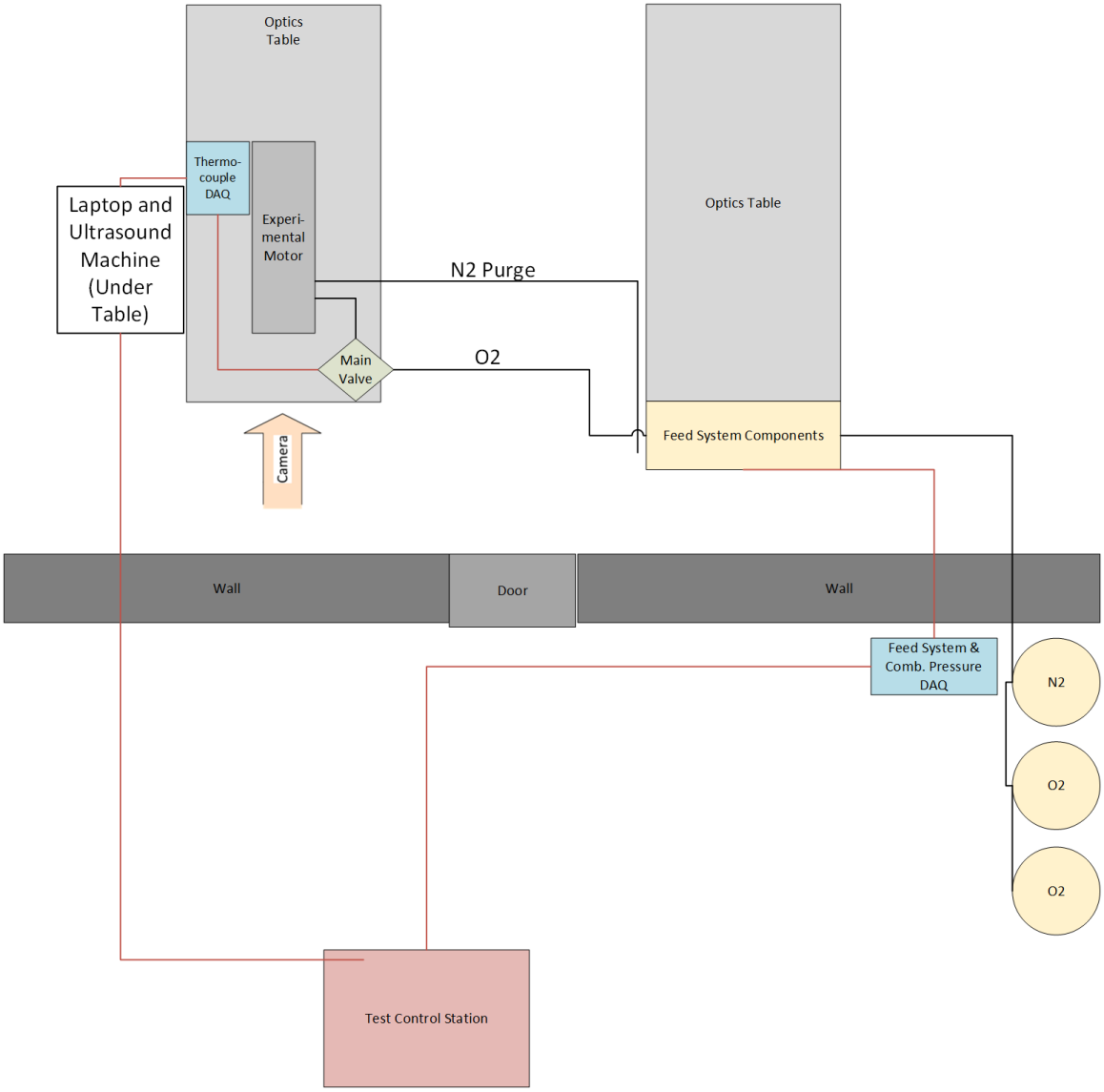

Figure E.2: The lab layout diagram shows how the motor and control systems are located in separate rooms.

Appendix F

Thermocouple Response Time

The response time of thermocouples is dependent on the diameter size of the wire used. The fastest response times are the thermocouples made from the smallest diameter wires. The smallest available wire size for K-type thermocouples is 12 μm. However, this wire was deemed too difficult to work with. It was very thin and was difficult to weld, as it was difficult to align to strands of wire.

With some experimentation, it was determined that the best option was 50 μm wire. According to the specifications provided by Omega Engineering [41], the response time constant should be about 0.01 seconds. Because the time constant is defined as the time it takes for the sensor to measure 63.5% of an instantaneous change in temperature, the time it takes for the sensor to read the actual temperature is roughly five time constants. Therefore, the a 50 μm wire would work well when sampling at 10 Hz.

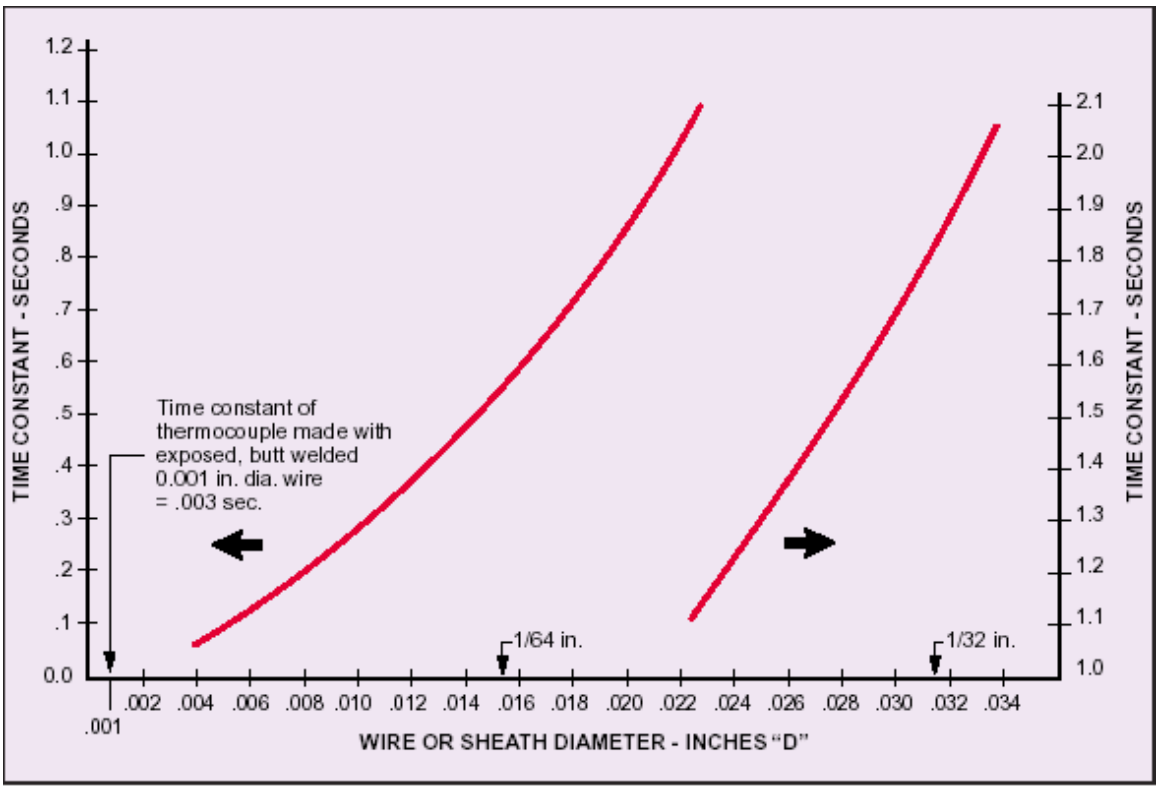

Figure F.1: The thermocouple response time depends on the wire diameter. Image courtesy of Omega Engineering. Reprinted with permission.

Appendix G

Data Acquisition and Control

This section of the appendix describes the data acquisition and control scheme used for the fabricated motor. Note that the control and acquisition scheme will be updated. The updated scheme can be found in another Appendix K.

G.1 Control System Overview

The motor control is managed by the "main LabView computer". This computer is tasked with controlling the feed system and recording feed system sensors as well as the pressure sensors in the motor. This data is enough to approximate the flow rates in the motor, the stability of the motor, and the C^* efficiency of the motor.

The thermocouple and ultrasound data is logged by a laptop placed under the optics table. This computer is much closer to the motor to reduce noise and voltage losses between the sensors and the motor. Additionally, because this computer is separated physically from the other sensors and motor controller, it is inherently more reliable.

G.2 The Main LabView Computer

As mentioned earlier, the main LabView computer is tasked with actively managing the feed system sensors and the flow rates in the feed system. During a test, two software packages are concurrently running. The first is the ERTune software package. This package connects to the dome-loaded pressure regulator and actively sets the driving pressure of the feed system. The second package is the LabView software package.

The LabView software package contains a VI that was developed to control the motor firing sequence and log data at approximately 1500 Hz. The main panel of the VI is shown in Figure G.1.

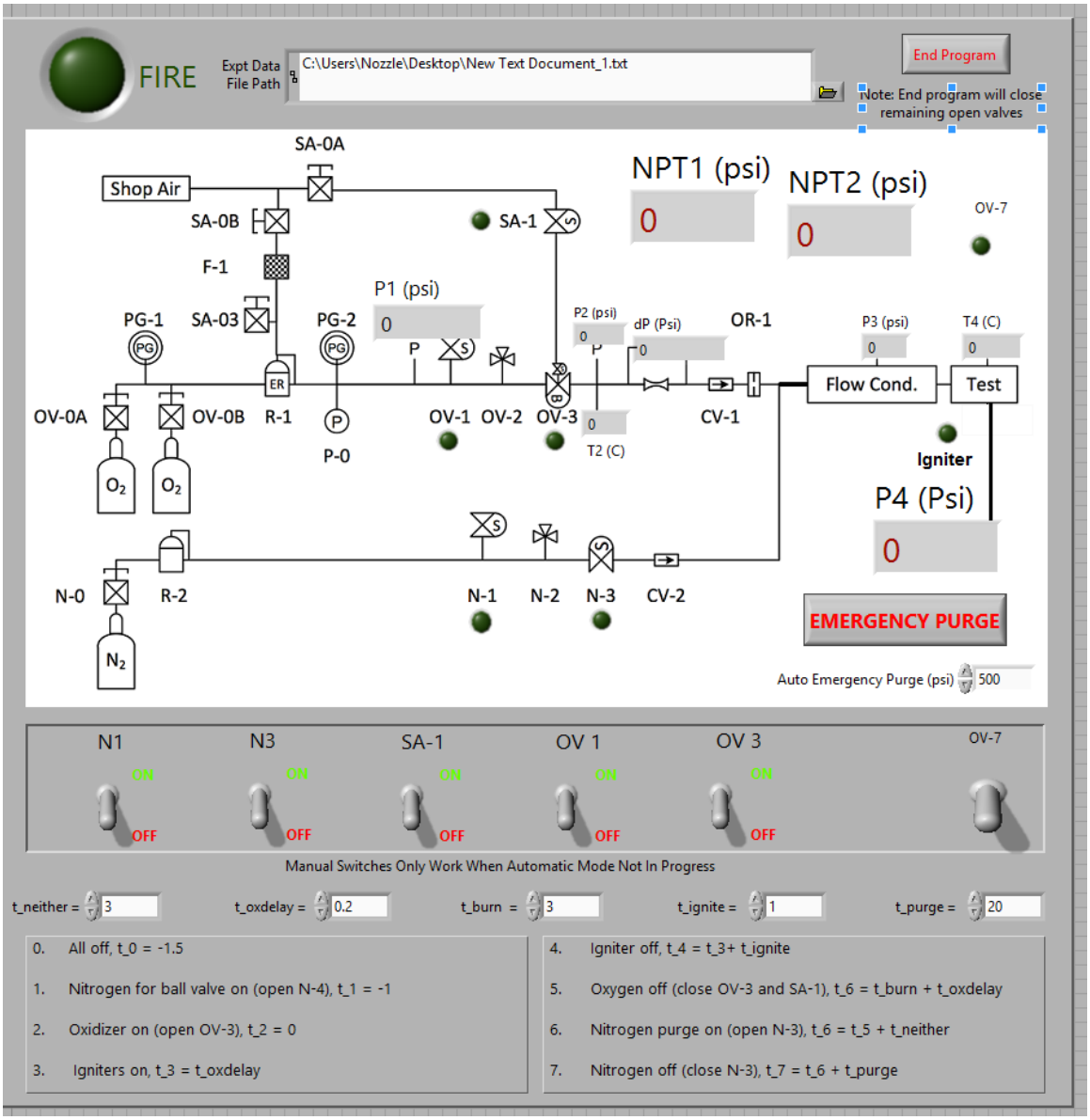

Figure G.1: The main front panel shows the control switches for the individual valves along with feed system conditions.

This LabView interface was originally developed for the Stanford Combustion Visualization Facility, and another interface at JPL was developed using similar control logic. Both of these systems have proven problematic in terms of ignition timing.

Looking back at the data, the timing sequences achieved do not always agree with what was desired. Because of this, it is likely that the ignition control timing is not consistent and is likely at least partially the cause of failed ignitions.

Other more professional systems, such as those in use by NASA and SpaceX, involve separating the timing control sequence hardware and the data collection hardware. Having a hardware controller that is only tasked with timing sequences (without the overhead of an operating system or other concurrently running software packages) is highly recommended for any system requiring precise and reliable timing.

Because of this, a new control system design is being developed from the ground up and is described in Appendix K.

G.3 Ultrasound and Thermocouple Data Acquisition

A separate laptop was used to log the ultrasound and thermocouple data. The thermocouple data was logged by an MCCDaq USB 2408 device. This device was the only affordable 24-bit thermocouple DAQ with fast sampling rates. The ultrasound data was logged through a USB-TTL interface (see Section G.4).

Because this data was logged on a different computer than the other motor data (flow rates, pressure transducers, etc.), some sort of communication was required so that the data could be aligned during post processing.

It was decided that the easiest and most reliable method of aligning the data would be to match the main oxidizer valve timing. A wire was run from the main oxidizer valve to a digital input line of the MCCDaq USB2408 device through a relay. The relay provided isolation from the ground planes and reduced noise.

The MCCDaq device therefore logged the thermocouple data, ultrasound data, and the power status of the main oxidizer valve for every experiment. With this data, it was simple to align all of the data.

Because the laptop was placed under the motor, it was not realistic (nor safe) to approach the laptop to start recording data prior to a firing. Therefore, a small network router was placed under the table as well. The laptop was connected to the router, and another computer was connected to the same router from the control room. From there, a remote connection was established into the laptop under the computer, and a record command was sent over the network. This approach was found to be very reliable and convenient and should be considered by other groups. However, a downside of this logging scheme is that a laptop must be placed in close proximity to a rocket motor, which

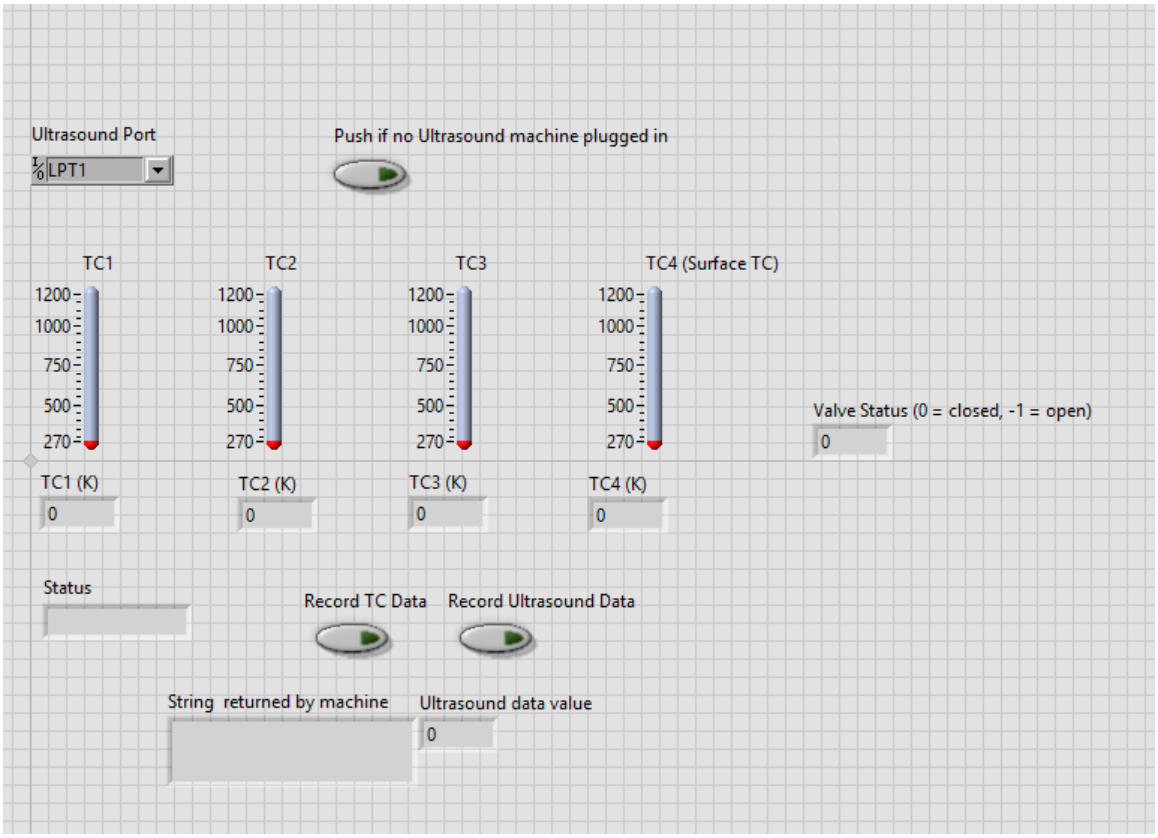

Figure G.2: The front panel for the ultrasound logging computer shows the control switches for logging ultrasound and thermocouple data. It also shows the status of the main power valve, which is logged for timing purposes.

might be problematic for some users. My specific laptop was covered under an accidental damage warranty and I was not concerned about losing the laptop.

G.4 Guide to Capturing Ultrasound Data over USB

Getting the Ultrasound data into the computer was a tricky problem that required collaboration with NDTSystems directly. This is because logging ultraound data on a computer is not considered typical use. Most systems are designed to be used in the field and high frequency logging is not necessary.

When the Raptor Ultrasound System was first purchased, the onboard software was in a primitive (but still usable state). Because of this, the serial-USB port was not active and a different scheme was needed. Jerry Rutherford of NDT Systems provided the pinouts for the ultrasound machines 44-pin connector that allowed us to log data by mimmicking a movement on a virtual scanning

device. Although this configuration proved to work, it was never tested in a motor firing.

Prior to the motor tests, NDTSystems provided the lab with a firmware update for the machine. This update provided USB functionality and allowed for the transfer of ultrasound thickness data over the USB interface.

I've developed two methods to capturing data over the USB serial interface. The Ultrasound machine acts as a virtual COM port (VCP) that can communicate with another TTL or RS232 device with a baud rate of 115200 Hz. Currently, the only way to request data is to send a "?" command over the line to the machine. The machine then immediately responds with the displayed thickness on the machine. Future software updates will allow for more functionality, such as the ability to change settings, take screenshots, and much more.

The onboard serial module on the Ultrasound device is manufactured by Future Technologies Devices International, Limited (FTDI). For any communication with a computer, the proper drivers need to be installed. At the moment, drivers are available for OS-X based, Windows based, and Linux based computers. The correct driver is the VCP driver, which can be found at Reference [86].

G.4.1 Capturing Ultrasound Data over LabView

The first developed method to log data was through LabView. This setup allowed for logging data to a simple file at a fixed frequency. The interface setup is shown in Figure G.3. It should be noted that the free NI-Visa package is required for this setup. This may limit the use of this particular method of capturing data.

It should also be noted that at the moment, the NI-Visa package has a bug and the VI will fail if data is captured for too long a time period. Therefore, it is recommended to run the package (whether recording data or not) for a maximum of five minutes (depending on the computer). Therefore, the VI should only be started just prior to a motor firing. Future software updates may resolve this issue.

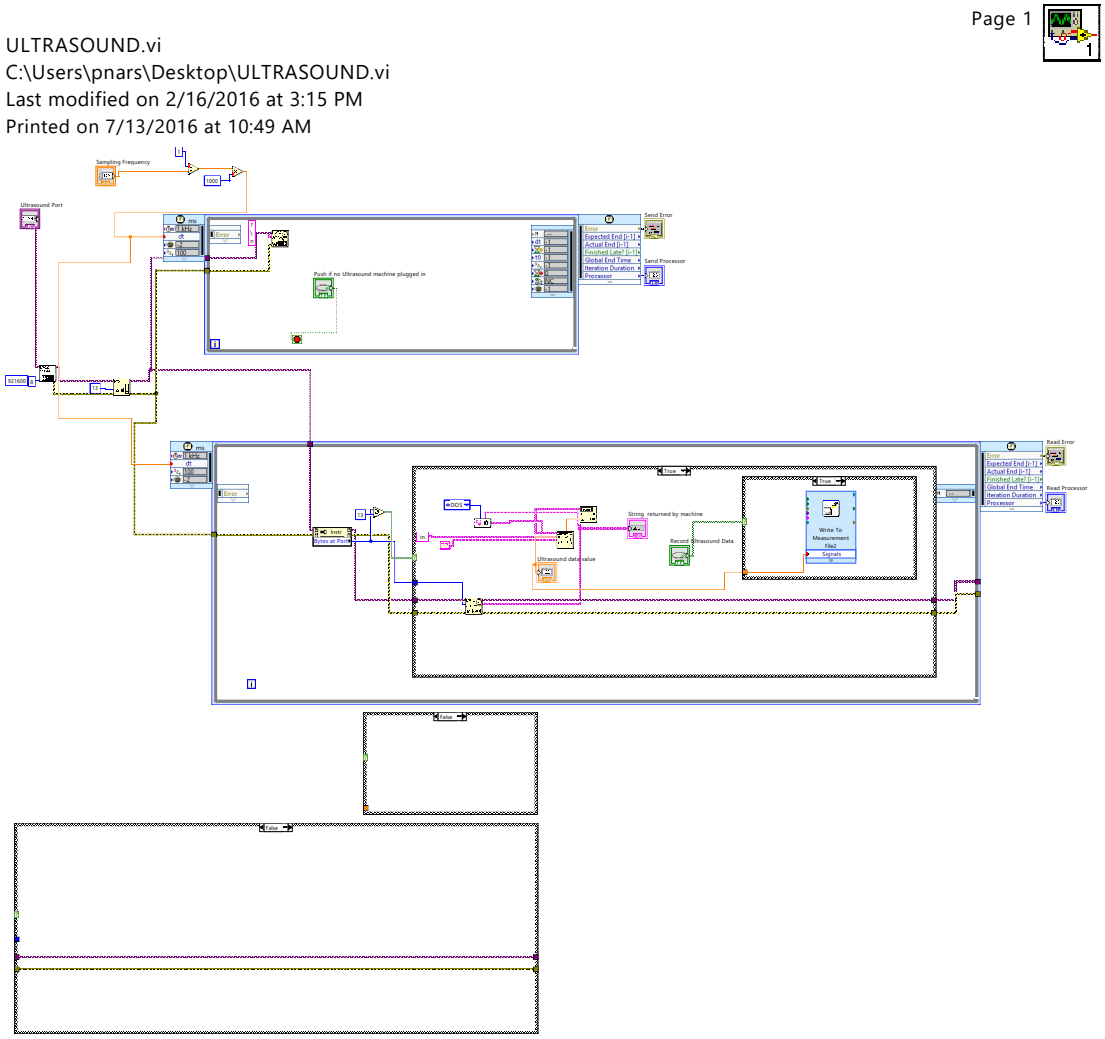

Figure G.3: The diagram for capturing ultrasound data involves parallel loops running at the same time. One loop sends a thickness request messages, while another loop analyzes the read data.

G.4.2 Capturing Ultrasound Data Through Python

In addition to capturing data through LabView, I also developed a simple Python library to capture data programmatically. This package was used to scan a full fuel grain with ultrasound with a robotic scanning platform, which was built over a summer with Adrian Costantino, a summer research student visiting from CalTech. This library is useful when event-based logging is desired. A record is only recorded on command, not at a particular frequency.

This method also gets around the buggy LabView software and because it runs on an open environment, it can run on any platform that can run Python. To date, I've tested it on OSX and Windows without any issues. The library code is presented below, as well as a sample test case.

---

ultraSoundMachine.py

```
#ultraSoundMachine.py
#This class allows one to connect to a Raptor Ultrasound machine (or another ultrasound machine manufactured by
     NDT Sytsems)
#and record data.


import serial
class ultraSoundMachine:
    """This class is used to talk to the ultrasound machine"""

    def __init__(self,comPort):
        self.port = comPort #COM port is specified upon call.
        self.baudRate=115200 #this is the baud rate to use.  May need modification.
        self.lastReadings=[]
        self.ser=serial.Serial(self.port)
        self.ser.baudrate=self.baudRate
        self.ser.timeout=0.5 #wait time before time-out.  This works well.
        print self.ser


    def sendCommand(self,command):
        #send generic command.  Not needed externally for simple reading of data.
        #user should use this only if they are trying to do something fancy
        self.ser.write(command+'\n')

    def readData(self):
        return self.ser.readline()


    def readDataPoint(self):
        #This is for an ultrasound machine.  It will give the reading displayed on the screen
        #this is the best way to acquire ultrasound thickness measurement
        #externally
        self.ser.write('?')
        dataLine = self.readData()
        data=float(dataLine[0:-5])
```

```
        self.lastReadings.append(data)
        return data

    def disconnect(self):
        self.ser.close()
```

---

ultrasoundMachineExample.py

```
#ultraSoundMachineExample.py
#This script connects to an ultrasound machine at COM3 and then
#reads three data points and prints them
#and then disconnects the ultrasound machine and exits.
import time
import ultraSoundMachine
raptorMachine = ultraSoundMachine.ultraSoundMachine("COM3") #connect to the ultrasound machine at port 'COM3'
time.sleep(1) #wait to give the machine a chance to connect
i=0
while (i<3):
    print raptorMachine.readDataPoint() #read and print a thickness reading from the ultrasound machine
    i = i+1

raptorMachine.disconnect() #disconnect from the machine
```

The only critical note about this Python library is that the correct COM port must be specified in order to connect to the ultrasound machine. Once connected, a simple "?" command will return the desired data.

Appendix H

Operating Procedures

This appendix chapter contains the operating procedures for fabricating the Stanford Initiator (along with MSDS information on the igniter components), spin-casting the fuel grains, welding thermocouples, installing thermocouples, and for running the experiment (and associated cold flow tests).

H.1 Igniter Fabrication and Assembly Procedures

The igniter fabrication and assembly procedures begin on the next page.

Stanford Initiator Fabrication Procedures

Pavan Narsai

Last Updated: August 12, 2016

Date: _____
Igniter Components Fabricated:_____
Number of Components Fabricated:_____

Summary:

The following procedures are for fabricating a full batch of the Stanford Initiator. This includes the glow plug igniter and the secondary slug. It is important to understand the full Stanford Initiator assembly before proceeding.

Contact:
Contact Greg Zilliac from NASA AMES regarding any questions or supplies:
gregory.g.zilliac@nasa.gov

Emergency Contacts:
Contact Information for Stanford EH&S:
Robert Porterfield, Fire Protection Engineer
650-725-1343; rporterfield@stanford.edu

Contact Information for Police/Fire/911:
(650) 329-2413

Stanford Initiator Assembly:
The full assembly consists of four main parts: These are:

1. Glow plug igniter: This modified from a McCoy MC59 glow plug. This is consumable (one time use ONLY)
2. Copper Ring: This seals the glow plug igniter into housing. This is consumable and is bundled with a new McCoy MC59.
3. Housing for secondary slug: This is a part made specifically for a motor that houses a secondary slug. This part is reusable (with proper cleaning).
4. Secondary Slug. This part is consumable.

An image of the assembly is provided below:

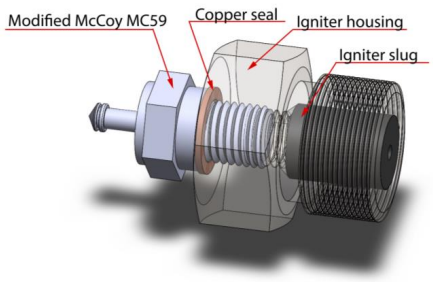

Part 1: Supplies Needed

The following PPE are required:

1. Safety goggles
2. Disposable gloves
3. Ventilated room
4. Face Mask
5. Proper clothing (short sleeve top preferred)

The following materials are required:

1. Mortar and Pestle
2. Sieve (5μm preferred)
3. Magnesium (Mg) Powder – High quality and fine powders necessary.
4. Container for magnesium powder (with cutout for sieve on top)
5. Potassium Nitrate (KNO3)
6. Nitrocellulose (NC) powder –High quality necessary.
7. Sulfur
8. Epoxy – Previous batches have used DevCon 1 hour mix. A long cure time is necessary
9. Large supply of new McCoy MC59
10. Glow plug holder (plate with ~48 threaded holes)
11. Spreading rod (like a dough spreader)
12. Acetone
13. Stamp for the correct size secondary slug
14. Small drill and small drill bit (1/16")
15. High quality nitrocellulose ping pong ball
16. Scale to measure masses
17. Zip lock bags
18. Marker / Pen for labels
19. Various cups for sieved supplies

Part 2: Mixture Ratios

The following are the mass fraction ratios of the primary igniter mixtures. These are listed here for reference so that it is known how much supplies to prepare.

1. Glow plug igniter mixture:
    a. 45% KNO3
    b. 30% Mg
    c. 20% NC powder
    d. 5% Sulfur
2. Secondary Slug Mixture
    a. 60% KNO3
    b. 20% Mg
    c. 20% Epoxy

For reference, list mass of required materials here:

1. Glow plug igniter mixture:
    a. KNO3: _____
    b. Mg:_____
    c. NC powder:_____

   d. Sulfur:_____
2. Secondary Slug Mixture
   a. KNO3:_____
   b. Mg:_____
   c. Epoxy (Total):_____

Part 3: Prepare Materials
This portion of the procedures should take several hours if not longer. It is very important to slowly and carefully perform this step, as these processes are critical to the success of the manufactured batch. **Take your time and do it properly.**

Prepare Magnesium
1. Pour magnesium powder into container and close container with a lid attached to a sieve.
2. Shake magnesium powder into a cup labelled for magnesium powder.
3. Ensure the integrity of the sieve attached to the lid of the container every few minutes.

Prepare Potassium Nitrate
1. Take a large chunk of KNO3 from supply and place in mortar
2. Break the KNO3 into fine particles with pestle into fine particles
3. Break the KNO3 into finer particles
4. Sieve the KNO3 into a cup and label the cup

Prepare Nitrocellulose Powder
1. Place NC powder or chunks into mortar
2. Break the NC into fine particles with pestle
3. Break the NC powder into even finer particles
4. Sieve the NC powder into a cup and label the cup.

Prepare Sulfur
1. Take some Sulfur from supply and place in mortar
2. Break the Sulfur into fine particles with pestle
3. Break the Sulfur into even finer particles
4. Sieve the Sulfur powder into a cup and label the cup

Part 4: Prepare Glow plug Igniter Mixture
This portion describes how to make the glow plug initiator mixture for use in modifying the MC59 glow plug.
1. Mix the proper mass fractions of supplies into more and mix with pestle slowly but thoroughly.
2. Once mixed, place in cup and dissolve into acetone.
3. Mix thoroughly.
4. Pour mixture onto a flat plate or table.
5. Let dry for 1+ Hrs (overnight works too).

6. When dry, break up into fine powder in mortar and pestle.
7. Place fine powder into a container with sieve attached to cap.

Part 5: Assemble the Glow plug igniter

This portion of the procedures describes how to complete the glow plug igniter.

1. Take large batch of McCoy MC59 glow plugs and place the copper seals in ziplock bag. They will not be needed until igniter assembly.
2. Place each McCoy MC59 onto plate with 48 threaded holes. Thread the glow plugs in a consistent direction and thread until the beginning of the threads are flush with the plate.
3. Place the plate (with glow plugs mounted) into a wide container.
4. Shake glow plug mixture (through the sieved container) into the port holes for the glow plugs.
5. When the glow plugs appear full, shake the glow plug plate so that igniter mixture settles into the glow plugs.
6. Repeat Steps 4 and 5 until the glow plugs are completely full of mixture
7. Put ping pong ball (or nitrocellulose) into container. Mix with acetone until honey-like viscosity is reached.
8. Seal the glow plug mixture into the glow plugs by pouring some of the mix from Step 7 onto the cap. **ENSURE THAT THE SEAL ONLY COVERS THE HOLE AND DOES NOT FLOW ONTO THE THREADS OR THE PLATE.**
9. If the seal over-flows, it will likely break off during handling or assembly, rendering the glow plug and igniter assembly useless.
10. When dry, remove all glow plugs from threaded plate and store invidivually in ziplock bags.
11. **DO NOT USE REGULAR MULTIMETER TO MEASURE RESISTANCE.** Use Kelvin Bridge to measure resistance, if necessary, of each assembled glow plug, and label individually.
12. Each glow plug is stored separately so that if the seal breaks (in the bag), the bag will be left with a black residue, and it will be immediately clear that the glow plug needs to be refilled and sealed.

Part 6: Fabricate the Secondary Stage

This portion describes how to make the secondary slug for the igniter assembly.

1. Prepare roller and guide for roller. (Roller should be offset from flat surface by desired height of secondary slug).
2. Have stamp ready. The stamp should produce a cylindrical shape with OD of the desired OD of the final secondary slug. A short straight tube works well. Swagelok 3/8” tube makes a usable size for the igniters used in lab.
3. Mix the dry contents of the Secondary Slug mixture together in a cup.
4. Mix in the proper amounts of epoxy into the mixture.
5. Add acetone until the mixture can be easily mixed. The consistency should be similar to cookie dough. **MIX WELL.**
6. Wearing gloves, take mixture and work into a ball like shape.

7. Place mixture onto flat surface and go over with roller (which has raised supports).
8. The mixture should now be flat with height of the desired size.
9. Stamp out the slugs. If using a tube, drive the tube straight down through the mixture. Now lift tube and move towards a flat surface. Blow through the tube straight onto flat surface. If done correctly, a nice flat igniter will be delivered to the flat surface. (This takes practice).
10. Take the left over mixture and rework into a ball.
11. Repeat Steps 7-10 until no more usable mixture.
12. Let the secondary slugs dry overnight.
13. If desired, drill small hole through central axis of each slug (1/16"). Be careful how the slugs are mounted**. DO NOT HOLD SLUG IN HAND DIRECTLY WHILE DRILLING.**
14. Store slugs in zip lock bags. (Not necessarily individually).

Part 7: Assemble the Igniter.

This portion of the procedures describes how to assemble all major components of the igniter to complete the Stanford Initiator. This requires a motor to be ready for fire.

1. Make sure all igniter components are ready.
2. Clean the secondary slug housing (if necessary). Make sure it is dry.
3. Sand down the OD (slowly) of the secondary slug so that it fits into the secondary slug housing.
4. Place small amount of epoxy along circumference of secondary slug and install into secondary housing. Be careful not to allow epoxy to flow onto the axial faces. If epoxy gets on the axial faces, the secondary slug could fail to ignite.
5. Wait a minimum of 4 hours (24 hours recommended) for a good cure.
6. Install onto motor (without glowplug). Check to make sure that the Oring on the secondary housing (if present) is in good shape.
7. When the motor is ready for safe for fire, place copper ring onto glow plug igniter and thread glow plug igniter into the secondary slug housing. Be very careful not to damage the nitrocellulose seal.
8. Tighten the glow plug igniter until tight and copper ring deforms to form a good seal. Do not overtighten such that the copper breaks.
9. Attach the glow plug igniter.
10. The motor is now ready for fire. *An absolute minimum of 2A and 1W are required for ignition, although higher is recommended.*

Notes:

The grinding and mixing of the ingredients needs to be further studied, as they have a first order impact on the initiator performance. The Stanford initiators have DOT clearance for transportation and a Materials Safety Datasheet (MSDS) and have been proven to not fire given power less than 1W. See

"Peregrine Initiator Test Report", Stanford University and "Ground Test Pyrotechnic Plan, Peregrine Sounding Rocket Project, Rev E", Zilliac, G., June 23, 2008, NASA Ames Research Center, Moffett Field, CA 94035

H.2 Fuel Grain Casting Procedures

The fuel grain spin-casting procedures begin on the next page.

Fuel Grain Spin-Casting Procedures

Pavan Narsai

Last Updated: July 30, 2016

Date: _____

Summary:

The following procedures are spin casting a wax grain.

Emergency Contacts:
Contact Information for Stanford EH&S:
Robert Porterfield, Fire Protection Engineer
650-725-1343; rporterfield@stanford.edu

Contact Information for Police/Fire/911:
(650) 329-2413

Safety

- At least two people are needed
- Safety goggles must be worn
- Clothing may get ruined with wax
- Heat resistant gloves will be needed

Tools to have ready

- Mallet
- Alley Key (3/16") - It's recommended to have at least 2
- Tape
- Adjustable Wrench
- Tube & Funnel for pouring
- Scale

Preparation

- Make sure casting table is clean and only casting machine related hardware are on it
- Cover nearby electronics with tarp
- Heat paraffin to desired temperature. It was previously found that ~120C works well

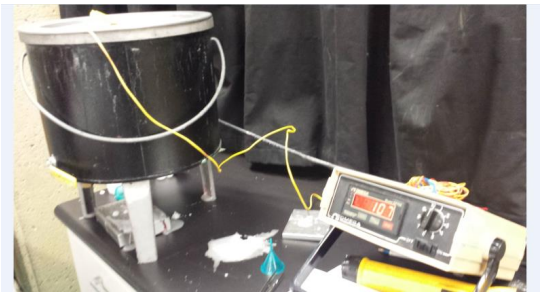

- Make sure all bolts on the spin casting machine are tight

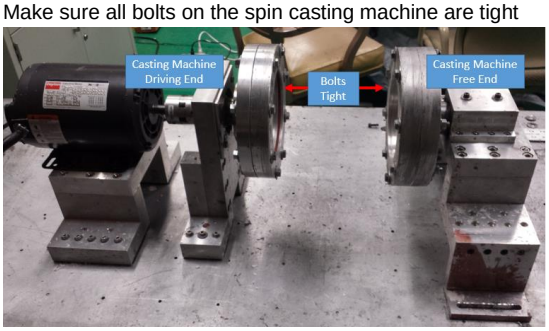

- Make sure that the threaded studs and washers are ready for assembly
- Clean the end caps and remove any paraffin residue
- Make sure the spin casting machine cover is nearby for easy assembly
- Put up a warning sign on the door that reads “DO NOT ENTER! ROTATING MACHINERY” and is visible from outside

Electronics Preparation

Note that the machine works with two switches, one next to the casting machine and the other remote switch in the room with the combustion experiments. The machine will not run if either of them are set to the OFF position.

- Make sure the remote casting switch is set to the OFF position

- Turn on the power for the casting machine
- Set the machine to the desired speed (55.0 on the machine works well for a roughly 1.5” OD grain)
- The speed refers to a Hz cycling rate of the motor

- Press the RUN button

Pouring

- Tape the bottom endcap so it seals the hole from the outside
- Get a scale in place and tare with the bottom end cap and casting tube

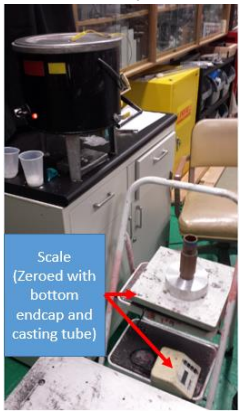

- Align the casting tube and bottom endcap roughly in center of scale
- Align the scale and the melting pot so that it is easy to pour
- Person pouring the paraffin should now wear heat resistant gloves
- Pour paraffin using the valve on the melting pot

- Small tubes fill quickly so be careful. Pour to the desired weight

- Put the top end cap on and tighten with mallet

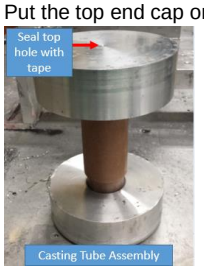

- Place some tape to seal the top hole

Spinning

- Turn off the melting pot
- Assemble the casting machine and casting tube assembly
    - One person should push the casting tube assembly onto the driving end of the casting machine
    - The other person should then push the free end of the casting machine onto the casting tube assembly to fix the casting tube assembly in place
- One person should push so that the free end of the machine is securely pressing into the casting tube assembly

- The other person should quickly tighten bolts securing the free end of machine onto the table. Make sure that the free end is set on top of the rubber sheets

- All available people (2 minimum) should now place the casting machine cover over the machine and through the threaded studs
- Quickly tighten the butterfly nuts with the rubber sheets and washers on all 4 corners

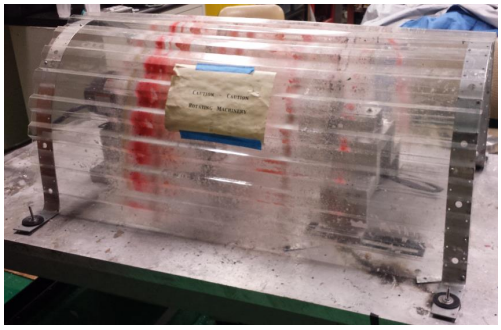

- All people should leave the room

- Turn the remote switch to the ON position

- The machine should ramp up. Some vibrating noises are normal and are sometimes loud.
- If any out-of-ordinary sounds are heard, **TURN OFF THE REMOTE SWITCH IMMEDIATELY**, and wait for casting machine to stop spinning before entering the room
- If normal, leave machine spinning until the cure time, which is usually between 30 mins and 2 hours. For a roughly 1.5" OD grain, the cure time is about 40 minutes
- When done casting turn the remote switch to the OFF position
- Wait for the machine to stop spinning before entering the room
- When the machine has stopped, it is safe to turn the power off for the casting machine
- Remove cover and the securing bolts for the free end
- It may take significant force to remove the grain from the casting tube. For some sizes, a grain removal tool is available

H.3 Thermocouple Welding Tips and Procedures

The thermocouple welding tips and procedures begin on the next page.

Thermocouple Welding Procedures

Pavan Narsai

Last Updated: August 8, 2016

Summary:

The following procedures are helpful in welding fine wire K-type thermocouples. These instructions could easily be adapted for other types of thermocouples. Note that although these procedures are helpful in welding thermocouples, the actual practice of welding thermocouple wires takes time, patience, a steady hand, and a lot of practice.

Contact:
Contact Pavan Narsai, pnarsai@stanford.edu

Requirements:

- Thermocouple Welder and associated hardware. (Hot Spot 2 Thermocouple Welder)
- High Quality Wire Cutters and Strippers (Xcelite SAS 3210)
- 50μm Fine Gauge K-Type Thermocouple Wire (Alumel and Chromel)
- 75μm Fine Gauge Insulated Thermocouple Wire
- Thermocouple Reader
- Safety Googles
- Painters tape
- USB Microscope (for inspection)

Note – It is very important to have a high quality set of wire cutters and strippers available. These are used to strip the insulation of the fine gauge insulated wires. The tool used for the fabrication of the thermocouples in this research is shown below.

Part 1: Prepare the Thermocouple Welder and Tools
Prepare the pliers, wire cutters, thermocouple wire and welding block on wooden work surface (avoid metal surfaces as they may cause grounding issues)

Part 2: The Thermocouple Junction Weld
This section describes key steps in making the thermocouple junction weld. This junction weld is the thermocouple sensor, so a good quality weld is desired.

1. Cut the Alumel (- or Red) wire to length. Set aside. Attempt to make clean cuts perpendicular to the wire
2. Cut the Chromel (+ or Yellow) wire to length, which should be noticeably longer than the Alumel wire.
3. Place the two wires parallel such that they meet on one end and are nearly touching along their entire length. (The Chromel wire will extend past the Alumel wire)
4. Cross the wires once near the center of the Alumel wire. With the needle nose plier probe for the thermocouple welder, clamp the crossing. Adjust the cross location so that the clamp is in the plier jaws and the edge of both wires extend about a millimeter outside the jaws. With careful and steady hands, adjust the ends of the wires so that they just touch at the ends.
5. Make sure all other wires are out of the area and all ground points are clear (The vice and graphite block) so no shorting is possible.
6. Bring the plier close to graphite block but not near enough to arc.
7. Press and hold the weld button
8. Steadily bring the wire close to a corner of the graphite block. When close to touching, the wire will arc.
9. Release the weld button
10. Inspect the weld. If the weld is good, place the thermocouple junction and wires on a piece of paper and tape with painters tape to protect the weld and wires.

11. If the weld isn't good, repeat from step 1.

Part 3: The Wire Weld

This section describes the steps in welding the 50μm wire to the 75μm extension wire. This section is difficult so it is recommended to first try to weld an extension wire and an unwelded bare wire.

1. First prepare the extension wire by cutting the alumel and chromel wires to equal lengths and strip each side of each by about 10mm.
2. Take the Alumel (red) insulation wire and wrap the Alumel bare wire around the exposed metal of the insulated wire 2-3 times.
3. Tape onto the graphite block such that the wrapped portion is securely on top of the graphite (but exposed).
4. Clamp the graphite probe with the plier.
5. Very carefully place the sharp point of the probe onto the wrapped section and aim so that the point is touching the 50μm wire that is wrapped onto the 75μm wire. Be very gentle to not apply too much force.
6. With other hand, tap the weld button. This will many times burn the wire, but with the right amount of force, this will create a solid weld.
7. Test the assembly with thermocouple reader, iced water, and boiling water.

H.4 Thermocouple Installation Procedures

The thermocouple installation procedures begin on the next page.

Thermocouple Installation Procedures

Pavan Narsai

Last Updated: August 8, 2016

Summary:

The following procedures are helpful in installing thermocouples into the nozzle.

Contact:
Contact Pavan Narsai, pnarsai@stanford.edu

Requirements:
Set of thermocouples
Ceramic Tubes cut to length (McMaster P/N 87175K71)
Ceramic Paste (Cotronics Resbond 906)
Mixing cup and mixing stick
Eyedropper
Thin paintbrush
Long needle nose pliers

Part 1: Prepare Thermocouples

1. Carefully insert each wire lead of the thermocouple into a port in the ceramic tubes. Pull through until the junction is centered just outside of the port. Allow some wiring to remain slacked for strain relief.
2. Carefully mix about 5 grams total of Resbond 906 and lightly coat the junction with thin paintbrush.
3. Set Aside

Part 2: Prepare the Nozzle

1. Insert the nozzle in the aft end according to the test procedures or the installation instructions.
2. Verify that the thermocouple installation holes are aligned with the ports on the aft end.

Part 3: Install Thermocouple

This section of the procedures must be followed through completely for each thermocouple. (Installing thermocouples is a time-consuming process)

1. Place the thermocouple assembly adjacent to aft end assembly.
2. Arrange aft end block such that the desired port hole is facing upward.
3. Mix the proper amounts of Resbond 906 (100 parts filler with 40-44 parts binder) in a plastic cup. (Avoid paper, as the paper absorbs the binder).
4. Using an eyedropper, place 2-3 drops into the thermocouple port hole. Use enough to fill roughly half the port volume.
5. Place thermocouple assembly into port hole (use pliers to hold aft section of the ceramic tube).

6. Lift the thermocouple assembly and put back in 2-3 times. (This helps to push the paste all the way to the bottom of the hole and ensures that the thermocouple gets installed at the bottom of the port).
7. Push the thermocouple assembly gently all the way down to ensure proper installation.
8. Allow the paste to dry for 2 hours at ambient conditions.
9. Carefully take the aft assembly and bake for 1 hour at 250 F.
10. Bake for another 2 hours at 300 F.
11. Repeat for all other thermocouples.

H.5 Hot Fire and Cold Flow Procedures

The Hot Fire and Cold Flow procedures begin on the next page.

Nozzle Erosion Test Experiment

Operating Procedures

Pavan Narsai

Last Updated: Jul 30, 2016

(Taken from Stanford Combustion Visualization Experiment Operating Procedures, by Beth Jens, July 15, 2014)

Cold Flow Test#: _____

Hot Fire Test#: _____

Date: _____

Fuel: _____

Desired Pressure: _____

Desired Ox. Flow Rate:_____

Logistics of Hotfire Tests:

The following procedures are for running hot fires experiment. These tests will take place in the basement of Durand, room 053A. This room has been designated for this type of activity, so no one has to be notified prior to testing.

Emergency Contacts:
Contact Information for Stanford EH&S:
Robert Porterfield, Fire Protection Engineer
650-725-1343; rporterfield@stanford.edu

Contact Information for Police/Fire/911:
(650) 329-2413

Contact Information for Facilities:
Jaime Eredia, Facilities Administrator
(650) 725-7452 work, (650) 996-0531 cell, jeredia@stanford.edu

Prior to Test (day before if possible):

1. Prepare Combustion Chamber
    a. Check that combustion chamber is clean. If not, follow cleaning instructions in the back of this document
    b. Place both insulators into combustion chamber and drill the pressure transducer hole using a 1/8" or smaller into the aft insulator.
    c. Weigh all of the combustion chamber elements
        i. Fuel Grain Insulator:_____
        ii. Aft Insulator:_____
        iii. Fuel Grain:_____
        iv. Mixer:_____
        v. Post Combustion Chamber (PCC) Straight Section:_____
        vi. PCC Chamber Ramp Section:_____
        vii. EPDM Spacer:_____
    d. Use RTV to set the fuel grain into fuel grain insulator and weigh:_____
    e. Weigh the combustion chamber internals:_____
    f. Place the combustion chamber internals into the combustion chamber.
    g. Apply crytox to oring groves on combustion chamber and also on the straights that are machined onto the combustion chamber.
    h. Take picture of a view down the combustion chamber and note the front ID of the fuel grain:_____
    i. Cover the assembly to keep it clean

2. Prepare the Aft End (if necessary)
    - **a. Nozzle MUST NOT be removed from aft end until all of its tests are completed (once removed, nozzle thermocouples are unusable)**
    - b. Apply liberal amount of crytox to both oring grooves on nozzle
    - **c.** To insert nozzle, first put on the aft oring with liberal amount of crytox
    - **d.** Push the nozzle from the back of the aft end all the way until the back plane of nozzle lines up with back plane of aft end
    - **e.** Push nozzle forward until the front oring groove is exposed. DO NOT PUSH FURTHER THAN NECESSARY
    - **f.** Insert the front oring and apply liberal amount of crytox
    - **g.** Push nozzle back until the back walls of both nozzle and aft end align
    - **h.** Bolt on the brass nozzle holder plate and the aft support plate assembly.
    - **i.** Nozzle assembly is now ready for thermocouples to be installed, Follow procedure to making and installing embedded thermocouples
    - **j.** Insert ultrasound transducer with (antisieze as couplant) noting that the oring is present in the aft end.
    - **k.** Cover aft end section to keep it clean

3. If fore end window is required for test (and not already installed):
    - a. Disassemble the fore end sections including the feed system elements and the fore end mounting plate. Keep all parts ox-clean. Keep all bolts.
    - b. Remove the fore end fitting (injector), if present.
    - c. Remove and 2 spacers and oring.
        - i. If any of them look degraded and uncleanable, discard them and use new one.
    - d. Apply crytox to oring groove and face that compresses the spacer
    - e. Insert inner spacer and oring, with crytox
    - f. Apply crytox to the outside of the window edge, where the oring will seal.
    - g. Carefully insert window into fore end block, with the chamber going into the fore end first.
    - h. Push the window straight in. It will be slightly below level of fore-end face when fully inserted.
    - i. Place the outer spacer on the window.
    - j. Install the fore end mounting plate using the four ¼”-20 bolts. Make sure to place the tie rod washers before attaching the plate. Tighten slowly in a star pattern.
    - k. Tighten fore end section onto the optics table
    - l. Re-attach all feed system elements
4. Carefully and slowly install glow plug(s) into igniter fitting(s).

a. Cover the section to keep it clean.

5. Assemble the motor
    a. The fore-end section should already be bolted onto the optics table
    b. Insert the combustion chamber into fore-end assembly
    c. Insert the aft end assembly onto aft portion of combustion chamber assembly.
    d. Tighten down bolts on aft end section onto the optics table
    e. Check all mounting bolts and ensure everything is tight.
    f. Insert tie rods through the fore end section and tighten into the aft end section of the motor.
        i. To tighten, it helps to use two nuts on the tie rod. The back nut can be used as a driving nut.
        ii. Opposite is true to remove tie rods
    g. Install pressure transducers on fore end section and on combustion chamber. They should be preattached to MS-port fittings which easily seal the motor.
    h. Cover the setup to keep it clean

6. Check igniter battery voltage: _____ V (should be >12 V). If low, charge it using the charger in 051 Durand
7. Check all camera batteries and charge if needed
8. Check that memory cards are installed and clear
9. Leak check feed system if any components have been replaced

Set Up for Test:

1. Ensure the hand ball valves are correctly opened and closed.
    a. OV 4 and OV 6 need to be closed.
    b. OV 5 needs to be opened.
    c. Check the nitrogen valves as well.
    d. Check to make sure the lines are continuous until the chamber (quick disconnect is connected)

    Have a second person look at the setup and agree that the correct valves are opened and closed. Name:_____

2. Run USB extenders from NI DAQ and ER5000 to LabVIEW Computer and plug in
3. Ensure E-Stop button is pressed in
4. Check that all “Connect A” wires are connected to power strip A and all “Connect B” wires are connected to power strip B (3 plugs in each)
5. Turn on power strip A and power strip B
6. Remove covering from vent on electronic regulator
7. Turn on LabVIEW Computer (for Flow control)
    a. User Name: Nozzle
    b. Password: rR43v3r

   c. Open LabView
8. Turn on Thermcouple recording computer and load the labview software
9. Set ultrasound machine settings and ensure data properly fed to thermocouple data computer
10. Turn OFF internet
11. Turn OFF firewalls on all LAN computers
12. Remote in using the LAN and teamViewer
13. Check vent is in place
14. Remove all nonessential equipment and/or materials from the test area
15. Remove cover
16. Record temperature _____, and barometric pressure _____ in the test room
17. Plug in and turn on viewing cameras
18. Set up high speed video camera
    a. Fix cameras to stands
    b. Manually focus and set cameras
    c. Set to desired film settings:

NOTES ON DESIRED SETTINGS:	
CAMERA WIN	CAMERA OTHER
Shutter Spd:	Shutter Spd
FPS	FPS
FStop	FStop
ISO	ISO
FOCUS	FOCUS

19. Check for observers, warn them and put up “Danger” signs
20. Ensure that the shop air vent valve is closed
21. Turn on shop air in 051
22. Close doors to 053A/B, place signs on the exterior of each warning that testing is in progress
23. Go to LabVIEW computer. Open LabVIEW file titled “NozzleErosionExperiment_v1”
24. Enter filename to which data will be saved. Include date.
25. Record times here: $t_{oxdelay}$ = _____ s, t_{burn} = _____ s, t_{ignite}= _____ s, t_{purge} = _____ s, $t_{neither}$ = _____ s.
26. Set Emergency shut down chamber pressure: $P_{Emergency}$ = _____ psi
27. Open ER5000 program. Start the graph. Ensure that the setpoint pressure (the red line on the graph) is set to 0 psia
28. Ensure that the PID control values are set at:
    a. $K_P = 600$
    b. $K_D = 40$
    c. $K_I = 400$
    d. Integral limits:
        i. Max = 35

ii. Min = -35
iii. Deadband = 0.00

29. Release E-stop button
30. Run file titled NozzleErosionExperiment_v1. Ensure “Fire” is not pressed. Cycle through opening and closing all valves, listening for click of each one:
    a. N-1 _____
    b. N-3 _____
    c. SA-1 _____
    d. OV-1 _____
    e. OV-3 _____
    f. OV-7 _____
    g. Manual Purge _____

31. Plug in ignition battery
32. Check voltage / resistance across ignition output. SHOULD BE ZERO / OPEN LOOP
    a. DO NOT check resistance across glow-plug igniters with a regular multimeter.
    b. Plug in igniter cap wiring
    c. Slowly and carefully plpug the igniter cap into the glow plug **(after completing steps a and b)**
    d. Close door
33. Visually check that N_2 regulator is fully closed (unscrewed)
34. Nitrogen
    a. Turn nitrogen cylinder full open
    b. Record pressure in nitrogen cylinder:_____ psi
    c. Set regulator to 700 psi

35. Oxygen
    a. Open one cylinder slightly then quickly close to ensure that regulator is in fully closed position. If it was slightly open then the line will fill to approx. 20psi. Wait until the pressure in the downstream line is vented (indicating that the regulator has also closed) before opening the bottles any further.
    b. Open SA1 and OV3 (open up line until ball valve for main experiment)
    c. Open both GOx bottles full open
    d. Record pressure in oxygen cylinder_____ psi
    e. Using ERTune, ramp up the oxygen line pressure 5 psi/sec to increase the line pressure by 100 psi at a time with a dwell time of 10 seconds at each increment until reaching a test pressure of _____ psi. Cycle SA1 every minute or so. (OV3 should remain open).
36. Cycle power on viewing camera

Run Test:

1. Cycle SA1. (Turn off and turn back on). Ensure SA1 and OV3 are open.
2. Ensure all feed system sensors are working (4 pressure transducers, 1 differential pressure transducer, 2 thermocouples).
3. Start high speed camera recording
4. Mental Checklist
    a. Have I plugged in the igniter battery?
    b. Have I plugged in the igniters?
    c. Have I started recording data?
    d. Have I started recording the cameras?
    e. Have I started recording the live camera?
    f. “Spectrometer?”
5. Press “fire”
    a. SA1 remains open whole time. OV3 remains open whole time
    b. Oxidizer on (open OV-7), igniter on
    c. Igniter off
    d. Oxygen off (close OV-7)
    e. Nothing
    f. Nitrogen On (open N-3)
    g. Nitrogen off (close N-3)

Shut Down

1. Stop camera recording
2. Ensure all valves in LabVIEW are off with exception of OV3 and SA1
3. If a purge was not completed as part of test, complete one now.
    a. Open N-3 for at least 10 seconds
4. Oxygen Cylinders:
    a. Check to ensure that the oxidizer gas cylinders are full (for next test)

Oxidizer must be at or above 1500 psi.
O2 pressure: _____ psi

b. Turn both GOX cylinders full closed
c. Leave ERTune set at test pressure and then empty GOX line using vent valve (use OV-1)
d. Close SA1 and OV3

5. Close ERTune

6. Nitrogen cylinders:
   a. Check to ensure that the N_2 gas cylinders are full (for next test)
      Nitrogen must be at 1000 psi or more.
      N2 pressure: _____ psi
   b. Turn GN2 cylinder full closed
   c. Empty GN2 line by opening N-1
   d. When GN2 regulator reads 0 psi, close regulator
7. Warn person by cylinders of the sound of shop air venting then press E-stop

It is now safe to enter test room

8. Disconnect igniter cap from glow plug.
9. Turn off viewing camera
10. Turn off shop air and vent the shop air line
11. Email data from LabVIEW computer and transfer videos from Beth's and Jonah's computers
12. Remove signs from hallway
13. Turn off electronics power board A and B
14. Cover the electronic regulator vent
15. Take pictures
16. Remove combustion chamber internals and weigh:
    a. Post Combustion Chamber Graphite_____
    b. Mixer_____
    c. Graphite Ramp_____
    d. Fuel Grain + insulator_____
    e. EPDM_____
    f. Aft Insulator_____
    g. endID_____
17. Weigh the fuelgrain + fore-insulator combination.
18. Cover Experiment Sections to keep clean.
19. Disconnect high speed camera usb connections (only if video has finished downloading)
20. Turn off all computers
21. Unplug USB wires from LabVIEW computer and pack away

EMERGENCIES:

No ignition:

1. Hit emergency stop button on LabVIEW display

2. If emergency button doesn't work, hit E-stop, purge (open N3) and stop running LabVIEW.
3. After purging, open LabVIEW and follow shut-down procedures

Computer Crash in Middle of Test:

1. Press E-stop
2. Start Nitrogen purge manually
3. Turn off computer
4. Empty shop air
5. When system is secure then turn back on computer and release E-stop
6. Open ER tune
7. Fill shop air
8. Follow shut down procedures

Oxidizer Valve Doesn't Close:

1. Hit E-stop
2. Purge (Open N-3 for 10 seconds)
3. Release E-stop
4. Follow shutdown procedure from step 3.

Overpressure:

4. System should shut down automatically if chamber pressure reading exceeds allowed pressure.
    a. If it does not:
        i. Hit emergency stop button on LabVIEW display
        ii. If emergency button doesn't work, hit E-stop, purge (open N3) and stop running LabVIEW.
        iii. If program is terminated, all valves should fail closed.

Fire:

1. Hit E-stop
2. Start purge
3. Have person by air supply close main supply valve and open vent
4. Assess situation. Can you use fire extinguisher?
    a. If yes: try to put out the fire.
    b. If fire is too far up the line then do not use extinguisher
5. If not able to put out fire ourselves then have everyone leave room and building
    a. Hit fire alarm on way out
    b. Call emergency number: (650) 329-2413
        i. Give details: Rm. 053A, Durand Bldg.
6. If fire is under control then end purge and follow shut-down procedures

Oxidizer Mass Flow:

1. Check that LabVIEW Computer is turned on, if it is not, turn on LabVIEW Computer
    a. User Name: Nozzle
    b. Password: rR43v3r
2. Visually check to make sure igniter is NOT installed
3. Nitrogen
    a. Turn Nitrogen cylinder full open
       Pressure in Nitrogen cylinder:_____
    b. Set regulator to 700 psi
4. Oxygen
    a. Turn both Oxygen cylinders full open
       Pressure in Oxygen cylinder 1:_____ cylinder 2:_____
    b. Follow hot fire procedures to fill oxygen. Do not plug in igniter
5. Close OV-4, then open slowly
6. Open OV-3
7. Monitor differential pressure transducer data
8. Repeat steps 5-7 until desired mass flow is achieved.

Appendix I

Image Processing of Fast Burning Fuels Source Code

This section describes the code layout and prerequisites for the image processing algorithm used in this research.

I.1 Code Layout

The image processing code requires Python and OpenCV 3 to be installed on the host system. OpenCV can be a bit difficult to install. On OSX, OpenCV was built from the source files using CMAKE. On OSX, no additional codecs or files were required to analyze the video files.

On Windows, while installing OpenCV was notably easier, the ffmpeg libraries for OpenCV were additionally required to analyze videos. This was a bit challenging, but instructions can be found online to do so. Note that in both Windows and OSX, not all video formats are supported.

The code is broken into three scripts to easily and efficiently analyze the video. The first script (calibration.py) simply helps the user calibrate the scale from a video recorded prior to the burn.

The second script (trackRegression.py) was the image processing script. This script ran through the frames in the video files and captured the port sections and logged the relevant data. This code also outputs each frame as a separate .png image with the tracked port areas overlayed onto the source image.

The third script (analyzeData.py) analyzed the data by generating the relevant fuel regression plots.

I.2 Source Code

---

calibration.py

```
#calibration.py
#This code takes the calibration video and generates an approximate scale factor (needs perspective correction)

import numpy as np
import cv2
print "The detected version of openCV is "+str(cv2.__version__)
import pylab
import scipy.signal

hotFireNumber = 9
scaleFactor = 2

#define some constants based on test number
if hotFireNumber == 9:
    hotFireDate = "Dec 8, 2015"
    fileName = 'Test9'
    inputVideo = 'scaling video.MOV'
    startFrameNumber = 40
    endFrameNumber = 40
    framesPerSecond=600

elif hotFireNumber == 10:
    hotFireDate = 'Janary 19, 2016'
    fileName = 'Test10'
    inputVideo = 'Calibration.MOV'
    startFrameNumber=430
    endFrameNumber = 3969
    framesPerSecond=600
    lowerGray = 75
    upperGray = 255

#now add the file name so we can open
inputVideo = fileName+'/'+inputVideo

try: #load the video
    print "Attempting to open the video file"
    vid = cv2.VideoCapture(inputVideo)
    fps = vid.get(cv2.CAP_PROP_FPS)
    Frames = vid.get(cv2.CAP_PROP_FRAME_COUNT)
    codec = vid.get(cv2.CAP_PROP_FOURCC)

    print 'FPS = '+str(fps)
    print 'Frames='+str(Frames)


except:
    print "Could not open the video file"
```

```
    raise

ret, frame = vid.read()
#grab the first frame
currentFrame = 0
TargetFrame = 510 #define which frame to use for calibration

#define font constants and colors and draw the title label
font = cv2.FONT_HERSHEY_SIMPLEX
fontColor = (0,0,255)
lineColor = (255,255,255)
titleText = "Hot Fire %d: "%(hotFireNumber)+hotFireDate+" Calibration"

#skip to frame of interest
for i in range(0,startFrameNumber): #skip frames until we get to the target frame
    ret, frame = vid.read()
    currentFrame = currentFrame+1


#now we have the desired frame
ret, frame = vid.read() #read it

#then upscale the frame
frame1 = cv2.resize(frame, None, fx=scaleFactor, fy=scaleFactor, interpolation= cv2.INTER_LANCZOS4)

#remove noise
blur = cv2.medianBlur(frame1,55)

#convert to gray scale (so we can find circles)
gray = cv2.cvtColor(blur,cv2.COLOR_BGR2GRAY)

cimg = gray
#find the circles
circles = cv2.HoughCircles(cimg,cv2.HOUGH_GRADIENT,1,30*scaleFactor,
                                param1=30,param2=40,minRadius=60,maxRadius=0)

circles = np.uint16(np.around(circles)) #convert the circles

#draw the circles and display the biggest diameter
for i in circles[0,:]:
        # draw the outer circle
    cv2.circle(frame1,(i[0],i[1]),i[2],lineColor,1)
        # draw the center of the circle
    cv2.circle(frame1,(i[0],i[1]),2,(0,0,255),3)
    #compute diameter
    diameter = 2*i[2]
    #print it to the command prompt
    print "The diameter is %d pixels"%(diameter)

#write information on the frame
cv2.putText(frame1, titleText,(0,15),font,0.3,fontColor,1)
cv2.putText(frame1,'Frame %d'%(currentFrame),(0,30),font,0.3,fontColor,1)
cv2.putText(frame1, 'Diameter: %d Pixels'%(diameter),(0,45),font,0.3,fontColor,1)

#show the frame and save it
cv2.imshow('ViewPort',frame1)
```

```
cv2.imwrite(fileName+'/CalibrationImage.png',frame1)
cv2.waitKey(1)

print "Done running the code"
vid.release()
```

---

trackRegression.py

```
#trackRegression.py
#this code loads a video from a test and tracks the port and outputs raw data.


#import prerequisites
import numpy as np
import cv2
import pylab
import scipy.signal
import sys
import time

kernelSize=5
startTimeSpeed = time.time()

#default color/filter settings
lower_blue = np.array([0,0,90])
upper_blue = np.array([40,145,255])
lowerGray = 75
upperGray = 255

scaleFactor = 2 #upscaling factor

#define hotFireNumber desired
hotFireNumber = 10

#define test specific information, such as date, fileName, and start and end frame numbers
if hotFireNumber == 9:
    trueWidth = 1.375/(106*scaleFactor) * 0.0254
    hotFireDate = "Dec 8, 2015"
    fileName = 'Test9'
    inputVideo = 'fore_end_clipped.mp4'
    startFrameNumber = 1
    endFrameNumber = 2920
    framesPerSecond=600
    lowerGray = 75
    upperGray = 255

elif hotFireNumber == 10:
    trueWidth = 1.375/(318./2*scaleFactor) * 0.0254
    hotFireDate = 'Janary 19, 2016'
    fileName = 'Test10'
    inputVideo = 'windowTrimmed.mov'
    startFrameNumber=750
```

```
    endFrameNumber = 3969
    framesPerSecond=600
    lowerGray = 75
    upperGray = 255

#define output filenames
outputVideo = 'output.mp4'
grayDataFile = 'grayOutput.csv'
HSVDataFile = 'HSVOutput.csv'

#now add the file name prefix (based on the input video data).  This stores the output data
#in an organized fashion
inputVideo = fileName+'/'+inputVideo
outputVideo = fileName+'/'+outputVideo
grayDataFile = fileName+'/'+grayDataFile
HSVDataFile= fileName+'/'+HSVDataFile

#set blank list to store time data
times = []

def getInformationFromImage(thresh,trueWidth):
    #This function looks at each image and finds the contours
    #and outputs relevant information, such as diameter, area, perimeter, and a handle to the contours

    #find contours first
    image, contours1, hierarchy = cv2.findContours(thresh,cv2.RETR_TREE,cv2.CHAIN_APPROX_SIMPLE)
    #sort contours by arc length
    contours1.sort(key = len)

    #if we detected an arc, then we found a contour and we can do math
    if len(contours1)>=1:
        M = cv2.moments(contours1[-1])
        perimeter = cv2.arcLength(contours1[-1],True)*trueWidth
        area = M['m00']*trueWidth*trueWidth
    else:
        perimeter = 0
        area = 0

    if perimeter > 0:
        hydraulicDiameter = (4*area/perimeter)
    else:
        hydraulicDiameter = 0

    return area, hydraulicDiameter, perimeter, contours1

def writeTextInformation(image, position,title,font,fontColor, area,perimeter,hydraulicDiameter,contours):
    #this function writes text information to the frame for post-analysis and also draws the contours
    cv2.putText(image, title,(0,position),font,0.3,fontColor,1)
    cv2.putText(image, 'Area: %f'%(area),(0,position+15),font,0.3,fontColor,1)
    cv2.putText(image, 'Perimeter: %f'%(perimeter),(0,position+30),font,0.3,fontColor,1)
    cv2.putText(image, 'Hy. Diameter: %f'%(hydraulicDiameter),(0,position+45),font,0.3,fontColor,1)

    cv2.drawContours(image, contours, 0, fontColor, 1)
    return image

def writeTitleInformation(image,hotFireNumber,date,frame,position,font,fontColor):
```

```
    #this function writes title information to the frame for post-analysis
    titleText = "Hot Fire %d: "%(hotFireNumber)+date
    cv2.putText(image, titleText,(0,position),font,0.3,fontColor,1)
    cv2.putText(image,'Frame %d'%(frame),(0,position+15),font,0.3,fontColor,1)
    return image

def writeDataToFile(file, area, diameter, perimeter,tim):
    #this function writes a line of data to the output file.
    file.write('%f,%f,%f, %f \n'%(area, diameter, perimeter,tim))
    return

def readDataFile(fileName):
    #this file reads the data from a file and outputs the areas, diameters, perimeters and times
    dataFile = open(fileName,'r')
    areas = []
    diameters=[]
    perimeters=[]
    times = []


    for line in dataFile.readlines():
        #print line
        datasTemp = line.split(',')
        areas.append(float(datasTemp[0]))
        diameters.append(float(datasTemp[1]))
        perimeters.append(float(datasTemp[2]))
        times.append(float(datasTemp[3]))

    dataFile.close()
    return areas,diameters,perimeters, times



#now all functions and definitions are set.
#we can now load a video and start analyzing data


#First load up the write files
print "Starting the data file"
grayFile = open(grayDataFile,'w')
HSVFile = open(HSVDataFile,'w')




try: #open the video file, if possible
    print "Attempting to open the video file"

    #extract necessary information, such as codec
    vid = cv2.VideoCapture(inputVideo)
    fps = vid.get(cv2.CAP_PROP_FPS)
    Frames = vid.get(cv2.CAP_PROP_FRAME_COUNT)
    codec = vid.get(cv2.CAP_PROP_FOURCC)

    print 'FPS = '+str(fps)
```

```
    print 'Frames='+str(Frames)
    #vid.read()
    if vid.grab() == True: #we we were able to open file, then read 1st frame
        ret, frame = vid.read()
        width, height = frame.shape[:2] #from first frame we can determine
        #the original resoltuion

        #resize the video here (this will be output resolution)
        width = width*scaleFactor
        height = height*scaleFactor

        print "Video output resolution is %d x %d"%(width, height)
        fourcc = cv2.VideoWriter_fourcc('m','p','4','v') #this code works on mac
        out = cv2.VideoWriter(outputVideo, fourcc,fps,(height,width))   #define the output video file for this
             analysis
    else:
        print "Could not open the video file" #if you get this, something weird happened. try making this work
             with some
        #other video first.

except:
    print "Could not open the video file" #if you get this....try confirming FFMPEG is installed correctly
    raise

ret, frame = vid.read()

currentFrame = 0

#FONT definitions (type and color)
font = cv2.FONT_HERSHEY_SIMPLEX
#fontColor = (12,135,76)
fontColor = (0,0,255)
lineColor = (128,255,0)

grayColor = (120,255,255)
HSVColor  = (0,255,0)
titleColor = (0,0,255)


titleText = "Hot Fire %d: "%(hotFireNumber)+hotFireDate


print "Starting the image processing"
print "Analyzing Frame     ",
while(currentFrame<startFrameNumber): #This while loop skips to the starting frame number
    ret, frame = vid.read()
    currentFrame = currentFrame+1



while(currentFrame < endFrameNumber): #this is the main loop for the video. We analyze frame
#by frame

    ret, frame = vid.read()

    #upscale the image here
```

```
    frame1 = cv2.resize(frame, None, fx=scaleFactor, fy=scaleFactor, interpolation= cv2.INTER_LANCZOS4)

    #get an HSV copy of the image
    hsv = cv2.cvtColor(frame1, cv2.COLOR_BGR2HSV)
    #filter HSV
    mask = cv2.inRange(hsv, lower_blue, upper_blue)

    #blur HSV
    maskBlur = cv2.medianBlur(mask,49)

    kernel = np.ones((kernelSize,kernelSize),np.uint8)
    #maskBlur = cv2.dilate(maskBlur,kernel,iterations=5)
    #maskBlur = cv2.erode(maskBlur,kernel,iterations=4)



    #convert original image to gray, and blur to reduce noise
    gray = cv2.cvtColor(frame1,cv2.COLOR_BGR2GRAY)
    gray = cv2.medianBlur(gray,49)
    gray = cv2.medianBlur(gray, 5)

    #threshold the gray image
    ret,thresh = cv2.threshold(gray,lowerGray,upperGray,cv2.THRESH_TOZERO)

    #get data from the images
    area, hydraulicDiameter, perimeter,contours = getInformationFromImage(thresh,trueWidth)
    areaHSV, hydraulicDiameterHSV, perimeterHSV,contoursHSV = getInformationFromImage(maskBlur,trueWidth)

    ##write data to the image for the video
    frame1 = writeTitleInformation(frame1,hotFireNumber,hotFireDate,currentFrame,15,font,titleColor)
    frame1 = writeTextInformation(frame1, 75,'Grayscale',font,grayColor, area,perimeter,hydraulicDiameter,contours
         )
    frame1 = writeTextInformation(frame1, 210,'HSV Filter',font,HSVColor, areaHSV,perimeterHSV,
         hydraulicDiameterHSV,contoursHSV)

    #advance the time step
    times.append(currentFrame*1./framesPerSecond)
    currentFrame = currentFrame + 1


    #Uncomment the bottom line to output each individual frame (takes time)
    cv2.imwrite('Test%d/IndividualFrames/Frame%d.png'%(hotFireNumber, currentFrame-1), frame1)

    #store the data to a  file (this makes > 10% boost in computation time
    #because you dont need to store a long list.
    writeDataToFile(grayFile, area, hydraulicDiameter, perimeter,times[-1])
    writeDataToFile(HSVFile,areaHSV,hydraulicDiameterHSV,perimeterHSV,times[-1])

    out.write(frame1)    #record frame for output video
    sys.stdout.write('\b\b\b\b%4d'%(currentFrame)) #this outputs to the prompt neatly
    sys.stdout.flush()


print "Done running the code"
print "Closing the data files"
```

```
#close the data files
grayFile.close()
HSVFile.close()

#close the video files
out.release()
vid.release()

#close the monitor windows
cv2.destroyAllWindows()

#compute how long the code took to run.
endTimeSpeed = time.time()
print "The total time it took to run this code"
print "Was %d seconds"%(endTimeSpeed-startTimeSpeed)
```

---

analyzeData.py

```
#analyzeData.py
#this script loads the trackRegression.py data
#and generates all relative plots.

import numpy
import scipy.signal
import pylab
import math

#these next few lines allow for latex style axis labels
#but take care, they cause errors when trying to save
#to EPS and only work on some computers
#this is why they are commented below

#import numpy as np

#pylab.rcParams['text.usetex'] = True
#pylab.rcParams['text.latex.unicode'] = True

#pylab.rc('text',usetex=True)
#pylab.rc('font',family='serif')

def filterDataSet(diameters, areas):
    #this function filters the data at the same time.

    N = 1 #filter order
    Wn = 5./framesPerSecond#cutoff frequency

    B, A = scipy.signal.butter(N,Wn,output='ba')
    #apply the filter
    diametersFiltered = scipy.signal.filtfilt(B,A, diameters)
    areasFiltered = scipy.signal.filtfilt(B,A, areas)

    diametersFiltered = scipy.signal.filtfilt(B,A, diametersFiltered)
```

```
    areasFiltered = scipy.signal.filtfilt(B,A, areasFiltered)

    return diametersFiltered, areasFiltered

def readDataFile(fileName):
    #this function reads the data and outs them as lists
    dataFile = open(fileName,'r')
    areas = []
    diameters=[]
    perimeters=[]
    times = []

    for line in dataFile.readlines():
        #print line
        datasTemp = line.split(',')
        areas.append(float(datasTemp[0]))
        diameters.append(float(datasTemp[1]))
        perimeters.append(float(datasTemp[2]))
        times.append(float(datasTemp[3]))

    dataFile.close()
    return areas,diameters,perimeters, times

#set the test number
hotFireNumber = 9

if hotFireNumber == 9:
    #set the constants...copied from before so may be unnessary
    hotFireDate = "Dec 8, 2015"
    fileName = 'Test9'
    inputVideo = 'fore_end_clipped.mp4'
    startFrameNumber = 1
    endFrameNumber = 2920
    framesPerSecond=600
    lowerGray = 75
    upperGray = 255
    massFlowRate = 49./1000 #g/s
    xlimits = [0.7,4.3]


    linTime=[0.69,2.5,3.57,04.375]
    linAreas=[0.0001,0.00021,0.00024,0.0003]
    linDiameters=[0.010,0.015625,0.01655,0.0185]

elif hotFireNumber == 10:
    hotFireDate = 'Janary 19, 2016'
    fileName = 'Test10'
    inputVideo = 'windowTrimmed.mov'
    startFrameNumber=750
    endFrameNumber = 3969
    framesPerSecond=600
    lowerGray = 75
    upperGray = 255
    massFlowRate = 24.37/1000 #g/s
    xlimits = [3.3,4.9]
```

```
#set the output data files
grayDataFile = 'grayOutput.csv'
HSVDataFile = 'HSVOutput.csv'

#now add the file name prefix
grayDataFile = fileName+'/'+grayDataFile
HSVDataFile= fileName+'/'+HSVDataFile

#read the data files for gray and HSV
areasGray,diametersGray,perimetersGray,times = readDataFile(grayDataFile)
areasHSV,diametersHSV,perimetersHSV,times = readDataFile(HSVDataFile)

#filter the data
filteredGrayDiameters, filteredGrayAreas = filterDataSet(diametersGray,areasGray)
filteredHSVDiameters, filteredHSVAreas = filterDataSet(diametersHSV,areasHSV)

#now do the plotting stuff
pylab.figure('Hydraulic Diameter')
pylab.plot(times, diametersGray)
#pylab.plot(times, diametersFiltered,'r')
pylab.plot(times,diametersHSV)

pylab.plot(times,filteredGrayDiameters)
pylab.plot(times,filteredHSVDiameters)
#pylab.plot(linTime,linDiameters)

#pylab.title('Hydraulic Diameter vs time')
pylab.title('Hot Fire %d'%(hotFireNumber))
pylab.ylabel('Hydraulic Diameter, m')
pylab.xlabel('Time, s')
pylab.legend(['Grayscale Diameter','HSV-Filter Diameter','Grayscale Filtered Diameter','HSV-Filter Filtered
     Diameter'],loc=4)
pylab.savefig(fileName +'/Diameter vs time.png')

pylab.figure('Area')
pylab.plot(times,areasGray)
pylab.plot(times,areasHSV)
pylab.plot(times,filteredGrayAreas)
pylab.plot(times,filteredHSVAreas)
#pylab.plot(linTime,linAreas)
#pylab.plot(times, areasFiltered,'r')
pylab.title('Hot Fire %d'%(hotFireNumber))
pylab.ylabel(r'Port Area, m^2')
pylab.xlabel('Time, s')
pylab.legend(['Grayscale Diameter','HSV-Filter Diameter','Grayscale Filtered Diameter','HSV-Filter Filtered
     Diameter'],loc=4)

pylab.savefig(fileName +'/Area vs time.png')

#now we can do more plots
def computeDifferential(r,index,dT):
    return (r[index+1]-r[index-1])*1./(2*dT)

rDotsGray=[]
rDotsHSV=[]
fluxesGray=[]
```

```
fluxesHSV= []

print "Computing the differentials"
#compute a and n and then plot them
for i in range(1,len(times)-1):
    if (filteredGrayDiameters[i]>0.005) and (filteredGrayAreas[i]>0.00005):
        rDotsGray.append(computeDifferential(filteredGrayDiameters, i, 1./framesPerSecond)*2.)
        fluxesGray.append(massFlowRate/(filteredGrayAreas[i]))
    else:
        #pass
        rDotsGray.append(0)
        fluxesGray.append(0)

for i in range(1,len(times)-1):
    if (filteredHSVDiameters[i] > 0.005) and (filteredHSVAreas[i]>0.00005):
        rDotsHSV.append(computeDifferential(filteredHSVDiameters, i, 1./framesPerSecond)*2.)
        fluxesHSV.append(massFlowRate/(filteredHSVAreas[i]))
    else:
        #pass
        #print "hello"
        rDotsHSV.append(0)
        fluxesHSV.append(0)

dimlessGray=[]
dimlessHSV=[]

nlessGray=[]
nlessHSV=[]
reducedTime= times[1:-1]

#published regression rates
n = 0.6
a=0.672E-3

for i in range(0,len(rDotsGray)):
    #print fluxesGray[i]
    if (fluxesGray[i] > 0):
        dimlessGray.append(rDotsGray[i]/(fluxesGray[i]**n))
        nlessGray.append(math.log(abs(rDotsGray[i])/a)/math.log(abs(fluxesGray[i])))
    else:
        dimlessGray.append(0)
        nlessGray.append(0)

for i in range(0,len(rDotsHSV)):
    if (fluxesHSV[i] > 0):
        dimlessHSV.append(rDotsHSV[i]/(fluxesHSV[i]**n))
        #print math.log(rDotsHSV[i])
        nlessHSV.append(math.log(abs(rDotsHSV[i])/a)/math.log(abs(fluxesHSV[i])))
    else:
        dimlessHSV.append(0)
        nlessHSV.append(0)

pylab.figure('normalizedRDot')

#some more plots
pylab.plot(reducedTime,dimlessGray)
```

```
pylab.plot(reducedTime,dimlessHSV)
pylab.plot([0,5],[a,a])
pylab.xlabel('Time, s')
pylab.ylabel(r'a={\dot{r}/{G^n}')
pylab.title('Hot Fire %d'%(hotFireNumber))
#pylab.ylabel(r"\displaystyle a = \frac{\dot{r}}{G_{ox}^n}")
pylab.ylim([-0.0015,0.0015])
pylab.xlim(xlimits)
pylab.legend(['Filtered Gray-scale data','Filtered HSV data','Published Constant'],loc=3)
pylab.savefig(fileName+'/rDotOverMassFluxn.png')

#pylab.figure('fluxVsDiffR')
#pylab.plot(fluxesGray,rDotsGray)
#pylab.plot(fluxesHSV,rDotsHSV)
pylab.figure('timevsFlux')
pylab.xlim(xlimits)
pylab.plot(reducedTime,fluxesGray)
pylab.savefig(fileName+'/timevsFlux.png')

pylab.figure('timevsRDot')
pylab.xlim(xlimits)
pylab.plot(reducedTime,rDotsGray)
pylab.savefig(fileName+'/timevsRdot.png')

pylab.figure('nExponent')
pylab.plot(reducedTime,nlessGray)
pylab.plot(reducedTime,nlessHSV)
pylab.plot([0,5],[0.62,0.62])
pylab.title('Hot Fire %d'%(hotFireNumber))
pylab.xlim(xlimits)
pylab.xlabel('Time, s')
pylab.ylabel('n exponent')

pylab.legend(['Filtered Gray-scale data','Filtered HSV data','Published Constant'],loc=3)
pylab.savefig(fileName+'/nExponent.png')
print "done"
pylab.show()

#lets output the data so it can be read by other files
f = open(fileName+'/outputPlotDataForUse.csv','w')
f.write('time\tdiameter\trDot\n')
for i in range(0,len(reducedTime)):
    f.write('%f, %f, %f\n'%(reducedTime[i],filteredGrayDiameters[i],rDotsGray[i]))
f.close()
```

Appendix J

Testing Summary

This section of the Appendix contains the full data summary of the 22 tests.

Table J.1: This is first page of the data summary for all tests conducted for this research.

Test Number	**Condition**	**Avg. Ox. Flow Rate** ($\frac{g}{s}$)	**Avg.** $\frac{O}{F}$	**Avg. Fore End Pressure** (MPa)	**Avg. Aft End Pressure** (MPa)	**Starting Fuel ID** (cm)	**Ending Fuel ID** (cm)	**Starting Ox. Mass Flux** ($\frac{kg}{m2s}$)	**Ending Ox. Mass Flux** ($\frac{kg}{m2s}$)
1	A	49.6	1.7	1.56	1.54	2.02	3.36	155	55
2	A	49.6	1.9	1.40	1.33	1.72	2.79	210	80
3	A	49.2	1.81	1.39	1.38	1.46	2.76	290	80
4	A	49.8	2.06	1.41	1.33	1.80	2.81	200	80
5	A	49.3	2.11	1.39	1.31	1.63	2.68	240	90
6	A	49.5	2.02	1.48	1.43	1.73	2.22	210	130
7	A	50.1	1.99	1.49	1.44	1.83	3.43	190	55
8	A	50.4	1.95	1.54	1.48	1.80	3.07	200	70
9	A	50.0	2.04	1.43	1.35	1.84	3.66	190	50
10	B	24.4	1.65	1.54	-	1.63	2.81	120	40
11	B	23.7	1.51	1.52	1.52	1.91	3.45	80	25
12	C	89.5	2.25	1.75	1.61	1.93	3.99	300	70
13	C	91.3	1.81	1.71	1.56	1.65	3.99	430	75
14	C	87.8	2.38	1.75	1.60	1.86	3.99	320	70
15	E	50.2	1.97	2.29	2.24	1.88	3.10	180	65
16	E	50.1	1.9	2.35	2.31	1.79	3.02	200	70
17	E	50.27	1.9	2.31	2.27	1.76	3.13	205	65
18	F	90.1	1.72	2.34	2.25	1.40	3.99	590	70
19	F	88.2	2.36	2.24	-	2.10	3.33	250	100
20	D	24.0	1.47	2.12	2.12	2.08	2.92	70	35
21	D	23.9	1.34	2.17	2.17	1.93	3.05	80	35
22	A	50.5	2.01	1.50	1.33	1.91	3.99	180	40

Table J.2: This is second page of the data summary for all tests conducted for this research.

Test Number	**Burn Time (s)**	**Ideal C^* ($\frac{m}{s}$)**	η_{C^*}	**Avg. Nozzle Throat Heat Flux ($\frac{MW}{m^2}$)**	**Avg. Ultrasound Nozzle Erosion ($\frac{mm}{s}$)**	**Avg. Visual Nozzle Erosion ($\frac{mm}{s}$)**
1	3.55	1747	0.84	-	-	-
2	2.24	1791	0.72	35.27	-	-
3	2.27	1773	0.74	32.57	-	-
4	2.13	1807	0.72	34.84	-	-
5	1.96	1806	0.74	34.2	-	-
6	0.79	1803	0.85	-	-	-
7	3.96	1803	0.86	32.3	-	-
8	2.9	1798	0.87	31.5	0.05	0.03
9	4.22	1806	0.85	31.15	0.07	0.03
10	3.37	1729	0.91	35.23	0	-0.01
11	5.8	1671	0.9	31.75	0	-0.01
12	3.57	1810	0.87	24.9	0.09	0.11
13	3.4	1775	0.82	31.3	0.01	0
14	3.33	1811	0.92	31.7	0.1	0.09
15	2.62	1770	0.89	46.3	0.09	0.06
16	2.69	1795	0.9	46.7	0.07	0.05
17	2.97	1778	0.91	50.3	0.08	0.04
18	3.14	1753	0.83	51.5	0.21	0.14
19	2.33	1812	0.93	49.3	0.2	0.12
20	2.87	1655	0.84	56.1	0	-0.02
21	3.49	1577	0.85	47.1	0	-0.01
22	4.33	1807	0.84	36.6	0.07	0.04

J.1 Pressure Traces

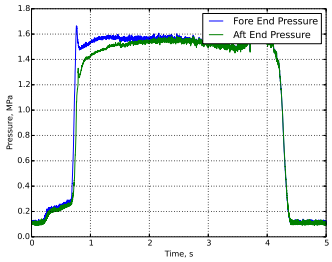

Test 1

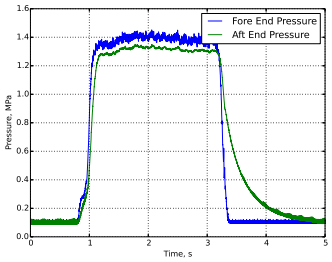

Test 2

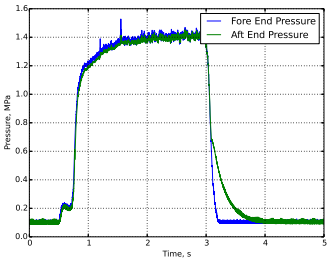

Test 3

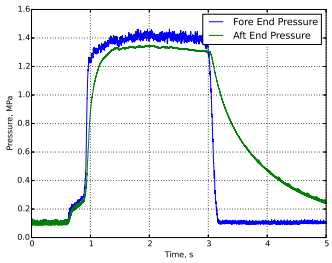

Test 4

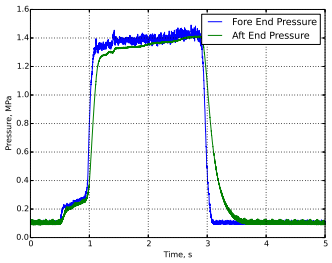

Test 5

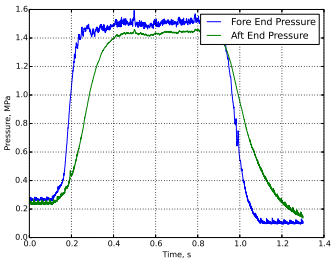

Test 6

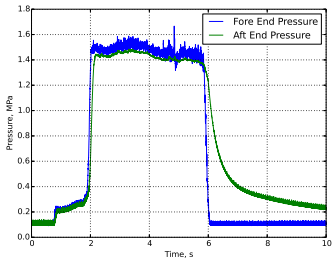

Test 7

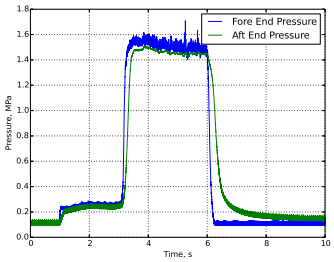

Test 8

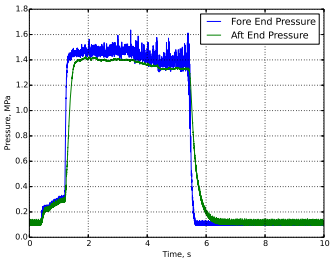

Test 9

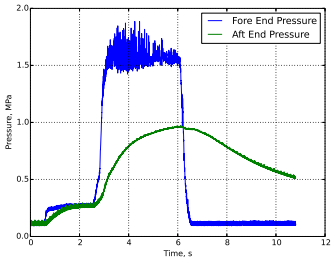

Test 10*

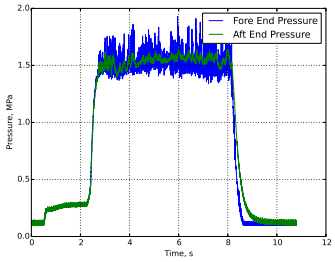

Test 11

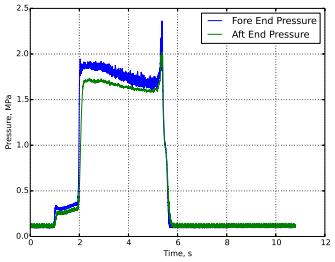

Test 12

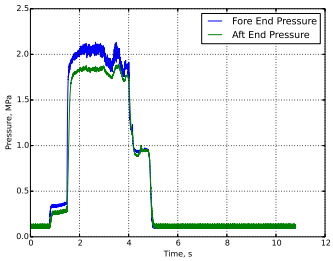

Test 13

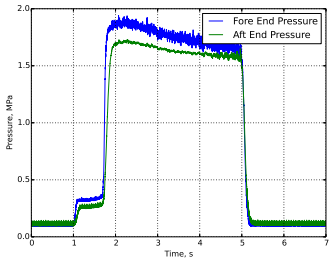

Test 14

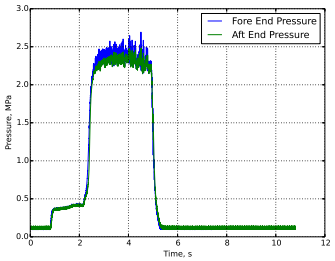

Test 15

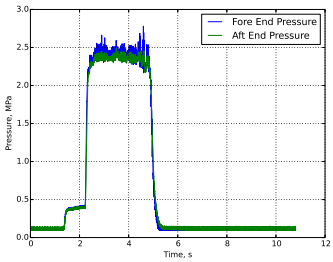

Test 16

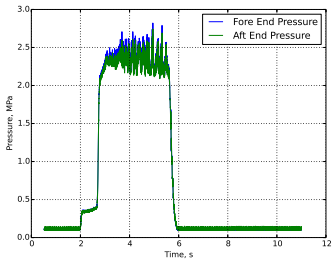

Test 17

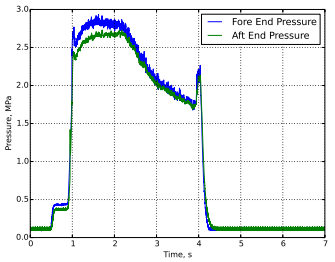

Test 18

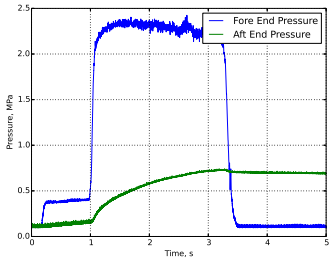

Test 19*

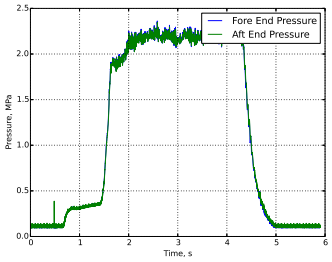

Test 20

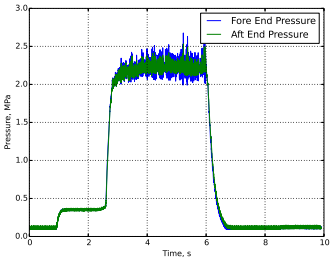

Test 21

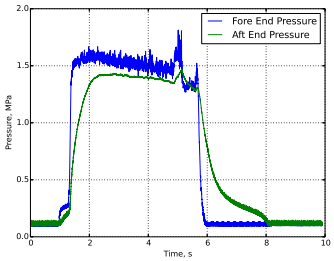

Test 22

*: The aft pressure transducer was damaged during Test 10 and Test 19. The average aft pressure measurement was approximated to compute η_{C^*}.

J.2 Oxygen Mass Flow Rates

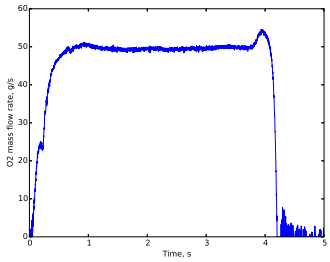

Test 1

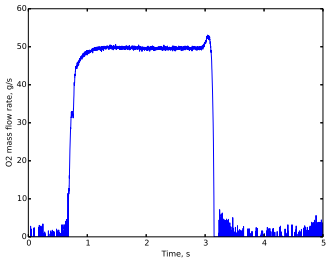

Test 2

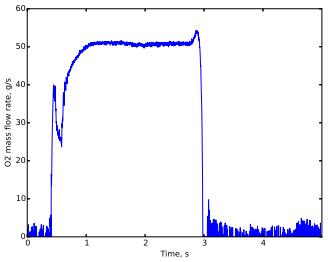

Test 3

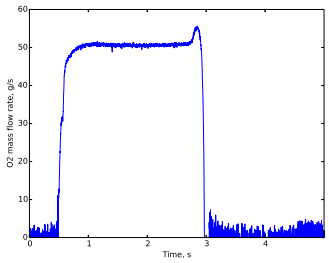

Test 4

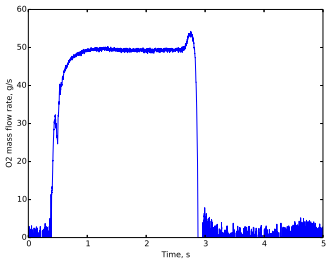

Test 5

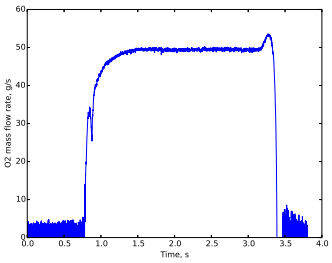

Test 6

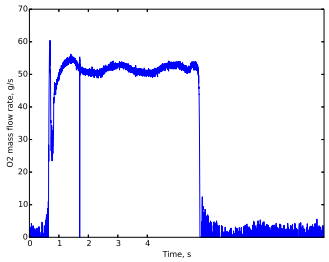

Test 7

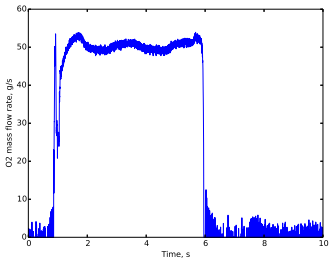

Test 8

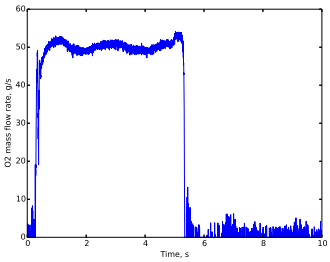

Test 9

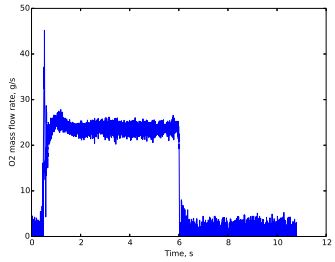

Test 10

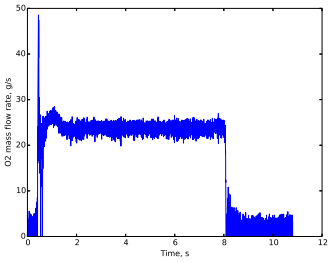

Test 11

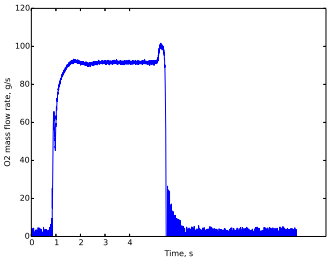

Test 12

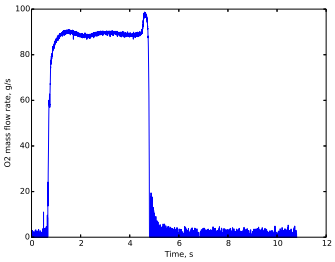

Test 13

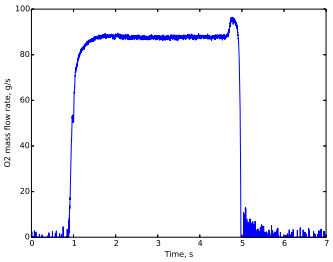

Test 14

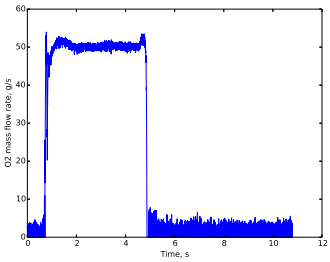

Test 15

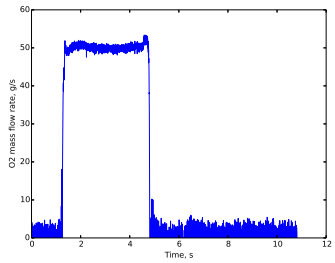

Test 16

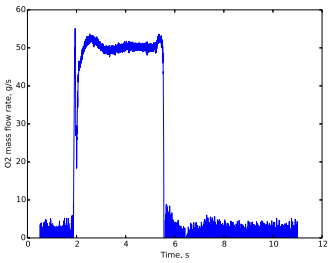

Test 17

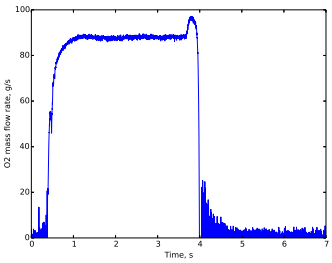

Test 18

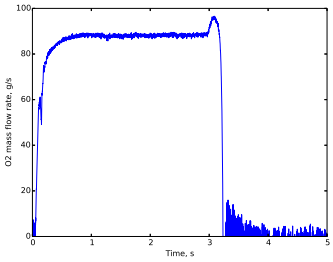

Test 19

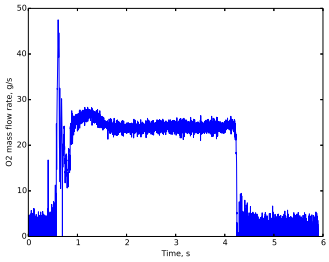

Test 20

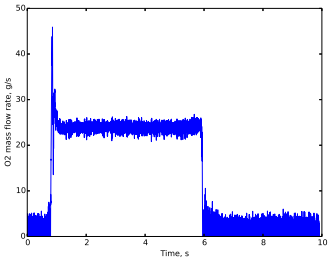

Test 21

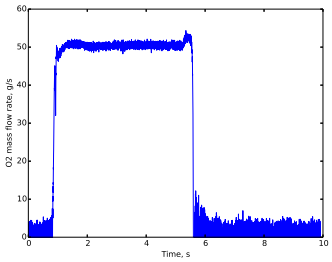

Test 22

J.3 Nozzle Erosion

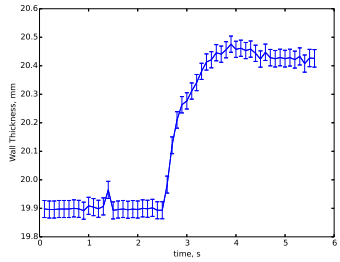

Test 8

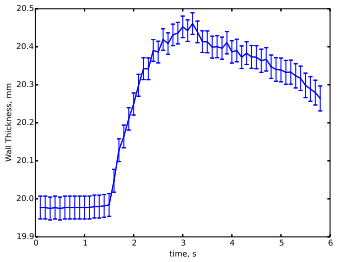

Test 9

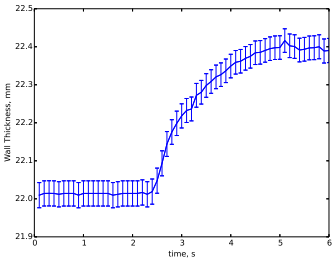

Test 10

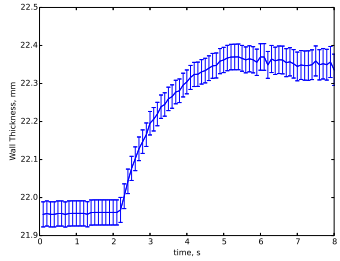

Test 11

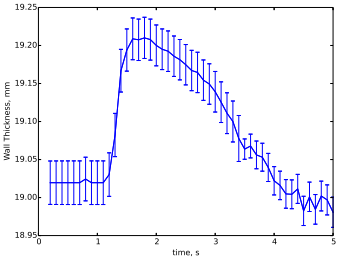

Test 12

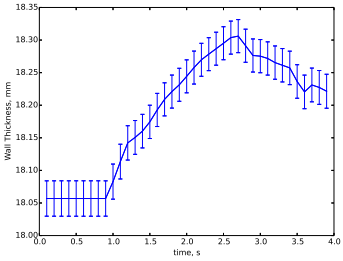

Test 13

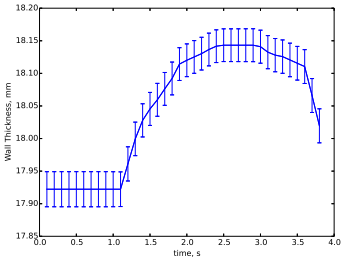

Test 14

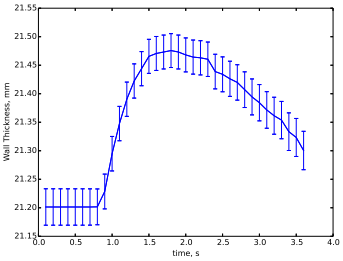

Test 15

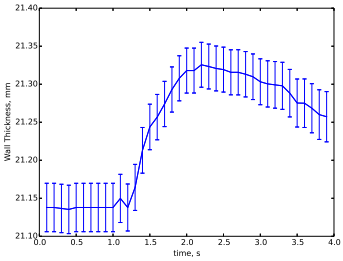

Test 16

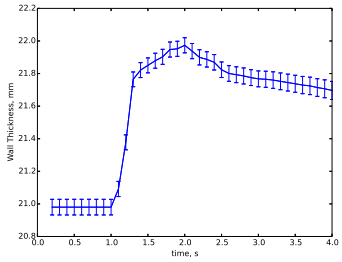

Test 17

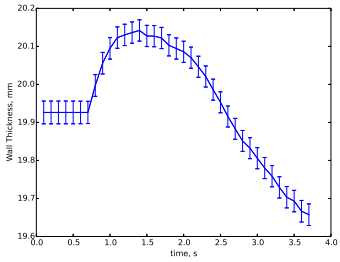

Test 18

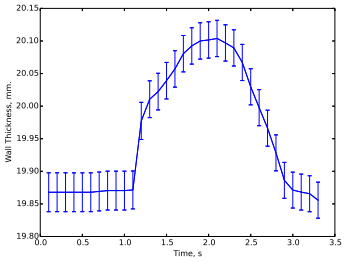

Test 19

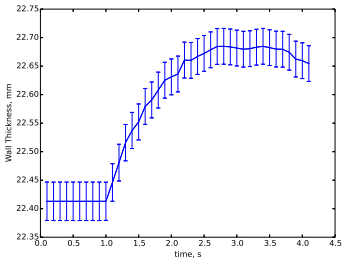

Test 20

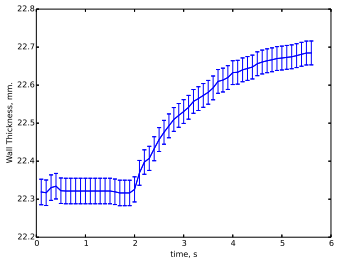

Test 21

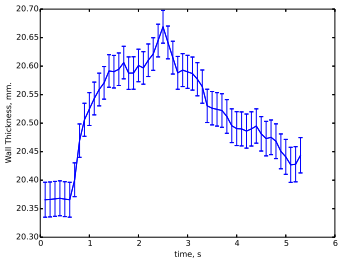

Test 22

J.4 Nozzle Heat Fluxes

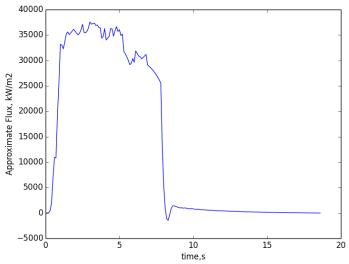

Test 2

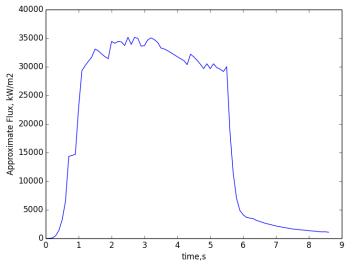

Test 3

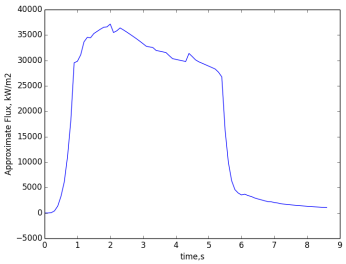

Test 4

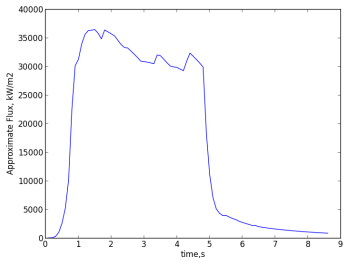

Test 5

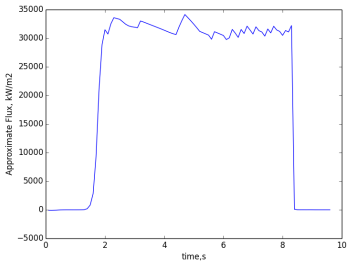

Test 7

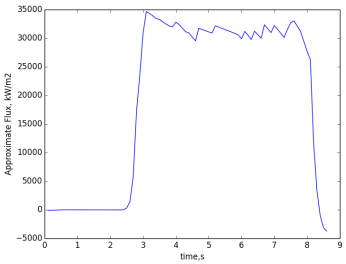

Test 8

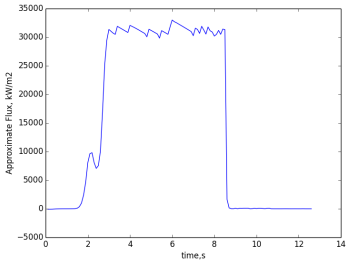

Test 9

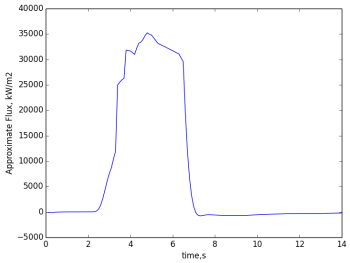

Test 10

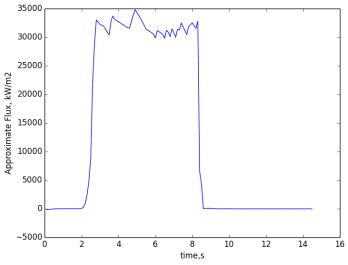

Test 11

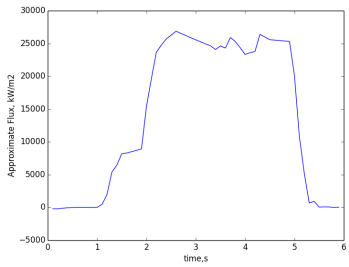

Test 12

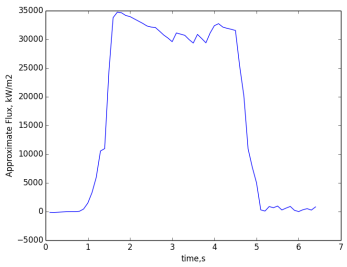

Test 13

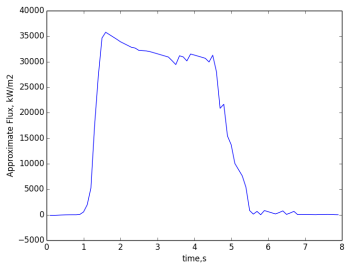

Test 14

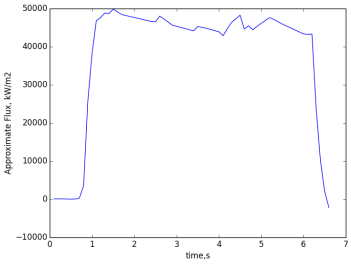

Test 15

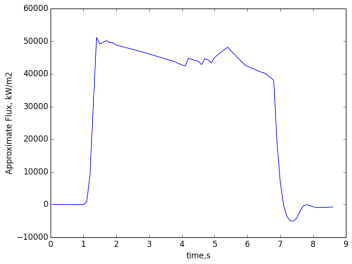

Test 16

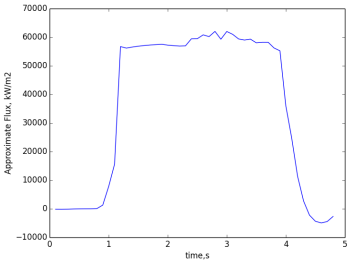

Test 17

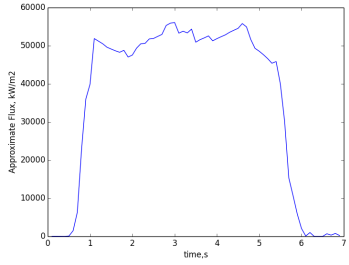

Test 18

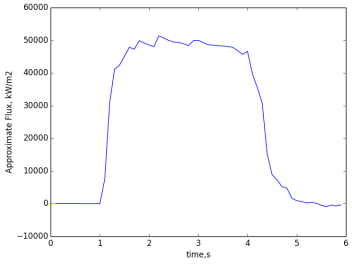

Test 19

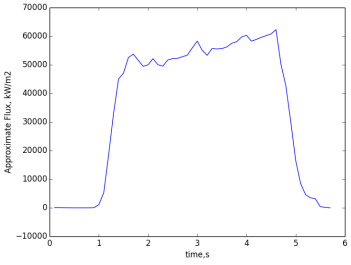

Test 20

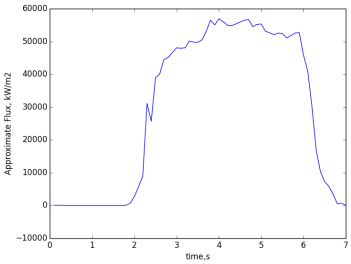

Test 21

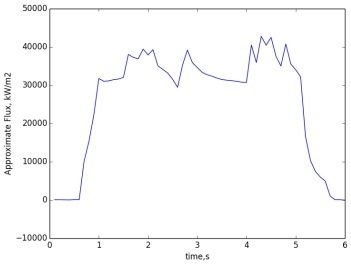

Test 22

Appendix K

New Ignition System Guide

This section of the Appendix introduces the new controller and Labview interface for controlling a rocket motor and data acquisition. The previous system was designed for the Stanford Combustion Visualization Facility and had some undesirable faults. The biggest issue was that the Data Acquisition Hardware and Software was not only in charge of acquiring the data, but it was also in charge directly controlling the valve timing sequences (which require precise timing for successful ignition). The previous system did neither of these well, as both acquiring data and controlling precise timing events is a difficult task for a single data acquisition card. To fix this, the valve control is removed from the data acquisition hardware and software altogether. The new system utilizes a microcontroller to control the valves. The microcontroller communicates directly with the Acquisition software through Serial (at a Baud Rate of 115200 Hz) messages. These messages command the controller to open or close valves (for non-timing critical events), or to perform pre-programmed sequences for timing critical events, such as hot fires. The microcontroller is also programmed with certain blocks of memory allocated in EEPROM for timing information. This allows for the direct editing of timing sequences through the data acquisition software without having to reprogram the controller with new code. Furthermore, this setup allows for data acquisition at much higher rates. Preliminary tests have shown that data can be collected at over 5 kHz, well over the maximum of 1500 Hz of the previous setup.

While the new system is not currently integrated into the lab hardware, it is fully described here and is recommended to be used for any future experiments that are conducted in the lab.

K.1 Controller Command Codes

This section describes the controller command codes programmed into the microcontroller. These can be modified in the controller programming software, which is given on Page 327. There are two main modes programmed into the microcontroller. The first mode is the MAIN mode. In

this mode, the microcontroller has access to control any digital output (valves or other hardware). When powered on, the microcontroller goes into this mode. The second mode is the EEPROM mode. This mode allows for the editing of the EEPROM memory blocks allocated to storing the timing information. Because this information is stored in EEPROM, it persists even on reset. The microcontroller communicates its state and echoes commands over the serial interface. Because of this, it is easy to log what commands were given (and when), and also to determine the state of the controller.

Note that all commands in the MAIN mode require **capital letters**. This is intentionally done so to accidentally provide EEPROM commands in the MAIN mode. This safety measures ensures valves will not open if the user mistakenly thinks they are in the EEPROM mode.

K.1.1 The MAIN Mode

Upon power up, the microcontroller enters into the control state. The following messages appear:

Rocket Controller Version Number 1
You have entered MAIN mode. To enter EEPROM Mode, enter «

All command codes in this state require two characters. If just one character is sent, the controller will wait until another is sent. The following set of commands are available:

- Output control: The individual valves (or other hardware) can be controlled via their associated letter (See Table K.1 for the pin output list). The control sequence for these controls is: first send a message for the output letter ("A","B","C", through "T") and then specify the desired state ("1" or "0"). For example, to turn on the first digital output pin, the required message would be "A1". To turn the same pin off, the command would be "A0". The controller currently has twenty digital outputs programmed (for use on Arduino Mega-type boards).

- Pre-programmed sequences: The sequence command currently has the letter "Z" reserved. To fire a sequence of pre-programmed commands, the letter "Z" should be sent along with the desired sequence number (for example, "Z1"). Currently the controller has 2 sample sequences programmed onto the board. They simply flash the on-board LED with intervals that are specified by the values stored in the EEPROM. These sequences have the option of utilizing the pin interrupt feature, which stops the sequence. This could be used as a safety measure in case of over-pressurization events.

- Controller Status: Because timing and control sequences are critical, there is no "heart-beat" programmed into the microcontroller. Instead, the user can query the controller with a "+" command followed by any character. If the controller is behaving properly, it will respond with the following message:

The rocket controller is alive and healthy.

Currently in MAIN mode.

- Read the EEPROM Values: The user can directly read the stored EEPROM data with the "?" command followed by any character. The controller will respond with:

EEPROM Values Printed Below

EEPROM VALUE 0

<EEPROM value>

EEPROM VALUE 1

<EEPROM value>

EEPROM VALUE 2

<EEPROM value>

EEPROM VALUE 3

<EEPROM value>

EEPROM VALUE 4

<EEPROM value>

EEPROM VALUE 5

<EEPROM value>

- Enter the EEPROM mode: The user can enter the EEPROM mode by sending a "<" command followed by any character. If the user is already in the EEPROM mode, the controller will respond with a message stating that it is already in the EEPROM mode.
- Enter the MAIN mode: Although the user should already be in the main mode at this point, the universal command to enter the main mode is ">" followed by any character. If the user attempts to enter the MAIN mode while already in the main mode, the controller will respond with a message stating that it is already in the main mode.

K.1.2 The EEPROM Mode

The EEPROM mode is a special mode reserved for writing data to the EEPROM blocks reserved for timing information. Currently, 6 addresses have been reserved to store 6 timing points (of type unsigned long integers). The range of the stored each stored point is between 0 and $2^{32} - 1$. The Arduino Mega boards have capability to store much more EEPROM information, so future upgrades can be applied. Each data point requires 4 bytes of EEPROM storage, and the Arduino has 4kb available for EEPROM storage.

Note that all EEPROM commands related to writing to the EEPROM data require a lower case letter. This prevents the accidental opening or closing of valves while mistakenly in the MAIN mode.

The command codes in this mode are described below:

- Store a value to an EEPROM memory block: All EEPROM memory blocks are specified by their lower case letters ("a","b","c", through "f"). All values are stored in units of milliseconds, although a control sequence can utilize the stored data in seconds or microseconds if desired. The command sequence to program memory block "a" with the value of 94305 is "a94305". The microcontroller will respond with:

  I got the command a with Value 94305

- Read the EEPROM values: The command to read the EEPROM values is the same as in the MAIN mode. Simply send a "?" command followed by any character.

- Check controller status: As in the MAIN mode, the user can check the controller status by sending the "+" command followed by any character. If in a controllable state, the microcontroller will respond with a message stating it is in the EEPROM mode.

- Enter the MAIN mode: To enter the main mode, enter the ">" command followed by any character"

- Enter the EEPROM mode: Although the user is already in the EEPROM mode at this point, if the "<" command followed by any character is sent, the controller will respond with a message stating that it is already in the EEPROM mode.

K.2 Controller Pin Layout

This section describes the pin layout on the Arduino Mega so that any future user could easily utilize this controller in their experimental setup. Note that the Arduino Mega runs on 5V. It cannot handle more than 5V and any applied voltages over this limit could cause irreparable damage to the controller. Furthermore, the output current limit for each pin is only 40mA. Therefore, relays are required for each pin for most controls.

Table K.1: The pins reserved for the controller.

Pin Number	Notes
2	Reserved as the interrupt pin. Pull high for interrupt event.
3	Control for Output A (Output 1)
4	Control for Output B (Output 2)
5	Control for Output C (Output 3)
6	Control for Output D (Output 4)
7	Control for Output E (Output 5)
8	Control for Output F (Output 6)
9	Control for Output G (Output 7)
10	Control for Output H (Output 8)
11	Control for Output I (Output 9)
12	Control for Output J (Output 10)
13	Control for Output K (Output 11). This pin has an LED on the microcontroller
14	Control for Output L (Output 12)
15	Control for Output M (Output 13)
16	Control for Output N (Output 14)
17	Control for Output O (Output 15)
18	Control for Output P (Output 16)
19	Control for Output Q (Output 17)
20	Control for Output R (Output 18)
21	Control for Output S (Output 19)
22	Control for Output T (Output 20)
USB	Port reserved for the Test Control Stand

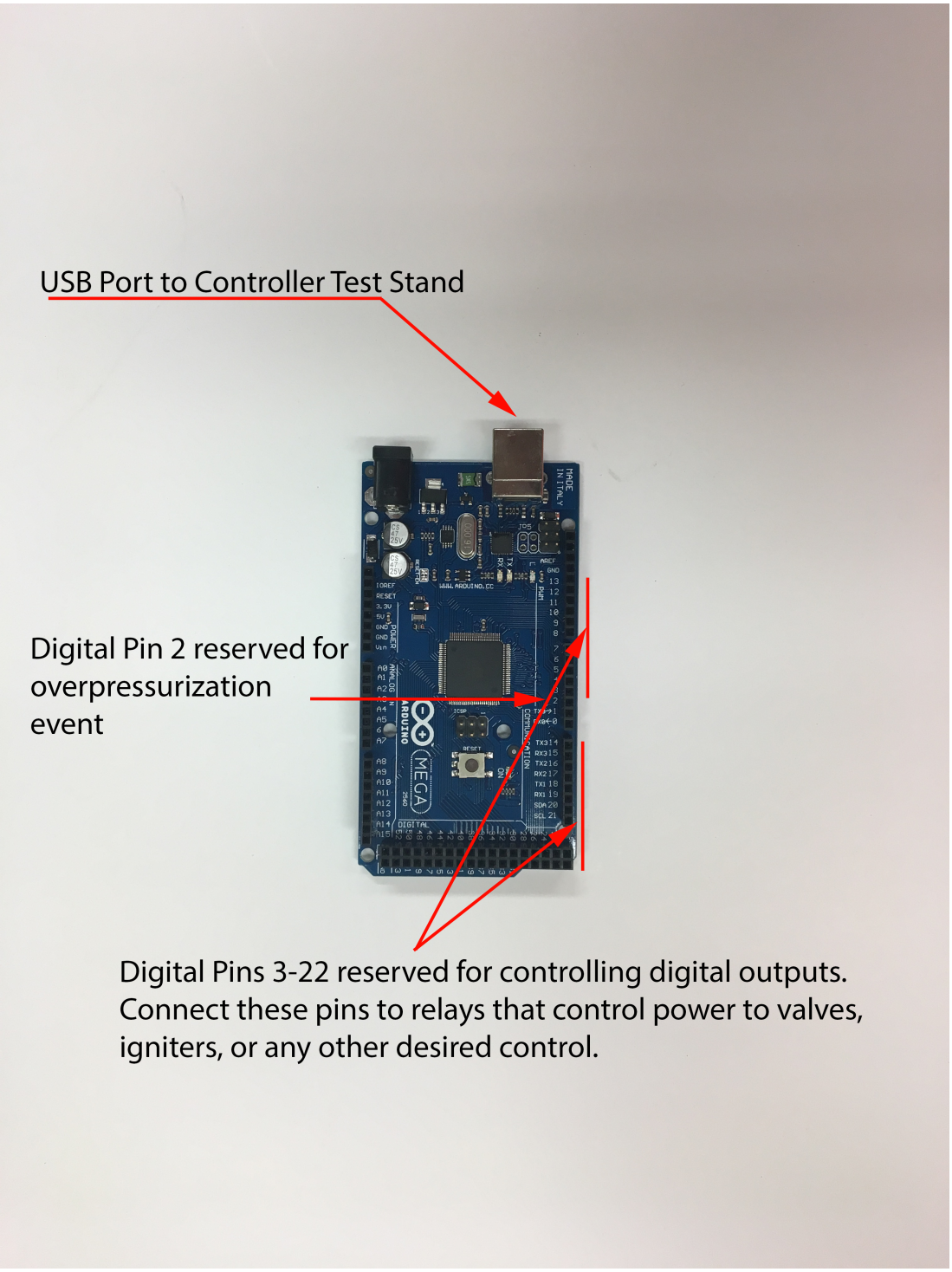

Figure K.1: The pins reserved for the controller.

K.3 Controller Programming Source Code

This section provides the source code for the microcontroller.

```
#include <EEPROM.h>

const unsigned int VERSIONNUMBER = 1;
int interruptPin = 2; //THIS IS RESERVED FOR OVER PRESSURIZATION --> CANCEL FIRE ROUTINE AND GO INTO SAFE MODE (
     TURN OFF OXYGEN VALVES THEN ENTER MAIN MODE STATE FOR MANUAL PURGE)
int dOut1Pin = 3; //A
int dOut2Pin = 4; //B
int dOut3Pin = 5; //C
int dOut4Pin = 6; //D
int dOut5Pin = 7; //E
int dOut6Pin = 8; //F
int dOut7Pin = 9; //G
int dOut8Pin = 10; //H
int dOut9Pin = 11; //I
int dOut10Pin = 12; //J
int dOut11Pin = 13; //K
int dOut12Pin = 14; //L
int dOut13Pin = 15; //M
int dOut14Pin = 16; //N
int dOut15Pin = 17; //O
int dOut16Pin = 18; //P
int dOut17Pin = 19; //Q
int dOut18Pin = 20; //R
int dOut19Pin = 21; //S
int dOut20Pin = 22; //T
//Note the OFFSET between dOUT__ and Pin number..Pins 0 and 1 are reserved for communications.  Pin 2 is reserved
     for the interrupt


// EEPROM Memory locations.  Note each EEPROM data is stored in unsigned longs, which take up 4 bytes each.
int addr0 = 0;
int addr1 = 4;
int addr2 = 8;
int addr3 = 12;
int addr4 = 16;
int addr5 = 20;

// EEPROM Variable Names.  Store 0 values and on setup() it will load the saved data
unsigned long EEPROMValue0 = 0;
unsigned long EEPROMValue1 = 0;
unsigned long EEPROMValue2 = 0;
unsigned long EEPROMValue3 = 0;
unsigned long EEPROMValue4 = 0;
unsigned long EEPROMValue5 = 0;
//


//CODE START BELOW
//first define some useful functions

void INTERRUPTSAFEMODE() {
```

```
  //This is the overpressurization interrupt.
  //Let the user know that over pressureization has occured.
  //Turn off all outputs (pull low)
  //Then perform a software reset.
  //The software reset mechanism is not the best, but is only software solution currently available
  //For the Arduino Mega
  detachInterrupt(digitalPinToInterrupt(interruptPin));
  Serial.println("INTERRUPT DETECTED");
  Serial.println("This usually corresponds to overpressurization");
  Serial.println("ENTERING INTO A SAFE STATE");
  Serial.println("TURNING OFF ALL THE VALVES");
  Serial.println("YOU WILL NEED TO MANUALLY PURGE");
  Serial.println("It is recommended to reboot the controller manually");
  Serial.println("This can be done via the reset button or exiting labview and unplugging the controller");

  //IN INTERUPPT MODE, TURN OFF ALL OUTPUTS AND RESET THE CONTROLLER.
  int setPin = 0;
  digitalWrite(dOut1Pin, setPin);
  digitalWrite(dOut2Pin, setPin);
  digitalWrite(dOut3Pin, setPin);
  digitalWrite(dOut4Pin, setPin);
  digitalWrite(dOut5Pin, setPin);
  digitalWrite(dOut6Pin, setPin);
  digitalWrite(dOut7Pin, setPin);
  digitalWrite(dOut8Pin, setPin);
  digitalWrite(dOut9Pin, setPin);
  digitalWrite(dOut10Pin, setPin);
  digitalWrite(dOut11Pin, setPin);
  digitalWrite(dOut12Pin, setPin);
  digitalWrite(dOut13Pin, setPin);
  digitalWrite(dOut14Pin, setPin);
  digitalWrite(dOut15Pin, setPin);
  digitalWrite(dOut16Pin, setPin);
  digitalWrite(dOut17Pin, setPin);
  digitalWrite(dOut18Pin, setPin);
  digitalWrite(dOut19Pin, setPin);
  digitalWrite(dOut20Pin, setPin);

  asm volatile("  jmp 0"); //software reset.  Watchdog timers are better method, but don't work properly on
       Arduino Mega without new bootloader
}

void EEPROM_writeLong(int ee, unsigned long value)
{ //This function writes a datapoint to the EEPROM address.
  unsigned long TempValue = EEPROM_readLong(ee);
  if (TempValue != value) {
    byte* p = (byte*)(void*)&value;
    for (int i = 0; i < sizeof(value); i++)
      EEPROM.write(ee++, *p++);
  }
}

unsigned long EEPROM_readLong(int ee)
{//This function reads a datapoint from EEPROM address
  unsigned long  value = 0;
  byte* p = (byte*)(void*)&value;
```

```
  for (int i = 0; i < sizeof(value); i++)
    *p++ = EEPROM.read(ee++);
  return value;
}

void readEEPROM() {
  //This function simply reads the EEPROM Data and stores it locally for use.
  EEPROMValue0 = EEPROM_readLong(addr0);
  EEPROMValue1 = EEPROM_readLong(addr1);
  EEPROMValue2 = EEPROM_readLong(addr2);
  EEPROMValue3 = EEPROM_readLong(addr3);
  EEPROMValue4 = EEPROM_readLong(addr4);
  EEPROMValue5 = EEPROM_readLong(addr5);
}

void setup()
{//This sets the pins as outputs, disables any interrupts, and basically just starts the controller.
  detachInterrupt(digitalPinToInterrupt(interruptPin)); // we turn this off to prevent reset loops during over
       pressurization.  Only look for over pressure during a fire sequence.
  readEEPROM(); //load the saved EEPROM Data from memory
  Serial.begin(115200); //Set the BAUD RATE for communcations
  Serial.println("Rocket Controller Version Number " + (String) VERSIONNUMBER);
  //SET ALL DIGITAL PINS TO OUTPUT
  pinMode(dOut1Pin, OUTPUT);
  pinMode(dOut2Pin, OUTPUT);
  pinMode(dOut3Pin, OUTPUT);
  pinMode(dOut4Pin, OUTPUT);
  pinMode(dOut5Pin, OUTPUT);
  pinMode(dOut6Pin, OUTPUT);
  pinMode(dOut7Pin, OUTPUT);
  pinMode(dOut8Pin, OUTPUT);
  pinMode(dOut9Pin, OUTPUT);
  pinMode(dOut10Pin, OUTPUT);
  pinMode(dOut11Pin, OUTPUT);
  pinMode(dOut12Pin, OUTPUT);
  pinMode(dOut13Pin, OUTPUT);
  pinMode(dOut14Pin, OUTPUT);
  pinMode(dOut15Pin, OUTPUT);
  pinMode(dOut16Pin, OUTPUT);
  pinMode(dOut17Pin, OUTPUT);
  pinMode(dOut18Pin, OUTPUT);
  pinMode(dOut19Pin, OUTPUT);
  pinMode(dOut20Pin, OUTPUT);
}

void EEPROMMode() {
  //THIS IS THE EEPROM MODE
  int keepGoing = 1;
  unsigned long value; //place to store the read value
  char command; //place to store the command

  Serial.println("You have entered EEPROM Mode");
  Serial.println("To exit EEPROM Mode, send the command >>");

  while (keepGoing == 1) { //infinite loop... Stay here until an exit command is requested.
    while (Serial.available() > 1) {
```

```
//same format...command + value
command = (char) Serial.read();
value = (unsigned long) Serial.parseInt();

switch (command) {
//THIS IS EEPROM MODE...ONLY HAVE EEPROM OPTIONS HERE
  case 'a'://write to the first address
    EEPROM_writeLong(addr0, value);
    Serial.println("I got the command " + (String) command + " with Value " + (String) value);
    break;

  case 'b': //write to the second address
    EEPROM_writeLong(addr1, value);
    Serial.println("I got the command " + (String) command + " with Value " + (String) value);
    break;

  case 'c': //write to the third address
    EEPROM_writeLong(addr2, value);
    Serial.println("I got the command " + (String) command + " with Value " + (String) value);
    break;

  case 'd': //write to the fourth address
    EEPROM_writeLong(addr3, value);
    Serial.println("I got the command " + (String) command + " with Value " + (String) value);
    break;

  case 'e': //write to the fifth address
    EEPROM_writeLong(addr4, value);
    Serial.println("I got the command " + (String) command + " with Value " + (String) value);
    break;

  case 'f': //write to the sixth address
    EEPROM_writeLong(addr5, value);
    Serial.println("I got the command " + (String) command + " with Value " + (String) value);
    break;

  case '>': //exit the EEPROM Mode
    Serial.flush();
    Serial.println("Exiting the EEPROM Mode to go into MAIN mode");
    loop();
    break;

  case '?': //print the EEPROM information
    printEEPROM();
    break;

  case '<': //already in EEPROM Mode
    Serial.println("You are already in EEPROM Mode.");
    break;

  case '+':
    Serial.println("The rocket controller is alive and healthy.");
    Serial.println("Currently in EEPROM Mode");
    break;

}
```

```
    }
  }
}

void printEEPROM() {
  //This function reads all of the EEPROM values and writes them over the Serial Interface
  Serial.println("EEPROM Values Printed Below");
  readEEPROM();
  Serial.println("EEPROM VALUE 0");
  Serial.println(EEPROMValue0, DEC);
  Serial.println("EEPROM VALUE 1");
  Serial.println(EEPROMValue1, DEC);
  Serial.println("EEPROM VALUE 2");
  Serial.println(EEPROMValue2, DEC);
  Serial.println("EEPROM VALUE 3");
  Serial.println(EEPROMValue3, DEC);
  Serial.println("EEPROM VALUE 4");
  Serial.println(EEPROMValue4, DEC);
  Serial.println("EEPROM VALUE 5");
  Serial.println(EEPROMValue5, DEC);
}

void loop()
//This is the main loop.  It hosts the MAIN mode.
{

  char command; //store command here
  char value;  //store value (1 or 0) here
  int pinCommand;  //this is reserved for converting value for use.

  Serial.println("You have entered the MAIN mode.  To enter EEPROM Mode, enter <<");
  int keepGoing = 1;
  while (keepGoing == 1) {
    while (Serial.available() > 1) //wait until 2 characters are on the serial queue
    {
      command = (char)Serial.read();
      value   =  (char) Serial.read();
      if (value == '1') {
        pinCommand = 1;
      }
      else {
        pinCommand = 0;
      }

      Serial.flush(); //clear any additional commands.
      switch (command) {
        //capital letters alter valve states (and the fire command)
        //lower case commands are related to eeprom commands.  They do nothing here
        //THIS IS THE MAIN VALVE COMMANDS. PROGRAM IN VALVE COMMANDS HERE

        case 'A':
          digitalWrite(dOut1Pin, pinCommand);
          Serial.println("I got a command " + (String) command + " with Value " + (String) value);
          break;

        case 'B':
```

```
  digitalWrite(dOut2Pin, pinCommand);
  Serial.println("I got a command " + (String) command + " with Value " + (String) value);
  break;

case 'C':
  digitalWrite(dOut3Pin, pinCommand);
  Serial.println("I got a command " + (String) command + " with Value " + (String) value);
  break;

case 'D':
  digitalWrite(dOut4Pin, pinCommand);
  Serial.println("I got a command " + (String) command + " with Value " + (String) value);
  break;

case 'E':
  digitalWrite(dOut5Pin, pinCommand);
  Serial.println("I got a command " + (String) command + " with Value " + (String) value);
  break;

case 'F':
  digitalWrite(dOut6Pin, pinCommand);
  Serial.println("I got a command " + (String) command + " with Value " + (String) value);
  break;

case 'G':
  digitalWrite(dOut7Pin, pinCommand);
  Serial.println("I got a command " + (String) command + " with Value " + (String) value);
  break;

case 'H':
  digitalWrite(dOut8Pin, pinCommand);
  Serial.println("I got a command " + (String) command + " with Value " + (String) value);
  break;

case 'I':
  digitalWrite(dOut9Pin, pinCommand);
  Serial.println("I got a command " + (String) command + " with Value " + (String) value);
  break;

case 'J':
  digitalWrite(dOut10Pin, pinCommand);
  Serial.println("I got a command " + (String) command + " with Value " + (String) value);
  break;

case 'K':
  digitalWrite(dOut11Pin, pinCommand);
  Serial.println("I got a command " + (String) command + " with Value " + (String) value);
  break;

case 'L':
  digitalWrite(dOut12Pin, pinCommand);
  Serial.println("I got a command " + (String) command + " with Value " + (String) value);
  break;

case 'M':
  digitalWrite(dOut13Pin, pinCommand);
```

```
  Serial.println("I got a command " + (String) command + " with Value " + (String) value);
  break;

case 'N':
  digitalWrite(dOut14Pin, pinCommand);
  Serial.println("I got a command " + (String) command + " with Value " + (String) value);
  break;

case 'O':
  digitalWrite(dOut15Pin, pinCommand);
  Serial.println("I got a command " + (String) command + " with Value " + (String) value);
  break;

case 'P':
  digitalWrite(dOut16Pin, pinCommand);
  Serial.println("I got a command " + (String) command + " with Value " + (String) value);
  break;

case 'Q':
  digitalWrite(dOut17Pin, pinCommand);
  Serial.println("I got a command " + (String) command + " with Value " + (String) value);
  break;

case 'R':
  digitalWrite(dOut18Pin, pinCommand);
  Serial.println("I got a command " + (String) command + " with Value " + (String) value);
  break;


case 'S':
  digitalWrite(dOut19Pin, pinCommand);
  Serial.println("I got a command " + (String) command + " with Value " + (String) value);
  break;

case 'T':
  digitalWrite(dOut20Pin, pinCommand);
  Serial.println("I got a command " + (String) command + " with Value " + (String) value);
  break;

case 'Z': //THIS IS THE FIRE COMMAND
  Serial.println("I got a command " + (String) command + " with Value " + (String) value);
  Serial.println("Starting the fire sequence!");
  fireSequence(value); //go to the fire sequence.  Value decides which sequence to compute.  SEE BELOW
  Serial.println("Fire sequence completed");
  break;

case '<': //Go into EEPROM Mode
  EEPROMMode();
  break;

case '?': //Print the EEPROM
  printEEPROM();
  break;

case '>': //Already in main Mode
  Serial.println("You are already in main mode");
```

```
          break;

        case '+':
          Serial.println("The rocket controller is alive and healthy.");
          Serial.println("Currently in MAIN Mode.");
          break;
      }
    }
  }
}

void fireSequence(char sequence) {//THIS FUNCTION IS PREPROGRAMMED FIRE SEQUENCES.  EDIT / ADD NEW ONES HERE

  if (sequence == '1') { //This first example sequence is called when Z1 is sent.  This
    //Example has the over pressureization enabled.

    attachInterrupt(digitalPinToInterrupt(interruptPin), INTERRUPTSAFEMODE, RISING); //enable interrupt pin
    //for overpressurization safety
    Serial.println("Overpressurization Interrupt Enabled"); //let the user know.

    readEEPROM(); //read the EEPROM one last time before the sequence.  This makes sure that the
    //controller is using the latest available timings.

    //begin sequence
    digitalWrite(dOut11Pin, 1);
    delay(EEPROMValue0);
    digitalWrite(dOut11Pin, 0);
    delay(EEPROMValue1);
    digitalWrite(dOut11Pin, 1);
    delay(EEPROMValue2);
    digitalWrite(dOut11Pin, 0);
    delay(EEPROMValue3);
    digitalWrite(dOut11Pin, 1);
    delay(EEPROMValue4);
    digitalWrite(dOut11Pin, 0);
    delay(EEPROMValue5);
    digitalWrite(dOut11Pin, 1);
    delay(100);
    digitalWrite(dOut11Pin, 0);
    //end sequence

    detachInterrupt(digitalPinToInterrupt(interruptPin)); //if the code makes it here
    //that means everything remained under the safe pressure
    //If the interrupt was activated, the controller would not make it to this
    //portion of the code.


    return;
  }


  //NOTE ON THE INTERRUPT -- IF INTERRUPT FIRES SOMETIME AFTER THE OXYGEN VALVE HAS OPENNED, THE OX VALVE WILL
       CLOSE.
  //THE INTERRUPT WILL CLOSE ALL OUTPUTS AND RESET THE CONTROLLER.  MANUAL PURGE WILL NEED TO BE COMPLETED
  //AND USER WILL LIKELY WANT TO VENT THE LINES SAFELY
```

```
  if (sequence == '2') {
    //This is the second example fire sequence.
    //No interrupt protection is enabled on this sequence.
    readEEPROM();
    digitalWrite(dOut11Pin, 1);
    delay(EEPROMValue0); //delay is measured in milliseconds.
    digitalWrite(dOut11Pin, 0);
    delay(EEPROMValue1);
    digitalWrite(dOut11Pin, 1);
    delay(EEPROMValue2);
    digitalWrite(dOut11Pin, 0);
    delay(EEPROMValue3);
    digitalWrite(dOut11Pin, 1);
    delay(EEPROMValue4);
    digitalWrite(dOut11Pin, 0);
    delay(EEPROMValue5);
    digitalWrite(dOut11Pin, 1);
    delay(EEPROMValue0);
    digitalWrite(dOut11Pin, 0);
  }
 return;

 //The user will need to update the fire sequences for their individual uses.  The LABVIEW software can be
 //set up so it only fires the desired sequence.  This way each experiment can have its own labview file
 //so the wrong fire sequence would never be called.  Just be sure to check the EEPROM values before each
 //fire.
}
```

K.4 Test Stand Control Software Guide

This section describes the LabView interface for the controller and the experiment.

The LabView interface was completely rebuilt from the original VI that was used when the Stanford Combustion Visualization Facility was first used. That VI was build with multiple if statements, which slowed the system down quite a bit.

K.4.1 The Wiring Diagram

The new VI design utilizes multiple parallel loops with event based actions. This programming technique is more modern and makes the VI more responsive, understandable, and easier to modify. There are three main loops in the VI. The first is the main user interface loop. This loop handles all events that occur when a user pushes a button or moves a switch. There is an event loop within this main loop that handles quick events, such as sending a message to the micro-controller. Because the Serial protocol is run at a high baud rate, the serial communication actions remain within this main user interface loop. Additionally, this main loop handles the case when the fire button is hit.

Because the fire sequence is expected to take several seconds (the actual timing sequence is handled by the micro-controller), the main loop sends messages to the two other loops via variables

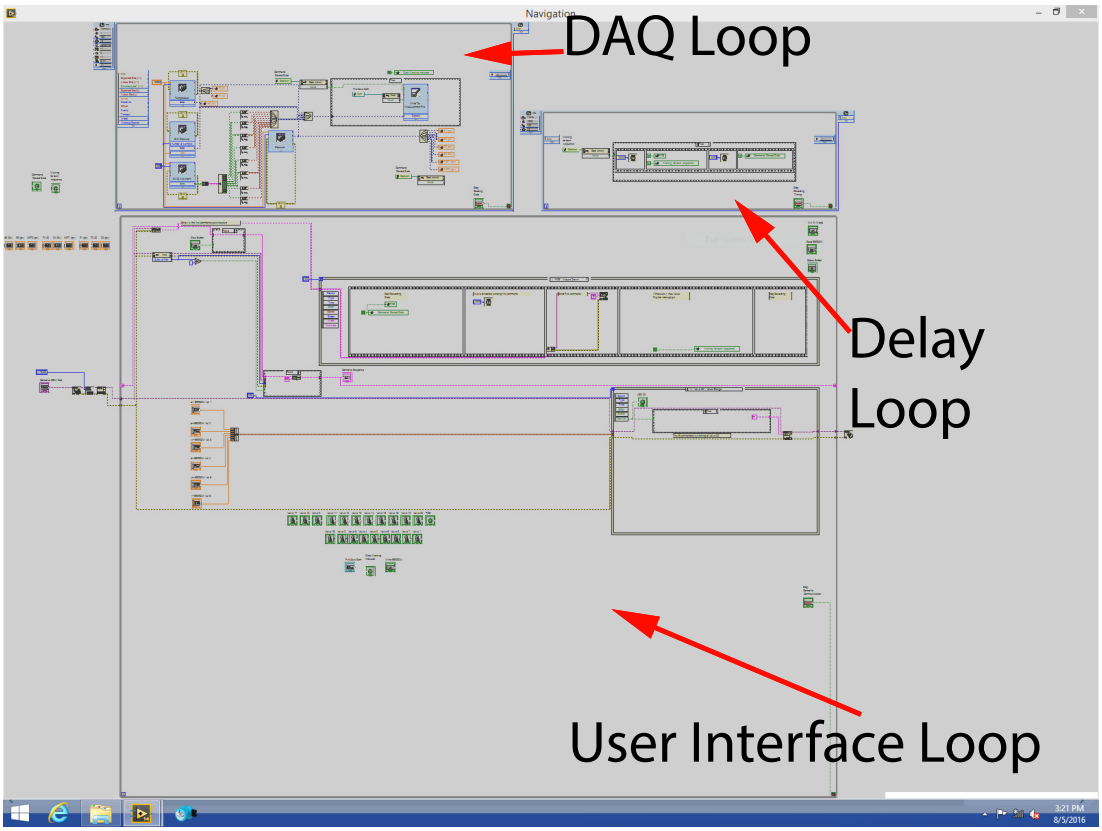

Figure K.2:]
The wiring diagram shows the three main loops used in the programming of the control stand VI. Note that the VI is relatively simple and easy to modify.

and LEDs. Essentially, the main user interface loop sends a fire message to the micro-controller, and tells the DAQ loop to record data, and tells the timing delay loop to wait a specified time before sending a message to the DAQ loop to stop recording data.

Because the data acquisition and the timing delay are occurring in different parallel loops, the user interface remains active and the computer does not seem to be locking up. This was problematic on the previous VI, where at times the delay between clicking on a switch and the actual response of the valve could be measured in seconds.

Another benefit of the parallel loop structure is that the VI is much simpler to update. If the user wants to add a new switch, the only change needed within the user interface loop is to add an event case where the switch was pressed.

The second loop is the DAQ loop. This loop is in charge of acquiring data and recording data when requested. The DAQ is always collecting data at a fast sampling rate. This sampling rate needs to be adjusted so that it is maximized and still reliable. This adjustment cannot take place

until all upcoming sensors are in place.

The DAQ receives a record message when the Command Record Data LED is enabled. This LED gets enabled automatically when the Fire command is sent. The sequence during the fire sequence is as follows:

- Fire button is pressed
- Start recording data LED is enabled
- There is a two second wait period (to allow for the DAQ loop to begin recording data)
- The fire sequence message is sent to the micro-controller
- The wait loop is instructed to wait 20 seconds and then turn off the record data LED
- The main user interface loop returns to normal
- After 20 seconds, the wait loop sends a message to the DAQ loop to stop recording data
- The DAQ loop stops the recording of data

While this sequence of events are admittedly confusing at first glance, they are actually simple and are straightforward to program into LabView.

The wait loop is relatively straightforward. Whenever the "Fire" "Waiting for burn sequence" LEDs get enabled, the loop activates and waits 20 seconds before disabling the record data LED and the wait loop LED. This essentially sets the amount of time that the DAQ is recording data. It may need to be adjusted for long burn experiments.

K.4.2 The LabView Front Panel

The LabView interface is straightforward and easy to operate. The most important note is to select the COM port for the microcontroller before running the VI.

A tab on the right side allows for communication with the microcontroller. This includes fields for programming the EEPROM values, reading EEPROM values, checking the status of the controller, and entering the MAIN mode. Notably missing is the EEPROM mode button. This button is not required, as the other buttons allow for programming and reading the EEPROM mode directly, so no EEPROM mode is needed. On the right, there is a field that shows the messages received from the microcontroller. If these messages get too long, the user can clear the log by pressing the clear button.

The main figure on the VI is a picture of the feed system. The pressure and temperature sensors on the feed system are drawn relative to their positions on the VI, so the user has a good idea about the state of the system.

The top of the VI features a large fire button and 3 LED's. The three LED's correspond to status of the DAQ (whether or not it is recording data) and if the data is being collected. If the Data Working Indicator sporadically flashes, that means there is a fault somewhere in the system and data is not being continuously acquired. The third LED is the delay LED. This is the delay programmed in to allow the DAQ to collect enough information about the burn. Recall that the microcontroller controls the burn time, so the DAQ must collect data for longer than that programmed into the microcontroller.

On the bottom are a row of switches. These switches correspond to the outputs used on the feed system. When the system is installed onto the current setup, the labels of these switches will need to be updated, which is a rather simple task.

There is also a set of switches in the Unused Digital Outputs section. These switches are outputs that currently are not being used. If the user needs more digital outputs, these outputs are already programmed into the microcontroller and LabView software, so the only additional task required is dragging the switch outside and placing the additional switches in the desired location.

On the bottom is a set of buttons labeled under the Dangerous Controls category. These buttons stop the running parallel loops and should only be pressed when needed. Pressing all three of these buttons should stop the VI from running. For obvious reasons, it is not recommended to press these buttons while the valves are powered, when there is pressure in the feed lines, or when the motor is firing. Pressing these buttons can result in the loss of control over the digital outputs.

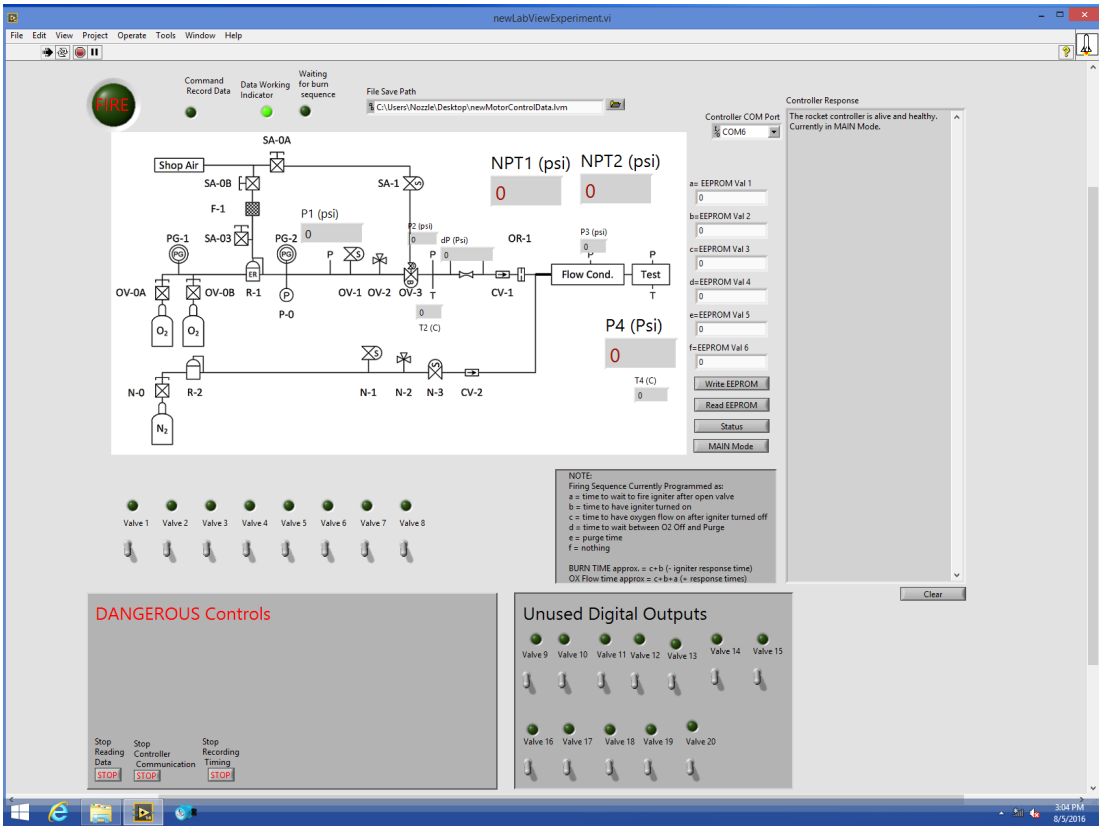

Figure K.3:]
The front panel on the new control stand LabView VI is straightforward to use. Note that the VI is easily modified.

References

[1] Space Propulsion Group,Inc., "Hybrid Rockets History - A Brief History of Hybrid Rocket Technology," http://www.spg-corp.com/News_12.php, (Accessed on 07/14/2016).

[2] Sutton, G., *Rocket propulsion elements*, Wiley, Hoboken, N.J, 2010.

[3] Space Exploration Technologies, "Merlin Engines," http://www.spacex.com/news/2013/03/26/merlin-engines, (Accessed on 07/22/2016).

[4] Space Exploration Technologies, "SpaceX Falcon 9 Test Flight 1 Press Kit," http://www.nbbd.com/events/spacex/100604-Falcon9PressKit.pdf, (Accessed on 07/22/2016).

[5] Chandler, A. A., Cantwell, B. J., Hubbard, G. S., and Karabeyoglu, A., "Feasibility of a single port Hybrid Propulsion system for a Mars Ascent Vehicle," *Acta Astronautica*, Vol. 69, 2011, pp. 1066–1072.

[6] Boiron, A. J. and Cantwell, B., chap. Hybrid Rocket Propulsion and In-Situ Propellant Production for Future Mars Missions, Joint Propulsion Conferences, American Institute of Aeronautics and Astronautics, Jul 2013, 0.

[7] Story, G., Abel, T., Claflin, S., Park, O., Arves, J., and Kearney, D., chap. Hybrid Propulsion Demonstration Program 250K Hybrid Motor, Joint Propulsion Conferences, American Institute of Aeronautics and Astronautics, Jul 2003, 0.

[8] Rao, G. V. R., "Recent Developments in Rocket Nozzle Configurations," *ARS Journal*, Vol. 31, No. 11, Nov 1961, pp. 1488–1494.

[9] Stark, R., chap. Flow Separation in Rocket Nozzles, a Simple Criteria, Joint Propulsion Conferences, American Institute of Aeronautics and Astronautics, Jul 2005, 0.

[10] Hill, P., *Mechanics and thermodynamics of propulsion*, Addison-Wesley, Reading, Mass, 1992.

[11] Bartz, D., *Turbulent Boundary-Layer Heat Transfer From Rapidly Accelerating Flow of Rocket Combustion Gases and of Heat Air*, California Institute of Technology, 1963.

[12] Karabeyoglu, A., Zilliac, G., Cantwell, B. J., DeZilwa, S., and Castellucci, P., "Scale-Up Tests of High Regression Rate Paraffin-Based Hybrid Rocket Fuels," *Journal of Propulsion and Power*, Vol. 20, No. 6, Nov 2004, pp. 1037–1045.

[13] Karabeyoglu, A. M. and Arkun, U., chap. Evaluation of Fuel Additives for Hybrid Rockets and SFRJ Systems, Propulsion and Energy Forum, American Institute of Aeronautics and Astronautics, Jul 2014, 0.

[14] "NIST Chemistry WebBook," `http://webbook.nist.gov/chemistry/`, (Accessed on 06/22/2016).

[15] Gordon, S. and McBride, B., "Cinoyter Program for Calculation of Complex Chemical Equilibrium Compositions and Applicatoins," http://www.grc.nasa.gov/WWW/CEAWeb/RP-1311.pdf, 1994, Accessed: June 5, 2015.

[16] GraphiteStore.com, Inc, "Welcome to GraphiteStore.com - supplier of graphite, carbon-fiber and ceramic products and materials." `http://www.graphitestore.com/`, (Accessed on 06/22/2016).

[17] Hoenig, C., "High density-high purity graphite prepared by hot isostatic pressing in refractory metal containers," Aug. 9 1994, US Patent 5,336,520.

[18] Linseis, "LFA 1000/1000 HT, Thermal Diffusivity and Thermal Conductivity," `http://www.linseis.com/fileadmin/_migrated/content_uploads/Laserflash_LFA_1000_ENG.pdf`, (Accessed on 03/20/2015).

[19] Incropera, F., D., D., Bergman, T., and Lavine, A., *Fundamentals of Heat and Mass Transfer*, John Wiley & Sons, Inc., 2007.

[20] Pierson, H., *Handbook of carbon, graphite, diamond, and fullerenes : properties, processing, and applications*, Noyes Publications, Park Ridge, N.J, 1993.

[21] Page, D., *The Industrial Graphite Engineering Handbook*, UCAR Carbon Co., 1991.

[22] Marlowe, M., "Elastic Properties of Three Grades of Fine Grained Grauhite to 2000ÂřC," Tech. rep., General Electric Company, June 1970, NASA Contract NAS1-9852 Rpt. No. NASA CR-66933.

[23] Taylor, R. and Kimbrough, W., "Thermophysical properties of atjs graphite at high temperatures," *Carbon*, Vol. 8, No. 5, 1970, pp. 665 – 671.

[24] Zazula, J. M., "On Graphite Transformations at High Temperature and," *Pressure Induced By Absorption of the LHC Beam, CERN-LHC-Project-Note-78*, 1997.

[25] Gerlich, D. and Fisher, E., "The high temperature elastic moduli of aluminum," *Journal of Physics and Chemistry of Solids*, Vol. 30, No. 5, 1969, pp. 1197 – 1205.

[26] "Article: Elevated temperature physical properties of stainless steels," `http://www.bssa.org.uk/topics.php?article=139`, (Accessed on 06/22/2016).

[27] Zagzebski, J., *Essentials of Ultrasound Physics*, Mosby, St. Louis, 1996.

[28] Fung, Y. C., *A first course in continuum mechanics : for physical and biological engineers and scientists*, Prentice Hall, Englewood Cliffs, N.J, 1994.

[29] Fraden, J., *Handbook of modern sensors physics, designs, and applications*, Springer Verlag, New York, 2010.

[30] "Anti-Seize Compound Nickel Anti-Seize - 8 mL - Nickel | Anti-Seize Compounds," `http://rivetsonline.com/anti-seize-compound-nickel-anti-seize-8-ml-nickel.html`, (Accessed on 06/22/2016).

[31] Narsai, P. and Cantwell, B., *Measuring Nozzle Erosion in a Rocket Motor Using Ultrasound*, American Soc. for Nondestructive Testing, Columbus, Ohio, 2015.

[32] Tsang, D., Marsden, B., Fok, S., and Hall, G., "Graphite thermal expansion relationship for different temperature ranges," *Carbon*, Vol. 43, No. 14, 2005, pp. 2902 – 2906.

[33] Hidner, P., "Thermal Expansion of Artificial Graphite and Carbon," *Journal of Research of the Rational Bureau of Standards*, Vol. 13, 1934.

[34] Bartz, D., "A simple Equation for Rapid Estimation of Rocket Nozzle Convective Heat Transfer Coefficients," Vol. 27, 1957, pp. 49–51.

[35] Beck, J., Blackwell, B., and St. Clair, C. J., *Inverse Heat Conduction, Ill-posed Problems*, John Wiley & Sons, Inc., 1985.

[36] OİĹzisİğik, M., *Inverse heat transfer : fundamentals and applications*, Taylor & Francis, New York, 2000.

[37] Mills, A., *Heat transfer*, Prentice Hall, Upper Saddle River, N.J, 1999.

[38] Moin, P., *Fundamentals of Engineering Numerical Analysis*, Cambridge University Press, 2010.

[39] Liu, J., "A stability analysis on Beck's procedure for inverse heat conduction problems," *Journal of Computational Physics*, Vol. 123, No. 1, Jan 1996.

[40] Narsai, P., Momanyi, E., Venkataraman, K., Evans, B. J., and Cantwell, B. J., chap. Indirect Heat Flux Measurements at the Nozzle Throat of a Hybrid Rocket Motor, Propulsion and Energy Forum, American Institute of Aeronautics and Astronautics, Jul 2015, 0.

[41] Omega Engineering, Inc., "Thermocouple Response Time," http://www.omega.com/temperature/ Z/ThermocoupleResponseTime.html, 2015, Accessed: January 5, 2015.

[42] Omega Engineering, Inc., "Thermocouple Wire Special Limits of Error," `http://www.omega.com/pptst/SLE_Wire.html`, (Accessed on 06/1/2016).

[43] Chandler, A., Jens, E., Cantwell, B., and Hubbard, G. S., *Visualization of the Liquid Layer Combustion of Paraffin Fuel for Hybrid Rocket Applications*, American Institute of Aeronautics and Astronautics, 2015/07/02 2012.

[44] Chandler, A. A., Cantwell, B., Alonso, J. J., Christensen, R. M., and Hubbard, S., *An investigation of liquefying hybrid rocket fuels with applications to solar system exploration*, Ph.D. thesis, 2012, [electronic resource] / Ashley Anne Chandler.; online resource; Submitted to the Department of Aeronautics and Astronautics.; Thesis (Ph.D.)–Stanford University, 2012.

[45] Jens, E. T., Cantwell, B., Close, S., Hubbard, S., Jameson, A., and Zilliac, G. G., *Hybrid rocket combustion and applications to space exploration missions*, Ph.D. thesis, 2015, [electronic resource] / Elizabeth T. Jens.; online resource; Submitted to the Department of Aeronautics and Astronautics.; Thesis (Ph.D.)–Stanford University, 2015.

[46] Zilliac, G. and Karabeyoglu, M., *Hybrid Rocket Fuel Regression Rate Data and Modeling*, American Institute of Aeronautics and Astronautics, 2015/07/02 2006.

[47] Society of Automotive Engineers, "Connections for General Use and Fluid Power - Ports and Stud Ends with ASME B1.1 Threads and O-Ring Sealing - Part 3: Light-Duty (L Series) Stud Ends (J1926/3 Ground Vehicle Standard) - SAE Mobilus," `https://saemobilus.sae.org/content/j1926/3_201003`, (Accessed on 06/23/2016).

[48] Spectite Inc., "SPECTITE - Spectite Pressure and Vacuum Sealed feedthoughs, sealing glands for process applications," `http://www.spectite.com/wf.htm`, (Accessed on 06/5/2015).

[49] NDT Systems, Inc, "Flaw Detectors: RAPTOR," http://www.ndtsystems.com/raptor, 2016, Accessed: Nov 12, 2014.

[50] Omega Engineering Inc., "Reference Guide," `http://www.omega.com/temperature/pdf/tc_temp_limits_range.pdf`, 2015, (Accessed on 06/5/2015).

[51] Cotronics Corp., "SPECIAL PURPOSE HI-TEMP ADHESIVES," `http://www.cotronics.com/catalog/28%20%20%20905%20%20906.pdf`, (Accessed on 01/12/2015).

[52] Jens, E. T., Chandler, A. A., Cantwell, B., Hubbard, G. S., and Mechentel, F., *Combustion Visualization of Paraffin-Based Hybrid Rocket Fuel at Elevated Pressures*, American Institute of Aeronautics and Astronautics, 2015/07/02 2014.

[53] Emerson Process Management, "Tescom 44 Series Regulators," https://www.regulators-emerson.com/salesofficelocator/index.cfm, (Accessed on 05/5/2015).

[54] Wilcox, D., *Elements of fluid mechanics*, DCW Industries, La CanÌČada, Calif, 2005.

[55] Lohner, K., Dyer, J., Doran, E., Dunn, Z., and Zilliac, G., *Fuel Regression Rate Characterization Using a Laboratory Scale Nitrous Oxide Hybrid Propulsion System*, American Institute of Aeronautics and Astronautics, 2015/07/02 2006.

[56] The Candlewic Company, "160 Melt Point Wax - 5560 | Candlewic," http://www.candlewic.com/store/Product.aspx?q=c49,p525, (Accessed on 06/22/2016).

[57] The Candlewic Company, "Stearic Acid | Candlewic," http://www.candlewic.com/store/product.aspx?q=c11,p167&&title=Stearic-Acid, (Accessed on 06/22/2016).

[58] Daily, J. W. and Kruger, C., "Effects of cold boundary layers on spectroscopic temperature measurements in combustion gas flows," *Journal of Quantitative Spectroscopy and Radiative Transfer*, Vol. 17, No. 3, 1977, pp. 327 – 338.

[59] Zen Seeker, "Zen Candle Stoves," http://zenstoves.net/Wax.htm, 2014, Accessed: Mar 19, 2014.

[60] Royal Society of Chemistry, "Stearic Acid," http://www.chemspider.com/ChemicalStructure.5091.html, 2015, Accessed: December 9, 2015.

[61] Measurement Computing, "USB 2408 Series," http://www.mccdaq.com/usb-data-acquisition/USB-2408-Series.aspx, 2015, Accessed: June 5, 2015.

[62] National Instruments Corporation, "cDAQ-9174 - National Instruments," http://sine.ni.com/nips/cds/view/p/lang/en/nid/207535, (Accessed on 06/23/2016).

[63] National Instruments Corporation, "NI 9205 - National Instruments," http://sine.ni.com/nips/cds/view/p/lang/en/nid/208800, (Accessed on 06/23/2016).

[64] National Instruments Corporation, "NI 9237 - National Instruments," http://sine.ni.com/nips/cds/view/p/lang/en/nid/208791, (Accessed on 06/23/2016).

[65] National Instruments Corporation, "NI 9213 - National Instruments," http://sine.ni.com/nips/cds/view/p/lang/en/nid/208788, (Accessed on 06/23/2016).

[66] National Instruments Corporation, "NI 9401 - National Instruments," http://sine.ni.com/nips/cds/view/p/lang/en/nid/208809, (Accessed on 06/23/2016).

[67] Digi-key Electronics, "MediaSensorâĎć P51 Series - SSI Technologies Inc - Voltage Output, Millivolt or Volt | Online Catalog | DigiKey Electronics," http://www.digikey.com/catalog/en/partgroup/mediasensor-p51-series/11093, (Accessed on 06/23/2016).

[68] DCC Corporation, "HotSpot II Thermocouple Welder," `http://www.dcccorporation.com/hotspot2.html`, (Accessed on 06/27/2016).

[69] Omega Engineering Inc., "Fine Diameter Thermocouple Wire," `http://www.omega.com/pptst/SPIR.html`, (Accessed on 06/23/2016).

[70] McMaster-Carr, "McMaster-Carr - NON-Porous High Alumina Ceramic Tube, 2 Bore, .094" OD x .025" ID, 18" Length," `http://www.mcmaster.com/#87175k71/=12zf7m7`, (Accessed on 06/23/2016).

[71] Bendat, J., *Random Data : Analysis and Measurement Procedures*, Wiley, Hoboken, N.J, 2010.

[72] Jens, E. T., Narsai, P., Cantwell, B., and Hubbard, G. S., chap. Schlieren Imaging of the Combustion of Classical and High Regression Rate Hybrid Rocket Fuels, Propulsion and Energy Forum, American Institute of Aeronautics and Astronautics, Jul 2014, 0.

[73] Moffat, R. J., "Describing the uncertainties in experimental results," *Experimental thermal and fluid science*, Vol. 1, No. 1, 1988, pp. 3–17.

[74] Chiaverini, M., *Fundamentals of hybrid rocket combustion and propulsion*, American Institute of Aeronautics and Astronautics, Reston, Va, 2007.

[75] Bianchi, D. and Nasuti, F., chap. CFD Analysis of Hybrid Rocket Flowfields Including Fuel Pyrolysis and Nozzle Ablation, Joint Propulsion Conferences, American Institute of Aeronautics and Astronautics, Jul 2013, 0.

[76] Kays, W. M., *Convective heat and mass transfer*, McGraw-Hill Higher Education, Boston, 2005.

[77] DeLuca, L., Galfetti, L., Maggi, F., Colombo, G., Paravan, C., Reina, A., Tadini, P., Sossi, A., and Duranti, E., chap. An Optical Time-Resolved Technique of Solid Fuels Burning for Hybrid Rocket Propulsion, Joint Propulsion Conferences, American Institute of Aeronautics and Astronautics, Jul 2011, 0.

[78] Karabeyoglu, A., Cantwell, B., and Zilliac, G., *Development of Scalable Space-Time Averaged Regression Rate Expressions for Hybrid Rockets*, American Institute of Aeronautics and Astronautics, 2015/07/02 2005.

[79] Cantwell, B., *AA283 Aircraft and Rocket Propulsion*, Stanford University, Stanford, California, 2015.

[80] "OpenCV," http://opencv.org/, Accessed: June1, 2016.

[81] "Welcome to Python.org," https://www.python.org/, Accessed: June 1, 2016.

[82] Turkowski, K., "Filters for Common Resampling Tasks," *Graphics Gems*, Elsevier BV, 1990, pp. 147–165.

[83] Minichino, J., *Learning OpenCV 3 computer vision with Python : unleash the power of computer vision with Python using OpenCV*, Packt Publishing, Birmingham, UK, 2015.

[84] Jens, E. T., Miller, V. A., Mechentel, F. S., Cantwell, B. J., and Hubbard, S., chap. A Visual Study of the Combustion of High-Regression Rate and Classical Hybrid Rocket Fuels, Propulsion and Energy Forum, American Institute of Aeronautics and Astronautics, Jul 2015, 0.

[85] Cantwell, B., *Introduction to Symmetry Analysis*, Cambridge University Press, Cambridge, UK, New York, 2002.

[86] FTDI, Ltd., "D2XX Direct Drivers," `http://www.ftdichip.com/Drivers/D2XX.htm`, (Accessed on 07/08/2016).